

1998

Electroproduction of the S(11)meson(1535) resonance at high momentum transfer

Christopher Stephen Armstrong
College of William & Mary - Arts & Sciences

Follow this and additional works at: <https://scholarworks.wm.edu/etd>



Part of the [Physics Commons](#)

Recommended Citation

Armstrong, Christopher Stephen, "Electroproduction of the S(11)meson(1535) resonance at high momentum transfer" (1998). *Dissertations, Theses, and Masters Projects*. Paper 1539623925.
<https://dx.doi.org/doi:10.21220/s2-45ag-7c85>

This Dissertation is brought to you for free and open access by the Theses, Dissertations, & Master Projects at W&M ScholarWorks. It has been accepted for inclusion in Dissertations, Theses, and Masters Projects by an authorized administrator of W&M ScholarWorks. For more information, please contact scholarworks@wm.edu.

INFORMATION TO USERS

This manuscript has been reproduced from the microfilm master. UMI films the text directly from the original or copy submitted. Thus, some thesis and dissertation copies are in typewriter face, while others may be from any type of computer printer.

The quality of this reproduction is dependent upon the quality of the copy submitted. Broken or indistinct print, colored or poor quality illustrations and photographs, print bleedthrough, substandard margins, and improper alignment can adversely affect reproduction.

In the unlikely event that the author did not send UMI a complete manuscript and there are missing pages, these will be noted. Also, if unauthorized copyright material had to be removed, a note will indicate the deletion.

Oversize materials (e.g., maps, drawings, charts) are reproduced by sectioning the original, beginning at the upper left-hand corner and continuing from left to right in equal sections with small overlaps. Each original is also photographed in one exposure and is included in reduced form at the back of the book.

Photographs included in the original manuscript have been reproduced xerographically in this copy. Higher quality 6" x 9" black and white photographic prints are available for any photographs or illustrations appearing in this copy for an additional charge. Contact UMI directly to order.

UMI

A Bell & Howell Information Company
300 North Zeeb Road, Ann Arbor MI 48106-1346 USA
313/761-4700 800/521-0600

Electroproduction of the $S_{11}(1535)$ Resonance at High Momentum Transfer

A Dissertation Presented to
The Faculty of the Department of Physics
The College of William & Mary in Virginia

In Partial Fulfillment
of the Requirements for the Degree of
Doctor of Philosophy

by
Christopher S. Armstrong

1998

UMI Number: 9904269

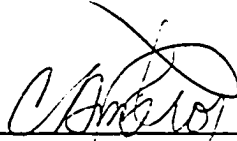
UMI Microform 9904269
Copyright 1998, by UMI Company. All rights reserved.

**This microform edition is protected against unauthorized
copying under Title 17, United States Code.**

UMI
300 North Zeeb Road
Ann Arbor, MI 48103

Approval Sheet

This dissertation is submitted in partial fulfillment of the
requirements for the degree of
Doctor of Philosophy

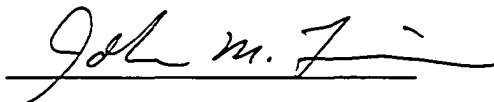


Christopher Stephen Armstrong

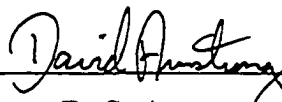
Approved, July 1998



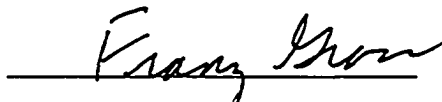
R. D. Carlini (Thesis Adviser)



J. M. Finn (Thesis Adviser)



D. S. Armstrong



F. L. Gross



P. Stoler

Rensselaer Polytechnic Institute

Dedication

Dedicated with love and appreciation to Alejandra,
who, while I played physics, was busy with the immeasurably
more important job of giving a good start to our children;

and dedicated also to my parents,
for giving me my own good start.

Contents

1	Introduction	2
1.1	The Goal of the Experiment	3
1.2	The $S_{11}(1535)$ Resonance and the $p\eta$ Decay Channel	5
1.3	Experimental Formalism	11
1.3.1	Kinematic Definitions	11
1.3.2	Cross Section and Multipole Definitions	14
1.3.3	Helicity Amplitudes	17
1.4	The Nonrelativistic Constituent Quark Model	21
1.5	Historical Review and Literature Survey	25
1.5.1	Quark Models of Hadrons	25
1.5.2	Perturbative QCD	29
1.5.3	Other Theoretical Approaches	29
2	Experimental Apparatus and Data Acquisition	33
2.1	Overview of the Experiment	33
2.2	The Accelerator	38
2.3	The Hall C Beamline Instrumentation	39
2.3.1	Beam Energy Measurement	39
2.3.2	Beam Position Measurement	39

2.3.3	Beam Current Measurement	41
2.4	The Cryogenic Target	41
2.5	Target Rastering	43
2.6	The Electron Spectrometer	43
2.6.1	The SOS Magnetic Elements	46
2.6.2	The SOS Scintillator Arrays	46
2.6.3	The SOS Drift Chambers	50
2.6.4	The SOS Gas Čerenkov Detector	50
2.6.5	The SOS Lead-Glass Calorimeter	52
2.7	The Proton Spectrometer	52
2.7.1	The HMS Magnetic Elements	54
2.7.2	The HMS Scintillator Arrays	56
2.7.3	The HMS Drift Chambers	57
2.8	Trigger Electronics and Data Acquisition	57
2.9	Materials in the Experimental Apparatus	61
3	Monte Carlo Simulation of the Experiment	63
3.1	Overview of the Simulation	63
3.1.1	Calculation of the Monte Carlo Yield	65
3.1.2	Passage Through Material	68
3.2	Event Generation	69
3.2.1	Resonance Production	69
3.2.2	Multi-Pion Background	71
3.2.3	Elastic Scattering	72
3.3	Radiative Processes	74
3.3.1	The Multi-Photon Prescription	78
3.4	The Spectrometer Monte Carlos	81

4	Data Analysis	83
4.1	Overview of the Analysis	83
4.2	Hall C Replay Software	85
4.2.1	Drift Distance Mapping and Track Reconstruction	86
4.2.2	Reconstruction of Target Quantities	88
4.2.3	Scintillator Timing Corrections	89
4.2.4	Particle Identification and Real-Accidental Separation	93
4.2.5	Calculation of Physics Quantities	99
4.2.6	Efficiencies	99
4.3	Post-Replay Analysis	104
4.3.1	Data Checks	105
4.3.2	Normalization for Beam Charge	105
4.3.3	Target Density and Length	106
4.3.4	Proton Absorption	108
4.3.5	Target Window Background	110
4.3.6	Accidental Coincidence and HMS y_{tar} Background Subtractions	110
4.3.7	Multi-Pion Background Subtraction	111
4.3.8	Data Cuts	118
4.3.9	Corrections	120
4.3.10	Extraction of the Differential Cross Section	122
5	Results and Conclusions	124
5.1	Estimation of Systematic Uncertainties	124
5.2	Extraction of $A_{1/2}^p$	129
5.2.1	Fits to the Angular Distributions	132
5.2.2	Assumed Form of R	133

5.2.3	Fits to $ E_{0+}(W) ^2$	133
5.2.4	Calculation of $A_{1/2}^p$	137
5.3	A Constraint on the $S_{11} \rightarrow p\eta$ Branching Fraction	142
5.4	Conclusions	144
A	Beam Current Measurement in Hall C	147
A.1	The Unser Monitor	148
A.2	The Beam Current Monitors (BCM1 and BCM2)	149
A.3	The BCM Electronics	152
A.4	Frequency Structure of the Hall C Beam	152
B	Reconstruction Optimization	156
C	Tabulated Cross Section Data	162
D	List of Collaborators	177

List of Tables

2.1	Kinematics for $Q^2 \approx 2.4 \text{ GeV}^2/c^2$	35
2.2	Kinematics for $Q^2 \approx 3.6 \text{ GeV}^2/c^2$	36
2.3	SOS Specifications	44
2.4	HMS Specifications	54
2.5	Materials List	62
4.1	Experimental Backgrounds	110
4.2	Standard Cuts	121
4.3	Corrections Applied to the Data	123
5.1	Estimates of Systematic Uncertainties	127
5.2	Cut Dependence of Final Results	128
5.3	Definition of Fits 1-3	135
5.4	$S_{11}(1535)$ Parameters	138
5.5	Uncertainties Specific to $A_{1/2}^p$	138
5.6	Results of Three Fits to $ E_{0+}(W) ^2$	138
5.7	Preferred Results	139

List of Figures

1.1	Inclusive Electron Scattering Data	6
1.2	The Proton- η Decay Channel	7
1.3	The World's Data for $\sigma_{\text{res}}(ep \rightarrow e'p\eta)$ at $W \approx 1535$ MeV (Previous Data)	8
1.4	$R = \sigma_L/\sigma_T$ for $ep \rightarrow e'p\eta$	9
1.5	Disparity in W Dependence of Previous Measurements	10
1.6	Born Diagram for Resonance Electroproduction	12
1.7	Q^2 Versus ν for ${}^1\text{H}(e, e')X$	13
1.8	Reaction Plane Coordinates	13
1.9	Target Coordinates	14
1.10	Feynman Diagrams	18
1.11	The Proton Helicity Amplitudes	20
1.12	The NRCQM System	22
1.13	A Cartoon $S_{11}(1535)$	22
1.14	The NRCQM Potential	24
1.15	The World's Data for $A_{1/2}^P(S_{11})$ via $ep \rightarrow e'p\eta$ (Previous Data)	28
1.16	Leading Order pQCD Diagrams	30
1.17	$Q^3 A_{1/2}^P$ for the $S_{11}(1535)$ (Previous Data)	31
2.1	Plan View of Hall C	34

2.2	Proton Momentum Versus $\theta_{pq,lab}$ for $Q^2 \approx 2.4 \text{ GeV}^2/c^2$	37
2.3	Proton Momentum Versus $\theta_{pq,lab}$ for $Q^2 \approx 3.6 \text{ GeV}^2/c^2$	37
2.4	The Accelerator	38
2.5	Hall C Beamline Instrumentation	40
2.6	A Cryogenic Loop	42
2.7	The Target Cells	42
2.8	The Electron Spectrometer (SOS)	45
2.9	The SOS Detectors	45
2.10	The SOS Scintillator Arrays	47
2.11	The SOS Scintillator Array Electronics	48
2.12	The SOS Trigger Electronics	49
2.13	An SOS Drift Chamber	51
2.14	Cross Section of an SOS Drift Chamber	51
2.15	The SOS Gas Čerenkov and Calorimeter Electronics	53
2.16	The Proton Spectrometer (HMS)	55
2.17	The HMS Detectors	55
2.18	The HMS Scintillator Arrays	56
2.19	An HMS Drift Chamber	58
2.20	Cross Section of an HMS Drift Chamber	58
2.21	The Coincidence Electronics	60
3.1	Monte Carlo Flow Diagram	66
3.2	Background Distributions (Data and MC)	73
3.3	SOS Focal Plane Quantities, ${}^1\text{H}(e, e'p)$	75
3.4	SOS Reconstructed Quantities, ${}^1\text{H}(e, e'p)$	75
3.5	HMS Focal Plane Quantities, ${}^1\text{H}(e, e'p)$	76

3.6	HMS Reconstructed Quantities, ${}^1\text{H}(e, e'p)$	76
3.7	Data to Monte Carlo Ratios for ${}^1\text{H}(e, e'p)$	77
3.8	Data and Monte Carlo W Distributions for an ${}^1\text{H}(e, e'p)$ Setting	77
3.9	External Bremsstrahlung	79
3.10	Internal Bremsstrahlung	79
3.11	Internal Hard Corrections	79
4.1	Time Walk	91
4.2	Calorimeter and Čerenkov Signals, I	96
4.3	Calorimeter and Čerenkov Signals, II	97
4.4	β_{tof} and Coincidence Time, I	100
4.5	β_{tof} and Coincidence Time, II	101
4.6	β_{tof} and Coincidence Time, III	102
4.7	Typical M_x^2 Distribution	103
4.8	SOS Pretrigger to BCM3 Ratio for $Q^2 \approx 2.4$	107
4.9	SOS Pretrigger to BCM3 Ratio for $Q^2 \approx 3.6$	107
4.10	The Proton Cone	109
4.11	Proton Absorption Measurements	110
4.12	W Versus M_x^2	114
4.13	Individual M_x^2 Fits, Technique 1	115
4.14	Integrated M_x^2 Fits, Technique 1	116
4.15	Integrated M_x^2 Fits, Technique 2	119
4.16	The Q^2 Correction	122
5.1	$Q^2 = 2.4 \text{ GeV}^2/c^2$ Angular Distributions	130
5.2	$Q^2 = 3.6 \text{ GeV}^2/c^2$ Angular Distributions	131
5.3	Threshold Breit-Wigner Energy Dependence	134

5.4	W Dependence of the Cross Section	136
5.5	Disparity in W Dependence	136
5.6	The World's Data for $\sigma_{\text{res}}(ep \rightarrow e'p\eta)$ at $W \approx 1535$ MeV	137
5.7	The World's Data for $A_{1/2}^P(S_{11})$ via $ep \rightarrow e'p\eta$	140
5.8	$Q^3 A_{1/2}^P$ for the $S_{11}(1535)$	141
5.9	Comparison Between Inclusive and Exclusive Data, $W \approx 1535$ MeV	144
A.1	The Unser Monitor	148
A.2	BCM Calibration	150
A.3	The BCM Cavity	151
A.4	The Electronics for BCM1 and BCM2	153
B.1	SOS Reconstruction	159
B.2	HMS Reconstruction	160
B.3	Elastic θ_{pq} Distribution.	161

Acknowledgements

My thanks go first and foremost to Alex, whose help made this work possible and whose presence in my life made the effort worthwhile. If I were able to, I would convey the happiness she has brought to me, but words do not suffice. Thank you.

Special thanks, too, to Mom and to Dad and Amy, who have always encouraged me to take on new challenges, and to Carola, for all she has done for Alex and me. The two of us have been the beneficiaries of a tremendous amount of support from our parents and from others in both of our families, and I thank them all.

On the technical side, I owe much to those who assisted me on a day-to-day basis (both early in my stay at CEBAF—er, Jefferson Lab—and later, during analysis of data, when the chain binding my ankle to my desk reached only the length of the C wing in CEBAF Center): Dave Mack, Joe Mitchell, Rolf Ent, and Steve Wood. I've benefitted enormously from their accessibility and their willingness to help a neophyte learn the ropes. Dave Mack in particular has been instrumental in making my time at Jefferson Lab productive and enriching, and much of my growth as a physicist over the last several years is a direct result of his guidance. Dave was also very generous with his time when it came to revising this dissertation; if it serves as a useful document in the future, he deserves a large amount of credit.

I would like to thank several members of our collaboration who did much of the initial work on this experiment, who offered me the opportunity to analyze these data, and who together gave me many insights: Paul Stoler, Valera Frolov, John Price, and Jim Napolitano.

I am grateful to the first of my two advisers, Mike Finn, for the leeway he gave me in my studies. From the start of our association he was mindful of my best interests (whether or not they happened to coincide with his!), and he graciously allowed me to pursue a bit of physics in which I had true ownership. My second adviser, Roger Carlini, has been a reliable source of excellent advice during my stay at Jefferson Lab. I also appreciate the time and feedback the other members of my committee—Franz Gross, David Armstrong, and Paul Stoler—have given me over the last several years. Special thanks go to John Price and David Armstrong for their helpful comments on this dissertation.

The magnitude of work that went into this experiment and the other early experiments in Hall C is quite impressive. As I now take stock of the construction (most of which I missed) and commissioning of the Hall and of the initial set of experiments, I am struck by those accomplishments and by the number of people who took part in them. In what follows, my apologies to anyone I've forgotten and to those whose work I am not even aware of.

Taken collectively, the construction of the spectrometers and associated detector packages required more effort than anything else in Hall C. Those whose contributions I'm most aware of are Ben Zeidman, Chen Yan, Bill Vulcan, Derek VanWestrum, Vardan Tadevosyan, David Potterveld, Hamlet Mkrtchyan, Dave Mack, Steve Lassiter, Hal Jackson, Paul Hood, Steve Hickson, Don Geesaman, Mike Fowler, Rolf Ent, Donal Day, Roger Carlini, Paul Brindza, Herbert Breuer, Joe

Beaufait, Keith Baker, and Kevin Bailey.

John Arrington is responsible for more of the Hall C replay software than any student has a right to be. Steve Wood and John, together with Don Geesaman, Pat Welch, and Kevin Beard, wrote the bulk of the Hall C analyzer. Steve Wood and Dave Abbott were responsible for much of the data acquisition hardware and software.

Joe Mitchell, Dave Meekins, Jim Dunne, and Bart Terburg were instrumental in getting the Hall C cryotarget into operation. I'd wager that together they put in hours as long as anyone at the Lab, and for that I'm grateful. My hat is also off to Kétévi Assamagan for his patient work on the SOS matrix elements and to Dipangkar Dutta, Gabriel Niculescu, and Jinsoek Cha for their work with the HMS reconstruction. The reconstruction effort for both spectrometers took place under the guidance of Rolf Ent. Dave Mack and Chris Bochna did much of the development work on the Hall C current monitors. Chen Yan and Paul Guèye were responsible for the beam position monitors and the fast rasters.

Several people had a hand in too many projects to list. Among those whose fingerprints are found all over the Hall are Bill Vulcan, Steve Hickson, and Joe Beaufait. I also must not forget to give special thanks to the families of Mike Fowler, Steve Lassiter, Bill Vulcan, and Steve Wood for the many late-night novice-user phone calls we made to their homes. My thanks also go to other Laboratory staff, post-docs, and fellow students who played roles in getting quality physics results out of Hall C: Pawel Ambrozowicz, Steve Avery, Chris Cothran, Bill Cummings, Dave Gaskell, Kenneth Gustafsson, Wendy Hinton, Adrian Honneger, Cynthia Keppel, Doug Koltenuk, Mike Miller, Rick Mohring, Ioana Niculescu, Joerg Reinhold, and Jochen Volmer.

I would like to acknowledge the excellent work of the Jefferson Lab accelerator group; during our experiment, when running the machine was not yet routine, this group delivered quality beam. Thumbs-up to S.U.R.A. and to Jefferson Lab, who directly bankrolled a substantial fraction of my graduate schooling, and to the U. S. Department of Energy and the National Science Foundation for indirect funding. Many thanks to the Jefferson Lab computer center staff, who kept my tired workstation in operation and fielded numerous dumb-user questions as I came down many learning curves, and to Marti Bennett, Cindy Garwood, Rachel Harris, and Heather Ashley for all their day-to-day help. Thanks also to Robert Michaels, who (to my amazement) allowed me to squat in his office during my time at the Lab; to Simon Capstick for communicating preliminary results; and to Volker Burkert, Latifa Elouadrhiri, and Steve Dytman for helpful discussions.

Hugs and wet slobbery kisses to the Game Night crowd, who helped make the last six years in W'burg a great time: Bari, Sandy, Jenn, Dave, Doug, Justin, and other sometimes visitors. What began as a way of blowing off steam in between homework sets soon became a weekly gathering of good friends. Memories of our nights together will be with Alex and the kids and I for a long time.

Thanks to all of my acquaintances for tolerating my increasingly frequent discourses on the issue of animal rights. I know that as my eyes have been opened to the injustices that occur in this society, I've tended to vent on those nearby; sorry about that. . . (Yikes, here he goes!) I still find

it hard to believe that in the time I've been in graduate school, we in the U.S. have killed roughly 48,000,000,000 (yes, that's forty-eight *billion*) animals. That's almost 200 animals for every human in the U.S. That is nearly *one million animals for every American who died in the war in Vietnam*.

The majority of those 4.8×10^{10} animals we killed for food (cow, pig, and chicken carcasses are current favorites), or in the course of making food from animal products (baby cows killed so their mothers produced breast milk, mother cows killed once their milk production declined in young adulthood, male 'layer' chicks killed because they could not produce eggs and didn't grow quickly enough to be efficiently turned into food), with the byproducts used for clothing (in the form of dead-animal skin); others we killed in the name of science (often in search of cures for diseases that arise from eating dead animals and animal products) or hunted for 'sport'. Don't get me started lecturing about the fact that these practices are extracting an enormous toll on the environment; or the fact that raising and killing animals is an incredible waste of food and other resources; or the facts that, as primates closely related to chimpanzees, bonobos, and gorillas, our diet has until recently consisted mostly of vegetables and fruits (and insects, too, but I won't go there), and that most western diseases occur in large part because we've deviated from this diet; or the fact that the history of human society involves a long march towards inclusion and the granting of rights to sentient beings previously given no moral consideration. Don't get me started lecturing about the fact that *a rational person objectively assessing the philosophy of rights must acknowledge that nonhuman animals deserve basic rights*. These topics I leave to the literature [Veg98, Mar97, Spi96, Rol92]. This is not, after all, the appropriate forum for a discussion of moral, health, and environmental issues. And besides, if you get me started we'll be here all night.

ANIMAL
LIB!

Finally, thanks to you, dear reader, for putting up with me this long (now you know what my friends endure). What follows is science.

Abstract

The amplitude of the $S_{11}(1535)$ resonance at values of four-momentum transfer $Q^2 > 0$ is not explained by the nonrelativistic constituent quark model, and is currently a topic of theoretical interest; in addition, the large branching fraction of this resonance to the proton- η decay channel is not well understood. There is also controversy concerning the Q^2 regime in which perturbative QCD becomes important in describing nucleon resonances such as the S_{11} . The $p(e, e'p)\eta$ reaction is an excellent system in which to study this resonance and address the issue of possible perturbative effects: the $p\eta$ channel is not accessible to the Δ (isospin- $\frac{3}{2}$) resonances and couples only weakly to N^* (isospin- $\frac{1}{2}$) resonances other than the $S_{11}(1535)$.

The differential cross section for the process $p(e, e'p)\eta$ was measured in Hall C of the Thomas Jefferson National Accelerator Facility (TJNAF) in experiment E94-14 in December 1996. The angular distribution at center-of-momentum energies near the $S_{11}(1535)$ was measured for $Q^2 \approx 2.4$ and $3.6 \text{ GeV}^2/c^2$ (the latter being the highest- Q^2 exclusive measurement of this process to date). The Short Orbit Spectrometer (SOS) was used to detect recoil electrons and the High Momentum Spectrometer (HMS) was used to detect outgoing protons, with the η identified via missing mass. Results of fits to the differential cross section and an extraction of the helicity amplitude $A_{1/2}^p$ are presented. The cross section obtained from these new data is about 30% lower than that of the only other high- Q^2 exclusive measurement of this process. Comparison with a recent analysis of inclusive (e, e') data provides a lower bound on the $S_{11}(1535) \rightarrow p\eta$ branching fraction of $b_\eta = 0.45$.

**Electroproduction of the $S_{11}(1535)$ Resonance
at High Momentum Transfer**

Chapter 1

Introduction

This thesis describes a measurement of the differential cross section for the process $p(e, e'p)\eta$ performed in Hall C of the Thomas Jefferson National Accelerator Facility (TJNAF or Jefferson Lab, formerly CEBAF) in November and December of 1996 and the subsequent data analysis. The experiment E94-14 measured the angular distribution of the $e + p \rightarrow e' + p + \eta$ process in the invariant mass region around 1535 MeV, where it is dominated by electroproduction of the $S_{11}(1535)$ resonance [i.e., the process $e + p \rightarrow e' + S_{11}(1535)$]. We present the result of multipole fits to the angular distribution and extract the helicity amplitude $A_{1/2}^p$, which is a quantity important for constraining quark models. We also use the high- Q^2 datum of this work together with a fit to inclusive data to put a lower bound on the $S_{11}(1535) \rightarrow p\eta$ branching fraction.

In this chapter we discuss the goals of the experiment, which were to test quark models of the baryon and to search for the scaling that might indicate the onset of Perturbative Quantum Chromodynamics (pQCD). We review the experimental formalism necessary to describe the measurement. We review the basic quark model and give a historical survey of the theoretical and experimental developments surrounding the study of baryon resonances in general and the $S_{11}(1535)$ resonance in particular.

Chapter 2 explains the electron accelerator, cryogenic liquid hydrogen target, magnetic spectrometers, detectors, electronics, and other instrumentation used in the measurement.

Chapter 3 describes the Monte Carlo simulation of the experiment. This simulation included radiative processes, multiple scattering, ionization energy losses, and experimental resolutions. It

modeled background processes as well as the resonance process of interest. The simulation was used to obtain radiative corrections and the experimental acceptance, and it played a key role in the subtraction of the physics background.

Chapter 4 explicitly lists all steps taken during analysis of the data. We describe the techniques used to obtain corrections for various inefficiencies and used to perform normalization for beam charge. We detail the techniques used to subtract the physics background, and explain the checks performed on data and cuts made on those data.

In Chapter 5 we give our estimates of systematic uncertainties and explain how we arrived at those estimates. We also discuss the technique used to extract the helicity amplitude $A_{1/2}^P$ from the differential cross sections. We discuss the results of the analysis and highlight where important work remains to be done.

Appendix A is an overview of the techniques used to measure the beam current in Hall C. Appendix B discusses the procedure used to optimize the reconstruction matrix elements of the two spectrometers. Appendix C gives tabulated differential cross sections, and Appendix D lists the collaborators on the experiment.

1.1 The Goal of the Experiment

The quark model originated about thirty years ago. Since that time it has progressed from a simple mechanism with which to explain the low-lying baryon mass splittings into a family of sophisticated models that take conceptual cues from Quantum Chromodynamics (QCD). The Constituent Quark Model¹, or CQM, has enjoyed rather remarkable success on several fronts. The earliest models could qualitatively account for mass splittings among the ground-state baryons, and today various models give reasonable predictions for many charge radii, magnetic moments, and decay amplitudes. In this model the $S_{11}(1535)$ is an excited uud resonance in which one of the three quarks orbits the other two in an $l = 1$ state.

Ultimately, however, we know that the CQM is simply not the correct picture of reality. There is wide belief that QCD is the appropriate theory of the strong interaction; the naive model of the baryon as a collection of nonrelativistic massive quark states bound by an effective gluon

¹By constituent quark we mean a 'dressed' quark, i.e., a bare quark *together with* a gluonic cloud, the whole of which has a mass on the order of several hundred MeV.

confinement potential fails to represent baryonic structure, and it is perhaps surprising that the CQM describes hadrons as well as it does.

The first S_{11} electroproduction measurements in the mid 1970s showed that the form factor of this resonance fell more slowly with Q^2 than the dipole form factor and more slowly than the form factor of other baryons (such as the $D_{13}(1520)$, which is from the same $SU(6) \otimes O(3)$ [dimension, l^π] = [70, 1⁻] multiplet).² One possible explanation for this behavior at low Q^2 , a large longitudinal cross section, was effectively ruled out by a pair of longitudinal/transverse separation measurements that took place in the late 1970s. Subsequent measurements at higher Q^2 confirmed the surprising ‘stiffness’ of the S_{11} form factor.

Attempts to relativize³ the CQM have met with some success, especially in recent years, and some models now give reasonable predictions for hadronic form factors at moderate values of Q^2 ($\sim 2 \text{ GeV}^2/c^2$). In regimes where the CQM fails, we hope to gain further understanding of the baryon by discovering what degrees of freedom must be invoked to account for experimental data.

In the high- Q^2 regime we believe that QCD can be approximated using perturbative methods. Here it is expected that the quark-gluon couplings become small, and that baryon interactions can be treated using lowest-order Feynman diagrams. On one hand there are indications that pQCD applies only at very high gluon virtualities. On the other hand there is some reason to believe that nonperturbative contributions to hadronic form factors are radiatively suppressed (Sudakov corrections), which would result in perturbative manifestations in the low to medium- Q^2 regime.⁴ The point at which perturbative processes dominate hadronic form factors is currently the subject of debate.

There were two primary goals of this measurement. The first goal was to obtain high statistics exclusive differential cross section data on the process $ep \rightarrow e'p\eta$ at high Q^2 , which can reveal information about the $S_{11}(1535)$ resonance and, possibly, the composition of the second resonance region. The second goal was to extract the helicity amplitude $A_{1/2}^p$ for the $S_{11}(1535)$ resonance, which is useful not only for constraining quark models but also as a test of scaling, which is a possible indicator of perturbative effects. [The constraint on the S_{11} branching fraction to the proton- η decay channel was not an original goal of the measurement.]

²A more complete discussion of the experimental history, with references, follows (Section 1.2).

³‘Relativizing’ a model, an expression used commonly but loosely in the literature, refers to any attempt to incorporate the effects of relativistic kinematics or dynamics into the model.

⁴See Ref. [Sto93] for a good overview of this subject.

These data were taken concurrently with a measurement of the angular distribution of the process $e p \rightarrow e' p \pi^0$, from which one can extract multipoles of the $\Delta(1232)$ resonance, in particular the ratio E_{1+}/M_{1+} . Analysis of the Δ data formed the dissertation of V. Frolov [Fro98].

1.2 The $S_{11}(1535)$ Resonance and the $p\eta$ Decay Channel

Hadronic resonances decay via the strong force, and we can roughly characterize their decay time as the time it takes for light to propagate across the object. We estimate the lifetime of a hadronic resonance as

$$\Delta t \sim \frac{\Delta d}{\Delta v} \sim \frac{1 \text{ fm}}{c} \sim 3 \times 10^{-24} \text{ s} . \quad (1.1)$$

The uncertainty principle gives us a relationship between the minimum uncertainty in the energy of a particle and its lifetime. In natural units ($\hbar = c = 1$) we estimate the width of a typical hadron to be

$$\Delta m \sim \Delta E \sim \frac{1}{\Delta t} \sim \frac{1}{3 \times 10^{-24} \text{ s}} \sim 200 \text{ MeV} . \quad (1.2)$$

In the second resonance region (spanning roughly 200 MeV) there are at least eight resonances (see Fig. 1.1). There is clearly much overlap between different resonances, making the study of any single state rather difficult (particularly if it is not strong relative to its neighbors). Any technique that allows experimentalists to isolate a single resonance is very useful.

In the case of the $S_{11}(1535)$ just such an opportunity exists. This resonance is unique in that it dominates the proton- η decay channel. As shown schematically in Fig. 1.2, the N^* resonances⁵ can decay through the proton- η channel while the Δ resonances cannot. In addition, it happens that of the isospin- $\frac{1}{2}$ resonances eligible for decay to a proton and an η meson, only the $S_{11}(1535)$ does so to any appreciable extent.⁶ Thus when we detect an outgoing electron together with an outgoing proton and select the η in the final state using missing mass we largely isolate the $S_{11}(1535)$ resonance.

The (neutral) η meson was first observed in 1961 [Pev61]. The initial η photoproduction

⁵We use N^* generally to denote isospin- $\frac{1}{2}$ baryon resonances, and the name $N^*(1535)$ interchangeably with $S_{11}(1535)$. Here the asterisk (*) denotes the fact that the N^* is an excited state. The '11' subscript on the S_{11} indicates that the resonance is isospin- $\frac{1}{2}$, spin- $\frac{1}{2}$. The 'S' (for S-wave) is a carry-over from π production, and denotes the zero orbital angular momentum of the final state in $N^*(1535) \rightarrow N\pi$.

⁶The physical cause for this large $S_{11} \rightarrow p\eta$ branching fraction is not well understood in the context of the CQM. While the topic is largely beyond the scope of this work, we mention one possible explanation in Section 1.5.3.

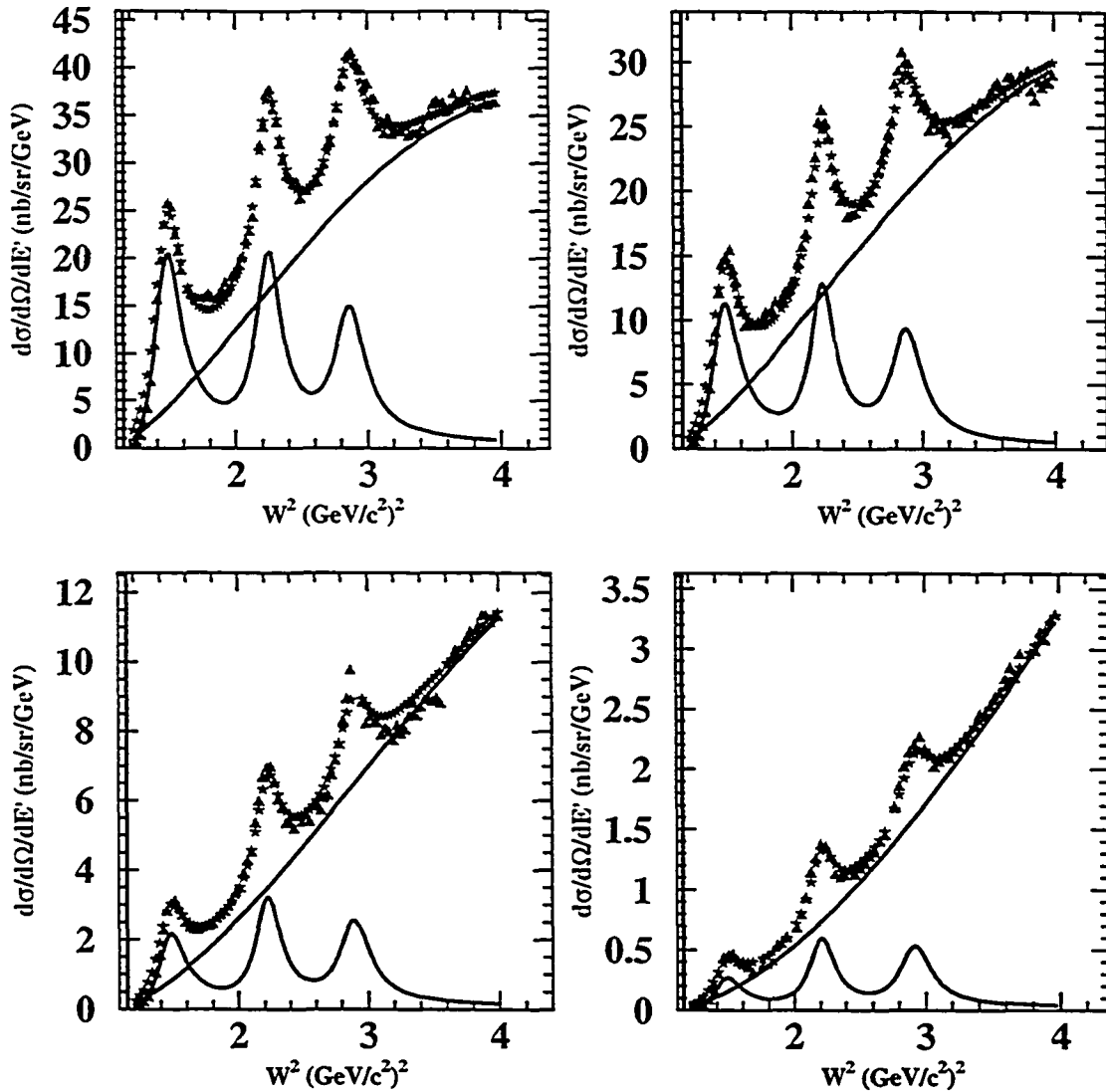


Figure 1.1: Data for ${}^1\text{H}(e, e')X$ (inclusive electron scattering from the proton) in the resonance region at four average values of momentum transfer, together with a global fit [Nic98]. From upper left to lower right, the plots are for $Q^2 = 1.3, 1.7, 2.2,$ and $3.1 \text{ GeV}^2/c^2$ (the value of Q^2 for each plot varies by $\approx 25\%$ from low to high W^2 ; we give the value of Q^2 at the second resonance region). The gray triangles are recent data from TJNAF, and the black stars give the total fit (resonant plus nonresonant parts). The monotonically increasing line in each plot shows the nonresonant part of the fit to the data, and the other line shows the resonant part. In each case the three resonance regions are clearly visible, but all three decrease rapidly with increasing Q^2 . The figure is courtesy of I. Niculescu.

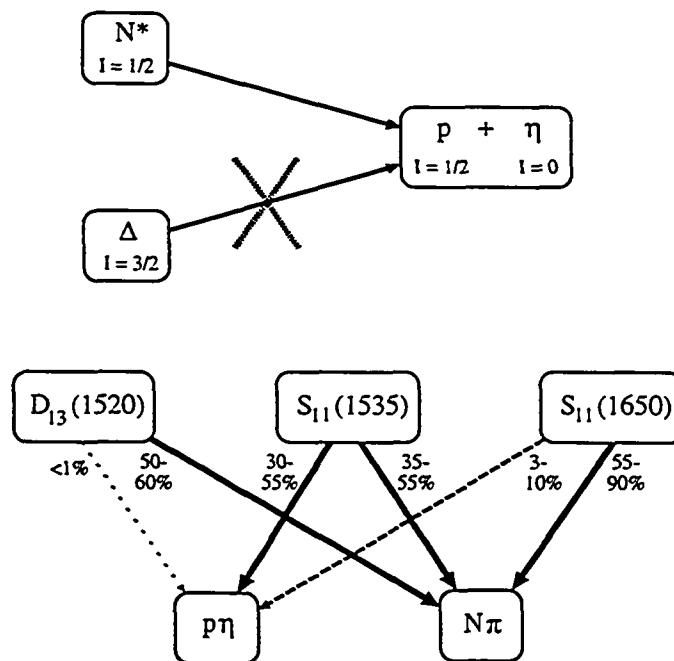


Figure 1.2: The proton- η decay channel. The top figure indicates that the Δ resonances, which are isospin- $\frac{3}{2}$, do not have access to the proton- η decay channel. The bottom figure gives rough values of the branching fractions into the proton- η and $N\pi$ channels for some of the resonances in the second region.

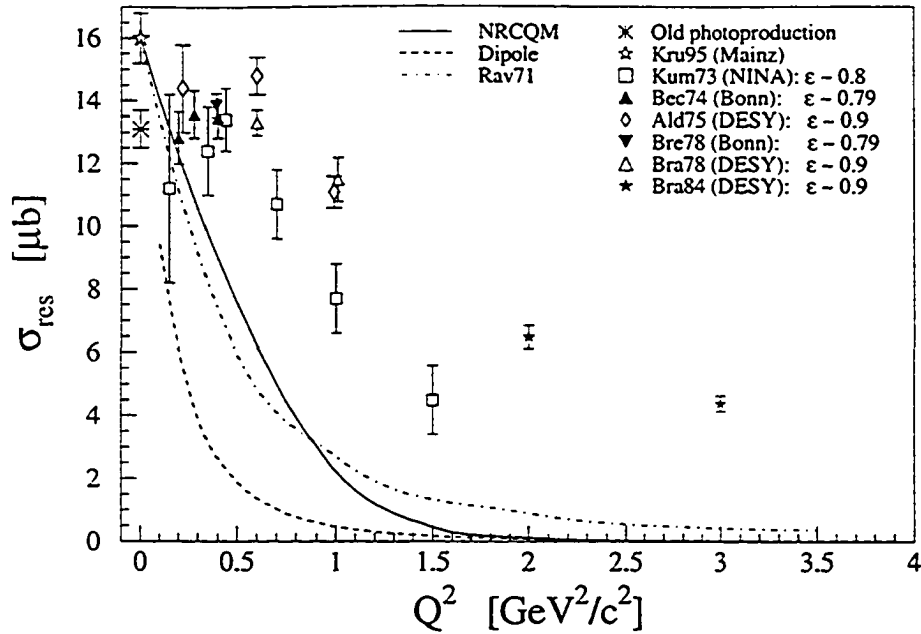


Figure 1.3: The world's data for the cross section $\sigma_{\text{res}}(ep \rightarrow e'p\eta)$ at $W \approx 1535$ MeV, prior to the present measurement. The NRCQM (from Ref. [War90]), dipole [$\sigma_{\text{res}} \propto (1 + Q^2/0.71)^{-4}$], and Ravndal [Rav71] results have been normalized at $Q^2 = 0$ to recent photoproduction data.

measurements took place in the 1960s, and it shortly became clear that the $p\eta$ channel was predominantly S -wave (see Ref. [Baj69] and references therein).

During the early 1970s there were a series of measurements of the S_{11} via the proton- η decay channel (see Fig. 1.3). The first measurement of the η electroproduction cross section was made at NINA [Kum73], followed shortly thereafter by measurements at Bonn [Bec74] and at DESY [Ald75]. Taken together these measurements covered the Q^2 range from 0 to $1.5 \text{ GeV}^2/c^2$. Assuming S_{11} dominance of the $p\eta$ channel (as was indicated by previous photoproduction results [Baj69]), these early electroproduction experiments indicated that the S_{11} cross section was significantly stronger as a function of Q^2 than the dipole form factor [Ald75] and other baryons, such as the $D_{13}(1520)$ [Bra78, Bra84].

One possible explanation at low Q^2 for the unexpected strength as a function of Q^2 (or 'stiffness') of the $S_{11}(1535)$ was that the cross section contained a large longitudinal component (which, as noted in footnote 12 on page 18, would not be seen in photoproduction). Two longitudinal/transverse separations were performed in the late 1970s [Bre78, Bra78] that effectively ruled out this possibility (see Fig. 1.4). While these measurements have large uncertainties associated

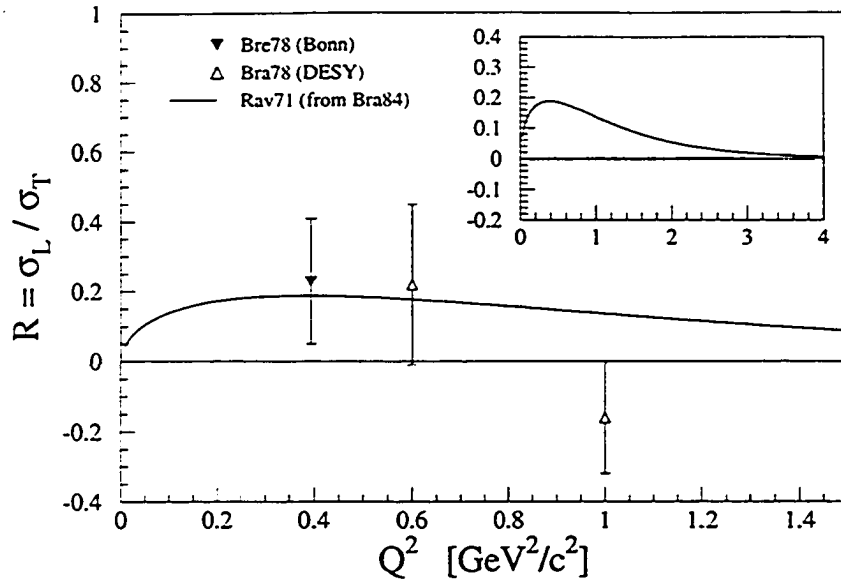


Figure 1.4: Measurements of $R = \sigma_L / \sigma_T$ for the process $ep \rightarrow e'p\eta$. The error bars reflect both statistical and systematic errors. The curve is a calculation from the quark model (Ref. [Rav71] as presented in Ref. [Bra84]), with the inset showing an extension to high Q^2 . This parameterization of the momentum dependence of R (which is given in Section 5.2.2) was assumed in this work for purposes of calculating the helicity amplitude $A_{1/2}^p$.

with them, they are the only data we presently have on the longitudinal component of this resonance. Most theoretical models predict that any longitudinal component would drop somewhat faster with Q^2 than the transverse piece. Therefore, the most that we can say about the ratio $R = \sigma_L / \sigma_T$ in the Q^2 region of the present work (~ 3 GeV²/c²) is that it is probably less than 10%, with some large uncertainty.

In the late 1970s a coincidence experiment was performed at DESY that probed higher in Q^2 than any previous measurement [Hai79, Bra84]. The experiment, similar to the present work, obtained angular distributions at $Q^2 \approx 2$ and 3 GeV²/c² that confirmed the basic S -wave nature of the $p\eta$ channel and showed a larger cross section at high Q^2 than the earlier measurement at $Q^2 \approx 1.5$ GeV²/c².

There is considerable disagreement about the energy dependence of the $ep \rightarrow e'p\eta$ cross section (and thus the resonance width Γ_R) (see Fig. 1.5). Note that the threshold of the $p\eta$ channel is at $W_{\text{thr}} = m_p + m_\eta \approx 1486$ MeV (only about 50 MeV away from the resonant mass), and has a noticeable effect on the energy dependence.

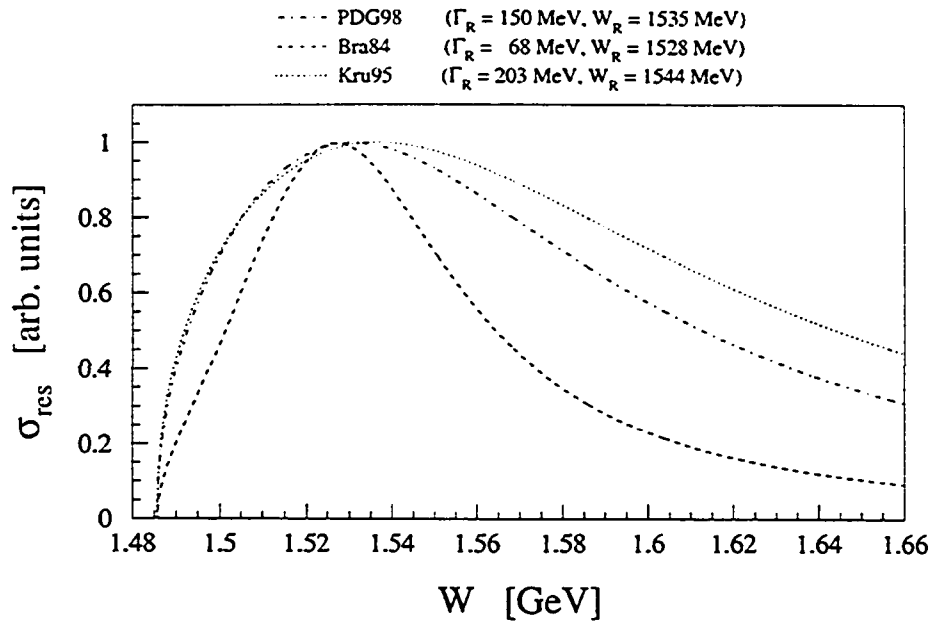


Figure 1.5: There is significant disparity in the W dependence of the $ep \rightarrow e'p\eta$ cross section as reported by different groups. Here we plot the energy-dependent Breit-Wigner curve using W_R and Γ_R as measured by Refs. [Bra84] and [Kru95], and using the estimated values given by the Particle Data Group, or PDG [PDG98]. The curves have been normalized to the same peak magnitude.

Until the current measurement, no high- Q^2 electroproduction experiments had taken place after the 1970s DESY measurement. Within the last five years, however, there have been a number of photoproduction experiments. In 1995 the results of three $\gamma p \rightarrow p\eta$ measurements were reported [Kru95, Pri95, Dyt95]. Most notably, the former obtained precise angular distributions and found a small interference contribution to the $p\eta$ channel from the $D_{13}(1520)$. The present work extends exclusive data on the $S_{11}(1535)$ to $Q^2 \approx 3.6 \text{ GeV}^2/c^2$, also achieving higher statistics than previous electroproduction measurements.

1.3 Experimental Formalism

1.3.1 Kinematic Definitions

We use the metric

$$g_{\mu\nu} = \begin{pmatrix} 1 & 0 & 0 & 0 \\ 0 & -1 & 0 & 0 \\ 0 & 0 & -1 & 0 \\ 0 & 0 & 0 & -1 \end{pmatrix}, \quad (1.3)$$

so that the inner product of two four-vectors $A = (E_a, \mathbf{p}_a)$ and $B = (E_b, \mathbf{p}_b)$ is given by $A \cdot B = E_a E_b - \mathbf{p}_a \cdot \mathbf{p}_b$. It follows that the square of the mass associated with a particle of four-momentum A is given by $m_A^2 = A \cdot A = E_a^2 - |\mathbf{p}_a|^2 > 0$ (a quantity which is invariant with choice of reference frame).

For the present experiment we are considering the interaction between an electron and a hydrogen nucleus (proton), which we model using the one-photon-exchange approximation. We picture the reaction schematically as shown in Fig. 1.6 and define the following quantities:

- $k_i = (E, \mathbf{k}_i)$, the four-momentum of the incident electron, with $|\mathbf{k}_i| \approx E$ (i.e., $m_e \approx 0$);
- $k_f = (E', \mathbf{k}_f)$, the four-momentum of the outgoing electron, with $|\mathbf{k}_f| \approx E'$;
- $p_i = (m_p, \mathbf{0})$, the four-momentum of the target proton (at rest in the lab frame);
- $p_f = (E'_p, \mathbf{p}_f)$, the four-momentum of the outgoing proton;
- $q = (\nu, \mathbf{q})$, the four-momentum transferred to the target.

With the above definitions and approximations we find that the mass-squared of the virtual photon is $q^2 = \nu^2 - |\mathbf{q}|^2 = -4EE' \sin^2(\theta_e/2) < 0$. A quantity more commonly used is the negative of the mass-squared, $Q^2 \equiv -q^2 > 0$. In similar fashion the square of the mass of the resonant state is $W^2 = (q + p_i)^2 = q^2 + m_p^2 + 2m_p\nu$ (see Fig. 1.7). Some other quantities that we will make use of are:

- the electromagnetic coupling constant $\alpha = \frac{e^2}{2\pi} \approx \frac{1}{137}$;
- the missing energy $E_x = E - E' + m_p - E'_p$;

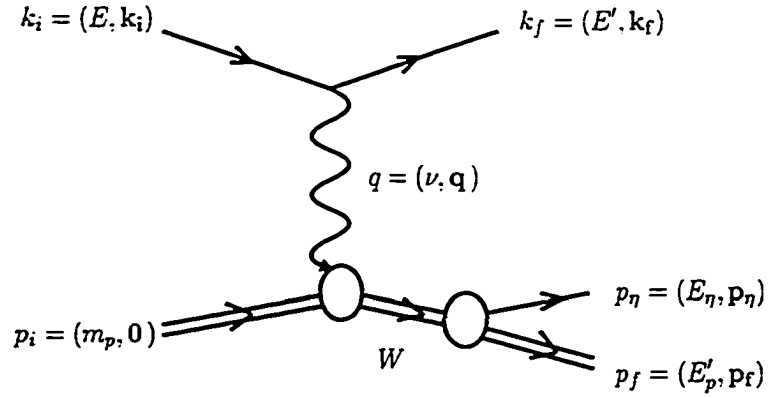


Figure 1.6: The Born diagram of the resonance electroproduction process.

- the missing momentum $\mathbf{p}_x = \mathbf{k}_i - \mathbf{k}_f - \mathbf{p}_f$;
- the square of the missing mass for $e + p \rightarrow e' + p + X$, $M_x^2 = E_x^2 - |\mathbf{p}_x|^2$;
- the electron scattering angle θ_e ; the angle of the outgoing proton with respect to \mathbf{q} , θ_{pq} ; and the missing momentum polar and azimuthal angles θ_x^* and ϕ_x , defined with respect to \mathbf{q} and the electron scattering plane. See Figure 1.8. A “*” superscript on θ_x^* or ϕ_x denotes measurement in the center-of-momentum (c.m.) of the pX system.

We also define several coordinate system variables used both in the analysis of these data and in much of the Hall C literature. Coordinates used at the target and in the detectors of either spectrometer are based on the coordinate system used in Transport (a program for modeling magnetic optics [Tra80]). We define \hat{z} to be along the central ray of the spectrometer in the direction of motion of the particles, \hat{x} to be in the dispersive direction towards higher momentum (roughly towards the floor), and $\hat{y} = \hat{z} \times \hat{x}$ (to the left when looking towards positive z). See Figure 1.9.

Given the above definitions of x and y relative to the central ray of the spectrometer, we define two slopes, x' and y' : x' is the slope of the particle trajectory projected onto the x - z plane (i.e., $x' \equiv \frac{dx}{dz}$), and y' the slope projected onto the y - z plane ($y' \equiv \frac{dy}{dz}$). In particular, we make use of these four quantities measured at $z = 0$ ($x_{\text{tar}}, y_{\text{tar}}, x'_{\text{tar}},$ and y'_{tar}) and at z of a plane nominally centered between the two drift chambers in the detector hut of either spectrometer ($x_{\text{fp}}, y_{\text{fp}}, x'_{\text{fp}},$

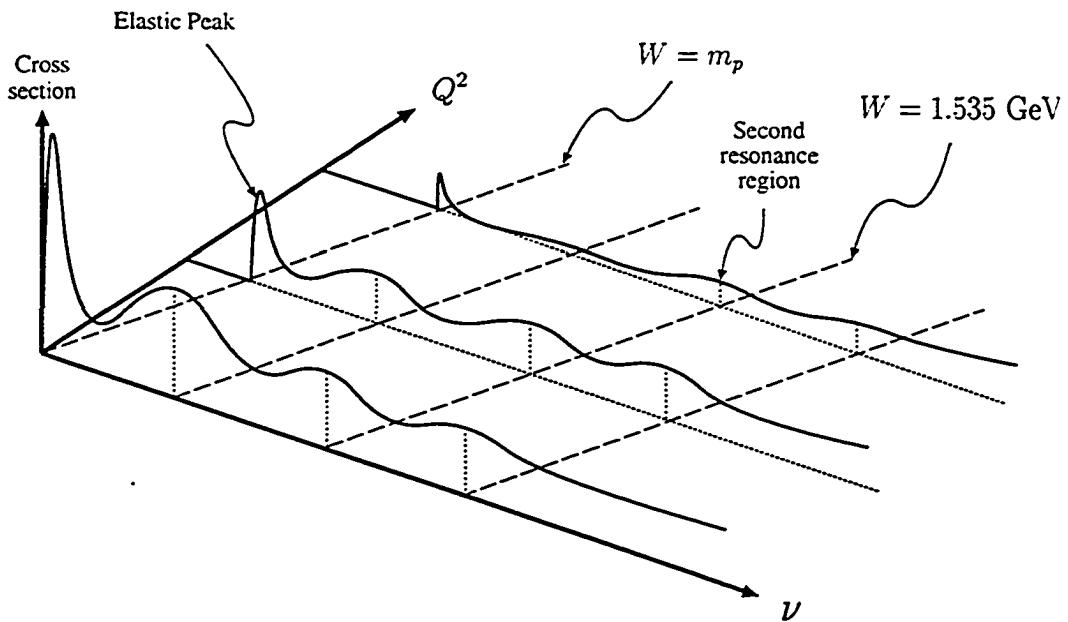


Figure 1.7: A diagrammatic figure of Q^2 versus ν for ${}^1\text{H}(e, e')X$. Q^2 , ν , and W are related by $W^2 = -Q^2 + m_p^2 + 2m_p\nu$. The dashed lines are lines of constant W .

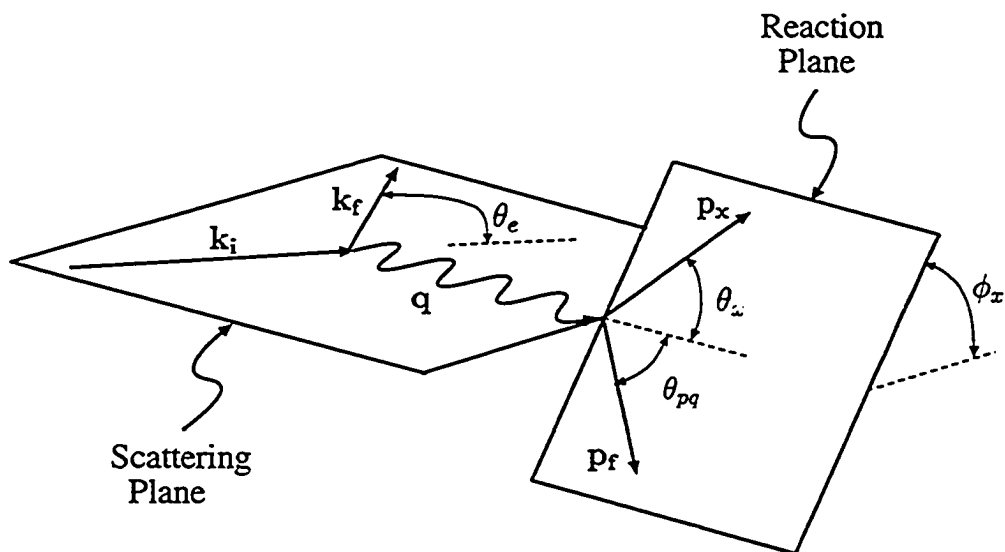


Figure 1.8: The scattering and reaction plane coordinate systems. For the events of interest the 'missing' quantities (p_x , θ_x , and ϕ_x) correspond to those for the η meson (p_η , θ_η , and ϕ_η).

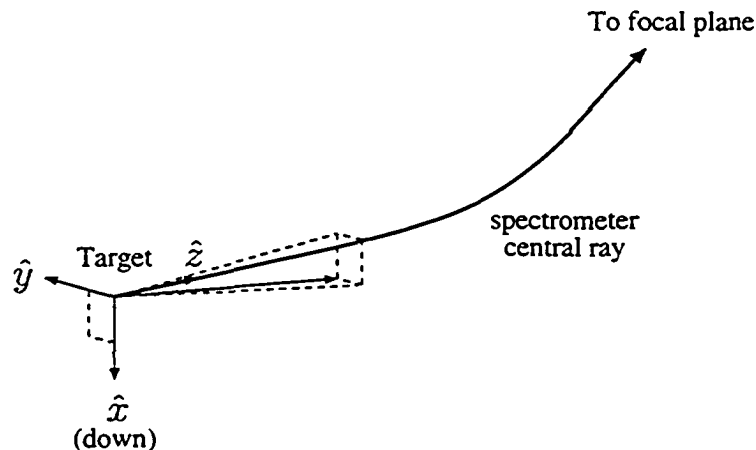


Figure 1.9: The definition of the target coordinates. Shown is a momentum vector originating at $x_{\text{tar}} = y_{\text{tar}} = 0$ with $x'_{\text{tar}} > 0$, $y'_{\text{tar}} > 0$.

and y'_{fp} .⁷ In addition, we define δ to be the fractional deviation of particle momentum (p) from the spectrometer central momentum (p_0): $\delta \equiv (p - p_0)/p_0$.

To reiterate: x'_{tar} is the slope of the particle trajectory projected onto a vertical plane through the optical axis of the spectrometer (with positive x'_{tar} toward the floor); y'_{tar} is the slope of the particle trajectory projected onto the floor (with positive y'_{tar} towards beam-left, looking into the spectrometer).

1.3.2 Cross Section and Multipole Definitions

The reaction of interest in the present work is $ep \rightarrow e'p\eta$. Following standard convention [Kum73, Bec74, Ald75] we express the five-fold differential cross section in terms of the virtual photon flux factor and, given a virtual photon, the c.m. cross section for the electroproduction of the proton- η pair (sometimes called the virtual photon cross section):

$$\frac{d^5\sigma}{d\Omega_e dE'_e d\Omega_\eta} = \Gamma_\tau(E, E', \theta_e) \frac{d^2\sigma}{d\Omega_\eta}(\gamma_\nu p \rightarrow p\eta) . \quad (1.4)$$

⁷This plane between drift chambers, commonly called the ‘focal plane’ in Hall C documentation and elsewhere in this work, is *not* in fact the true optical focal plane of the spectrometer.

Here $\Gamma_\tau(E, E', \theta_e)$ is the flux of transverse virtual photons (using the Hand convention [Han63]),

$$\Gamma_\tau(E, E', \theta_e) = \frac{\alpha}{2\pi^2} \frac{E'}{E} \frac{K}{Q^2} \frac{1}{1-\varepsilon}, \quad (1.5)$$

and the quantity K , called the equivalent real photon energy, is the energy required of a real photon to excite a proton into a resonance of mass W

$$K = \frac{W^2 - m_p^2}{2m_p}. \quad (1.6)$$

The longitudinal polarization of the virtual photon is given by

$$\varepsilon = \frac{1}{1 + 2 \frac{|q|^2}{Q^2} \tan^2(\theta_e/2)}. \quad (1.7)$$

We will also make use of the cross section differential in the variables W , Q^2 , and ϕ_e ,

$$\frac{d^5\sigma}{dW dQ^2 d\phi_e d\Omega_\eta^*} = \Gamma_\tau(W, Q^2) \frac{d^2\sigma}{d\Omega_\eta^*}(\gamma_\nu p \rightarrow p\eta), \quad (1.8)$$

where we incorporate the Jacobian $J(E, E', \theta_e | W, Q^2, \phi_e) = W/(2m_p E E')$ into the expression for the virtual photon flux,

$$\Gamma_\tau(W, Q^2) = \frac{\alpha}{4\pi^2} \frac{W}{m_p E^2} \frac{K}{Q^2} \frac{1}{1-\varepsilon}. \quad (1.9)$$

We write the unpolarized virtual photon cross section in terms of transverse, longitudinal,⁸ and interference contributions:

$$\begin{aligned} \frac{d^2\sigma}{d\Omega_\eta^*} &= \frac{d^2\sigma_T}{d\Omega_\eta^*} + \varepsilon \frac{d^2\sigma_L}{d\Omega_\eta^*} \\ &+ \sqrt{2\varepsilon(\varepsilon+1)} \frac{d^2\sigma_{TL}}{d\Omega_\eta^*} \cos \phi_\eta + \varepsilon \frac{d^2\sigma_{TT}}{d\Omega_\eta^*} \cos 2\phi_\eta. \end{aligned} \quad (1.10)$$

Following the normal procedure the individual contributions $\frac{d^2\sigma_i}{d\Omega_\eta^*}$ ($i = T, L, TL, TT$) are expressed in terms of multipoles [Wal69, War90]. In this notation, $E_{l\pm}$, $M_{l\pm}$, and $S_{l\pm}$ denote electric, magnetic, and scalar excitation multipoles, respectively; l gives the orbital angular momentum, and the ' \pm ' gives the total angular momentum via $j = l \pm \frac{1}{2}$. If we retain only S , P , and D -waves that

⁸See footnote 12 on page 18 for a brief description of these terms

are proportional to the dominant E_{0+} and S_{0+} multipoles, we have [Kno95]:⁹

$$\begin{aligned} \frac{d^2\sigma_{\tau}}{d\Omega_{\eta}^*} &= \frac{|\mathbf{p}_{\eta}^*| W}{m_p K} \left\{ |E_{0+}|^2 - \text{Re} [E_{0+}^* \{ 2 \cos \theta_{\eta}^* M_{1-} \right. \\ &\quad \left. - (3 \cos^2 \theta_{\eta}^* - 1) (E_{2-} - 3 M_{2-}) \}] \right\}; \end{aligned} \quad (1.11)$$

$$\begin{aligned} \frac{d^2\sigma_{\perp}}{d\Omega_{\eta}^*} &= \frac{Q^2}{|\mathbf{q}^*|^2} \frac{|\mathbf{p}_{\eta}^*| W}{m_p K} \left\{ |S_{0+}|^2 + 2 \text{Re} [S_{0+}^* \{ \cos \theta_{\eta}^* S_{1-} \right. \\ &\quad \left. - 2 (1 - 3 \cos^2 \theta_{\eta}^*) S_{2-} \}] \right\}; \end{aligned} \quad (1.12)$$

$$\begin{aligned} \frac{d^2\sigma_{\tau\perp}}{d\Omega_{\eta}^*} &= \sqrt{\frac{Q^2}{|\mathbf{q}^*|^2}} \frac{|\mathbf{p}_{\eta}^*| W}{m_p K} \left\{ -\sin \theta_{\eta}^* \text{Re} [E_{0+}^* (S_{1-} + 6 \cos \theta_{\eta}^* S_{2-}) \right. \\ &\quad \left. + S_{0+}^* \{ M_{1-} + 3 \cos \theta_{\eta}^* (M_{2-} - E_{2-}) \}] \right\}; \end{aligned} \quad (1.13)$$

$$\frac{d^2\sigma_{\tau\tau}}{d\Omega_{\eta}^*} = \frac{|\mathbf{p}_{\eta}^*| W}{m_p K} \left\{ -3 \sin^2 \theta_{\eta}^* \text{Re} [E_{0+}^* (E_{2-} + M_{2-})] \right\}, \quad (1.14)$$

where θ_{η}^* (ϕ_{η}) is the polar (azimuthal) angle of the η meson as defined in Section 1.3.1, and the momentum of the η in the c.m. of the hadronic resonance, $|\mathbf{p}_{\eta}^*|$, is given by

$$|\mathbf{p}_{\eta}^*| = \frac{\{ [W^2 - (m_p + m_{\eta})^2] [W^2 - (m_p - m_{\eta})^2] \}^{1/2}}{2W}. \quad (1.15)$$

The photon polarization ε was fixed (at about 0.5) for this experiment, so separation of the longitudinal and transverse contributions to the cross section was not possible. Therefore we can parameterize the virtual photon cross section in terms of its angular dependence:

$$\begin{aligned} \frac{d^2\sigma}{d\Omega_{\eta}^*} &= A + B \cos \theta_{\eta}^* + C \cos^2 \theta_{\eta}^* + D \sin \theta_{\eta}^* \cos \phi_{\eta} \\ &\quad + E \sin \theta_{\eta}^* \cos \theta_{\eta}^* \cos \phi_{\eta} + F \sin^2 \theta_{\eta}^* \cos 2\phi_{\eta}, \end{aligned} \quad (1.16)$$

where the parameters A – F are given by

$$A = \frac{|\mathbf{p}_{\eta}^*| W}{m_p K} \left\{ |E_{0+}|^2 + \varepsilon \frac{Q^2}{|\mathbf{q}^*|^2} |S_{0+}|^2 \right.$$

⁹Here the asterisk (*) is used to denote both a c.m. quantity (\mathbf{p}_{η}^*) and the complex conjugate of a complex number (E_{0+}^*).

$$- \left(\operatorname{Re} [E_{0+}^* (E_{2-} - 3M_{2-})] + 4\varepsilon \frac{Q^2}{|q^*|^2} \operatorname{Re} [S_{0+}^* S_{2-}] \right) \Bigg\}; \quad (1.17)$$

$$B = \frac{|P_\eta^*| W}{m_p K} \left\{ -2 \operatorname{Re} [E_{0+}^* M_{1-}] + 2\varepsilon \frac{Q^2}{|q^*|^2} \operatorname{Re} [S_{0+}^* S_{1-}] \right\}; \quad (1.18)$$

$$C = \frac{|P_\eta^*| W}{m_p K} \left\{ 3 \left(\operatorname{Re} [E_{0+}^* (E_{2-} - 3M_{2-})] + 4\varepsilon \frac{Q^2}{|q^*|^2} \operatorname{Re} [S_{0+}^* S_{2-}] \right) \right\}; \quad (1.19)$$

$$D = \frac{|P_\eta^*| W}{m_p K} \left\{ -\sqrt{2\varepsilon(\varepsilon+1)} \sqrt{\frac{Q^2}{|q^*|^2}} \operatorname{Re} [E_{0+}^* S_{1-} + S_{0+}^* M_{1-}] \right\}; \quad (1.20)$$

$$E = \frac{|P_\eta^*| W}{m_p K} \left\{ -3\sqrt{2\varepsilon(\varepsilon+1)} \sqrt{\frac{Q^2}{|q^*|^2}} \operatorname{Re} [2E_{0+}^* S_{2-} + S_{0+}^* (M_{2-} - E_{2-})] \right\}; \quad (1.21)$$

$$F = \frac{|P_\eta^*| W}{m_p K} \left\{ -3\varepsilon \operatorname{Re} [E_{0+}^* (E_{2-} + M_{2-})] \right\}. \quad (1.22)$$

The parameters A – C contain contributions from both transverse (σ_T) and longitudinal (σ_L) components of the cross section, while the D and E terms arise from longitudinal-transverse interference (σ_{TL}), and the F term arises from transverse-transverse interference (σ_{TT}). Note that the parameters A and C share some common terms, and if $A \gg C$, the former reduces to

$$\begin{aligned} A &\approx \frac{|P_\eta^*| W}{m_p K} \left\{ |E_{0+}|^2 + \varepsilon \frac{Q^2}{|q^*|^2} |S_{0+}|^2 \right\} \\ &\approx \frac{|P_\eta^*| W}{m_p K} |E_{0+}|^2 (1 + \varepsilon R). \end{aligned} \quad (1.23)$$

Assuming that the resonant part of the exclusive cross section dominates the nonresonant part, R here refers to the longitudinal-to-transverse ratio of the resonance itself [*i.e.*, not the ratio that is directly measured from inclusive (e, e') scattering].

1.3.3 Helicity Amplitudes

The Born diagrams for the s , u , and t -channel processes resulting in a proton- η final state are shown in Fig. 1.10. For the two resonance diagrams, three terms enter the cross section: the $\gamma p N^*$

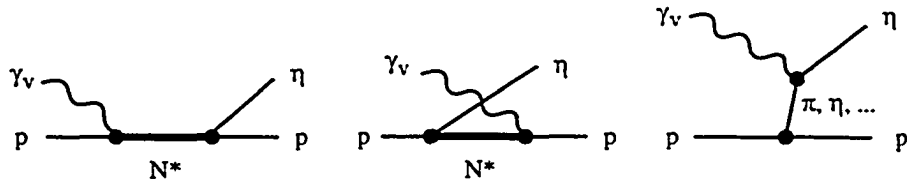


Figure 1.10: Born-level Feynman diagrams for the s , u , and t -channel processes that result in a proton- η final state. Since the η meson is neutral there is no contact (or ‘seagull’) diagram.

coupling (or ‘decay amplitude’), the N^* propagator, and the $\eta p N^*$ coupling. The former coupling is governed by the electromagnetic force, the latter by the strong force. Likewise, the three terms entering the t -channel process are the $pp\pi$ and $\gamma\pi\eta$ couplings and the meson propagator.

One of the goals of the experimental hadronic physics community in the last few decades has been to devise measurements against which predictions of QCD-inspired quark models can be tested. While predictions of the observed hadronic mass splittings (spectroscopy), magnetic moments, and charge radii are all requisite for a successful quark model, it has been pointed out that predictions of coupling strength are a more fundamental quark model test [Dre72]. In particular, measurements of couplings and their Q^2 dependence test the quark model wave functions. These couplings are conveniently expressed in terms of the transition matrix elements between states of different helicity.

The helicity λ of a particle is defined as the projection of its spin in its direction of motion. Massive particles with spin s can in general have the $2s + 1$ helicity states $-s, -s + 1, \dots, s - 1, s$, while massless objects are restricted to helicity $\pm s$.^{10,11} In particular, virtual photons (nonzero mass) may assume the helicity states $\lambda_\gamma = 0, \pm 1$, while real (massless) photons are restricted to $\lambda_\gamma = \pm 1$.¹² For the present work we are interested in proton targets, which are states of helicity $\lambda = \pm \frac{1}{2}$.

The helicity *amplitude* is the matrix element which connects states of different helicity. For an

¹⁰See, for example, Ref. [Gro93], pp. 53–56.

¹¹Note that the sign of the helicity for a massive particle is necessarily frame-dependent; one can always choose a Lorentz transformation such that the direction of motion of the particle (and thus its helicity) is reversed.

¹²Photons with helicity ± 1 have electromagnetic fields transverse to their direction of motion, and are called ‘transverse’; photons of helicity 0 have an electric field aligned with their direction of motion, and are called ‘longitudinal’ or ‘scalar’. Photoproduction (with photon mass $q^2 = -Q^2 = 0$) measures only the transverse component of the cross section; electroproduction ($q^2 < 0$) probes both the transverse and longitudinal components. See, for example, Ref. [Per87], pp. 82–83.

initial nucleon state $|N\rangle$ with helicity λ and final excited state $|N^*\rangle$ with helicity λ' we can write

$$A_{\lambda'}^{NN^*} = \langle N^*, \lambda' | \mathcal{H}_{em} | N, \lambda \rangle, \quad (1.24)$$

where \mathcal{H}_{em} is the electromagnetic transition Hamiltonian. We use superscripts to denote the initial and final hadrons (or, more commonly, just the initial hadron) and a subscript to indicate the final state helicity. Dependence on Q^2 or on the initial hadron and photon helicities may be indicated parenthetically. We use 'A' to denote amplitudes due to excitation by transverse photons, 'S' to denote those associated with longitudinal photons.

We represent the helicity transition of a proton into an excited resonant state schematically in Fig. 1.11. A consequence of parity conservation is that, for a transition from helicity λ to λ' ,

$$A(-\lambda', -\lambda) = PP'(-1)^{(J'-J)}A(\lambda', \lambda), \quad (1.25)$$

where P (P') and J (J') are the intrinsic parity and spin of the initial (final) state, respectively [Jac59]. In the case of a proton ($J^P = \frac{1}{2}^+$) excited to an S_{11} resonance ($J^P = \frac{1}{2}^-$), we have that

$$A(-\lambda', -\lambda) = A(\lambda', \lambda). \quad (1.26)$$

In other words, there are two ways to combine photon and proton helicities to get (say) a final state of helicity $\frac{1}{2}$, but for parity-conserving electromagnetic interactions those two $A_{1/2}$ amplitudes are the same. Furthermore note that, since the $S_{11}(1535)$ is a spin- $\frac{1}{2}$ resonance, the $A_{3/2}$ amplitude does not apply to this work.

The amplitude $A_{1/2}$ for the process $\gamma p \rightarrow S_{11}(1535)$ is expressed in terms of the contribution of the $S_{11}(1535)$ to the E_{0+} multipole *at the resonance mass* $W = W_R$ by Ref. [PDG76]¹³

$$\begin{aligned} A_{1/2} &= \left[(2J+1) \pi \frac{|\mathbf{P}_\eta^*|_R W_R}{m_p K} \frac{W_R}{m_p} \frac{\Gamma_R^2}{\Gamma_\eta} \right]^{1/2} \text{Im} [E_{0+}(W = W_R)] \\ &= \left[2\pi \frac{|\mathbf{P}_\eta^*|_R W_R}{m_p K} \frac{W_R}{m_p} \frac{\Gamma_R}{b_\eta} \right]^{1/2} |E_{0+}(W = W_R)|. \end{aligned} \quad (1.27)$$

¹³Note the distinction between multipoles, which characterize the reaction $e p \rightarrow e' p \eta$ (i.e., specific to the $p\eta$ channel, but through *all* possible intermediate states), and the helicity amplitude, which applies only to the excitation process $e p \rightarrow N^*$ (i.e., specific to the resonant state N^* but independent of any particular decay channel).

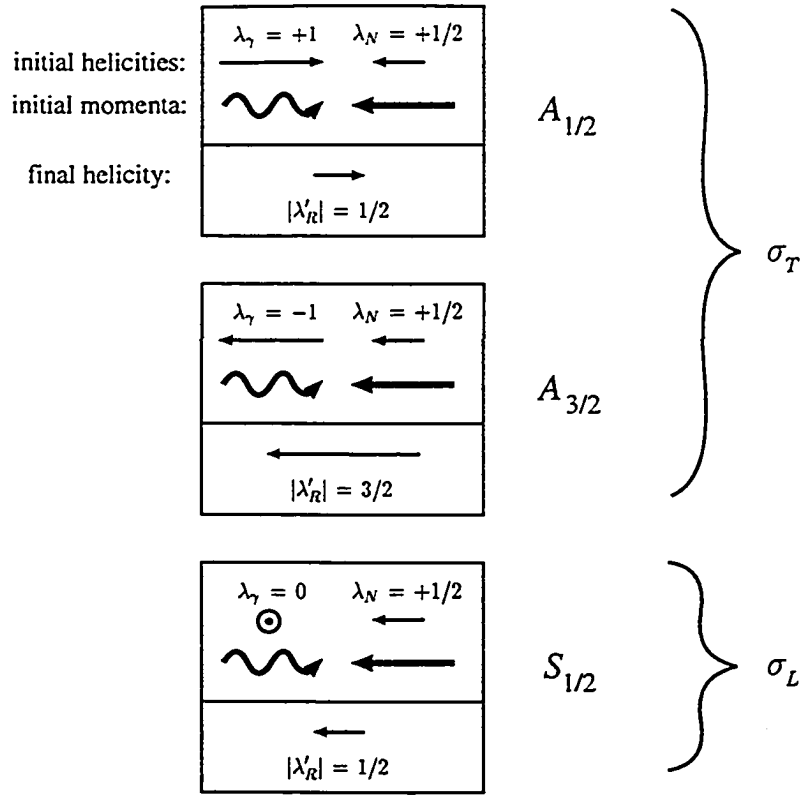


Figure 1.11: Proton helicity amplitudes in the c.m. frame. Note that $A_{1/2}$ and $A_{3/2}$ both apply to real and virtual photons while $S_{1/2}$ applies only to virtual photons. Only the $A_{1/2}$ and $S_{1/2}$ apply to the present experiment, since the $S_{11}(1535)$ is a spin- $\frac{1}{2}$ object.

Here Γ_η and Γ_R are the partial and full widths of the resonance, and we have made use of $J = \frac{1}{2}$ and the branching fraction $b_\eta = \Gamma_\eta/\Gamma_R$ for the process $S_{11}(1535) \rightarrow p\eta$. For reference we also relate $A_{1/2}$ to the resonant part of the experimentally measured cross section at the resonance mass. If S -wave multipoles dominate, integration of the resonant part of Eq. 1.10 over Ω_η^* yields

$$\begin{aligned}\sigma_{\text{res}} &= \sigma_T + \varepsilon\sigma_L \\ &= \sigma_T (1 + \varepsilon R),\end{aligned}\tag{1.28}$$

with

$$\sigma_T = 4\pi \frac{|\mathbf{p}_\eta^*|_R W_R}{m_p K_R} |E_{0+}(W_R)|^2\tag{1.29}$$

and

$$\sigma_L = 4\pi \frac{|\mathbf{P}_\eta^*|_R W_R}{m_p K_R} \frac{Q^2}{|\mathbf{q}^*|^2} |S_{0+}(W_R)|^2. \quad (1.30)$$

Neglecting contributions of resonances other than the $S_{11}(1535)$, the combination of Eqs. 1.27, 1.29, and 1.28 yields

$$A_{1/2} = \left[\frac{W_R \Gamma_R}{2m_p b_\eta} \sigma_\tau(W = W_R) \right]^{1/2} \quad (1.31)$$

$$= \left[\frac{W_R \Gamma_R}{2m_p b_\eta} \frac{\sigma_{\text{res}}(W = W_R)}{1 + \epsilon R} \right]^{1/2}. \quad (1.32)$$

1.4 The Nonrelativistic Constituent Quark Model

Here we review the basic concepts underlying the Nonrelativistic Constituent Quark Model (NRCQM) of Isgur and Karl as it pertains to baryons [Isg77, Isg78], borrowing directly from reviews by Capstick [Cap88] and Isgur [Isg91]. In Section 1.5.1 we place this model in the proper historical context and review more recent developments.

The baryon in the Isgur-Karl NRCQM is treated as a system of three constituent quarks. Each constituent quark represents a state consisting of a current (massless) quark plus an associated gluon cloud, the whole of which is massive (on the order of a few hundred MeV) and effectively point-like. The model is inspired by the ‘flux tube picture’ [Isg83], in which the quarks move in an adiabatic potential bound by three gluonic flux tubes.

Working in the c.m. of the entire system, we have quarks ‘1’ and ‘2’ (which we label the ρ system) in some relative state of orbital angular momentum (see Fig. 1.12). The third quark, ‘3’, is in some orbital angular momentum state relative to the ρ system [we label the (ρ , quark 3) pair the λ system]. The nucleon, for example, consists of a ρ system in an S -wave ($l = 0$) state together with a λ system in an S -wave state. For the $S_{11}(1535)$ the ρ system is in an S -wave state¹⁴ while the λ system is in a P -wave ($l = 1$) state (See Fig. 1.13).

The assumed form of the Hamiltonian consists of spin-independent and spin-dependent parts:

$$H = H_{\text{s.i.}} + H_{\text{s.d.}}. \quad (1.33)$$

¹⁴Note that the ‘ S ’ of ‘ $S_{11}(1535)$ ’ does *not* refer to this S -wave state; see footnote 5 on page 5.

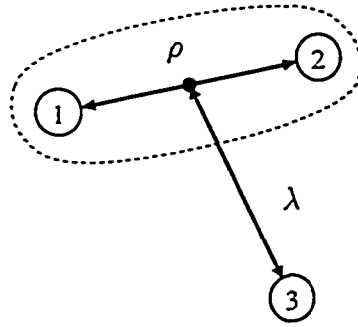


Figure 1.12: A schematic representation of the NRCQM system.

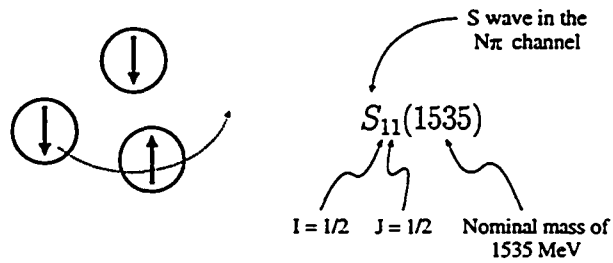


Figure 1.13: A cartoon of the $S_{11}(1535)$ in the constituent quark picture, together with an explanation of the notation.

The spin-independent part is given by

$$H_{\text{s.i.}} = \sum_i \left(m_i + \frac{p_i^2}{2m_i} \right) + \sum_{i<j} V(r_{ij}), \quad (1.34)$$

where the potential $V(r_{ij})$ contains color, linear confinement, and Coulomb terms (with r_{ij} denoting the separation between the i^{th} and j^{th} quarks):

$$V(r_{ij}) = C_{qqq} + \frac{1}{2} b r_{ij} - \frac{2\alpha_s}{3r_{ij}}. \quad (1.35)$$

The problem is rendered solvable by the assumption that the potential $V(r_{ij})$ can be approximated by a harmonic oscillator potential plus perturbation (see Fig. 1.14):

$$V(r_{ij}) \approx \frac{1}{2} K r_{ij}^2 + U(r_{ij}) \quad (1.36)$$

or, collecting all spin-independent terms except the perturbation into the harmonic oscillator Hamiltonian H_0 ,

$$H_{\text{s.i.}} = H_0 + \sum_{i<j} U(r_{ij}). \quad (1.37)$$

In the Isgur-Karl model the spin-dependent term is analogous to the hyperfine interaction of atomic physics (*i.e.*, the interaction between two intrinsic magnetic moments), with both a contact term and a tensor term:

$$\begin{aligned} H_{\text{s.d.}} &= H_{\text{hyp}}^{ij} \\ &= \sum_{i<j} \frac{2\alpha_s r_{ij}}{3m_i m_j} \left(\underbrace{\frac{8\pi}{3} \vec{S}_i \cdot \vec{S}_j \delta^3(\vec{r}_{ij})}_{\text{contact}} \right. \\ &\quad \left. + \underbrace{\frac{1}{r_{ij}^3} \left[\frac{3\vec{S}_i \cdot \vec{r}_{ij} \vec{S}_j \cdot \vec{r}_{ij}}{r_{ij}^2} - \vec{S}_i \cdot \vec{S}_j \right]}_{\text{tensor}} \right). \end{aligned} \quad (1.38)$$

The contact term enters when the two magnetic dipoles have zero relative orbital angular momentum, while the tensor term enters only when the pair has nonzero orbital angular momentum. Notably absent from the spin-dependent Hamiltonian are spin-orbit interactions; they are not

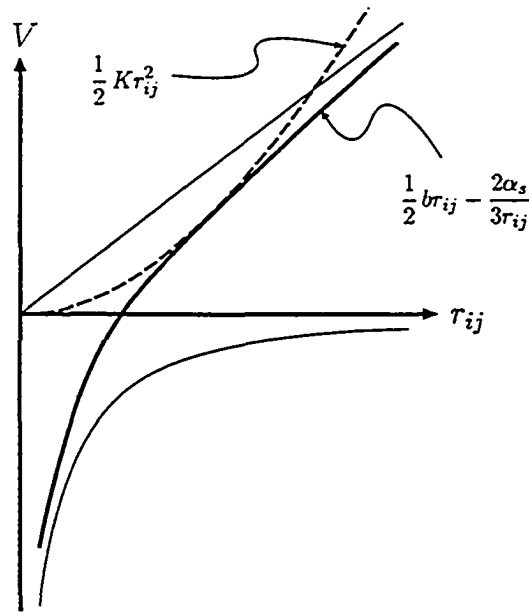


Figure 1.14: A figure showing the interquark potential in the NRCQM. The model assumes that the total potential (heavy solid line), which is the sum of the linear confinement term, the Coulomb $1/r$ term (thin solid lines), and the color potential C_{qqq} (not shown), can be approximated by a harmonic oscillator (dashed line) plus a perturbation over some range of quark separation distance r_{ij} .

included because they result in mass splittings larger than those observed.

The wavefunctions used in the Isgur-Karl model consist of spatial (ψ), spin (χ), flavor (ϕ), and color (C) parts. The spatial wavefunctions ψ are taken to be the eigenstates of H_0 , the usual harmonic oscillator wavefunctions with a change of variables appropriate for the ρ - λ system. In the case of the zero-strangeness sector (only u and d quarks), the quark masses are roughly equal, and the ρ and λ harmonic oscillators are degenerate. The spin wavefunctions are the usual angular momentum multiplets ($\chi = \uparrow\uparrow\uparrow, \frac{1}{\sqrt{2}}(\uparrow\downarrow\uparrow - \downarrow\uparrow\uparrow)$, etc.) and the flavor wavefunctions the usual flavor multiplets ($\phi = uuu, \frac{1}{\sqrt{3}}(uus + usu + suu)$, etc.). The color singlet $C = \frac{1}{\sqrt{6}}(\text{RBY} - \text{BRY} + \text{BYR} - \text{YBR} + \text{YRB} - \text{RYB})$ is antisymmetric; since the Pauli exclusion principle requires that the final baryon states are antisymmetric, the (space \times spin \times flavor) parts of the wavefunctions are constructed to be totally symmetric.

The matrix elements of both the perturbation $U(r_{ij})$ and the hyperfine interaction H_{hyp}^{ij} are calculated in these eigenstates of H_0 and diagonalized, yielding predictions for mass splittings of the light-quark baryons. The spectroscopic results of the model are quite successful [Cap88].

We forego discussion of the various ways in which relativistic effects have been incorporated into this model; the reader is referred to the literature pertaining to the individual models. It is worth noting, however, that relativization as performed by Godfrey and Isgur [God85] and Capstick and Isgur [Cap86] overcomes several criticisms of the model. In addition to the fact that relativistic kinematics and dynamics are incorporated, the value of the strong coupling α_s is smaller (and closer to the fundamental QCD value) than that required in the nonrelativistic formulation. The smaller α_s results in smaller spin-orbit forces, which no longer need be neglected. The spectroscopic predictions of the relativized model are better in some sectors and somewhat worse in others than those of the nonrelativistic model, but are in general very good *for both mesons and baryons* using the *same set of model parameters*. For more detail the interested reader is again referred to Ref. [Cap88].

We also forego discussion of the calculation of form factors (*i.e.*, the Q^2 dependence of amplitudes). A overview of the general concept is given in Ref. [Hal84], and discussion of how Q^2 dependence enters the calculations of a particular model may be found, for example, in Ref. [War90].

1.5 Historical Review and Literature Survey

1.5.1 Quark Models of Hadrons

We now take a step back and review the development of the quark model from a historical perspective, focussing in the later material on results specific to the $S_{11}(1535)$, to electroproduction, and to proton targets. Our intent is not to provide a comprehensive review but to touch on highlights and to give a starting point for further study.

In 1964 Gell-Mann [Gel64] and Zweig [Zwe64] introduced the idea of fractionally charged quarks (u,d,s) in a broken $SU(3)$ symmetry as a means of explaining the multiplet structure of spin- $\frac{1}{2}$ elementary particles (p, n, Σ^+ , Σ^0 , Σ^- , Λ , Ξ^0 , and Ξ^-). In this model the baryons are represented by quarks in various states of orbital excitation. The proton, for example, is a three-quark state with no orbital angular momentum; the $S_{11}(1535)$ consists of one quark in an $l = 1$ state relative to an $l = 0$ quark pair.

Shortly afterwards, color $SU(3)$ was applied to this simple (u,d,s) quark model in order to solve

the fermion statistics problem of three identical up quarks in the Δ^{++} system, thus preserving the exclusion principle for quarks [Gre64]. By requiring colored quarks to exist only in ‘colorless’ combinations (color singlets) one could also explain why the observed hadrons were limited to states of qqq (baryons), $\bar{q}\bar{q}\bar{q}$ (antibaryons), and $q\bar{q}$ (mesons) (and not other combinations, like qq or $qqqq$).

In 1969 Copley, Karl, and Obryk formulated a NRCQM using harmonic forces between pairs of quarks [Cop69]. Using this model they calculated matrix elements for single pion photoproduction off the proton and the neutron. The amplitudes compared reasonably well with experimental photoproduction data.

In 1971 Feynman, Kislinger, and Ravndal obtained a naive relativization of a quark model, also using harmonic interactions [Fey71]. The model was intentionally simplistic in order that they could use it to calculate as many observables as possible. They were able to predict photoproduction amplitudes (*i.e.*, amplitudes for $\gamma_v N \rightarrow N^*$) for a number of hadronic resonances. Ravndal extended those results to electroproduction by assuming a dipole form factor Q^2 dependence and deriving cross sections¹⁵ of many resonances [Rav71]. The model agreed reasonably well with the inclusive resonance data that existed at the time. In addition, it correctly indicated small longitudinal contributions in the resonance region, and it predicted the existence of the $P_{13}(1720)$.

By the early 1970s quark models were having some success predicting the spectroscopy of hadronic states. At the same time there was new experimental evidence indicating the existence of nucleon constituents; both the onset of Bjorken scaling in deep inelastic lepton scattering and the back-to-back jets arising from e^+e^- annihilation were clear signals of substructure.

Meanwhile some of the consequences of QCD (asymptotic freedom, infrared slavery) had been worked out, and the theory of exact color $SU(3)$ symmetry was rather well-supported (albeit indirectly) by several pieces of experimental evidence. Firstly, the experimental values of $R = \sigma(\text{hadrons})/\sigma(\mu^+\mu^-)$ from e^+e^- annihilation were close to those predicted by incorporating color into quark counting (off by a factor of three without color). Secondly, the presence of large transverse-momentum (p_T) events in μN scattering hinted at the existence of glue. Thirdly, the π^0 decay rate predicted using colored quarks agreed well with experiment (off by an order of magnitude without color).

¹⁵These cross sections fell more slowly than a pure dipole because of quark spin excitation terms.

By the mid 1970s several quark models of hadrons included QCD-inspired features. Horgan and Dalitz [Hor73, Hor74] and DeRújula, Georgi, and Glashow [Ruj75] used a one-gluon exchange (Coulomb-like) plus linear confinement potential together with constituent quarks to predict mass splittings between ground-state baryons. Kubata and Ohta predicted photoproduction amplitudes with a model that included the spin-orbit excitation [Kub76]. Foster and Hughes added quark form factors to a similar model and used it to predict the Q^2 -dependence of several resonance amplitudes [Fos82].

Isgur and Karl added the color hyperfine part of the two-body interaction potential to a quark model and used the model to calculate mass splittings and photon decay amplitudes for many baryons [Isg77, Isg78]. Koniuk and Isgur combined this model with a model for strong decays to explain the disparity between resonant states predicted by the quark model and those observed experimentally [Kon80]. Godfrey and Isgur later incorporated relativistic effects into this model and obtained mass predictions for mesons [God85], and Capstick and Isgur extended the relativization to baryons [Cap86].

One of the major shortcomings of the NRCQM has been its failure to reproduce hadronic form factors above a few GeV^2/c^2 or [as in the case of the $S_{11}(1535)$] even lower (see Fig. 1.15). As a result, much work in the last decade has gone towards incorporating relativistic effects in the CQM. Konen and Weber relativized the model using light-cone dynamics and obtained S_{11} helicity amplitudes [Kon90], and this work was more recently extended by Stanley and Weber [Sta95].

Warns and collaborators [War90] and Close and Li [Clo90, Li90] used relativized Hamiltonians together with the Isgur-Karl model wavefunctions to predict helicity amplitudes as a function of Q^2 . Both of these works used transition operators that included higher order terms consistent with those in the wavefunctions.

Capstick applied the transition operator of Close and Li to relativized-model wavefunctions and calculated photoproduction amplitudes for many baryon resonances [Cap92]. He pointed out the problematic nature of using such a model to rigorously calculate these amplitudes at $Q^2 > 0$. Helicity asymmetries (*e.g.*, $\frac{A_{1/2}^2 - A_{3/2}^2}{A_{1/2}^2 + A_{3/2}^2}$) and ratios of helicity amplitudes (*e.g.*, $\frac{A_{1/2}(D_{13})}{A_{1/2}(S_{11})}$), which do not suffer the same problems at $Q^2 > 0$ as the amplitudes themselves, were calculated. More recently, Capstick and Keister have investigated the effects of relativity by calculating helicity amplitudes for a number of baryons using light-front Hamiltonian dynamics [Cap95, Cap98].

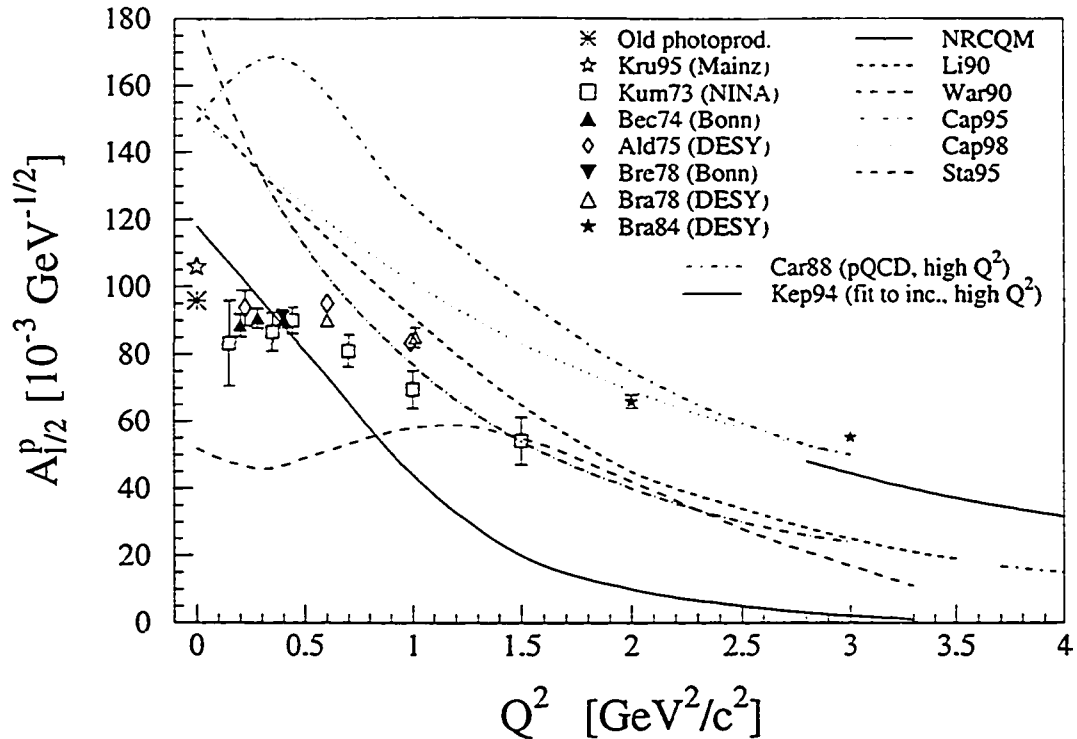


Figure 1.15: The world's data for $A_{1/2}^p(S_{11}(1535))$ measured via the $p\eta$ channel, prior to the present measurement, together with some theoretical predictions. The data points are calculated from $ep \rightarrow e'p\eta$, $W \approx 1535$ MeV cross section data assuming an S_{11} full width $\Gamma_R = 150$ MeV, $b_\eta = 0.45$, and R as shown in Fig. 1.4. The errors shown are statistical only; in particular, they do not reflect the substantial uncertainties in Γ_R and b_η . If any of these quantities differ from the values assumed here, all data points will scale together. Even with these uncertainties, however, the NRCQM cannot account for the data.

Diquark-Quark Model

The diquark-quark model, due to Anselmino, Kroll, and collaborators (see Refs. 17–22 of Ref. [Kro92]), represents an attempt to bridge the gap between CQM representations of baryons at low Q^2 and pQCD at high Q^2 . The diquark itself serves as a description of two-quark correlations, and it plays the role of an elementary baryon constituent that is bound to another constituent quark. The diquark form factor is parameterized in such a way as to asymptotically yield the ‘Hard Scattering Picture’ of Brodsky and Lepage [Lep80].

Kroll and collaborators [Kro92] and later Bolz and collaborators [Bol94] calculated the S_{11} transition form factors using this model. The calculations, which do not include radiative effects, are applicable mainly at high Q^2 . In this regime the model, while not yet refined, compares fairly

well with inclusive data.

1.5.2 Perturbative QCD

At high Q^2 (short distance scales), where the QCD coupling $\alpha_s(Q^2)$ becomes small and we approach asymptotic freedom, QCD can be treated perturbatively. It is expected that the reaction mechanism at high momentum transfer is dominated by leading order diagrams, which are those consisting of two gluons exchanged between three current quarks (See Fig. 1.16).¹⁶ Evaluation of the leading order diagrams yields the result that the quantity $Q^3 A_{1/2}^p$ approaches a constant at high Q^2 (see Ref. [Car86] for a nice explanation). As shown in Fig. 1.17, this asymptotic behavior is not seen in the existing exclusive electroproduction data.

In 1988 Carlson and Poor calculated the absolute normalization of the helicity amplitudes for several low-lying baryons in the pQCD limit [Car88]. The prediction for the asymptotic value of $Q^3 A_{1/2}^p$ for the linear combination of $S_{11}(1535)$ and $D_{13}(1520)$ (dominated by the former at high Q^2) ranged from 0.11 to 0.14 $\text{GeV}^{5/2}$, depending on the distribution amplitude¹⁷ assumed for the calculation. While the predicted value is somewhat lower than the data (even before it is approaching a constant), there were large uncertainties in this calculation arising from the distribution amplitudes. In addition, Stoler has pointed out that several questions have been raised regarding the validity of the procedure itself (see Ref. [Sto93]). Other authors have pointed out (see Refs. [Isg84, Rad91] and the references therein) that ‘soft’ (nonperturbative) effects might also cause the same type of scaling behavior as that predicted by pQCD.

1.5.3 Other Theoretical Approaches

Effective Lagrangian Approach

The effective lagrangian approach uses a Lagrangian calculated from tree-level diagrams (nucleon Born terms, resonance excitations, and t-channel vector meson exchange) together with the appropriate electromagnetic and strong coupling constants to phenomenologically describe a physical process. Benmerrouche, Mukhopadhyay, and collaborators have studied the $\gamma p \rightarrow p\eta$

¹⁶Here we are discussing (massless) current quarks, which are not to be confused with the constituent quarks of the CQM.

¹⁷The distribution amplitude is the momentum-space wavefunction integrated over transverse momentum.

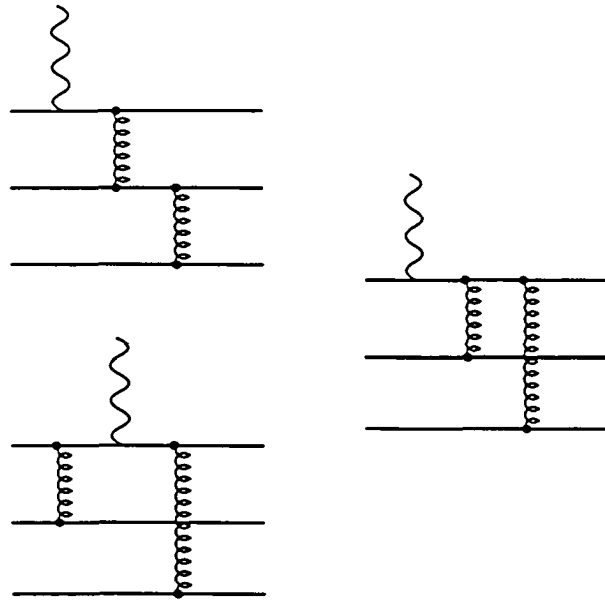


Figure 1.16: Leading order pQCD diagrams for an electromagnetically-induced baryon transition.

reaction, focussing first on photoproduction [Ben91, Ben95] and more recently on electroproduction [Muk96, Ben96, Ben97]. Using their model, fits to data allow the extraction of background terms, coupling constants, and helicity amplitudes. In the latest of these works, Benmerrouche has proposed a parameterization of the S_{11} form factors based on pQCD scaling laws [Ben97].

As pointed out in Section 1.3.3, the full width Γ_R of the S_{11} and the S_{11} branching fractions are needed to extract the helicity amplitude $A_{1/2}^P$ from data on η production. The uncertainty in our current knowledge of $A_{1/2}^P$ is in fact dominated by the uncertainties in these quantities. As a way of working around this problem, Benmerrouche, Mukhopadhyay, and Zhang have recently suggested extracting an ‘electrostrong’ form factor from η electroproduction data [Ben96]. This parameter, when combined with future knowledge of the N^* decay via the strong force (from hadron facilities, for example), could be used to find the helicity amplitude $A_{1/2}^P$.

Several recent effective lagrangian approach calculations have investigated the role of polarization observables in η photoproduction [Tia94, Kno95, Ben95]. This class of observables will likely play a large role in future experiments aimed at unfolding the contributions of the nondominant states to the $p\eta$ channel.

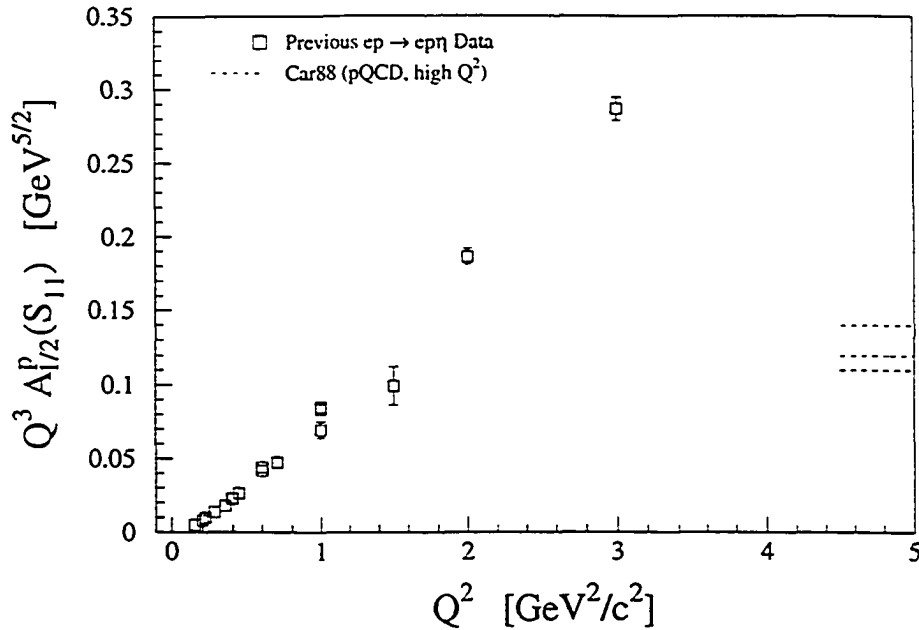


Figure 1.17: The quantity $Q^3 A_{1/2}^P$ for the $S_{11}(1535)$, calculated from $ep \rightarrow e'p\eta$, $W \approx 1535$ MeV cross section data prior to the present measurement. We assume $\Gamma_R = 150$ MeV, $b_\eta = 0.45$, and R as shown in Fig. 1.4. The substantial uncertainties in Γ_R and b_η are not shown (but all data would scale together). Ref. [Car88] gives three results, depending on the distribution amplitude used in the calculation.

Lattice QCD

Numerical simulations of QCD (lattice QCD) hold promise but at present such calculations are limited in scope. As of this writing several rough spectroscopic calculations have been performed in the valence (quenched) approximation [Lei92, All94, But94].

Coupled-Channel Model (Dynamical Formation)

Recent work has suggested that what we have so far been calling the $S_{11}(1535)$ resonance may in fact not be an s -channel resonance at all (that is to say, it may not be the result of a pole in the interaction potential). Denschlag showed that a strong background combined with the $p\eta$ threshold could exhibit resonance-like behavior [Den94].

More recently Kaiser, Siegel, and Weise have developed a model based on the $SU(3)$ chiral lagrangian in which the dynamics of coupled channels give rise to many of the features of the $S_{11}(1535)$ [Kai95, Kai97]. Most notably, they can at least partially account for the large

$S_{11}(1535) \rightarrow p\eta$ branching fraction (something that is problematic in the CQM), together with a reasonable prediction for the resonance width. In this model, the S_{11} is actually a quasi-bound $K\Sigma$ state, and the large branching fraction results from the strong $K\Sigma$ attraction together with the strong coupling of this state to the $N\eta$ channel. The Q^2 dependence for such a state has not yet been calculated; it should be noted, however, that the form factor for such a five-quark object would naively be expected to drop rapidly with Q^2 [Bur98].

Chapter 2

Experimental Apparatus and Data Acquisition

2.1 Overview of the Experiment

As stated in Chapter 1, this experiment measured the (unpolarized) differential cross section for the process $p(e, e'p)\eta$. It was performed in Hall C of TJNAF in November and December of 1996. The Short Orbit Spectrometer, or SOS, was used to detect outgoing electrons while the High Momentum Spectrometer, or HMS, was used to detect outgoing protons (see Fig. 2.1).

The data were taken at two average values of Q^2 , about 2.4 and 3.6 GeV^2/c^2 , with electron beam currents ranging from 80 to 100 μA . At each of the two Q^2 points the electron spectrometer was fixed in both angle and momentum, thus defining a central three-momentum transfer \mathbf{q} . The vector \mathbf{q} in turn determined the direction of a boosted decay cone of protons.¹ The proton spectrometer was stepped in angle and in momentum to capture as much of this decay cone as possible, with the kinematics chosen such that adjacent settings overlapped in these two variables. This approach reduced systematic uncertainties associated with imperfect knowledge of the spectrometer acceptance. The data used here consisted of 33 kinematic settings (78 runs of roughly one-half hour each) for the low- Q^2 point (see Table 2.1) and 21 settings (232 runs) for the high- Q^2

¹The opening angle of the cone (taking into account the finite acceptance of the electron spectrometer) was $\approx 20^\circ$ at the low- Q^2 point and $\approx 15^\circ$ at the high- Q^2 point.

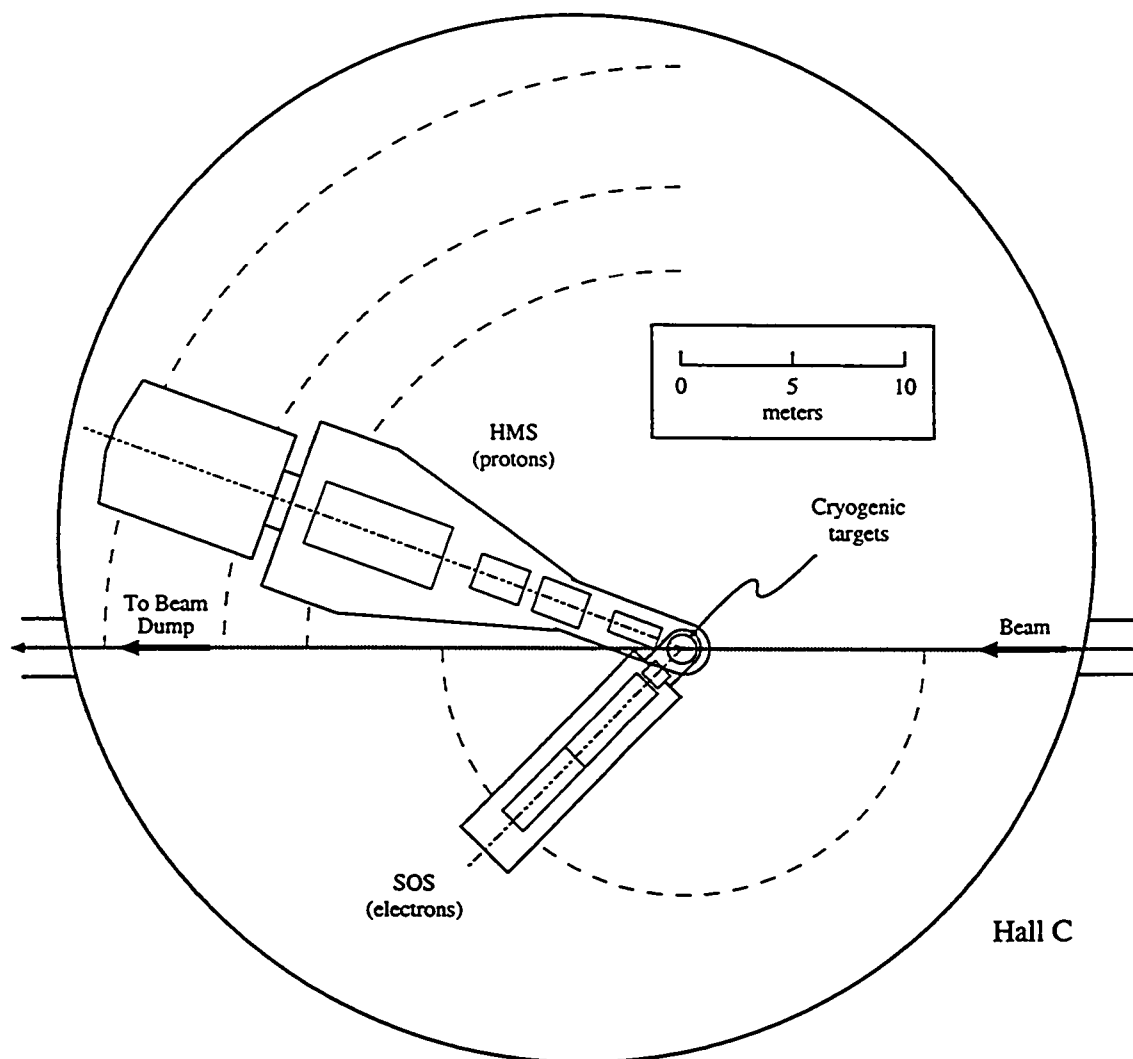


Figure 2.1: A bird's eye view of the Hall C end-station at TJNAF. The electron beam enters from the right, and the scattering takes place in the cryogenic target placed in the beamline. In this experiment, outgoing particles were detected by two magnetic spectrometers: the Short-Orbit Spectrometer (SOS) was used to detect electrons and the High-Momentum Spectrometer (HMS) was used to detect protons.

Electron Arm		Proton Arm	
P_{SOS} [GeV/c]	θ_{SOS} [degrees]	P_{HMS} [GeV/c]	θ_{HMS} [degrees]
1.40	46.0	1.35	15, 17, 19, 21, 23, 25
		1.55	15, 17, 19, 21, 23, 25, 27, 29
		1.70	15, 17, 19, 21, 23, 25, 27, 29
		1.90	15, 17, 19, 21, 23, 25, 27
		2.15	17, 19, 21, 23

Table 2.1: Spectrometer settings for the $Q^2 \approx 2.4 \text{ GeV}^2/c^2$ ($E = 3.245 \text{ GeV}$) data.

point (see Table 2.2).

Figures 2.2 and 2.3 show the laboratory proton momentum versus $\theta_{pq,lab}$ (the angle between the proton and three-momentum; see θ_{pq} of Fig. 1.8 on page 13) for the central electron kinematics of the two Q^2 points. The solid lines in the figures are equally spaced lines of constant W from $W_{thr} \approx 1486 \text{ MeV}$ to 1585 MeV . The dots along the solid lines indicate 10 degree increments in $\theta_{pq,cm}$. The dotted lines are contours at 15% of the maximum proton density (as determined by Monte Carlo simulation), which give a rough indication of the experimental coverage in $\theta_{pq,cm}$ (integrated over ϕ_{cm}).

The momentum acceptance of the electron spectrometer is large (in the neighborhood of 40%), allowing the simultaneous detection of electrons from elastic reactions ($W = m_p$), the first resonance region ($W \approx 1.2 \text{ GeV}$), and the second resonance region ($W \approx 1.5 \text{ GeV}$). The target nucleus in the experiment was ^1H , supplied in liquid form by a cryogenic loop positioned in the beam of incident electrons.

In the electron spectrometer (SOS), both a threshold gas Čerenkov detector and a lead-glass calorimeter were used to separate electrons from negatively charged pions. In the HMS, protons were separated from positively charged pions using a combination of coincidence time (the difference between the trigger times of the two spectrometers) and particle velocity, or β_{tof} (as measured by four planes of scintillator arrays in the detector stack). Details of the particle identification techniques are given in Chapter 4.

Electron Arm		Proton Arm	
P_{SOS} [GeV/c]	θ_{SOS} [degrees]	P_{HMS} [GeV/c]	θ_{HMS} [degrees]
1.50	48.0	1.80	17, 20, 23, 26
		2.00	14, 17, 20, 23, 26
		2.20	14, 17, 20, 23, 26
		2.45	14, 17, 20, 23
		2.70	14, 17, 20

Table 2.2: Spectrometer settings for the $Q^2 \approx 3.6 \text{ GeV}^2/c^2$ ($E = 4.045 \text{ GeV}$) data.

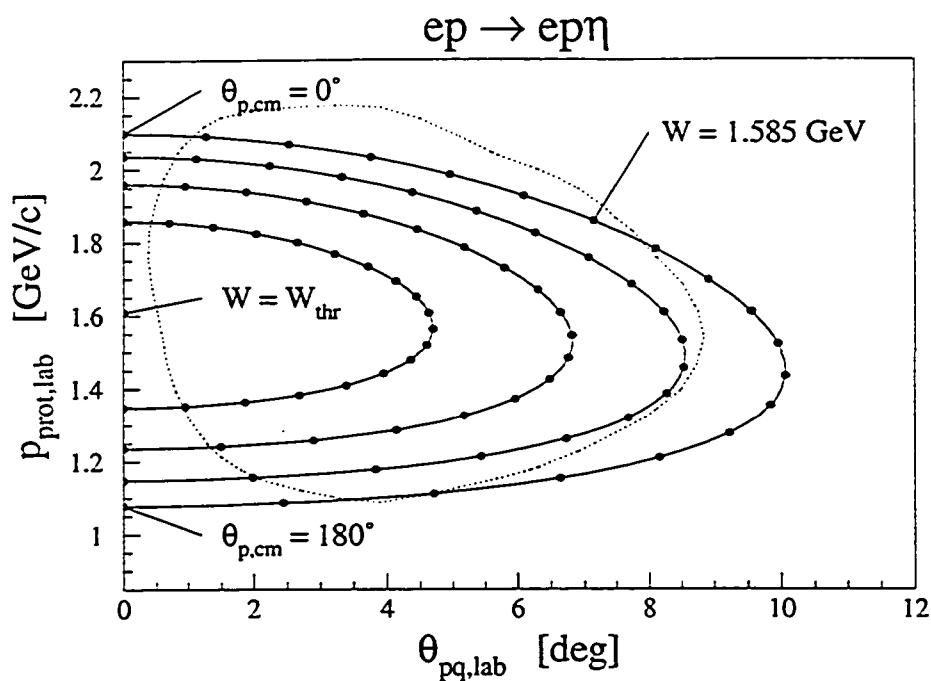


Figure 2.2: Proton momentum in the lab versus $\theta_{p,q,lab}$ for the $Q^2 \approx 2.4 \text{ GeV}^2/c^2$ central electron kinematics. See the text for a description of the curves.

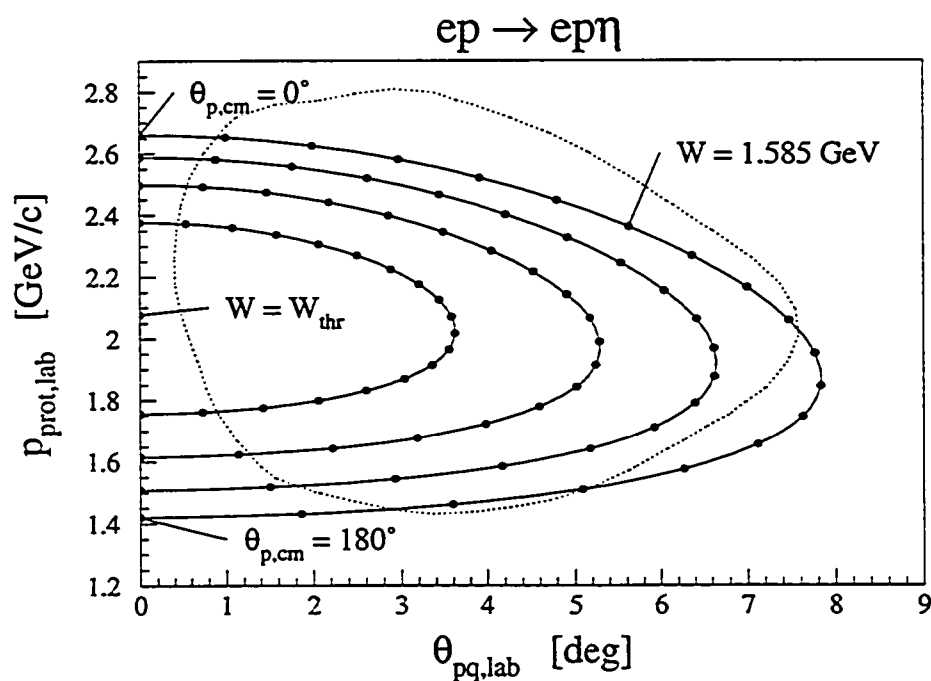


Figure 2.3: Proton momentum in the lab versus $\theta_{p,q,lab}$ for the $Q^2 \approx 3.6 \text{ GeV}^2/c^2$ central electron kinematics.

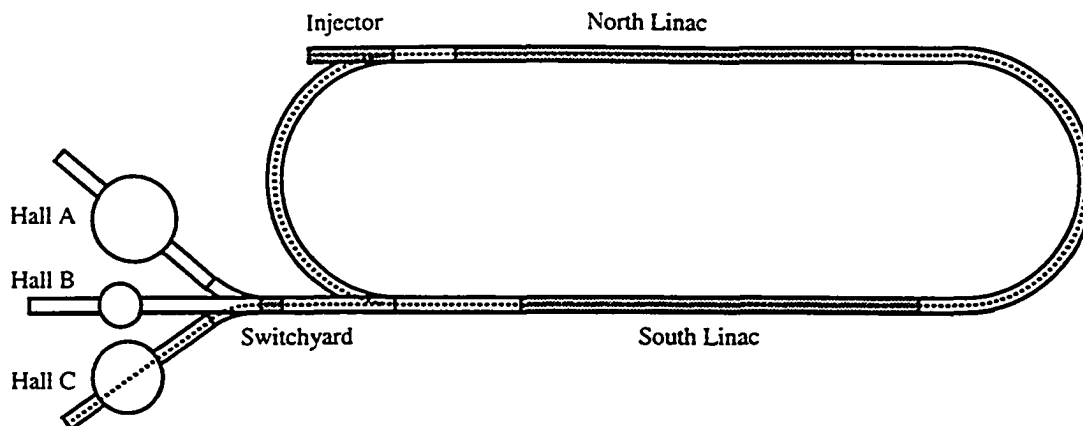


Figure 2.4: A schematic of the accelerator.

2.2 The Accelerator

One of the principle advantages of the electron accelerator at TJNAF is that it is capable of delivering a high-current, continuous-wave (CW) beam of electrons.² It is this current, and the resulting high luminosity, that makes possible experiments such as this one (where we sought good statistics even when studying an exclusive process at high Q^2).

The accelerator is in an oblong loop, or ‘racetrack’, configuration with a pair of linear accelerators (a split linac) situated on the two straightaways (see Fig. 2.4). Electrons are injected into the first linac at 45 MeV, acquire an additional 400 MeV, undergo a 180 degree bend, and gain another 400 MeV in the second linac. After the second linac the beam is either directed to one of the three experimental halls or sent around the loop again for further acceleration. The higher electron energies are achieved using the same linacs but separate beamlines in the arcs (because the required bending field is energy dependent), up to a maximum of five trips around the loop. Thus the beam energies available at the time of this experiment were discrete: 0.845, 1.645, 2.445, 3.245, or 4.045 GeV (*i.e.*, multiples of 0.8 GeV plus the 45 MeV injection energy).³ The present data were taken at the two highest beam energies, 3.245 GeV for the $Q^2 \approx 2.4 \text{ GeV}^2/c^2$ data and 4.045 GeV for the $Q^2 \approx 3.6 \text{ GeV}^2/c^2$ data.

²As described in Appendix A, the beam is not truly CW. The term applies, however, because the event-to-event time spread in the spectrometers and detectors is broader than the separation of the radio frequency (RF) pulses; thus the distribution of events as seen by the data acquisition system is effectively continuous.

³In the terminology used at the Laboratory, beam delivered to the experimental areas after one (two, three, four, five) trip(s) through the pair of linacs is *one (two, three, four, five) pass beam*.

2.3 The Hall C Beamline Instrumentation

2.3.1 Beam Energy Measurement

In October, 1996 (just prior to the start of the experiment) an absolute measurement of the energy of the nominal 4.045 GeV electron beam was made using the arc between the beam switchyard and Hall C as a spectrometer. Only the dispersive elements were energized to bend the beam (*i.e.*, all sextupoles, octupoles, and beam correctors were degaussed and turned off), giving the arc a dispersion of 12 cm/%. The position and direction of the beam was determined at the entrance and exit of the arc using two high-resolution movable-wire scanners [Yan94] (superharps C07 and C17 in Fig. 2.5). This absolute beam position and direction together with knowledge of the absolute $\int B \cdot dl$ of the arc dipoles as a function of current [Har89] allowed a calculation of the beam energy via

$$p = \frac{e}{\Theta_{\text{arc}}} \int B \cdot dl, \quad (2.1)$$

where e is the electron charge and Θ_{arc} is the bend radius of the arc (34.3°). The measured beam energy was 4.055 GeV, or 0.25% higher than nominal. Further discussion of this measurement technique may be found in Refs. [Neu92, Yan92, Yan93, Yan95], and details of this particular measurement in Ref. [Gue96].

During the analysis of data the constraints imposed by inclusive and coincidence elastic data indicated a beam energy of 4.040 ± 0.005 GeV, and this value was used in the analysis of the resonance data. This topic is discussed in Appendix B.

2.3.2 Beam Position Measurement

In the beamline preceding the target were five stripline cavity Beam Position Monitors (BPMs), whose outputs were recorded at 30 second intervals when taking data. Information from the two nearest the target (BPMs H00A and H00B in Fig. 2.5) together provided a measurement of the beam position on the target and the angle of incidence on the target. The position of the beam on the target in the horizontal and vertical directions was stable to within ± 1.25 mm, and the angles stable to within ± 0.5 mrad. The BPMs are described in Ref. [Kra93].

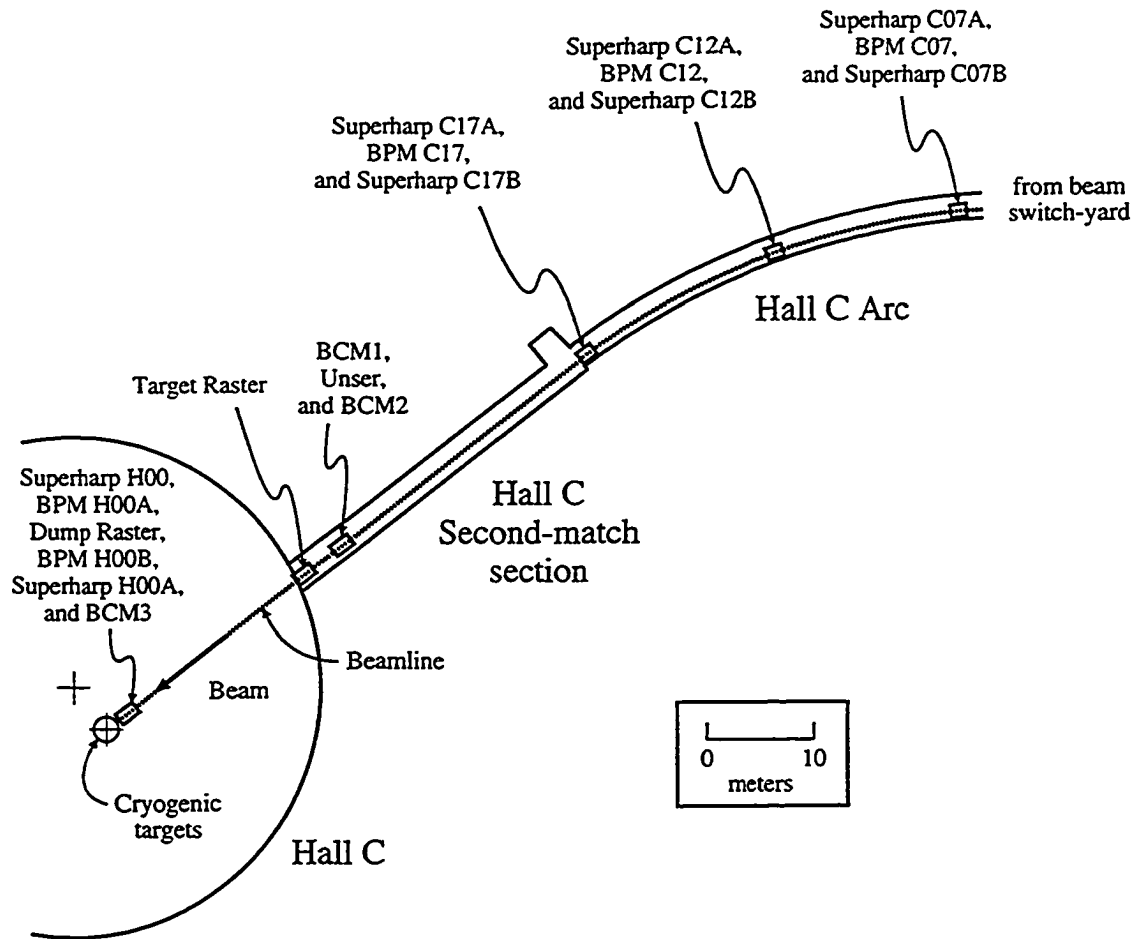


Figure 2.5: A schematic showing placement of the Hall C beamline instrumentation.

2.3.3 Beam Current Measurement

The charge delivered to Hall C was measured using several devices. Three resonant-cavity Beam Current Monitors (BCMs) made a continuous relative measurement of the beam current. These devices were periodically calibrated absolutely using an Unser current monitor. For a detailed description of these devices see Appendix A.

2.4 The Cryogenic Target

The target nucleus in this experiment was hydrogen, provided in liquid form in a loop with circulation maintained by an axial pump (see Fig. 2.6). The liquid H₂ was cooled with helium gas (15 K, 19 Atm) using a heat exchanger. The target liquid was maintained at (19.00 ± 0.05) Kelvin and about 26 psia (which corresponds to 2 K subcooling), and the target length was (4.36 ± 0.01) cm. The temperature was controlled using a calibrated heat-dependent resistor in the feedback loop of a dual-resistive-heater temperature control system.

The upstream window of the target was a piece of 71 μm (2.8 mil) 6061 series aluminum (see Fig. 2.7). The downstream window was formed from 3004 series aluminum (blank beer can stock) which had been chemically etched to a thickness of 137 μm (5.4 mils).

In addition to the liquid cryogenic targets there were ‘dummy’ targets (simple aluminum plates). These dummy targets mimicked the windows of an empty target to facilitate measurement of the background originating from target window interactions. The dummy targets were ten times as thick as the corresponding target windows in order to reduce the time needed for background measurement.

The cryogenic target stack was raised or lowered by an actuator in order to put the appropriate target cell in the beamline. Alternately, by rotating the cryotargets out of the way a ladder containing several solid targets could be lowered into the beamline. The solid targets were used for visual checks of the beam position and spot size (solid BeO₂ target) and for optics tests and calibrations (solid ¹²C targets).

More information about the target system is available in Refs. [Dun97], [Mee98], and [Ter98].

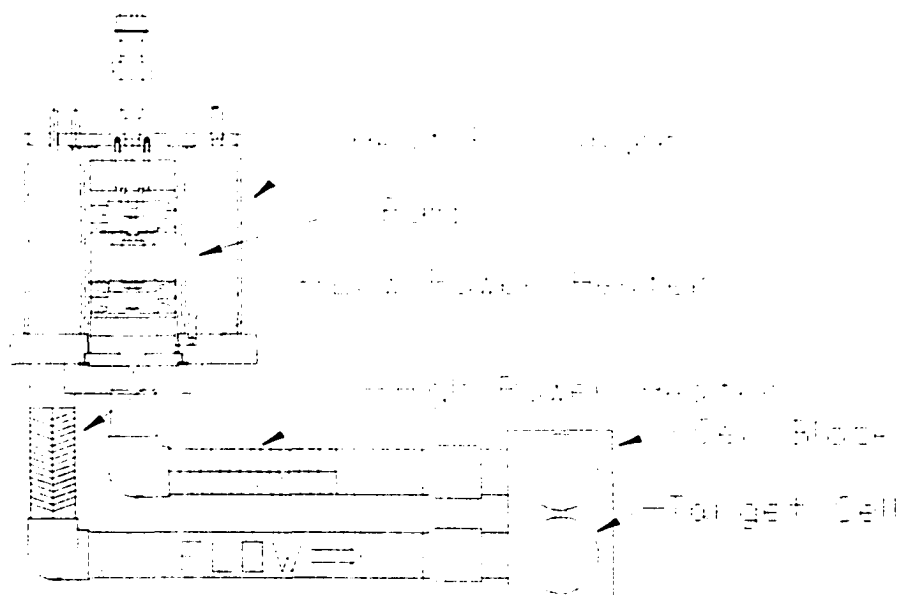


Figure 2.6: A head-on view of one of the three loops in the cryogenic target. The beam direction is out of the page. The figure is courtesy of D. Meekins.

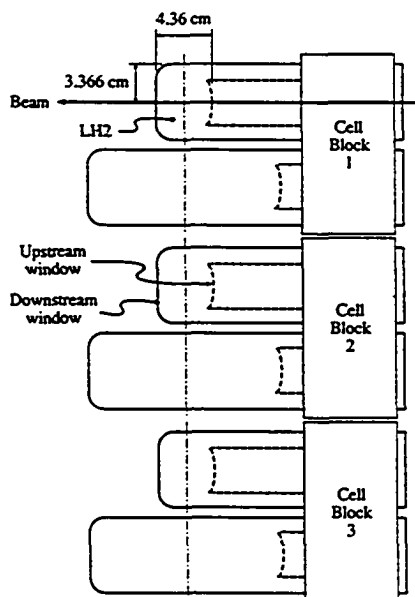


Figure 2.7: A side view of the three cryogenic target cell blocks, with two targets in each block (nominal lengths of 4.4 and 15 cm). Not shown are vertical baffles attached to the inner cell tubes which force liquid flow into the plane of the page where the beam traverses the target. Also not shown are 'dummy' targets used for measuring target window rates and a separate ladder holding several solid targets. All of the resonance data for this experiment were taken using liquid hydrogen in the 4.4 cm target of loop 1.

2.5 Target Rastering

As noted above, the electron beam at TJNAF was CW and high current. In addition, the size of the beam envelope was only about $\sigma \approx 140\mu\text{m}$. In order to prevent the beam from burning a hole through the windows of the target there were two steering magnets about 21 m upstream of the target (see the target rasters in Fig. 2.5) which rastered (or steered) the position of the beam on the target by ± 1 mm (with a corresponding angular change of less than ± 0.05 mrad).

The beam was steered independently in the vertical (x) and horizontal (y) directions according to sinusoidal signals. The frequencies of the magnet currents (17.0 kHz in the x , 24.2 kHz in y) were chosen to prevent the beam from tracing Lissajous figures on the target windows. The heat deposited by the beam in the windows and target liquid resulted in some localized density change; this effect and the correction for it are discussed in Chapter 4.

In addition to the target raster, there was a raster about 2.5 m upstream of the target designed to protect the beam dump (see the dump rasters in Fig. 2.5). This raster operated at a much lower frequency than the target raster (62.0 Hz in x , 91.0 Hz in y), and was designed to prevent excess localized heating on the beam dump. At the time of this experiment the dump raster had not been commissioned, and it was not used.

2.6 The Electron Spectrometer

The Hall C Short Orbit Spectrometer (SOS) (see Fig. 2.8) was used to detect outgoing electrons. This device was specifically designed with a short optical length in order to study short-lived hadrons, and in most Hall C coincidence experiments it was used to detect hadrons, whether decaying or not. The requirements of this experiment were unusual, though, in that the outgoing protons had momenta above the 1.75 GeV/ c upper limit of the SOS (see Table 2.3). This fact necessitated the use of the High Momentum Spectrometer (HMS) to detect protons, leaving the SOS for electron detection.

In addition to its short optical length, the SOS was designed to have large acceptance in both scattering angle and momentum. Toward this end, the device consists of a horizontally focussing quadrupole followed by two edge-focussing (primarily in the horizontal direction) dipoles

Quantity	Specification
Maximum Central Momentum	1.75 GeV/c
Momentum Acceptance / Resolution (σ)	$\approx 40\%$ / $\approx 0.1\%$
Dispersion	< 0.92 cm/%
Solid Angle (large collimator)	
Point Target	≈ 7.5 msr
4.4 cm Target	≈ 6.5 msr
Angular Acceptance / Resolution (σ)	
Horizontal	± 60 mrad / ± 5 mrad
Vertical	± 40 mrad / ± 1 mrad
Optical Length	7.4 m
Angular Range	13.4° to 165°
Net Upward Bend Angle	18°
Minimum Opening Angle with HMS	$\approx 29^\circ$

Table 2.3: The SOS operating specifications. Sources are Ref. [Ent97] (solid angles), data from this experiment (resolutions), and Ref. [Cum96] (other).

with opposing bend directions. The first dipole has an upward bend angle of 33 degrees and the second a downward bend of 15 degrees for a net upward bend of 18 degrees with respect to the horizontal. The magnetic tune used in this experiment was point-to-point⁴ in both the horizontal and dispersive directions. Changes in spectrometer rotation and magnetic field were made remotely from the counting room.

The spectrometer's angular acceptance was defined by an octagonal collimator made of 3.175 cm (1.25 inch) thick HeavyMet (a dense, machinable Tungsten-CuNi alloy).⁵ The aperture was machined with a taper, with edges parallel to a ray coming from a point target. In addition to the octagonal collimator, there was a so-called sieve slit (a collimator with many small holes) which was used to find the matrix elements of the focal-plane-to-target transformation (this procedure is discussed in Section 4.2.2 and Appendix B). For drawings of the collimator and sieve slit, as well as further details about many aspects of the Short Orbit Spectrometer, the reader is referred to Ref. [Cum96].

While the SOS was designed with the capability of being elevated out of plane, at the time of this experiment that feature had not been implemented. The SOS was equipped with two pairs of scintillator arrays, two drift chambers, and two threshold Čerenkov detectors, one gas and one aerogel. The aerogel detector was not used for this experiment and will not be discussed further.

⁴A point-to-point tune maps each distinct point at the target to a distinct point at the focal plane.

⁵A second, smaller acceptance-defining collimator was available but not used in this experiment.

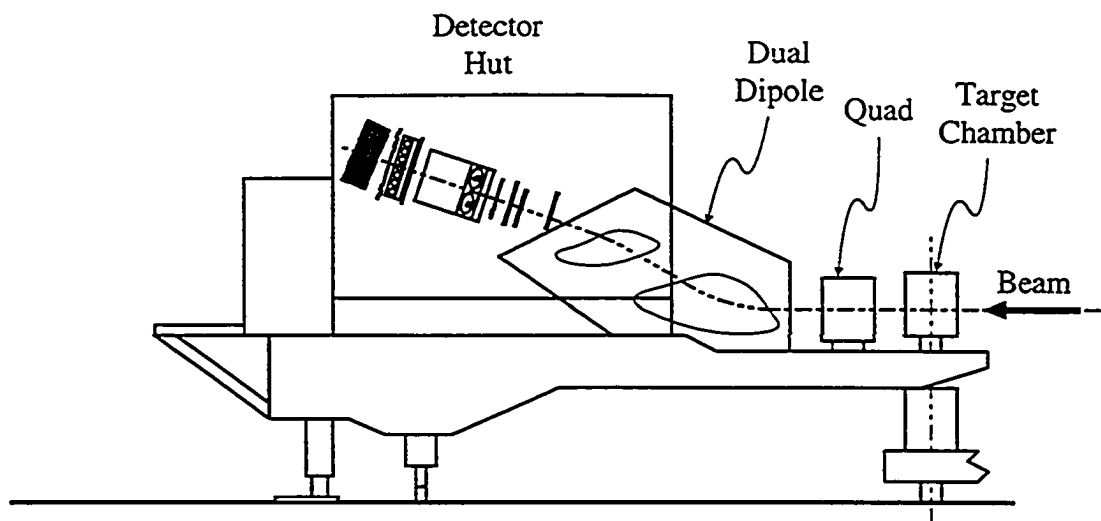


Figure 2.8: A side view of the electron spectrometer (SOS).

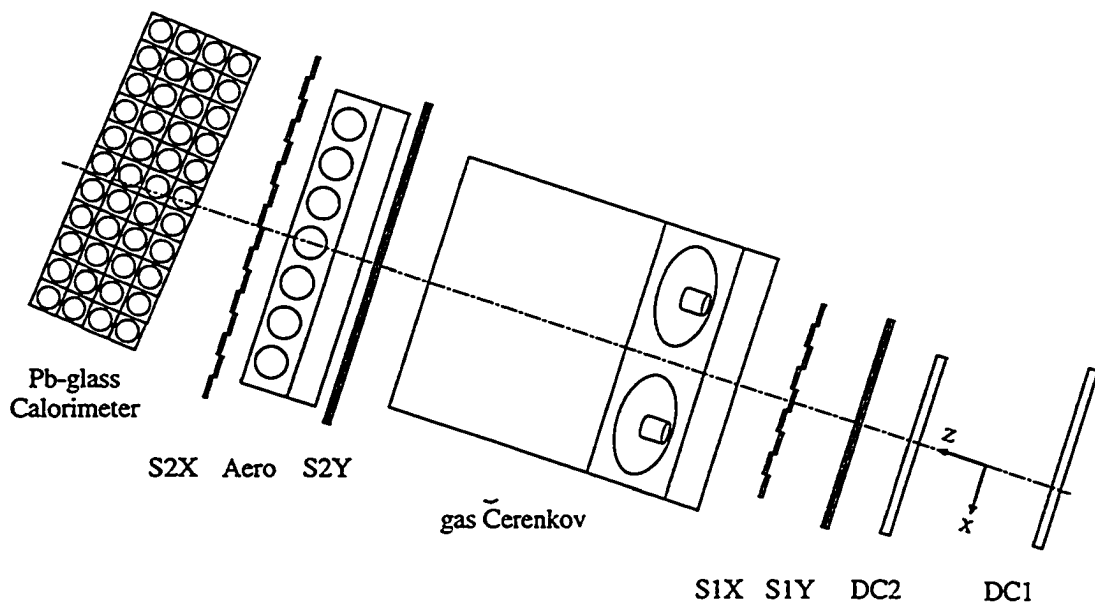


Figure 2.9: A side view of the electron spectrometer (SOS) detector stack, as seen from the door of the detector hut. The detected particles travel from right to left (along positive z). The y axis is out of the page.

2.6.1 The SOS Magnetic Elements

As noted above, the SOS consists of a horizontally-focussing quadrupole followed by two edge-focussing dipoles. The three magnets are all nonsuperconducting, and cooled by pressurized water. The magnets were operated in a point-to-point tune in both the bend (vertical) and nonbend (horizontal) directions. The fields for the quadrupole and both dipoles were determined by Hall probes situated in regions where the magnetic field was uniform.

The magnetic fields were set remotely from the counting room. In general the magnets were operated such that they began in a demagnetized state and followed this hysteresis curve to increasing current. When a decrease in current was necessary, the magnets were first demagnetized⁶ and the desired field approached from below. In practice, the kinematics of this experiment called for a single SOS magnet and angle setting at each of the two Q^2 points, and care was taken to not change the field setting during data taking.

2.6.2 The SOS Scintillator Arrays

The SOS detectors included four planes of scintillators, two towards the front of the detector stack and two towards the rear (see Fig. 2.9). Each plane consisted of staggered, slightly overlapping strips of scintillator (see Fig. 2.10) equipped at each end with light guides and photomultiplier tubes (PMTs) (Philips Components XP2282B). The first plane encountered by a particle, S1Y, had 9 scintillators arranged along the x direction (roughly vertically).⁷ The second plane, S1X, had 9 scintillators arranged in the y direction (horizontally). Towards the rear of the detector hut this arrangement was repeated with planes S2Y and S2X (9 and 16 scintillators, respectively).

The scintillator planes served two purposes: triggering of the data acquisition system and measurement of particle velocity using time-of-flight (β_{tof}) from the front to the rear of the detector hut. For triggering purposes, the signals from all of the PMTs on one side of each plane were OR'd together, and the resulting pair of signals AND'd together to form the trigger signal for that plane (see Fig. 2.11). In the case of the S1X plane, for example, the output signals of all PMTs on the left, or positive y , side were OR'd together into a signal S1X+. The AND of S1X+ and the

⁶The demagnetization procedure consisted of setting the field to the maximum current i_{max} ; setting to zero current; reversing magnet polarity and setting to a reverse current i_{rev} ; and setting to zero current. The reverse current i_{rev} required to end the procedure in a demagnetized state was determined from previous measurements [Pot98].

⁷The 'Y' in S1Y denotes not the orientation of the scintillators but the coordinate which was indicated by a hit.

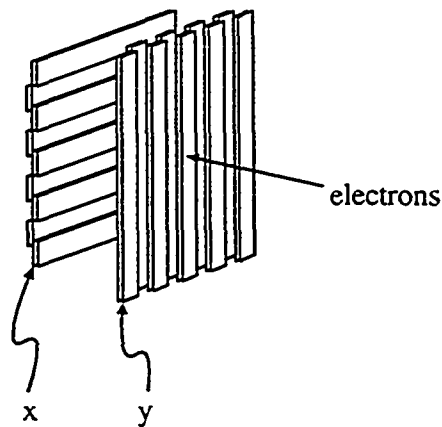


Figure 2.10: A schematic view of the forward pair of SOS scintillator arrays (S1). The light guides and PMTs are not shown; the figure is intended only to show the orientation and positioning of the scintillators. The rear pair of arrays (S2) was similar but was larger in the vertical direction and had 16 ‘x’ scintillators.

corresponding signal from the opposite side, S1X–, formed the signal S1X used for triggering purposes. A plane recorded a hit whenever an above-threshold signal from any PMT on one side of the plane arrived within about ± 60 ns of a signal from the opposite side of the plane. When three of the four scintillator planes recorded a hit within about ± 30 ns a pretrigger (or raw trigger) was formed in the trigger electronics (see Fig. 2.12).

High voltage for the PMTs was supplied locally but monitored and controlled remotely from the Hall C electronics room using EPICS (the Experimental Physics Industrial Control System) [EPI94]. The analog signals coming from the PMTs were routed directly up to the electronics room (which held all of the electronics shown in Figs. 2.11, 2.15, 2.12, and 2.21, as well as the corresponding HMS electronics).

Once in the electronics room the analog signal from the each of the PMTs was split by a 2:1 voltage divider. The smaller signal went to an analog-to-digital converter (ADC), the output of which was used to make pulse-height corrections to the timing (Section 4.2.3). The larger signal was discriminated, and the resulting logic signal was sent to a time-to-digital converter (TDC), a scaler, and to the logic devices that formed pretriggers.

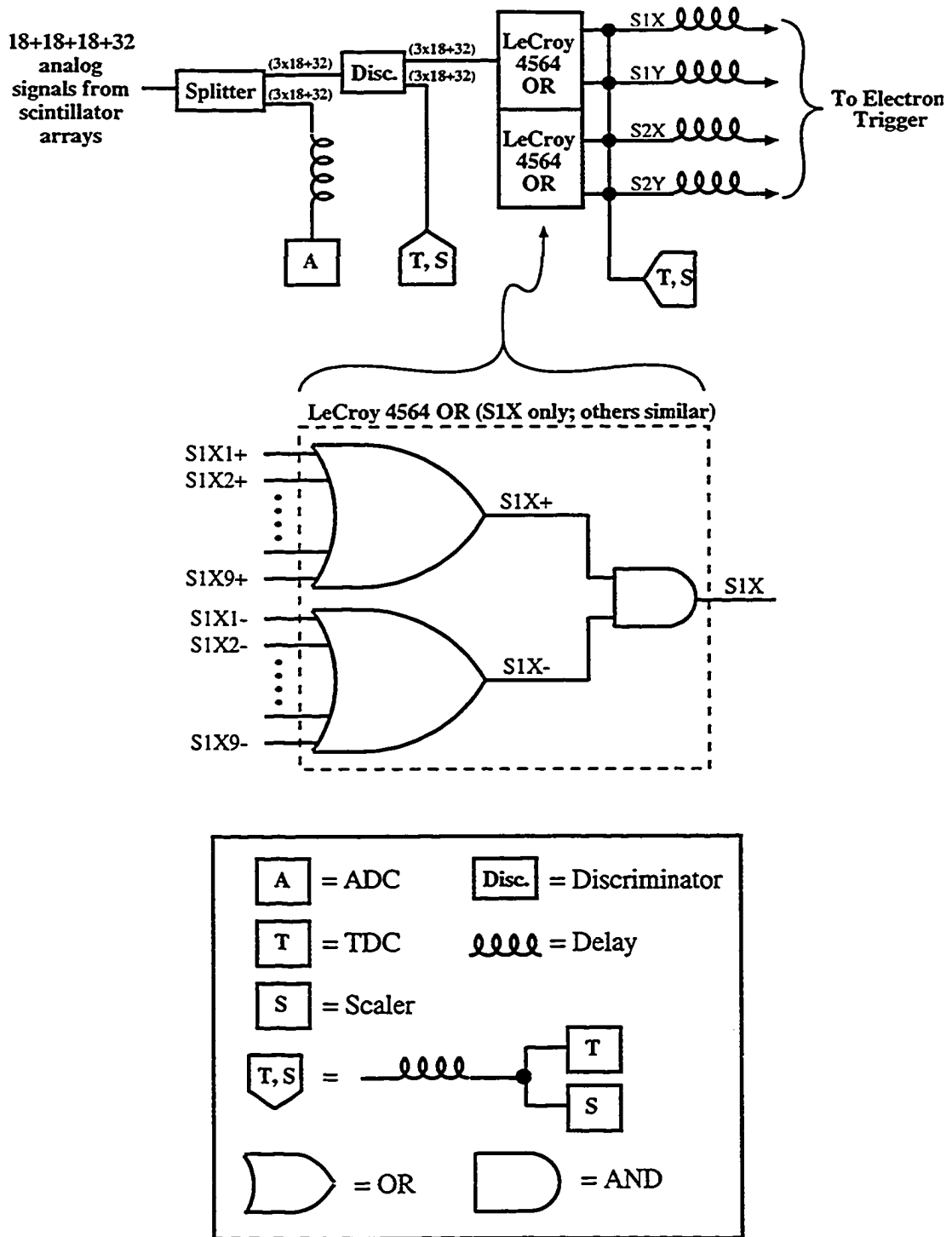


Figure 2.11: The SOS scintillator array electronics. Parenthetical numbers above a line indicate the multiplicity of signals.

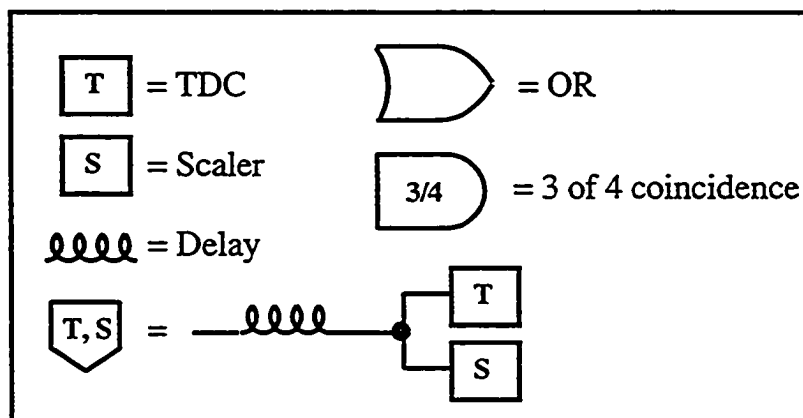
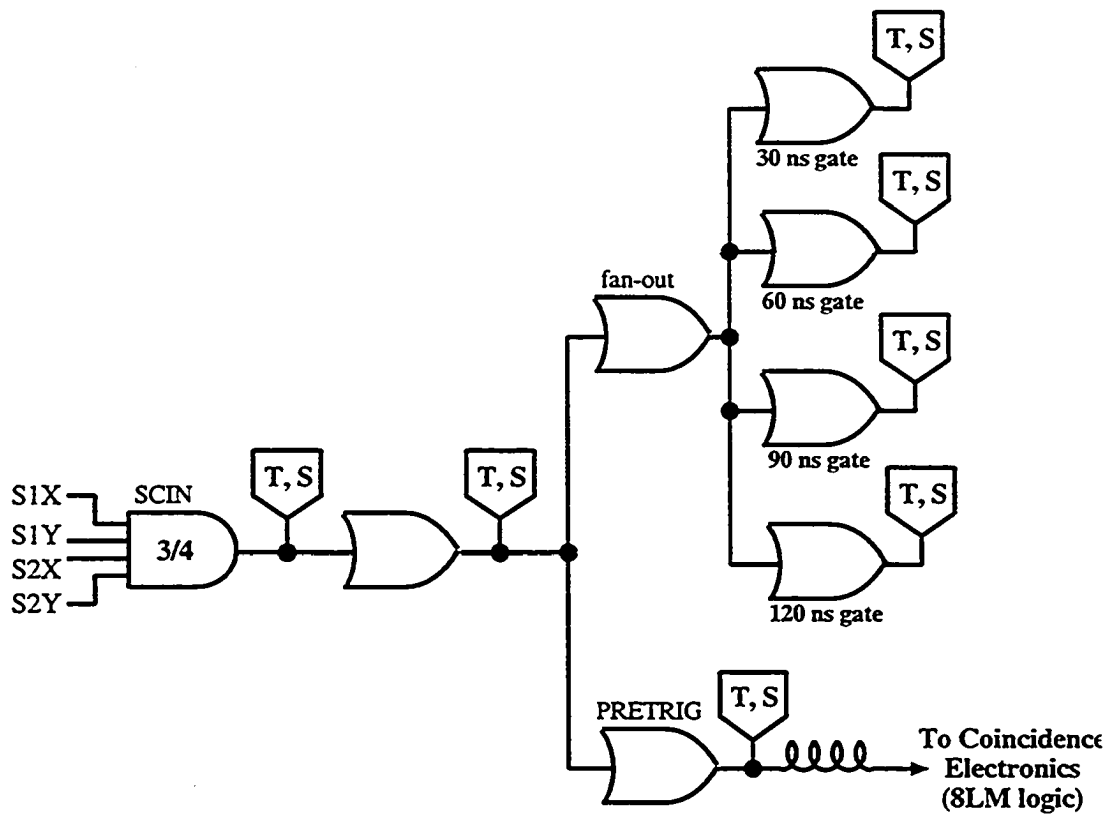


Figure 2.12: The SOS trigger electronics.

2.6.3 The SOS Drift Chambers

A pair of drift chambers (DC1 and DC2) provided track information for events in the SOS. Each chamber consisted of six planes of sense wires oriented as shown in Fig. 2.13.

The cell size of the chambers (the spacing between sense wires) was 1 cm. The field wires and inter-plane foils were kept at negative high voltage, while the sense wires were held at ground. The unprimed and primed planes were offset by one-half of a cell width in order to help remove the left-right ambiguity inherent in the drift-time measurement of a single plane (see Fig. 2.14). The chambers were located at the front of the detector stack to minimize the effect of multiple-scattering in the preceding vacuum window and air.

The gas used in the drift chambers was a 50:50 (by weight) argon-ethane mixture. The ethane acted as a quenching agent to decrease the electron drift velocity and hence increase the spatial resolution [Leo94]. The maximum drift time using this gas mixture was about 150 ns. The gas mixture was passed through alcohol bubblers at 0° C in order to extend the lifetime of the chambers.⁸ The flow rate through each of the chambers was maintained at about 200 SCCM (standard cubic centimeters per minute).

Each sense wire was directly connected to a circuit board (LRS2735DC) that amplified and discriminated the chamber signal. The discriminator thresholds were remotely adjustable but unchanged for the duration of the experiment.

When a trigger signal was sent from the trigger supervisor, multi-hit pipeline TDCs (LRS1887, located in a rack at the back of the SOS carriage) read timing information for all drift chamber channels that exceeded the discriminator threshold within the previous 4 μ s. Read-out controllers assembled the drift chamber information into event fragments and sent the data upstairs to the data acquisition computer. The algorithm used to find tracks from the drift chamber information is discussed in Section 4.2.1.

2.6.4 The SOS Gas Čerenkov Detector

The SOS had a threshold gas Čerenkov detector designed to distinguish electrons from negatively charged pions. The detector had four mirrors which focussed Čerenkov light onto four

⁸The addition of small amounts of alcohol to the gas mixture inhibits the growth of 'whiskers' from the cathodes and suppresses so-called dark currents; see Ref. [Blu93].

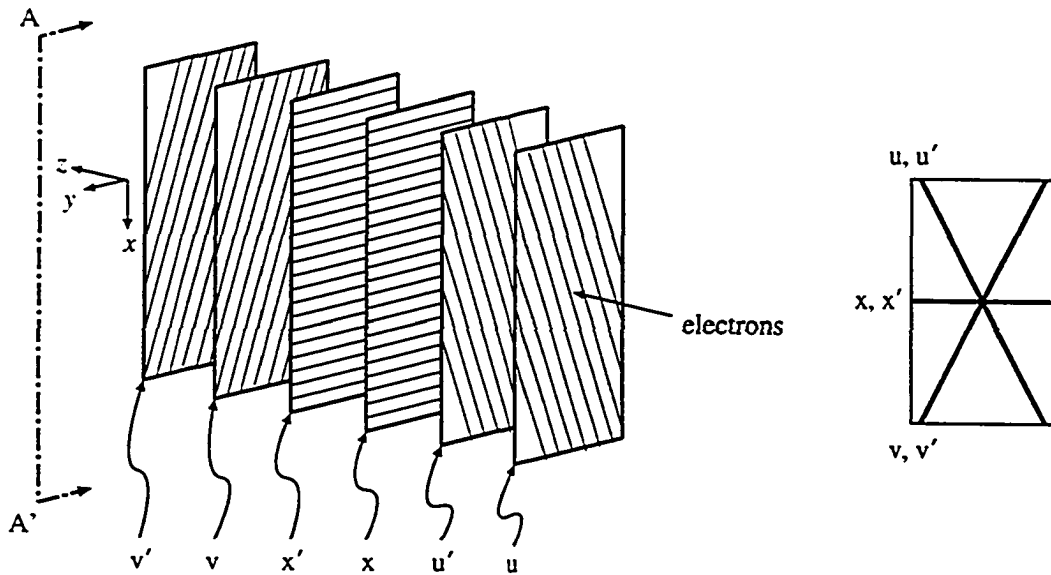


Figure 2.13: *Left)* An exploded view of the wires in a single SOS drift chamber. Neither the dimensions nor the number of wires are accurate, and the inter-plane foils are not shown; the figure is intended only to show the orientation of the wires and the ordering of the planes. The cross section A-A' is given in Fig. 2.14. *Right)* The orientation of the SOS drift chamber wires as seen by the incoming electrons.

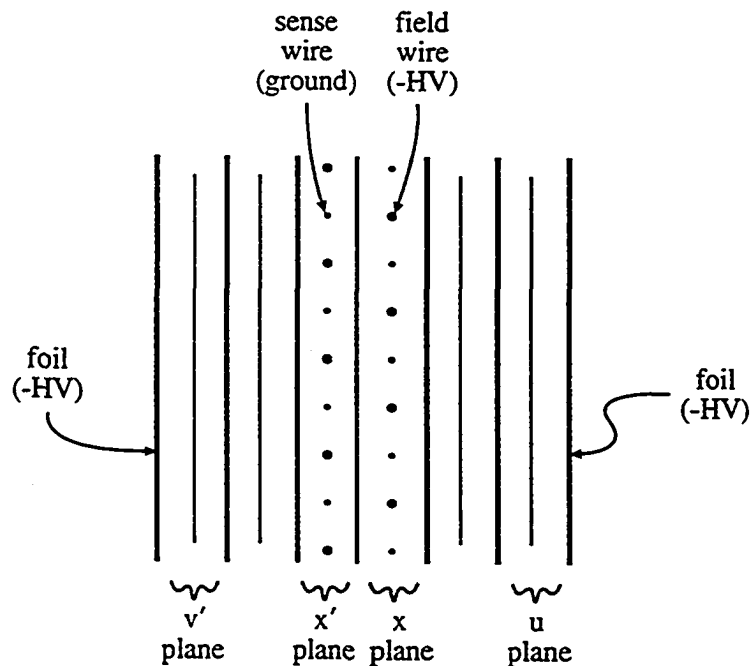


Figure 2.14: Cross section of a single SOS drift chamber.

PMTs (Burle 8854). During the experiment the detector was filled with Freon 12 (CCl_2F_2) at one atmosphere, yielding a velocity threshold of $\beta_t = 1/n = 0.9989$. The highest momenta seen by the SOS in this experiment was about 1.73 GeV/c, which corresponds to $\beta = 0.9967$ for pions and $\beta > 0.9999$ for electrons.

The Čerenkov PMT outputs were sent up to the Hall C electronics room, where they were split by a 1:1 voltage divider (see Fig. 2.15). One of the outputs went to an ADC which was read out when a trigger occurred. The other output was discriminated and sent to trigger electronics that were not used in this experiment.

The mirrors in place during the experiment had slight misalignments as well as some degradation of the surface finish. As a result the detector was slightly inefficient; nevertheless, it was deemed suitable for use in the analysis. See Section 4.2.4 for details.

2.6.5 The SOS Lead-Glass Calorimeter

At the rear of the SOS detector hut was an array of 44 blocks of TF1 lead glass, each 10 cm by 10 cm by 70 cm long, stacked 11 blocks high by four blocks (16 radiation lengths) deep. Each block was equipped at one side with a PMT (Philips Components XP3462B). The entire structure was tilted at 5 degrees with respect to the optical axis in order to prevent inefficiencies due to particles travelling along the interface between blocks.

The array served as an electromagnetic calorimeter. The measured energy deposition in the individual calorimeter blocks was summed and the resulting quantity used to separate electrons from negatively charged pions. The PMT outputs were sent up to the Hall C electronics room, where they were split by a 1:1 voltage divider (see Fig. 2.15). One of the outputs went to an ADC which was read out when a trigger occurred. The other output was sent to trigger electronics that were not used in this experiment. The performance of this detector is discussed in Section 4.2.4.

2.7 The Proton Spectrometer

The Hall C High Momentum Spectrometer (HMS) (see Fig. 2.16) was used to detect outgoing protons. As noted above, this decision was driven by the need to detect protons with momenta exceeding the upper limit of the SOS.

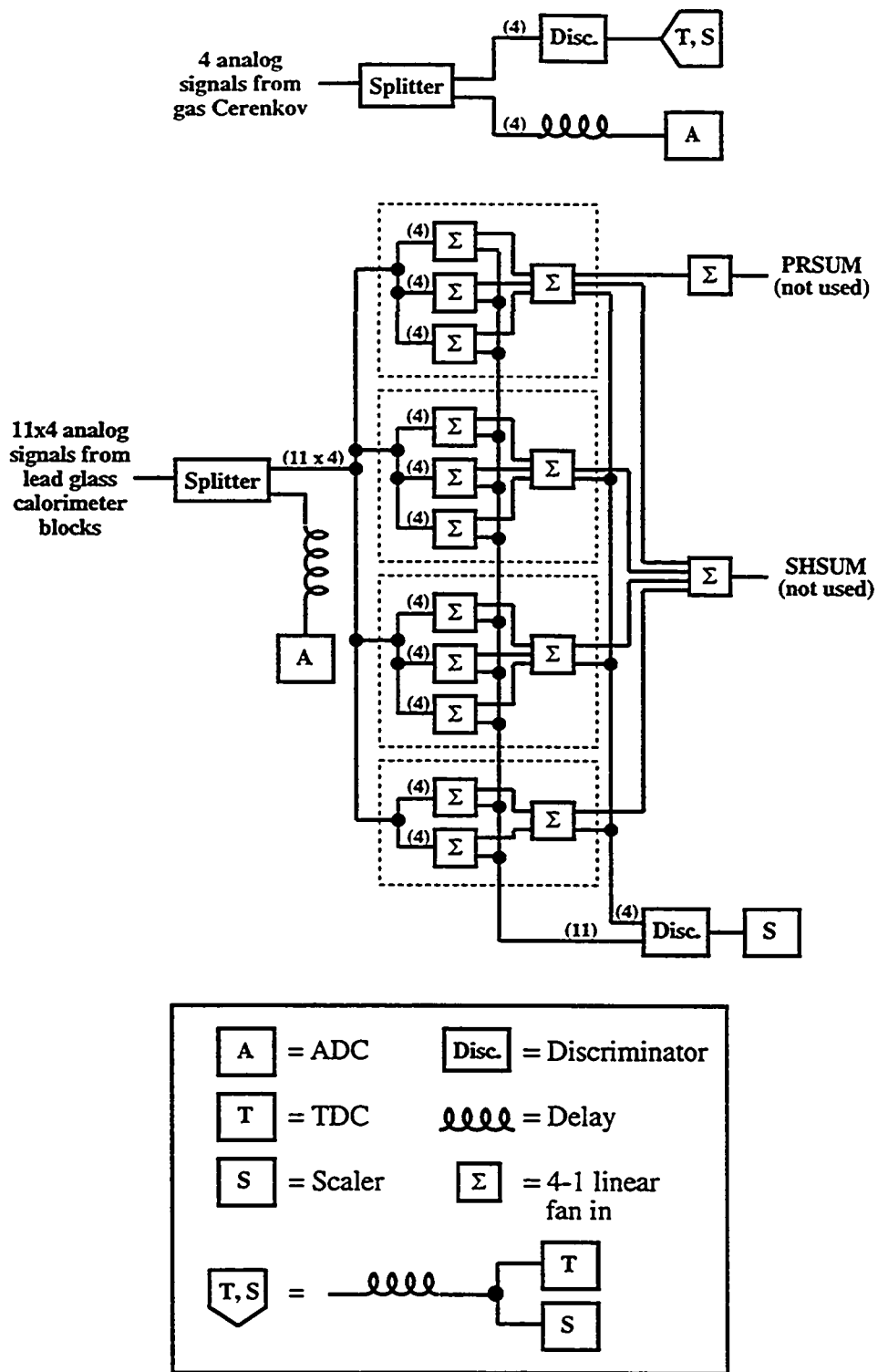


Figure 2.15: The SOS gas Čerenkov and calorimeter electronics. Parenthetical numbers above a line indicate the multiplicity of signals.

Quantity	Specification
Maximum Central Momentum	4.0 GeV/c
Momentum Acceptance / Resolution (σ)	$\approx 18\%$ / $\approx 0.1\%$
Dispersion	≈ 3.9 cm/% at $\delta = 0$
Solid Angle (large collimator)	
Point Target	≈ 7.0 msr
4.4 cm Target	≈ 6.5 msr
Angular Acceptance / Resolution (σ)	
Horizontal	± 25 mrad / ± 2 mrad
Vertical	± 70 mrad / ± 2 mrad
Optical Length	26.0 m
Angular Range	12.5° to 85°
Upward Bend Angle	25°
Minimum Opening Angle with SOS	$\approx 29^\circ$

Table 2.4: The HMS operating specifications. Sources are Ref. [Ent97] (solid angle), data from this experiment (angular resolutions), and Ref. [Yan91] (other).

The HMS consisted of three superconducting quadrupoles followed by a superconducting dipole, operated in point-to-point tune (in both directions) for this experiment. Changes in spectrometer rotation and magnetic field were made remotely from the counting room.

The angular acceptance of the spectrometer (see Table 2.4) was defined by an octagonal collimator made of 6.3 cm (2.48 inch) thick HeavyMet.⁹ As in the case of the SOS, the matrix elements of the HMS were optimized using data taken with a sieve slit (see Section 4.2.2 and Appendix B).

The HMS detector package was similar to that in the SOS. The HMS was equipped with two pairs of scintillator arrays, two drift chambers, a threshold gas Čerenkov detector, and a lead-glass electromagnetic calorimeter. The last two detectors were not used in this experiment, and will not be discussed further.

2.7.1 The HMS Magnetic Elements

The HMS is in a Quad-Quad-Quad-Dipole configuration, using a point-to-point tune¹⁰ in both the dispersive and nondispersive directions. The three quadrupoles were superconducting cold iron magnets with passive quench protection. The dipole was a cryogenically stable superconducting magnet.

⁹A second, smaller acceptance-defining collimator was available but not used in this experiment.

¹⁰The HMS-1 tune of Ref. [Yan91].

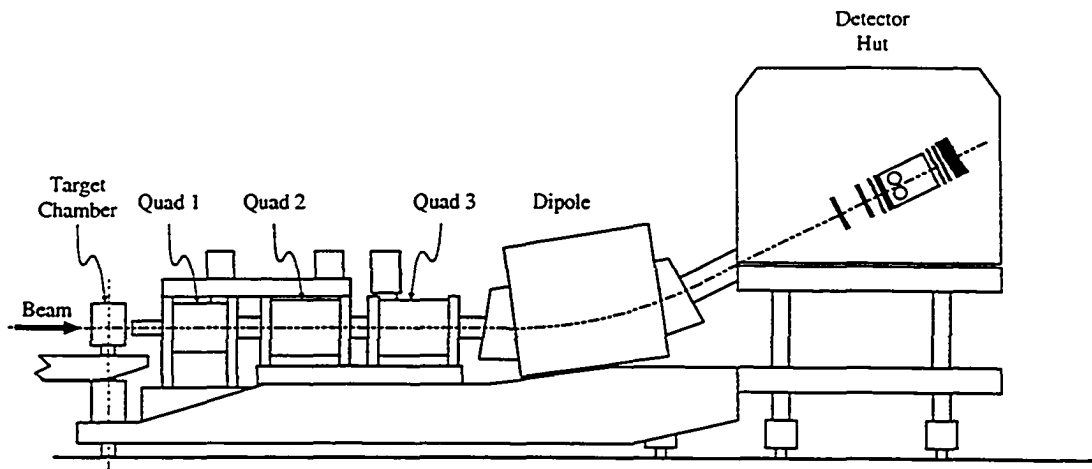


Figure 2.16: A side view of the proton spectrometer (HMS).

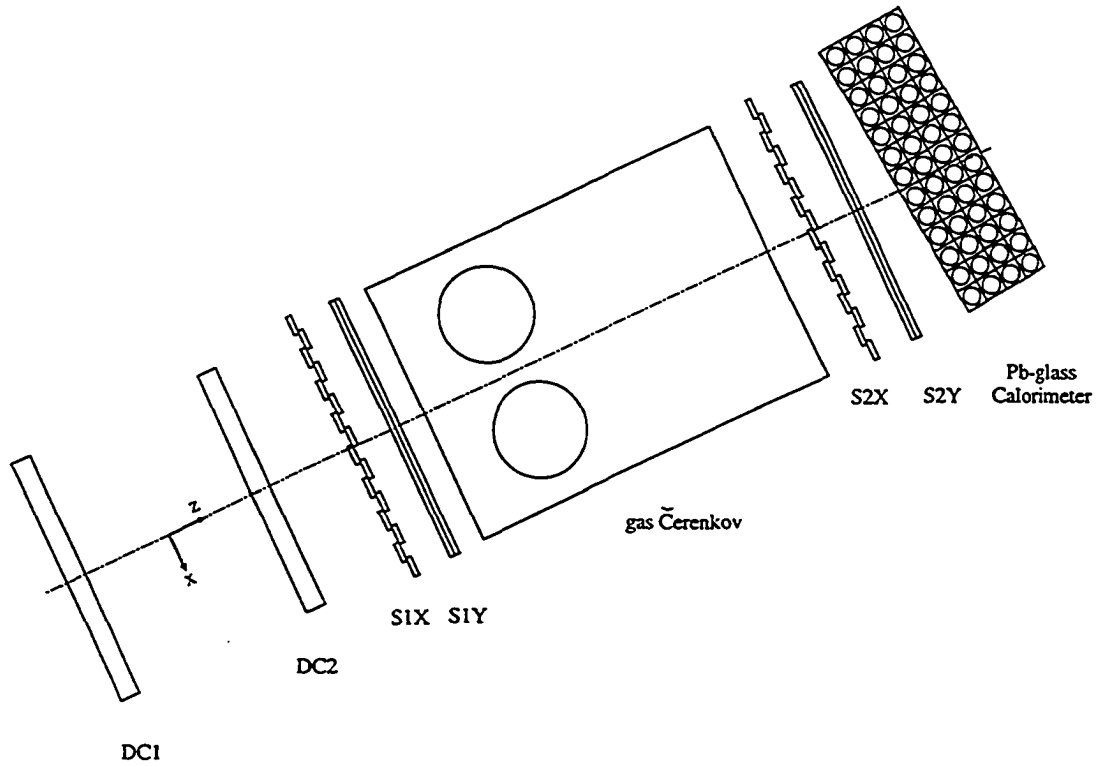


Figure 2.17: A side view of the proton spectrometer (HMS) detector stack, as seen from the door of the detector hut. The detected particles travel from left to right (along positive z). The y axis is into the page.

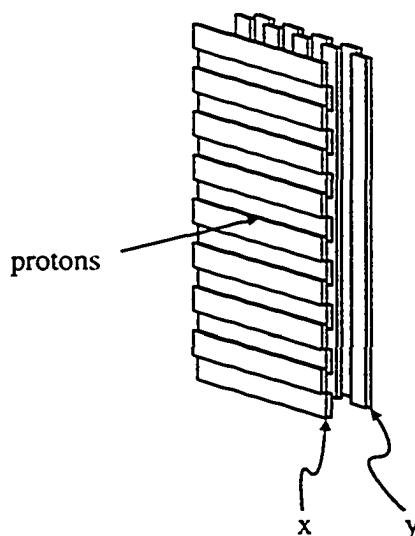


Figure 2.18: A schematic view of a pair of HMS scintillator arrays. The light guides and PMTs are not shown; the figure is intended only to show the orientation and positioning of the scintillators.

The magnetic fields were set remotely from the counting room. The field of the dipole was regulated using the output of an NMR (nuclear magnetic resonance) probe located outside the vacuum can in a region of uniform field. The quadrupoles were regulated by current. After each polarity change the magnets were cycled up to p_{\max} in order to put them on a repeatable hysteresis curve.

2.7.2 The HMS Scintillator Arrays

The HMS, like the SOS, had four planes of scintillators, two towards the front of the detector stack and two towards the rear (see Fig. 2.17). Each plane consisted of staggered, slightly overlapping strips of scintillator (see Fig. 2.18) equipped at each end with light guides and photomultiplier tubes (PMTs). The first plane encountered by a particle, S1X, had 16 scintillators arranged in the y direction (horizontally). The second plane, S1Y, had 9 scintillators arranged in the x direction (roughly vertically). Towards the rear of the detector hut this arrangement was repeated with planes S2X and S2Y, identical to S1X and S1Y, respectively.

The scintillator planes served two purposes: triggering of the data acquisition system and measurement of particle velocity using time-of-flight (β_{tof}) from the front to the rear of the detector hut. The trigger scheme and electronics were nearly identical to those used in the SOS (discussed

in Section 2.6.2 and shown in Fig. 2.12 on page 49).

2.7.3 The HMS Drift Chambers

Two drift chambers, DC1 and DC2, were used to provide track information for events in the HMS. Each chamber consisted of six planes of sense wires oriented as shown in Fig. 2.19.

The cell size of the chambers (the spacing between sense wires) was 1 cm. The field wires were held at negative high voltage, while the sense wires were grounded. The unprimed and primed planes were offset by one-half of a cell width in order help remove the left-right ambiguity inherent in a drift-time measurement of a single plane. The chambers were located at the front of the detector stack to minimize the effect of multiple-scattering in the preceding vacuum window and air.

The gas used in the drift chambers was the same argon-ethane mixture as that used in the SOS, flowed at a rate of 400 SCCM. The maximum drift time using this gas mixture was about 150 ns.

The sense wires were connected to circuit boards (LeCroy or Nanometrics) that amplified and discriminated the chamber signals. The discriminator thresholds were remotely adjustable but unchanged during the experiment. The electronics were similar to those used in the SOS, with the exception that they were located inside the HMS detector hut itself. The tracking algorithms used in the analysis are discussed in Section 4.2.1.

2.8 Trigger Electronics and Data Acquisition

The coincidence event rates in this experiment were modest (< 60 Hz), which allowed the use of a very simple triggering scheme. A valid SOS or HMS pretrigger was defined as any three-of-four coincidence of the four scintillator plane signals (S1X, S1Y, S2X, S2Y) of the corresponding spectrometer (pretrigger rates were less than 3 kHz in the SOS, 850 kHz in the HMS). Fig. 2.12 on page 49 shows the SOS trigger electronics (the HMS electronics were identical). The four gates in the upper right were used to measure electronic deadtime (less than 1.5 % for either spectrometer throughout this experiment).

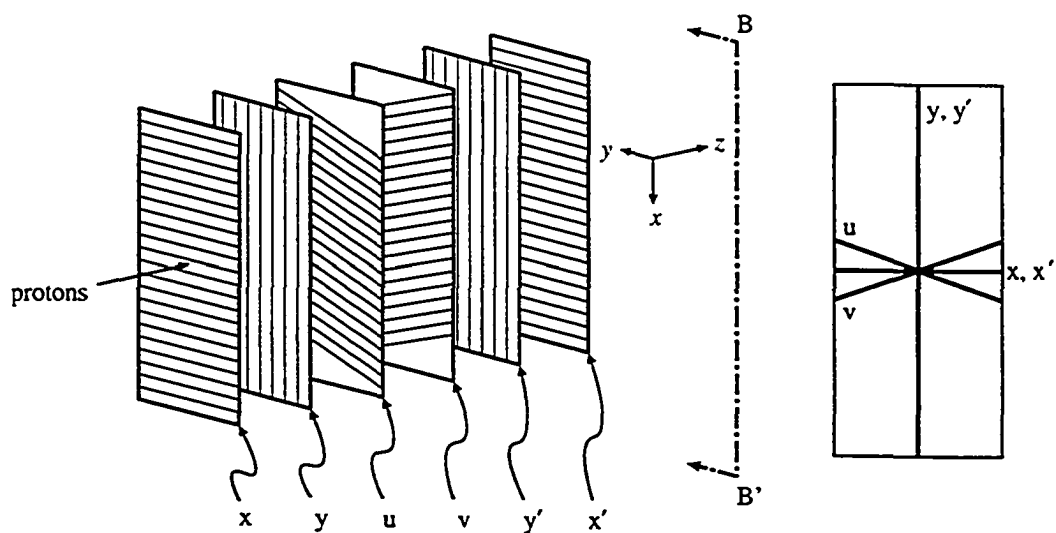


Figure 2.19: *Left)* An exploded view of the sense wires in a single HMS drift chamber. Neither the dimensions nor the number of wires are accurate, and the field wires are not shown; the figure is intended only to show the orientation of the sense wires and the ordering of the planes. The cross section B-B' is given in Fig. 2.20. *Right)* The orientation of the HMS drift chamber sense wires as seen by the incoming protons.

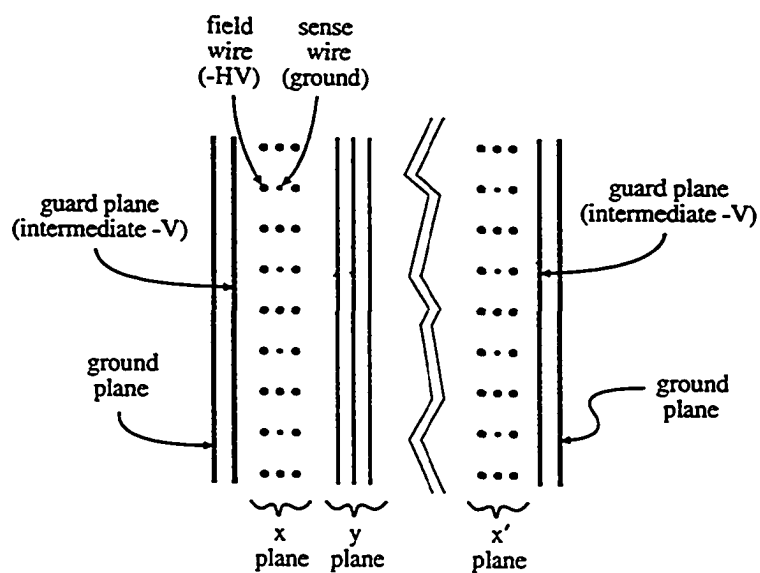


Figure 2.20: Cross section of a single HMS drift chamber.

A valid SOS or HMS pretrigger passed to the coincidence electronics (Fig. 2.21), where logic modules (the 8LM logic) determined the trigger type (SOS single, HMS single, or coincidence) and whether or not the data acquisition system was ready to accept an event. The SOS and HMS pretriggers into the coincidence logic were adjusted to give a coincidence window of about 60 ns.

If the 8LM logic passed an event, the resulting single-arm or coincidence trigger signal was sent to the trigger supervisor (a high-speed trigger interface designed by the TJNAF Data Acquisition group). The trigger supervisor handled prescaling and, for those events that passed the prescale, sent gates to the front-end electronics (ADCs and TDCs) for all detectors of the appropriate spectrometer(s). For coincidence events the triggers to each arm were retimed to the respective single-arm trigger (*i.e.*, the gate timing relative to the trigger was the same in each spectrometer for coincidence events as it was for single-arm events.)

The data acquisition software used in this experiment was CODA (CEBAF On-line Data Acquisition) version 1.4, written by TJNAF's Data Acquisition group [Abb95]. The code ran on a Hewlett-Packard 735 workstation located in the Hall C counting room and performed two main functions: run control and event building. Several FastBus crate controllers and VME/CAMAC computers (collectively referred to as Read-Out Controllers, or ROCs) served as the interface between the data acquisition computer running CODA and the front-end detector electronics.

The individual ROCs ran a multi-tasking operating system called VxWorks. They collected detector information directly from the front-end electronics and assembled the information into event fragments which were sent back to the data acquisition computer.

The run control portion of CODA performed initialization of the detectors (via user-supplied routines) and acquired event fragments, both via communication with the ROCs over a TCP/IP network. The CODA Event Builder merged the event fragments from individual ROCs into complete events, which were then written to disk. After the data obtained during the course of a run were recorded on hard-disk drives, they were backed up to the TJNAF tape 'silo' (a StorageTek robotic tape library) where they were available for subsequent off-line analysis.

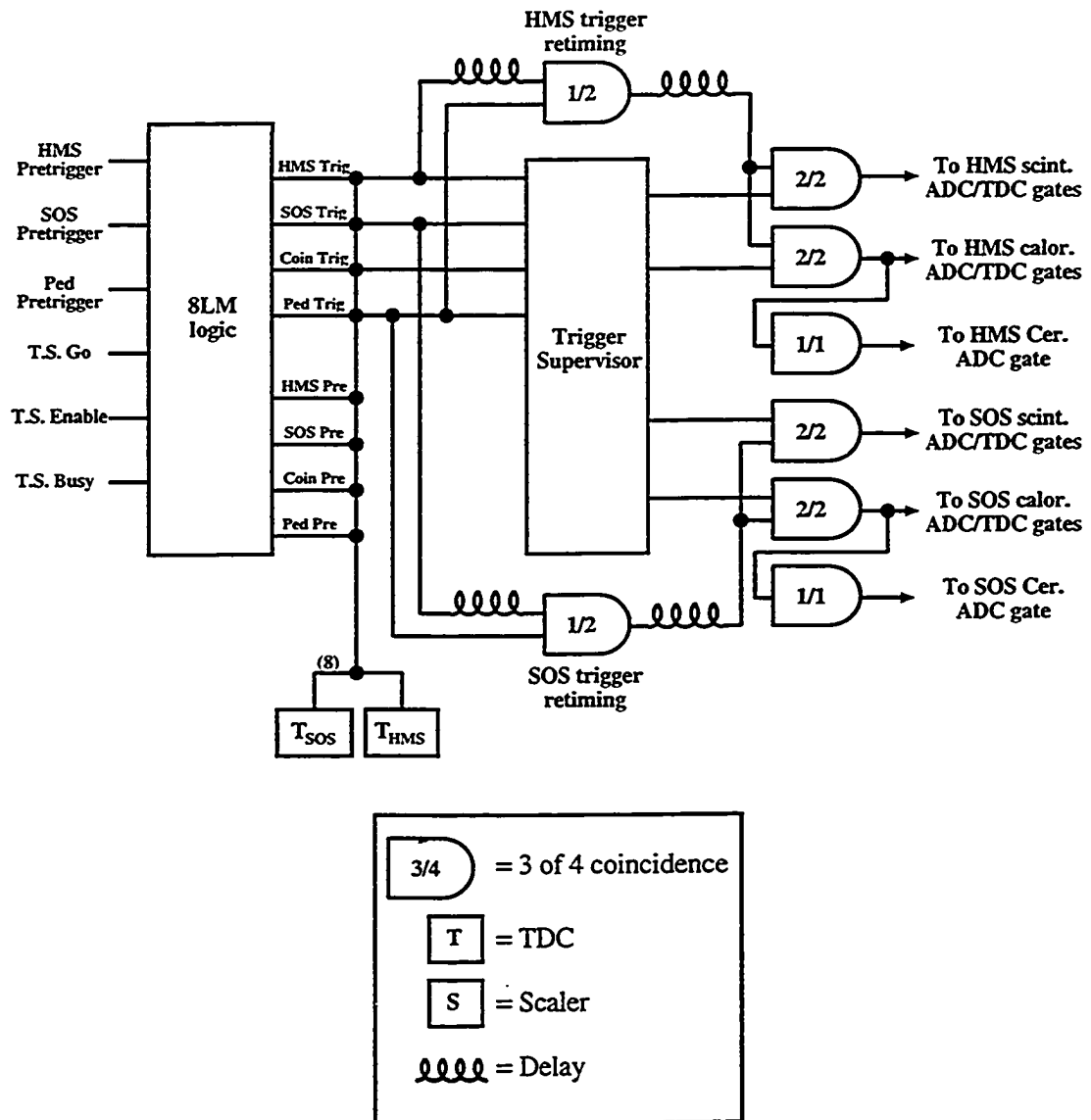


Figure 2.21: The coincidence electronics.

2.9 Materials in the Experimental Apparatus

The simulation of multiple scattering and ionization energy loss (Section 3.1.2) and external Bremsstrahlung (Section 3.3) requires information about materials in the experimental setup. Table 2.5 lists those materials traversed by the detected particles from the target through the detectors.

Object	Material	Density [g/cm ³]	Thickness [cm]	X ₀ [g/cm ²]	Radiation Lengths [%]
Upstream target window	Al 6061	2.70	0.0069	23.39	0.080
Target ¹¹	Liquid H ₂	0.0723	4.36	61.28	0.514
Downstream target window	Al 3004	2.70	0.0137	23.64	0.157
Tgt. Chamb. win.	Al	2.70	0.0203	24.01	0.228
Tgt. Chamb.-SOS gap	air	0.00121	≈ 15.	36.66	≈ 0.050
SOS entr. win.	kevlar	0.74	0.0127	55.2	0.017
	mylar	1.39	0.0076	39.95	0.026
SOS exit win.	kevlar	0.74	0.0381	55.2	0.051
	mylar	1.39	0.0127	39.95	0.044
Dipole-DC gap	air	0.00121	≈ 12.	36.66	≈ 0.04
SOS DC cathode foils	mylar	1.39	14(0.00127)	39.95	0.062
SOS DC sense/field wires ¹²	W, 30 μm, 12 planes, 60 μm, 12 planes	19.3	12(35.4 × 10 ⁻⁶)	6.76	0.121
SOS DC gas	Arg/ethane, 50/50 by weight	0.00154	12(0.6178)	27.38	0.042
Gaps through calorimeter	air	0.00121	≈ 257.	36.66	0.848
SOS S1Y ¹³	polystyrene	1.03	1.098	43.8	2.58
SOS S1X ¹³	polystyrene	1.03	1.04	43.8	2.45
SOS Ć windows	Al	2.70	2(0.05)	24.01	1.12
SOS Ć gas	Freon 12	0.00493	≈ 100.	23.67	≈ 2.08
SOS Ć Mirror and support	SiO ₂ , Rohacell	-	-	-	≈ 0.5
SOS S2Y ¹³	polystyrene	1.03	1.098	43.8	2.58
SOS Aerogel Ć windows	Al	2.70	2(0.0625)	24.01	1.41
SOS Aerogel Ć	Aerogel	-	9.0	-	≈ 6.
SOS S2X ¹³	polystyrene	1.03	1.04	43.8	2.45
SOS Calorimeter	TF1 lead glass	-	40.	-	1600.
Tgt. Chamb. wind.	Al	2.70	0.0406	24.01	0.457
Tgt. Chamb.-HMS gap	air	0.00121	≈ 15.	36.66	≈ 0.050
HMS entr. win.	kevlar	0.74	0.0381	55.2	0.051
	mylar	1.39	0.0127	39.95	0.044
HMS exit win.	kevlar	0.74	0.0381	55.2	0.051
	mylar	1.39	0.0127	39.95	0.044
Dipole-DC gap	air	0.00121	≈ 35.	36.66	≈ 0.12
HMS DC windows	mylar	1.39	4(0.00254)	39.95	0.035
HMS DC sense wires ¹²	W, 25 μm, 12 planes	19.3	12(6.33 × 10 ⁻⁶)	6.76	0.022
HMS DC field wires ¹²	Al/Au (99/1), 150 μm, 36 planes	2.70	36(0.00038)	23.38	0.158
HMS DC gas	Arg/ethane, 50/50 by weight	0.00154	12(1.8)	27.38	0.122
Gaps through S2Y	air	0.00121	≈ 239.	36.66	0.79
HMS S1X ¹³	polystyrene	1.03	1.067	43.8	2.51
HMS S1Y ¹³	polystyrene	1.03	1.067	43.8	2.51
HMS Ć windows	Al	2.70	2(0.102)	24.01	2.29
HMS Ć gas	N ₂	0.00125	150.	37.99	0.494
HMS Ć Mirror and support	SiO ₂ , Rohacell	-	-	-	≈ 0.5
HMS S2X ¹³	polystyrene	1.03	1.067	43.8	2.51
HMS S2Y ¹³	polystyrene	1.03	1.067	43.8	2.51
HMS Calorimeter	TF1 lead glass	-	40.	-	1600.

Table 2.5: Materials in the experimental setup. The first group is that material traversed (in part) by the incoming electron and (in part) both outgoing particles. The second group is that traversed by outgoing electrons only. The third group is that encountered by outgoing protons only. The entries in this table were used in the Monte Carlo calculations of multiple scattering, ionization energy loss, and external Bremsstrahlung.

¹¹The length given for the target liquid is that along the beamline.

¹²The thickness given is an effective thickness that accounts for wire spacing.

¹³The scintillators are 1.0 cm thick; the additional factor accounts for the overlap between paddles.

Chapter 3

Monte Carlo Simulation of the Experiment

This chapter describes the Monte Carlo simulation of the experiment. The program employed detailed models of both magnetic spectrometers and simulated the effects of radiative processes, multiple scattering, and ionization energy loss. It was used to obtain the experimental acceptance and radiative corrections for the resonance process under study as well as for ${}^1\text{H}(e, e')p$ and ${}^1\text{H}(e, e'p)$ scattering (used to verify understanding of the apparatus and to check the simulation of radiative processes) and to simulate the multi-pion background to the resonance production. In particular, for the resonance analysis the cross section in each $(W, \cos\theta_\eta^*, \phi_\eta)$ bin was obtained by multiplying the ratio of data to Monte Carlo yields for that bin by the value of the Monte Carlo model cross section at the bin center. In subsequent analyses the model cross section was iterated until convergence was reached. The details of this procedure are explained in Chapter 4.

3.1 Overview of the Simulation

Five different physical processes were modeled in the Monte Carlo (all of which are described more fully in Section 3.2):

- Electroproduction of an $S_{11}(1535)$ from hydrogen and its subsequent decay into a proton and

η :

$$e + p \rightarrow e' + S_{11} \rightarrow e' + p\eta \quad (3.1)$$

- Two-pion electroproduction via random population of three-body $p\pi\pi$ phase space:

$$e + p \rightarrow e' + p\pi^+\pi^- \quad (3.2)$$

- Two-pion electroproduction via a doubly-charged Delta resonance:

$$e + p \rightarrow e' + \Delta^{++}\pi^- \rightarrow e' + p\pi^+\pi^- \quad (3.3)$$

- A crude model of multi-pion electroproduction in which the electron spectrometer was populated randomly in (W, Q^2) space, weighted and subject to physical constraints, and the proton spectrometer was populated randomly in $(\Omega_p, |p'_p|)$ space. This model and the previous two pion production models simulated the background to the S_{11} electroproduction.
- Elastic scattering from hydrogen (${}^1\text{H}(e, e')p$ and ${}^1\text{H}(e, e')p$), used to verify the spectrometer acceptances, target reconstruction, and the modeling of radiative processes.

Prior to entering the main event loop, the Monte Carlo executed a preliminary event loop to determine central kinematics for the setting. These kinematics were used when calculating parameters (associated with radiative processes and ionization energy loss) whose event-to-event variation was not significant. Once in the main event loop the simulation proceeded as follows (see Fig. 3.1):

1. An interaction point in the target was chosen. The position z_{tar} along the beam was chosen randomly. The horizontal and vertical positions were chosen according to a sinusoid with randomly selected phase in order to simulate the ± 1 mm target rastering described in Section 2.5.
2. Energy loss in the target was applied to the incident electron (Section 3.1.2). Using z_{tar} together with the central kinematics for this setting the effects of external and internal Bremsstrahlung on the incoming electron were modeled (Section 3.3).

3. All quantities necessary to completely specify the vertex kinematics of the event were generated randomly in the appropriate phase space.
4. With all vertex quantities known, the effects of external and internal Bremsstrahlung on the outgoing electron and (optionally) proton were modeled. Ionization energy loss and multiple scattering in the target and related materials was simulated for both outgoing particles.
5. The model cross section (Section 3.2) was evaluated and scaled by a multiplicative radiation factor M_{corr} (Section 3.3), and the event accepted with a probability proportional to that scaled cross section.
6. The passage of each particle through its respective spectrometer was simulated. In addition to modeling the magnetic elements of the spectrometers, the 'single arm' Monte Carlo routines included the effects of drift chamber resolution and multiple scattering in the spectrometer materials. Particles that failed to pass through the fiducial volumes of the trigger detectors (hodoscopes) and, in the case of electrons, the volumes of the gas Čerenkov and calorimeter, were considered undetected. Target quantities were reconstructed. Detector efficiencies were not modeled.
7. Coincidence quantities were calculated and event information saved.

Once the main loop over events was complete the Monte Carlo code performed end-of-run calculations and stored event-by-event information in a CERNLIB HBOOK ntuple [CERNL].

3.1.1 Calculation of the Monte Carlo Yield

The simulated experimental yield Y for each process (*e.g.*, S_{11} , $\Delta^{++}\pi^-$) may be expressed as:¹

$$Y = N_e \left(\frac{N_p}{\text{unit area}} \right) \left[\int \sigma_{\text{MC}}(\mathcal{V}_{\text{gen}}) A R d\mathcal{V}_{\text{gen}} \right], \quad (3.4)$$

where

- N_e is the number of incident electrons, given by $\frac{Q}{1.602 \times 10^{-19}}$, where Q is the beam charge in Coulombs.

¹Here Y can refer to the yield in any particular piece of phase space (one small physics bin, say, or the entire acceptance) as long as that same phase space is understood throughout the equation.

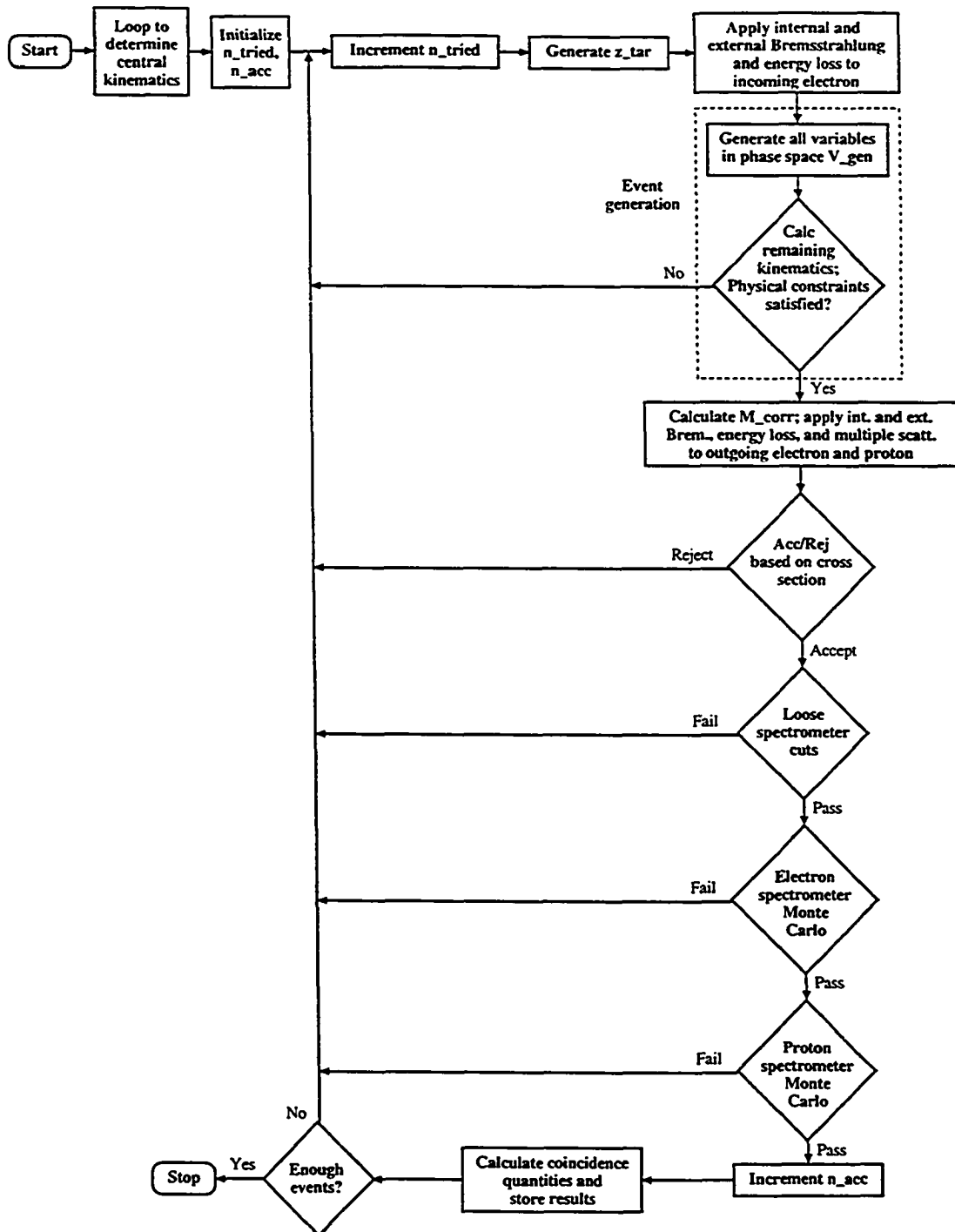


Figure 3.1: Flow diagram for the Monte Carlo simulation. The quantities n_{tried} (N_{tried}), n_{acc} (N_{accept}), and V_{gen} (\mathcal{V}_{gen}) are discussed in Section 3.1.1. The multiplicative part of the radiative correction, M_{corr} (M_{corr}), is discussed in Section 3.3.

- $N_p/(\text{unit area})$ is the number of target protons per unit area, given by $\frac{\rho_{\text{tar}} T_{\text{tar}} N_A}{M_{\text{tar}}}$, where
 - ρ_{tar} is the density of the target in g cm^{-3} ;
 - T_{tar} is the thickness of the target in cm;
 - N_A is the Avogadro constant, $6.0221 \times 10^{23} \text{ mol}^{-1}$;
 - M_{tar} is the target mass in atomic mass units (amu);
- $\sigma_{\text{MC}}(\mathcal{V}_{\text{gen}})$ is the model cross section, which in general depends on the variables of the generation volume \mathcal{V}_{gen} (in the case of the S_{11} the generation volume corresponds to $(W, Q^2, \phi_e, \Omega_\eta^*)$ space);
- \mathcal{A} represents the acceptance of the experimental apparatus, and
- R represents the effect of radiative processes.

The integration of the model cross section is over the appropriate phase space \mathcal{V}_{gen} . The Monte Carlo performs this integration using the acceptance-rejection technique,² calculating the value of the model cross section for each event and testing it against a trial value generated randomly on the interval $[0, \sigma_{\text{max}}]$, where σ_{max} is a constant chosen to be equal to or greater than the maximum value of $\sigma_{\text{MC}}(\mathcal{V}_{\text{gen}})$. The acceptance \mathcal{A} and radiative correction R are taken into account by accepting or rejecting the particles in their respective ‘single arm’ Monte Carlo routines and, in the case of radiation, modification of the model cross section.³ Once the Monte Carlo simulation has been performed (thus integrating the bracketed quantity in Eq. 3.4), we have for the general process

$$Y = N_e \left(\frac{N_p}{\text{unit area}} \right) \frac{N_{\text{accept}}}{N_{\text{tried}}} \Delta \mathcal{V}_{\text{gen}} \sigma_{\text{max}}, \quad (3.5)$$

²It is instructive to recall the one-dimensional case of integration by Monte Carlo. Given some function $y = f(x) \geq 0$ we approximate the definite integral $I = \int_{x_{\text{min}}}^{x_{\text{max}}} f(x) dx$ by selecting N_{tried} random values of x on the interval $[x_{\text{min}}, x_{\text{max}}]$. For each x_i we calculate $y_i = f(x_i)$ and select a random trial y_t on the interval $[0, y_{\text{max}}]$ (where all y are guaranteed to lie within 0 and y_{max}). A trial y_t is accepted if $y_t < y_i$, and the approximation to the definite integral is then given by $I_{\text{mc}} = (N_{\text{accept}}/N_{\text{tried}}) \cdot \mathcal{V}_{\text{gen}} \cdot y_{\text{max}}$, where the generation volume \mathcal{V}_{gen} in this case is simply $(x_{\text{max}} - x_{\text{min}})$. A nice discussion of the general topic is found in Ref. [Pre92].

³Note that the quantities \mathcal{A} and R are not numbers available on an *event-by-event* basis. They are instead quantities that arise from the use of the Monte Carlo to perform the integration of the bracketed quantity in Eq. 3.4.

where we have N_{accept} successful events out of N_{tried} events thrown into the volume V_{gen} .⁴ For the case of S_{11} production this becomes

$$Y = N_e \left(\frac{N_p}{\text{unit area}} \right) \frac{N_{\text{accept}}}{N_{\text{tried}}} (\Delta W \Delta Q^2 \Delta \phi_e \Delta \Omega_\eta^*) \sigma_{\text{max}} . \quad (3.6)$$

3.1.2 Passage Through Material

Multiple Scattering

The effect of small-angle multiple scattering on the electron and proton as they traversed material in the target and spectrometers was simulated (see Table 2.5 on page 62 for a list of materials). The angle θ_i in either the x or y plane was modified according to

$$\theta'_i = \theta_i + g \delta\theta_i , \quad (3.7)$$

where g is a random variable, Gaussian distributed with mean 0 and $\sigma = 1$, and the width is given by a fit to a Molière distribution [PDG98]:

$$\delta\theta_i = \frac{0.0136 \text{ GeV}}{\beta c p} \sqrt{x/X_0} [1 + 0.038 \ln(x/X_0)] . \quad (3.8)$$

Here $\delta\theta_i$ is the angular change in either x or y plane, βc and p are the velocity and momentum of the incident particle, and x/X_0 is the thickness of the scattering material in radiation lengths.

Ionization Energy Loss

The effect of energy loss due to ionization on the electron and proton as they travelled through the target was small but simulated nevertheless. For protons the most probable rate of energy loss was given by the Bethe-Bloch equation (see, for example, Refs. [Leo94] or [PDG98]):

$$-\frac{dE}{dx} = 0.3071 \frac{Z}{A} \frac{1}{\beta^2} \left[\ln \left(\frac{2m_e \beta^2 c^2 \gamma^2}{I} \right) - \beta^2 \right] , \quad (3.9)$$

where dE/dx is the rate of energy loss in $\text{MeV g}^{-1}\text{cm}^2$, Z and A are the atomic number and mass of the material being traversed, and $\gamma = (1 - \beta^2)^{-1/2}$. The density effect and shell corrections

⁴The Monte Carlo yield given here corresponds to a data yield that has been corrected for efficiencies.

were neglected, since the protons in this experiment were nearly minimum-ionizing. The average ionization potential I depends on the material through which the proton is travelling. Here we used a parameterization found in Ref. [Leo94]:

$$\begin{aligned} I &= Z(12 + 7Z^{-1}) \text{ eV} & Z < 13 \\ I &= Z(9.76 + 58.8Z^{-1.19}) \text{ eV} & Z \geq 13. \end{aligned} \quad (3.10)$$

A typical value for proton energy loss in the target hydrogen was 0.6 MeV, which in the worst case corresponded to 0.05 % of the energy of the outgoing proton.

For electrons we used for most probable rate of energy loss the relativistic approximation of the Bethe-Bloch equation due to Ref. [OBr74]:

$$-\frac{dE}{dx} = 0.3071 \frac{Z}{A} \frac{1}{2} \left[19.26 + \ln \left(\frac{t}{\rho} \right) \right], \quad (3.11)$$

where t is the thickness of the material in g/cm^2 and ρ is the density of the material in g/cm^3 . A typical value for electron energy loss in the target hydrogen was 0.9 MeV, which in the worst case corresponded to 0.08 % (0.03 %) of the energy of the outgoing (incident) electron.

3.2 Event Generation

3.2.1 Resonance Production

The cross section for electroproduction of the $S_{11}(1535)$ is conventionally expressed as a differential in electron solid angle Ω_e , incident electron energy E_e , and Ω_η^* , the solid angle of the η in the center-of-momentum (c.m.) frame of the hadronic resonance:

$$\frac{d^5\sigma}{d\Omega_e dE'_e d\Omega_\eta^*} = \Gamma_\gamma(E, E', \theta_e) \frac{d^2\sigma}{d\Omega_\eta^*}, \quad (3.12)$$

where Γ_γ is the virtual photon flux. In practice, since a region of the (E'_e, Ω_e) phase space is excluded by the threshold of the S_{11} at $W_{\text{thr}} = (m_p + m_\eta)$, it is more efficient to generate events in the variables W , Q^2 , ϕ_e (the azimuthal angle of the outgoing electron), and Ω_η^* (where the Jacobian between the two spaces is taken into account by using the appropriate form of the transverse virtual

photon flux Γ_τ , given in Eq. 1.9 on page 15):

$$\frac{d^5\sigma}{dW dQ^2 d\phi_e d\Omega_\eta^*} = \Gamma_\tau(W, Q^2) \frac{d^2\sigma}{d\Omega_\eta^*}. \quad (3.13)$$

In the Monte Carlo simulation, electron quantities were generated randomly⁵ over set limits in the variables W , Q^2 , and ϕ_e , and accepted within a volume somewhat larger than the acceptance of the electron spectrometer. If an event passed these tests then the quantities $\cos\theta_\eta$ and ϕ_η were randomly generated over 4π in the c.m. frame and all remaining kinematic quantities calculated. The resulting proton was boosted to the lab and the event retained only if the proton was in a volume somewhat larger than the acceptance of the proton spectrometer.

Remaining events were then accepted with a weight proportional to the product of Eq. 3.13 and M_{corr} , the multiplicative part of the radiative correction (discussed in Section 3.3). The form corresponding to Eq. 3.13 used to model the cross section in the Monte Carlo was

$$\sigma_{\text{MC}}(W, Q^2, \Omega_\eta^*) = \Gamma_\tau(W, Q^2) \sigma_{\text{MC,em}}(W, Q^2, \Omega_\eta^*), \quad (3.14)$$

with the model c.m. cross section of the form⁶

$$\sigma_{\text{MC,em}}(W, Q^2, \Omega_\eta^*) = A^2 \frac{|\mathbf{p}_\eta^*| W}{m_p K} \frac{W_R^2 \Gamma_R^2}{(W^2 - W_R^2)^2 + W_R^2 \Gamma^2(W)} + B_{\text{nr}} \sqrt{W - W_{\text{thr}}}, \quad (3.15)$$

where

- the momentum of the η in the c.m. of the hadronic resonance, $|\mathbf{p}_\eta^*|$, was given in Section 1.3.2;
- the energy-dependent resonance width $\Gamma(W)$ was parameterized in terms of the full S_{11} width Γ_R and the three largest S_{11} decay branching fractions, b_η , b_π , and $b_{\pi\pi}$:

$$\Gamma(W) = \Gamma_R \left(b_\eta \frac{|\mathbf{p}_\eta^*|}{|\mathbf{p}_\eta^*|_R} + b_\pi \frac{|\mathbf{p}_\pi^*|}{|\mathbf{p}_\pi^*|_R} + b_{\pi\pi} \right), \quad (3.16)$$

where the subscript ‘R’ in $|\mathbf{p}_\eta^*|_R$ denotes evaluation at $W = W_R = 1535$ MeV;

⁵The random number generator used throughout the Monte Carlo simulation was ran3 of Ref. [Pre92].

⁶Note that the validity of the final results were *not* dependent on having in the Monte Carlo an accurate form for the resonance cross section. Since the general analysis procedure (detailed in Section 4.3.10) was to renormalize the ratio of data to Monte Carlo yields by the Monte Carlo model cross section on a bin-by-bin basis, the final result was in principle not sensitive to the precise form of the model cross section. The fact that the iteration procedure converged served simply as a check on the procedure.

- the equivalent real photon energy $K = \frac{W^2 - m_p^2}{2m_p}$;
- The parameters A and B_{nr} are the magnitude of the resonant and nonresonant parts of the cross section.

The parameters A , B_{nr} , and Γ_R used in the Monte Carlo were assigned initial values (based on the findings of Ref. [Bra84]) at each Q^2 point and subsequently iterated. The fitted nonresonant term in the analysis was consistent with zero in all advanced stages, so B_{nr} was set to zero in the Monte Carlo. The value of Γ_R used in the Monte Carlo was iterated based on each successive analysis, with the result converging in a few iterations to that quoted in the final results (≈ 150 MeV). The resonance mass in the simulation was fixed at $W_R = 1535$ MeV, and the branching fractions were fixed at $b_\eta : b_\pi : b_{\pi\pi} = 0.45 : 0.45 : 0.10$.

S_{11} events that passed the cross section acceptance-rejection test were then passed in turn to the two spectrometer Monte Carlos (described in Section 3.4). Note that the Monte Carlo model cross section did not have an explicit Q^2 dependence (aside from a gross difference between the two Q^2 values). The data were instead corrected for Q^2 dependence, or ‘bin-centered’, at both of the points. This correction is described in Section 4.3.9.

3.2.2 Multi-Pion Background

As noted above, three processes were used to simulate the multi-pion background. In each case electrons were generated randomly in (W, Q^2) space and accepted with a probability proportional to the product of the virtual photon flux Γ_τ (Eq. 1.9 on page 15) and the square of a dipole form factor ($G_D^2 = [1 + Q^2/0.71]^{-4}$).

The first process (which we call ‘Model 1’) simulated two-pion electroproduction by randomly populating the three-body $p\pi\pi$ phase space. After generation of the electron quantities, proton and pion energies and angles were generated randomly in the c.m. frame, subject to the constraints of energy and momentum conservation.

The second process (‘Model 2’) simulated two-pion electroproduction via production of a $\Delta^{++}\pi^-$ pair and subsequent decay of the Δ^{++} into a $p\pi^+$ pair. The model was derived from a DESY streamer-chamber experiment [Wac76]. The doubly-charged $\Delta(1232)$ was distributed in

the c.m. frame according to Refs. [Sau78, Bre78],

$$\frac{d^2\sigma}{d\Omega_{\Delta^{++}}} = 0.6 - 0.9 \cos\theta^* + 1.1 \cos^2\theta^* . \quad (3.17)$$

The mass of the Δ was generated according to a Breit-Wigner expression, and the Δ subsequently allowed to decay isotropically in its c.m. frame.

The third process ('Model 3') simply generated proton quantities randomly in $(\Omega_p, |p'_p|)$ space subject to the physical constraints $W > m_p + 2m_\pi$ and $M_x > 2m_\pi$.

All three models represented the background reasonably well (see Fig. 3.2, and Fig. 4.15 on page 119). Discrepancies in final physics results using the models were fairly small ($\sim 5\%$); these differences were used to estimate the systematic uncertainty arising from the use of the models (Section 5.1).

3.2.3 Elastic Scattering

In the case of elastic scattering the model cross section was differential in Ω_e . Events were generated randomly in the quantities $\cos\theta_e$ and ϕ_e , subjected to a cross section acceptance-rejection test, and passed through the electron spectrometer Monte Carlo. The model cross section used was ([Hal84], p. 177)

$$\frac{d^2\sigma}{d\Omega_e} = \frac{\alpha^2 \cos^2 \frac{\theta}{2}}{4 E^2 \sin^4 \frac{\theta}{2}} \frac{E'}{E} \left(\frac{G_{E_p}^2 + \tau G_{M_p}^2}{1 + \tau} + 2\tau G_{M_p}^2 \tan^2 \frac{\theta}{2} \right) , \quad (3.18)$$

where θ , E , and E' are the usual electron quantities, α is the fine structure constant, and $\tau \equiv -q^2/4m_p^2$. The dipole form factor was used for G_{E_p} :

$$\begin{aligned} G_{E_p}(Q^2) &= G_D(Q^2) \\ &= \left(1 + \frac{Q^2}{0.71} \right)^{-2} , \end{aligned} \quad (3.19)$$

and the Gari-Krümpelmann parameterization [Gar85] was used for G_{M_p} :

$$G_{M_p}(Q^2) = F_1^p(Q^2) + F_2^p(Q^2) , \quad (3.20)$$

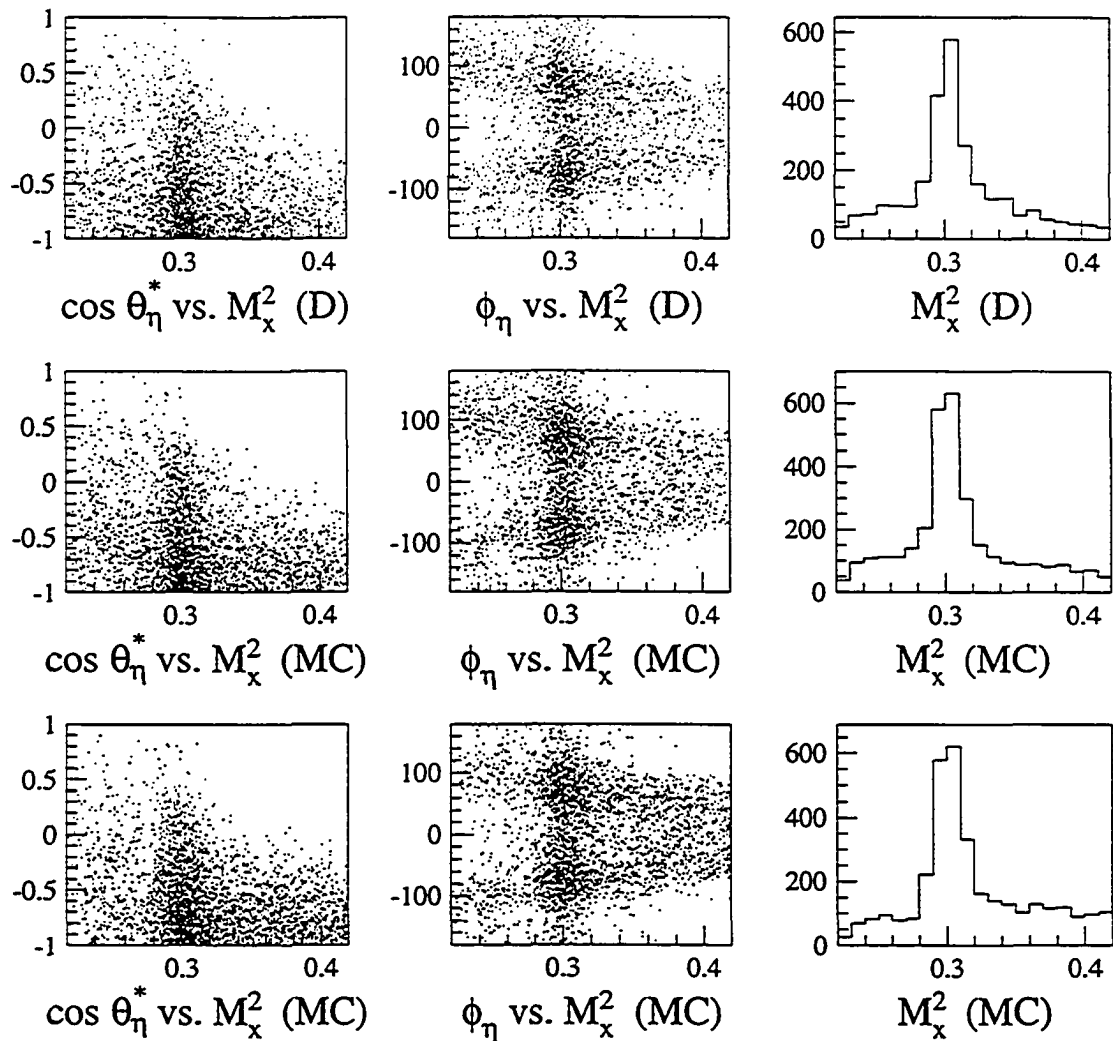


Figure 3.2: A comparison of data to Monte Carlo simulation for a typical kinematic setting. The top row shows $\cos \theta_\eta^*$ and ϕ_η versus M_x^2 , and M_x^2 , for the data. The second row shows the corresponding distributions for the Monte Carlo simulation, where the background was generated by 'Model 1'. The third row shows the Monte Carlo result using 'Model 3'. The 'Model 2' result is not shown but looked similar; this model was not used in later stages of analysis (see Section 5.1). Normalizations are arbitrary.

where

$$F_1^P(Q^2) = \frac{1}{2} [F_1^{IS}(Q^2) + F_1^{IV}(Q^2)] \quad (3.21)$$

and

$$F_2^P(Q^2) = \frac{1}{2} [\kappa_s F_1^{IS}(Q^2) + \kappa_v F_1^{IV}(Q^2)] . \quad (3.22)$$

Definitions for F_1^{IS} , F_1^{IV} , κ_s , and κ_v are given in Ref. [Gar85].

The simulation of inclusive elastic scattering, or ${}^1\text{H}(e, e')p$, and exclusive elastic scattering, or ${}^1\text{H}(e, e'p)$, was the same except that exclusive Monte Carlo events were tested for passage through the proton spectrometer. Figures 3.3 and 3.4 show the agreement between data and Monte Carlo simulation for SOS focal plane and reconstructed target quantities (and similarly, Figures 3.5 and 3.6 for the HMS). Figure 3.7 shows the ratio of data to Monte Carlo yields for six settings in which the angle of the SOS was changed, sweeping the elastic electrons across the momentum acceptance of the spectrometer. Most of the S_{11} resonance data in this experiment occupied the range $-15\% < \delta < 0\%$. Figure 3.8 shows the excellent reproduction of the radiative tail in the Monte Carlo.

3.3 Radiative Processes

When the experimentalist measures an $(e, e'p)$ cross section she is measuring not only the process depicted by the Born term (Fig. 1.6 in Chapter 1) but also associated higher-order processes. We separate these processes into three classes. The most straightforward to treat are *external Bremsstrahlung* (Fig. 3.9), in which the incoming or outgoing particle radiates one or more real photons in the field of a nucleus *other* than that which undergoes the hard scattering in which we are interested. In the present experiment external Bremsstrahlung was negligible for the proton; we only needed to treat that which occurred to the incoming and outgoing electron. External Bremsstrahlung is relatively easy to handle because the nuclei involved are physically distant from the hard interaction of interest, and so the cross sections add *without interference*.

The second class of processes is *internal Bremsstrahlung* (Fig. 3.10). The incoming or outgoing particle radiates one or more real ('soft') photons but, in contrast to the case above, the radiation occurs in the field of the nucleon that is also involved in the hard scattering (hence the label

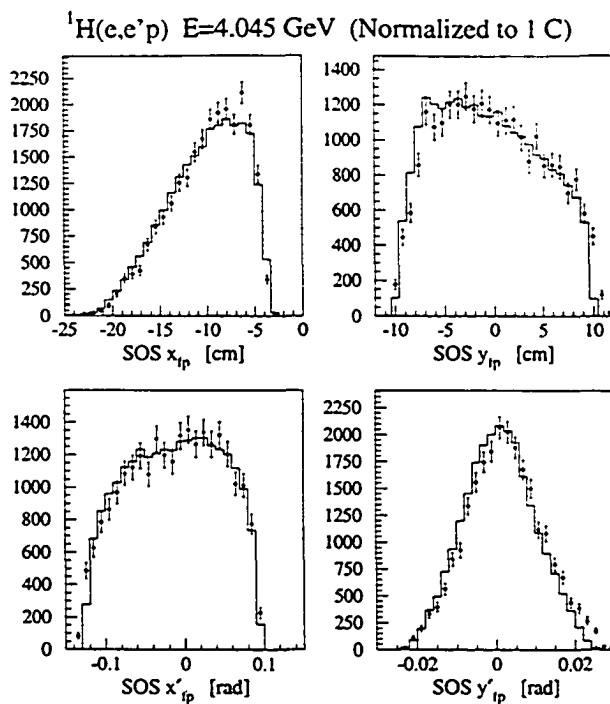


Figure 3.3: SOS focal plane quantities for $^1\text{H}(e,e'p)$, data (points) and Monte Carlo (lines).

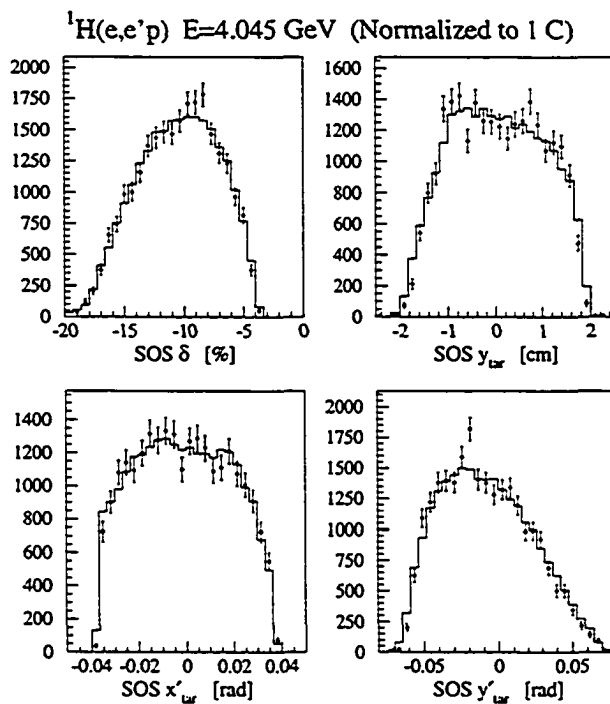


Figure 3.4: SOS reconstructed target quantities for $^1\text{H}(e,e'p)$, data (points) and Monte Carlo (lines).

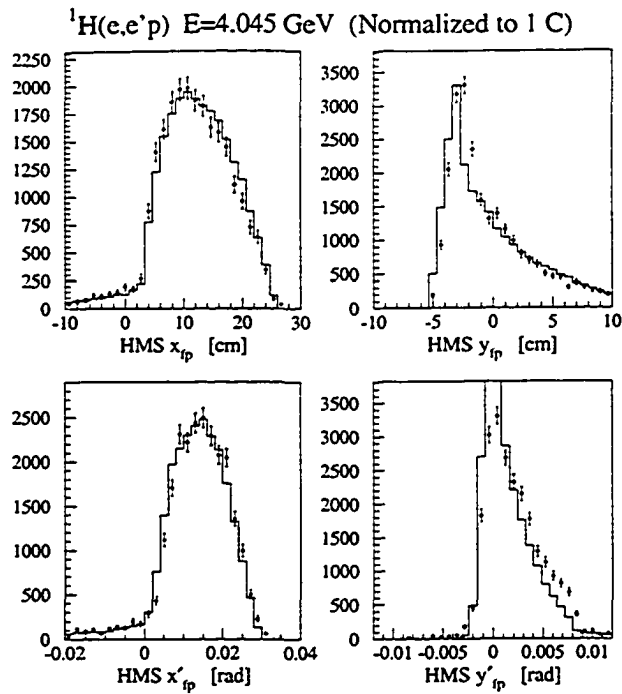


Figure 3.5: HMS focal plane quantities for $^1\text{H}(e, e'p)$, data (points) and Monte Carlo (lines).

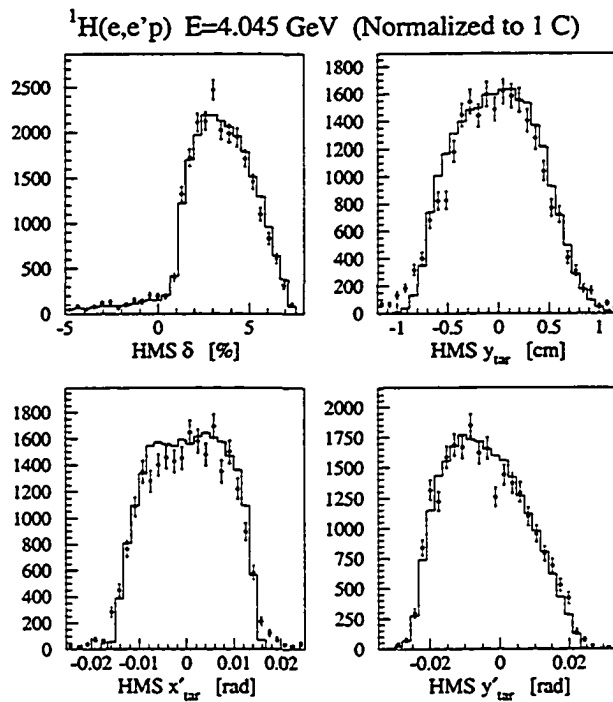


Figure 3.6: HMS reconstructed target quantities for $^1\text{H}(e, e'p)$, data (points) and Monte Carlo (lines).

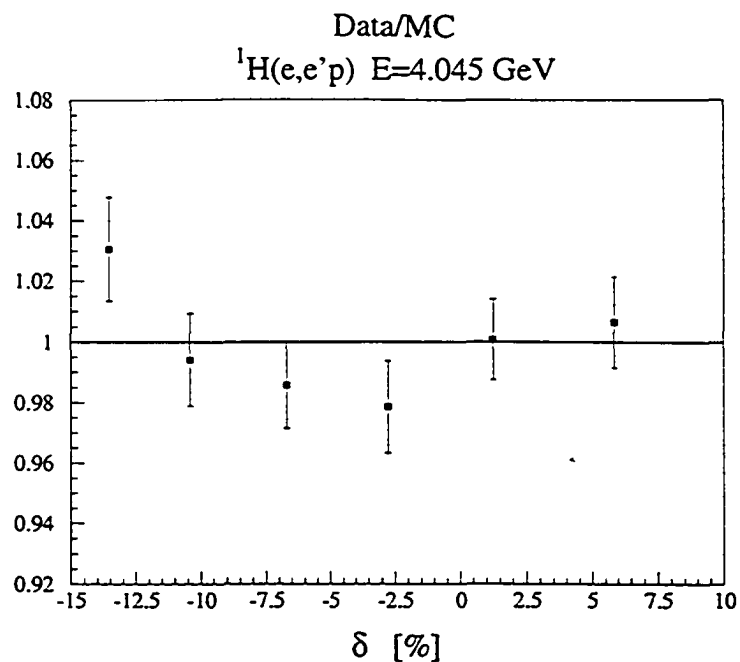


Figure 3.7: The ratio of data to Monte Carlo yields for six ${}^1\text{H}(e,e'p)$ settings.

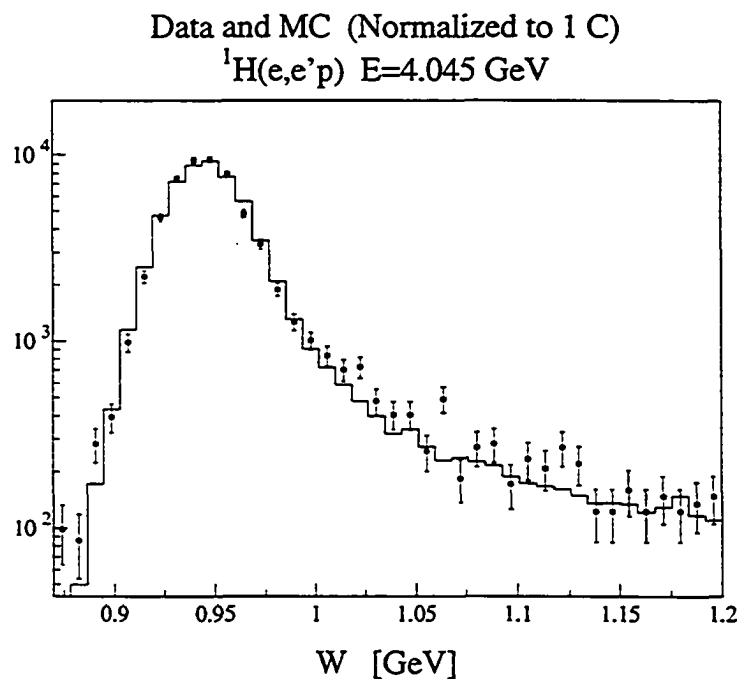


Figure 3.8: Data (points) and Monte Carlo (line) W distributions for an ${}^1\text{H}(e,e'p)$ setting.

‘internal’). The amplitudes for the different diagrams *interfere*, making evaluation of the effect more complicated than in the case of external Bremsstrahlung. In addition, for this experiment the case of internal Bremsstrahlung of the proton was modeled.

The third class of processes we label *internal hard* processes (Fig. 3.11). It includes virtual (‘hard’) photon vertex processes as well as vacuum polarization (loop diagrams).

3.3.1 The Multi-Photon Prescription

The procedure (and notation) used in this work to generate radiative corrections was the multi-photon prescription of Wasson and collaborators, discussed in detail in Refs. [Mak94, Mak98]. Here we give only the main result of the procedure, which is an extension to a coincidence framework of the standard techniques of inclusive radiative corrections of Mo and Tsai [Tsa61, Mo69, Ear73, Tsa74]. The Wasson work uses the soft photon approximation (the limit in which the energy E_γ of the radiated photon is much less than k_i, p_i, k_f, p_f , the momenta of the fermions in the initial and final states) and an ‘extended’ peaking approximation (in which the contributions of nonpeaked ep interference and ee terms are retained, thus preserving the total radiated strength).

There are two manifestations of radiative processes. The diagrams involving real photons (external and internal Bremsstrahlung) give rise to cut-dependent effects in which the event kinematics are modified. As a result of these processes events may radiate into or out of the region of interest (or the spectrometer altogether). The soft effects were simulated in the Monte Carlo by generating radiative events (for the incoming and outgoing electrons and outgoing protons) with the appropriate distribution in photon energy E_γ up to a maximum photon energy ΔE .⁷

The internal hard diagrams (the vertex and vacuum polarization diagrams), on the other hand, give rise to cut-independent effects. In this case the kinematics of the event are unaffected, and the result is a scaling of the cross section. The effect of the hard processes enters as a cut-independent multiplicative factor $(1 - \delta_{\text{hard}})$ that is applied to the cross section before undergoing acceptance/rejection testing (which is discussed in Section 3.1.1).⁸

For reference we list here the key equations of the multi-photon prescription of Wasson, *et al.*,

⁷This is not to be confused with the case for the original Mo and Tsai prescription, in which the integration is up to a maximum *total energy loss* ΔE .

⁸As noted above, we follow the notation of Wasson and collaborators; elsewhere in the literature the ‘hard’ correction is called the ‘finite’ correction.

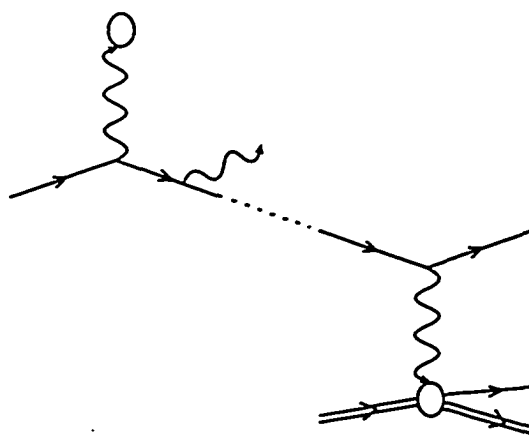


Figure 3.9: Feynman diagram for external Bremsstrahlung.

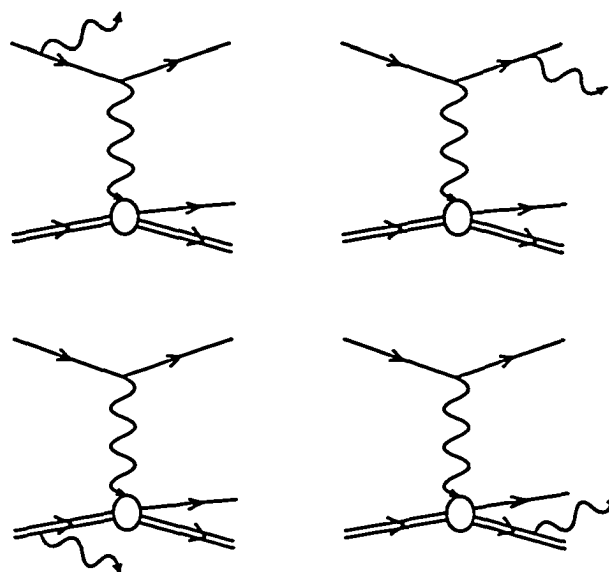


Figure 3.10: Feynman diagrams for internal Bremsstrahlung.

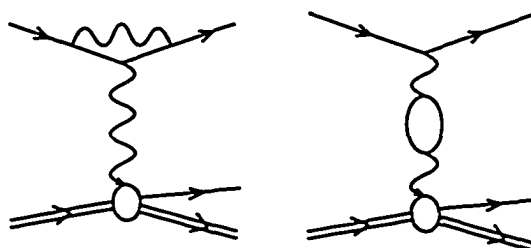


Figure 3.11: Feynman diagrams for internal hard corrections.

starting with the final result. The radiative effects are expressed as

$$\begin{aligned} \frac{d^8\sigma}{d\Omega_e dE'_e d\Omega_\eta^* dE_{\gamma_i} dE_{\gamma_f} dE_{\gamma_p}} &= \frac{d^5\sigma^{(1)}}{d\Omega_e dE'_e d\Omega_\eta^*} M_{\text{corr}} \\ &\times \frac{dE_{\gamma_i}}{E_{\gamma_i}^{1-\lambda_i-bt_i}} \frac{dE_{\gamma_f}}{E_{\gamma_f}^{1-\lambda_f-bt_f}} \frac{dE_{\gamma_p}}{E_{\gamma_p}^{1-\lambda_p}}. \end{aligned} \quad (3.23)$$

Here the i , f , and p subscripts denote quantities that apply to the incoming and outgoing electron and outgoing proton, respectively. The quantity $\frac{d^5\sigma^{(1)}}{d\Omega_e dE'_e d\Omega_\eta^*}$ is the one-photon-exchange cross section.

The integration of Eq. 3.23 over the photon energies E_{γ_i} , E_{γ_f} , and E_{γ_p} is performed using the Monte Carlo method. We have defined M_{corr} to contain the multiplicative factors

$$M_{\text{corr}} = (1 - \delta_{\text{hard}}) M_{\text{soft}} \bar{\Phi}_i^{\text{ext}}(E_{\gamma_i}) \bar{\Phi}_f^{\text{ext}}(E_{\gamma_f}), \quad (3.24)$$

where the internal hard effects are given by

$$\delta_{\text{hard}} = \delta_{e \text{ vert}} + \delta_{e \text{ vac}} + \delta_{\mu \text{ vac}} + \delta_{q \text{ vac}}, \quad (3.25)$$

with the first three terms as given by Ref. [Mo69], and the quark vacuum polarization correction as given in Ref. [TAS82]:

$$\delta_{e \text{ vert}} = \frac{2\alpha}{\pi} \left\{ 1 - \frac{3}{4} \ln \left(\frac{Q^2}{m_e^2} \right) \right\}; \quad (3.26)$$

$$\delta_{e \text{ vac}} = \frac{2\alpha}{\pi} \left\{ \frac{5}{9} - \frac{1}{3} \ln \left(\frac{Q^2}{m_e^2} \right) \right\}; \quad (3.27)$$

$$\delta_{\mu \text{ vac}} = \frac{2\alpha}{\pi} \left\{ \frac{5}{9} - \frac{1}{3} \ln \left(\frac{Q^2}{m_\mu^2} \right) \right\}; \quad (3.28)$$

$$\delta_{q \text{ vac}} = 2 \left\{ -1.523 \times 10^{-3} - 2.822 \times 10^{-3} \ln(1 + 1.218 Q^2) \right\}. \quad (3.29)$$

The multiplicative piece of the soft processes is given by

$$\begin{aligned} M_{\text{soft}} &= \frac{1}{\Gamma(1+bt_i)} \frac{1}{\Gamma(1+bt_f)} \\ &\times \frac{bt_i + \lambda_i}{(k_i)^{bt_i} (\sqrt{k_i k_f})^{\lambda_i}} \frac{bt_f + \lambda_f}{(k_f)^{bt_f} (\sqrt{k_i k_f})^{\lambda_f}} \frac{\lambda_p}{(\sqrt{m_p p^0})^{\lambda_p}}. \end{aligned} \quad (3.30)$$

Here the k s are electron momenta, p'^0 is the energy of the outgoing proton, and the Γ s are the standard Gamma function. The factors bt represent sums of (thickness t)-(parameter b) over all materials in the target and scattering chamber. The thickness t is in units of radiation lengths, and the parameter b is given in terms of the atomic charge Z of each material by

$$b = \frac{1}{9} \left(12 + \frac{Z+1}{ZL_1 + L_2} \right), \quad (3.31)$$

with

$$L_1 = \ln(184.15) - \frac{1}{3} \ln(Z); \quad (3.32)$$

$$L_2 = \ln(1194.) - \frac{2}{3} \ln(Z). \quad (3.33)$$

The λ s are given by

$$\lambda_e = \frac{\alpha}{\pi} \left[\ln \left(\frac{4k_i^2}{m_p^2} \right) - 1 + 2 \ln \left(\frac{k_i}{k_f} \right) + \ln \left(\frac{1 - \cos(\theta_e)}{2} \right) \right]; \quad (3.34)$$

$$\lambda_{e'} = \frac{\alpha}{\pi} \left[\ln \left(\frac{4k_f^2}{m_p^2} \right) - 1 + 2 \ln \left(\frac{k_i}{k_f} \right) + \ln \left(\frac{1 - \cos(\theta_e)}{2} \right) \right]; \quad (3.35)$$

$$\lambda_{p'} = \frac{\alpha}{\pi} \left[\ln \left(\frac{p'^0 + |\mathbf{p}'|}{p'^0 - |\mathbf{p}'|} \right) - 2 \right]. \quad (3.36)$$

The $\bar{\Phi}^{\text{ext}}(E_\gamma)$, which are energy distributions of the single-photon Bremsstrahlung spectrum, are included to first order using

$$\bar{\Phi}_i^{\text{ext}}(E_{\gamma_i}) = 1 - \frac{bt_i}{bt_i + \lambda_i} \frac{E_{\gamma_i}}{k_i}, \quad (3.37)$$

and similar for E_{γ_f} .

Figure 3.8 shows the excellent agreement between data and the Monte Carlo simulation for ${}^1\text{H}(e, e'p)$ scattering. Both the yield and the energy dependence of the tail are well-reproduced by the Monte Carlo simulation.

3.4 The Spectrometer Monte Carlos

If an event passed the cross section acceptance-rejection test, all kinematic quantities for the electron and proton were calculated and passed to routines that simulated the magnetic spectrom-

eters. These ‘single-arm’ Monte Carlos modeled the effects of various apertures in the devices and passage through both the magnetic elements and the detectors.⁹ ‘Detected’ events then underwent reconstruction back to the target.

Given an initial position and direction leaving the target, the electrons and protons were drifted (in field-free regions) or transported (in magnetic elements) forward in z . At strategic points their position was checked against that of collimators, magnetic elements, and other various apertures. If the particle impinged on any of these objects it was considered to have stopped.¹⁰

The forward transport of the electrons through the SOS model was done using eight sequential 6th order transport maps, with aperture checks at each point in between. The maps were obtained from COSY INFINITY¹¹ using the results of a field map of the magnetic elements. The transport of protons through the HMS magnetic elements was performed using eleven nonsequential 5th order transport maps (*i.e.*, each starting from the target interaction point), with aperture checks at every point in between. The maps were obtained from a COSY model of the HMS magnetic elements. In both spectrometers, the aperture checks were made at the entrance and exit positions of each magnetic element and at the z -position inside each magnetic element where the beam envelope was expected to reach its maximum size.

Events that were transported successfully through the magnetic elements of the spectrometers were then passed to code that simulated the detector huts. Here the particles were drifted through all the detectors, undergoing multiple scattering (Section 3.1.2) whenever they encountered air or other material. If a particle failed to pass through the fiducial volume of three of the four scintillator planes or, in the case of electrons in the SOS, failed to pass through the fiducial volume of the gas Čerenkov detector or electromagnetic calorimeter, the event was stopped.

If the event was considered detected, the hit positions at the drift chambers were smeared by the chamber resolution and the resulting values fit to a track at the focal plane. The track was then reconstructed back to the target using transport maps generated by COSY.

⁹The effect of proton absorption was not included in the Monte Carlo, but an overall correction was applied to the data. This correction is discussed in Section 4.3.4.

¹⁰Passage through these objects was not modeled; the effect of this process on the data (in particular, for protons in the HMS) is discussed in Section 4.3.6.

¹¹COSY INFINITY is a program that uses differential algebraic methods to model optical systems to arbitrary order [Ber90].

Chapter 4

Data Analysis

4.1 Overview of the Analysis

The general approach taken in this analysis was to generate Monte Carlo results as close to actual data as practicable, and to subsequently analyze the data and Monte Carlo results using the same software routines. As described in the last chapter, the Monte Carlo simulation employed detailed models of the spectrometers, modeled the effects of radiation, multiple scattering, and ionization energy loss, and incorporated both the resonance process of interest as well as processes mimicing the multi-pion background. Both the data and Monte Carlo results were then subjected to the same multi-pion background fit and subtraction algorithms.

Yields per unit charge (binned in W , $\cos\theta_\eta^*$, and ϕ_η) were extracted for both data and Monte Carlo. Angular distributions were calculated by taking, for each bin, the ratio of data yield to Monte Carlo yield and multiplying by the Monte Carlo model cross section ($\sigma_{MC,em}$ of Eq. 3.15 on page 70) integrated over that bin. The resulting differential cross sections were fit to a multipole expansion. The Monte Carlo model cross section was then iterated based on the results of the fit, and the process repeated.

The decision to analyze the data in this fashion, as opposed to the alternative application of Monte-Carlo-derived acceptance and radiation corrections to the data, was driven by the fact that the multi-pion background fit and subtraction were a potential source of large errors. Applying the same fit and subtraction algorithms to the data and to a good facsimile of the data and utilizing

the resulting ratio minimized those errors.

This chapter explains in detail each step taken during the analysis. In overview those steps were as follows (reference to more detailed discussion is given parenthetically):

1. The individual data runs were analyzed using the Hall C replay software, which performed timing analysis and track reconstruction and generated event ntuples as well as various reports and diagnostic histograms. Everything performed in the replay software is described in Section 4.2.
2. Histograms and scaler reports for each run were checked to ensure that no problems were evident in the data (Section 4.3.1).
3. A Monte Carlo simulation was performed for each kinematic setting (Chapter 3).
4. Cuts to spectrometer momenta and a loose cut to target position as determined by the HMS were made to both the coincidence data events and to the Monte Carlo results. Cuts to the coincidence data (but not Monte Carlo results) were made on particle ID (PID) quantities and coincidence time (Section 4.3.8).
5. Data and Monte Carlo results for each run were binned in W , $\cos\theta_\eta^*$, ϕ_η , and M_x^2 .
6. The binned data for each run were normalized for beam charge (Sections 4.3.2 and 4.3.3) and corrected for trigger, track reconstruction, and computer live time efficiencies (Section 4.2.6), proton absorption (Section 4.3.4), and then combined with data from other runs at the same kinematic setting.
7. The multi-pion background was fit and subtracted from the data at each setting (Section 4.3.7). The same algorithm was used to perform a background fit and subtraction on the Monte Carlo results for that setting.
8. A missing mass squared (M_x^2) cut was applied to the data and to the Monte Carlo results, and the results integrated over M_x^2 .
9. A correction was applied to bin-center the data to the nominal Q^2 (Section 4.3.9).
10. The differential cross section at each bin was calculated by multiplying the ratio of data yield to Monte Carlo yield by the integral of the model cross section over that bin. The results for

all settings at each Q^2 point were combined. The differential cross section data for each W bin were fit to a multipole expansion (Section 4.3.10).

4.2 Hall C Replay Software

The raw data obtained during the experiment were recorded to hard-disk drive and backed up within about a day to the TJNAF mass storage silo. Once in storage on the silo the data were available for retrieval and analysis by the Hall C replay software. The replay software performed the following for each physics event:

1. *CODA event decoding*—decode the hardware event information and translate into detector arrays.
2. *HMS and SOS reconstruction*—If the event had a trigger in the HMS (SOS), perform event reconstruction:
 - (a) *Track-independent time of flight (TOF) analysis*—Do pre-tracking analysis of scintillator information. Most importantly, find the time t_{start} of the particle's traversal of the focal plane (necessary to determine drift times in the drift chambers). Also estimate the hit position at each scintillator based on relative timing of signals from the two scintillator photomultiplier tubes (PMTs) and get a preliminary measurement of the particle velocity β_{tof} (used to reject cosmic rays when calculating the efficiency of track reconstruction).
 - (b) *Track-independent calorimeter analysis (SOS only)*—Perform pre-tracking analysis of calorimeter information to estimate the rate of energy loss dE/dx and total energy deposition E_{tot} (Section 4.2.4).
 - (c) *Track-independent Čerenkov analysis (SOS only)*—use ADC information from the Čerenkov detector to calculate the number of photo-electrons detected (Section 4.2.4).
 - (d) *Track reconstruction*—Use information from the two wire chambers to fit candidate tracks in the detector stack (Section 4.2.1). For each candidate track, do
 - i. *Target quantity reconstruction*—use matrix transformations to translate focal plane quantities into quantities at the target (Section 4.2.2);

- ii. *TOF analysis*—use timing information from the scintillators hit along the track to find β_{tof} associated with the track (Sections 4.2.3 and 4.2.4);
 - (e) *Track selection*—From all candidate tracks that meet loose requirements on β_{tof} , dE/dx (SOS only), and E_{tot} (SOS only), select the one with the best fit (lowest χ^2).
 - (f) *Single-arm calculations*—Calculate all single-arm physics quantities for the selected track (Section 4.2.5).
3. *Coincidence calculations*—If the event had both HMS and SOS triggers, calculate coincidence physics quantities (Section 4.2.5) and store all results.

Once all events had been analyzed, the replay software calculated various efficiencies (Section 4.2.6). The primary output of the replay software was a CERNLIB HBOOK ntuple [CERNL] containing event-by-event track information, reconstructed target quantities, timing and PID information, beam information, and calculated physics quantities. Predefined diagnostic histograms and reports detailing scaler activity during the run were also produced.

Many features of the SOS and HMS detectors were similar, as were many components of the replay software. Here we will discuss the two cases together, pointing out differences where they arise.

4.2.1 Drift Distance Mapping and Track Reconstruction

In the detector stack of each spectrometer was a pair of drift chambers used to determine particle tracks. The drift time t_{drift} (ranging from 0 to about 150 ns) of the electrons from the track to the chamber wire had to be mapped to a drift distance d_{drift} (ranging from 0 to 0.5 cm, the half-size of a drift cell) in order to supply useful tracking information. The drift distance corresponding to a particular drift time was in the form of a look-up table, with 138 entries from -24 to 250 ns.

The values in the table were obtained from data runs in which there was roughly uniform illumination of the chambers. The distribution of drift times summed over all cells was obtained for each chamber plane, and the map for each plane was determined by assuming the summed distribution to be flat.¹ In particular, for the vector v_i ($1 \leq i \leq 138$) of binned drift times for a

¹This assumption gave rise to tracking errors on the order of $\pm 20 \mu\text{m}$ [Arr96].

plane, the entries of the drift distance look-up table (a vector of length 138) were given by

$$d_i = \frac{\sum_{j=1}^i v_j}{\sum_{j=1}^{138} v_j} . \quad (4.1)$$

The table was obtained periodically (every few days or so) or at any sign of change to the track residuals,² since the time-to-distance translation depended on the composition of the drift chamber gas.³

With a satisfactory time-to-distance map in place the residuals to the single-chamber tracks typically had $\sigma \approx 70 \mu\text{m}$ for the SOS and $\sigma \approx 150 \mu\text{m}$ for the HMS.⁴ At this point the tracking portion of the replay software could construct tracks from the drift chamber information. For each event the tracking software would

1. *Find drift times*—The drift chambers yielded TDC values t_{tdc} for hits at individual wires, where the common stop of the TDC was formed by the trigger from the scintillators. An offset, t_{start} , was therefore necessary to translate t_{tdc} into a drift time. The final drift time was also corrected for timing offsets in circuit board traces and cables between the wire and the TDC as well as for the propagation time of the signal along the hit wire (this last correction was position dependent and relied on preliminary hit position information):

$$t_{\text{drift}} = t_{\text{tdc}} + t_{\text{start}} - t_{\text{trace}} - t_{\text{cable}} - t_{\text{prop}} . \quad (4.2)$$

2. *Map drift times to drift distances*—For each hit wire the measured drift time was converted to a drift distance using a linear interpolation between entries of the table described above.
3. *Find space points*—Individual hits in a single chamber were identified with space points, or clusters of hits. In order to qualify for consideration, a space point needed to have five (out of six) planes registering a hit (so-called ‘five out of six tracking’).

²By track residual we mean (for a particular hit on a drift chamber wire) the difference between the position at the wire as determined by the wire hit and the position at the wire as determined from the final track fit to either one or two chambers.

³In particular, the mobility of the chamber gas depended on the alcohol concentration, which in turn was a function of the alcohol temperature at the bubbler (Section 2.6.3).

⁴The residuals to complete tracks found between both chambers were larger ($\sigma \approx 150 \mu\text{m}$ and $\sigma \approx 250 \mu\text{m}$ for the SOS and HMS, respectively), in part because of multiple scattering. The residuals to single-chamber tracks, or stubs, were more indicative of the actual chamber resolution.

4. *Resolve left-right ambiguities*—For each space point, left-right ambiguities were resolved by fitting stubs (single-chamber tracks) to all possible combinations and selecting the stub with the best χ^2 .
5. *Construct candidate tracks*—Where a pair of stubs met loose criteria, candidate tracks were constructed by combining stubs from both chambers.⁵
6. *Fit tracks*—For each candidate track perform a fit and evaluate the goodness of that fit (final selection of a single track took place later).

A more detailed explanation of the HMS and SOS track reconstruction can be found in Refs. [Gee93] and [Abb94].

4.2.2 Reconstruction of Target Quantities

The detectors for both the electron spectrometer (SOS) and the proton spectrometer (HMS) directly measured particle position and angle (relative to the central ray) in the detector hut after passage through the magnetic elements of the spectrometer. In particular, the drift chamber tracks were expressed in terms of the quantities x_{fp} , y_{fp} , x'_{fp} , and y'_{fp} (as defined in Section 1.3.1). From these four focal plane quantities the replay software reconstructed the momentum of the particle (p) relative to the central momentum setting of the spectrometer (p_0), $\delta \equiv (p - p_0)/p_0$, together with three target quantities, y_{tar} , x'_{tar} , and y'_{tar} , using an N^{th} order transformation (where $N = 6$ for the SOS, 5 for the HMS). Collectively denoting the four reconstructed quantities by X_{tar} we have for i^{th} event

$$X_{tar}^i = \sum_{j,k,l,m=0}^N M_{jklm} (x_{fp}^i - x_0)^j (y_{fp}^i - y_0)^k (x'_{fp}^i - x'_0)^l (y'_{fp}^i - y'_0)^m, \quad (4.3)$$

where x_0 was a constant offset in x_{fp} at the focal plane (and similarly for the other quantities). Each target quantity X_{tar} had its own set of reconstruction matrix elements M_{jklm} , the optimization of which was rather involved. An overview of the procedure as well as plots indicating the quality of the reconstruction are given in Appendix B. The procedure is discussed in detail in Ref. [Ass97].

⁵Track multiplicity was generally low in this experiment. In the worst conditions (seen by the HMS), $\approx 5\%$ of all tracked coincidence events yielded 2 candidate tracks; $\approx 1\%$ yielded 3 candidates; $< 1\%$ yielded 4 or more.

It should be noted that, although the beam was rastered by ± 1 mm on the target, the resulting effect on reconstructed target quantities was within the resolution of the spectrometers. Since no correlation between the resonance data and the raster signals was observable, no explicit correction was made for this effect.⁶

4.2.3 Scintillator Timing Corrections

As described in Chapter 2, the analog signals from the four scintillator arrays of each spectrometer were routed up to the Hall C electronics room, where they were input to discriminators. One of the discriminator outputs was sent to a TDC, providing a measurement of the arrival time of each PMT signal. The measurement of particle velocity β_{tof} (discussed in Section 4.2.4) relied on reasonably accurate timing information from the scintillator arrays. Corrections were made to the scintillator timing to account for three effects:

1. propagation of light through the scintillator;
2. time walk induced by pulse-height variation;
3. cable and electronics timing offsets.

The first effect was corrected using the distance d_{prop} from the impact point of the detected particle (as determined by the reconstructed track) to the PMT, together with an effective propagation velocity v_{scin} for light in the scintillator. Since the light arriving at a PMT did not all travel directly (some arrived only after multiple internal reflections), the effective velocity depended on both the index of refraction of the material and dimensions of the scintillator paddle. Prior to this experiment, the value of v_{scin} for the scintillator geometries used in the Hall C spectrometers was determined from fits to data [Mac98] ($v_{\text{scin}} \approx 15$ cm/ns, where the velocity of light in the scintillator is $v = c/n \approx 20$ cm/ns).⁷ The time

$$t_{\text{prop}}^{i,e} = d_{\text{prop}}^e / v_{\text{scin}}^i \quad (4.4)$$

⁶As noted in Chapter 3, the raster was nevertheless included in the Monte Carlo simulation.

⁷In principle the value of v_{scin} itself also varied with the hit position along the length of the scintillator. For scintillation originating close to the end of a paddle a greater fraction of light reaching the PMT traveled directly (rather than via multiple reflections) than was the case for scintillation originating far away. In other words, v_{scin} was greater when d_{prop} was small than when it was large. Bench tests indicated that the magnitude of this effect was comparable to that due to the intrinsic resolution of the scintillators. Since timing resolution was not critical for this experiment no correction was made for this effect.

was subtracted from $t_{\text{pmt}}^{i,e}$, the hit time of the e^{th} event at the i^{th} PMT, to account for this propagation time (for the remainder of this section we will denote event-specific quantities with a superscript e and PMT-specific quantities with a superscript i). The propagation correction $t_{\text{prop}}^{i,e}$ varied from 0 to 8 ns.

The second effect, time walk, refers to the correlation between the ADC value $A_{\text{pmt}}^{i,e}$ of a PMT signal (its integrated strength) and its arrival time $t_{\text{pmt}}^{i,e}$ as measured when discriminated and sent to a TDC. The pulse shape of the analog signal from a PMT is only a weak function of amplitude; thus the greater the signal amplitude $A_{\text{pmt}}^{i,e}$, the sooner it crosses the threshold voltage of the discriminator (see Fig. 4.1). This effect is corrected⁸ by assuming a mathematical form for the leading edge of the analog PMT signal. Knowledge of $A_{\text{pmt}}^{i,e}$ then allows calculation of the expected time walk. Here we modeled the leading edge of the time-domain signal $P(t)$ seen by the ADC with a Lorentzian [ONe94]:

$$P^i(t) = \frac{k^i A_{\text{pmt}}^{i,e}}{(t^{i,e} - t_0)^2 + (\Gamma^i/2)^2} \quad (t^{i,e} < t_0), \quad (4.5)$$

where t_0 is the time at the peak of the pulse, Γ^i is the FWHM of the pulse, and k^i is a constant relating the pulse height at its maximum, $P_{\text{max}}^{i,e}$, to the ADC (integrated) readout $A_{\text{pmt}}^{i,e}$,

$$\begin{aligned} P_{\text{max}}^{i,e} &= P^i(t)|_{t^{i,e}=t_0} \\ &= \frac{k^i A_{\text{pmt}}^{i,e}}{(\Gamma^i/2)^2}. \end{aligned} \quad (4.6)$$

When sent to a discriminator with threshold P_{thr}^i , the difference between t_0 and the time $t_{\text{thr}}^{i,e}$ at which the pulse crosses the threshold (*i.e.*, the ‘walk’ time, within a constant offset) is

$$\begin{aligned} t_w^{i,e} &= t_0 - t_{\text{thr}}^{i,e} \\ &= \sqrt{\frac{k^i A_{\text{pmt}}^{i,e}}{P_{\text{thr}}^i} - (\Gamma^i/2)^2} \\ &= C_1^i \sqrt{A_{\text{pmt}}^{i,e}} - C_2^i, \end{aligned} \quad (4.7)$$

⁸The correction for time walk used here is a software correction; there also exist so-called *constant fraction* discriminators which correct for the effect in hardware.

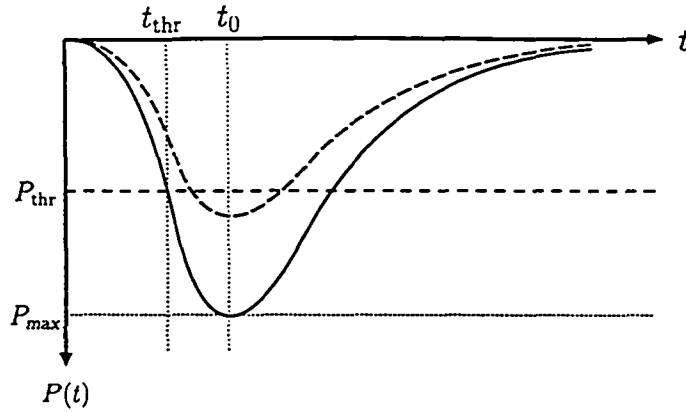


Figure 4.1: The time walk ($t_{\text{thr}} - t_0$) is caused by variations in the pulse height P_{thr} from the maximum value P_{max} .

where C_1^i and C_2^i are constants. The pulse height correction actually used in this analysis was

$$t_{\text{phc}}^{i,e} = C_1^i \sqrt{\max[0, (A_{\text{pmt}}^{i,e} - C_2^i)]}, \quad (4.8)$$

where the ‘max’ function prevented runaway corrections for pulses near the discriminator threshold. The pulse height correction $t_{\text{phc}}^{i,e}$, which was usually less than 2 ns, was subtracted from the hit time at each PMT.

C_1^i and C_2^i were determined for each PMT using off-line software to perform fits to a subset of the actual data.⁹ The code used data files, created by the standard replay software, that gave event-by-event ADC and TDC outputs from individual PMTs as well as focal plane track quantities and β .¹⁰ Differences in PMT times between certain reference scintillators and perpendicular scintillators in other planes were used, together with the known hit positions and particle velocities, to fit the constants C_1^i and C_2^i for optimal timing resolution.

The third effect, constant offsets from one PMT to another, was due to mismatch in cabling and electronics delays between the PMTs and their respective TDCs.¹¹ These offsets were corrected using software similar to the pulse height correction software discussed above. Using the same

⁹The pulse-height correction and offset fitting code was adapted by J. Arrington from similar SLAC software.

¹⁰The quantity β used here was either 1 (when using a clean sample of electrons or pions) or the value of β derived from reconstructed momentum (with knowledge, via kinematics, of the particle type). The quantity β_{tof} measured using time of flight in the detector stack (discussed in Section 4.2.4) could not be used for this analysis; rather, optimization of β_{tof} resulted from the scintillator corrections discussed here.

¹¹Although the cables were matched to within about 1 ns, timing variations of order 10 ns were introduced by the electronic delays (nominally 400 ns) used for timing adjustments.

data file, the software calculated differences in scintillator mean times (the mean of the two $t_{\text{pmt}}^{i,e}$ for a scintillator) between certain reference scintillators and perpendicular ('crossed') scintillators in other planes. With $\Delta t_{j,k,\text{meas}}^e$ the flight time as measured by the mean time of two scintillators, and $\Delta t_{j,k,\text{calc}}^e$ the expected time difference (from knowledge of scintillator positions together with particle velocity), values of C_3^i were obtained that minimized the difference $\Delta t_{j,k}^e$ between measured and calculated flight times between the j^{th} and k^{th} crossed scintillators:

$$\begin{aligned}
 \Delta t_{j,k}^e &= \Delta t_{j,k,\text{meas}}^e - \Delta t_{j,k,\text{calc}}^e \\
 &= \left\{ t_{\text{MT,corr}}^{j,e} - t_{\text{MT,corr}}^{k,e} \right\} - \Delta t_{j,k,\text{calc}}^e \\
 &= \left\{ \left[\frac{(t_{\text{pmt}}^{j1,e} - C_3^{j1}) + (t_{\text{pmt}}^{j2,e} - C_3^{j2})}{2} \right] \right. \\
 &\quad \left. - \left[\frac{(t_{\text{pmt}}^{k1,e} - C_3^{k1}) + (t_{\text{pmt}}^{k2,e} - C_3^{k2})}{2} \right] \right\} - \Delta t_{j,k,\text{calc}}^e , \tag{4.9}
 \end{aligned}$$

over all scintillator pairs and all events. Here the $t_{\text{pmt}}^{j,e}$ have been corrected for propagation time and pulse height walk using Eqs. 4.4 and 4.8. The correction for timing offsets was then

$$t_{\text{off}}^i = C_3^i . \tag{4.10}$$

This offset correction was up to 25 ns. As expected there was some interaction between the pulse height corrections and the offset corrections, and the final resolution benefitted from iterating the above analysis.

With all three corrections (Eqs. 4.4, 4.8, and 4.10) applied, we had for the corrected hit time at the i^{th} PMT for the e^{th} event

$$t_{\text{pmt,corr}}^{i,e} = t_{\text{pmt}}^{i,e} - t_{\text{prop}}^{i,e} - t_{\text{phc}}^{i,e} - t_{\text{off}}^i . \tag{4.11}$$

The mean time $t_{\text{scin}}^{j,e}$ for the j^{th} scintillator was then the average of $t_{\text{pmt,corr}}^{i,e}$ for the two scintillator PMTs (or just one if only one reported a good TDC time). The time was projected back to the

focal plane using the known travel distance $d_{fp}^{j,e}$ and particle velocity $\beta^e c$ according to

$$t_{fp}^{j,e} = t_{scin}^{j,e} - \frac{d_{fp}^{j,e}}{\beta^e c}, \quad (4.12)$$

and the time at the focal plane for the track, t_{fp} , was the average of all $t_{fp}^{j,e}$ for scintillator hits along the track.

4.2.4 Particle Identification and Real-Accidental Separation

In the electron spectrometer (SOS) two detectors distinguished between electrons and negatively-charged pions, a threshold gas Čerenkov detector and a lead-glass electromagnetic calorimeter. In the proton spectrometer (HMS) protons were separated from positively-charged pions using the particle velocity (measured using time of flight, or TOF, in the detector stack). The coincidence time between the two spectrometers was used to separate real from accidental coincidences.

Gas Čerenkov

The pedestal-subtracted ADC readout $A_{i,ADC}$ from each of the four Čerenkov PMTs was scaled to units of photo-electrons using a calibration constant C_i , and the sum of photo-electrons served as the Čerenkov signal:

$$\begin{aligned} N_{\text{sum,p.e.}} &= \sum_{i=1}^4 N_{i,\text{p.e.}} \\ &= \sum_{i=1}^4 C_i A_{i,ADC}. \end{aligned} \quad (4.13)$$

At the time of this experiment the mirrors of the SOS Čerenkov detector had small misalignments and some degradation of the reflective surfaces. As a result, the number of photo-electrons was low in a small area around the central axis; nevertheless, with the loose cut $N_{\text{sum,p.e.}} > 1$ the efficiency in this region was acceptable at a cost of rather poor rejection efficiency. A study using a clean sample of elastic electrons populating the same fiducial region and energy range as the actual data showed an efficiency of better than $\epsilon_{\text{cer}} = 99.5\%$ in the problematic area, but $99.9 \pm 0.1\%$ overall, with this cut (see Figs. 4.2 and 4.3), with a corresponding rejection efficiency (*i.e.*, the fraction of

pions correctly identified as such) of $\bar{\epsilon}_{\text{cer}} \approx 98\%$ (i.e., a rejection ratio of 49:1).¹²

Electromagnetic Calorimeter

The pedestal-subtracted signals from the 44 lead blocks of the calorimeter were summed to form a single calorimeter quantity, the total energy deposition:

$$\begin{aligned} E_{\text{tot}} &= \sum_{i=1}^{44} E_i \\ &= \sum_{i=1}^{44} C_i A_{i,\text{ADC}} . \end{aligned} \quad (4.14)$$

After selection of a single track, the energy deposition was normalized to the momentum associated with that track,¹³

$$E_{\text{norm}} = \frac{E_{\text{tot}}}{p_{\text{track}}} . \quad (4.15)$$

The lead-glass of the calorimeter was sufficiently thick (16 radiation lengths) to bring virtually all electrons below the critical energy (forming a peak at $E_{\text{norm}} \approx 1$; see Figs. 4.2 and 4.3). The resolution of the electron signal was $\sigma \approx 5\%/\sqrt{E [\text{GeV}]}$. The calorimeter signal due to pions was dominated by the creation of Čerenkov light (forming a peak at $E_{\text{norm}} \approx 0.25$) but had a long tail (at high E_{norm}) due to hadronic interactions. As a result, the calorimeter was highly efficient for detection of electrons, but with a poor rejection efficiency. A study using a clean electron sample similar to the actual data yielded a detection efficiency of $\epsilon_{\text{cal}} > 99.7 \pm 0.1\%$ for the cut $E_{\text{norm}} > 0.7$. The rejection efficiency for the same cut, on the other hand, was $\bar{\epsilon}_{\text{cal}} \approx 95\%$.

Electron Identification

Pion rejection was desirable but not critical, because accidental pions that passed all PID cuts populated the M_{π}^2 distribution smoothly and were removed by the background subtraction. In addition, the worst-case pion-to-electron ratios were modest in the kinematics of this experiment ($\pi^- : e^- \approx 5 : 1$ once loose cuts were applied to the electron spectrometer momentum). Since both PID detectors had good detection efficiency with loose cuts, it was decided to require hits in both.

¹²To clarify the notation: suppose $\epsilon = 99\%$, $\bar{\epsilon} = 90\%$. If we detect 1000 electrons and 500 pions, we properly identify some $1000\epsilon = 990$ electrons and mistakenly identify some $500(1 - \bar{\epsilon}) = 50$ pions as electrons.

¹³The standard Hall C analysis software also contained a calorimeter signal that summed energy deposition within some fiducial region of the selected track at the calorimeter; the signal used in this analysis had no such requirement.

Based on the studies noted above, the detection efficiency of the combined calorimeter-Čerenkov cuts was found to be $\varepsilon = \varepsilon_{\text{cer}} \varepsilon_{\text{cal}} = 99.6 \pm 0.14\%$. The rejection efficiency, which for reasons stated above was not crucial, was determined to be $\bar{\varepsilon} = 1 - (1 - \bar{\varepsilon}_{\text{cer}})(1 - \bar{\varepsilon}_{\text{cal}}) \approx 99.9\%$.

Calculation of TOF Particle Velocity (β_{tof})

The particle velocity β_{tof} was calculated in both spectrometers for each candidate track which had at least one scintillator hit along the track in both the front (S1) and rear (S2) pair of scintillator planes. The calculation was done by performing a least-squares fit of β_{tof} to the known scintillator positions z_i and corrected hit times $t_{\text{pmt,corr}}^{i,e}$ for scintillators on the track, using $\beta_{\text{tof}} c = z_i / (t_{\text{pmt,corr}}^{i,e} - t_{\text{fp}})$.

For the electron spectrometer, β_{tof} was used as a criterion in selecting a single track when more than one candidate existed. The distribution of β_{tof} for electrons in the SOS exhibited $\sigma_\beta \approx 0.029$, which corresponded to a scintillator resolution of $\sigma_{\text{scin}} \approx 170$ ps.¹⁴ The efficiency of the β_{tof} calculation in the SOS was virtually 100%. No explicit cut was made on this quantity.

For the proton spectrometer, β_{tof} was used as a criterion in selecting a single track. In addition, after a track was selected the corresponding β_{tof} was used to distinguish between protons ($\beta_p < 1$) and pions ($\beta_{\pi^+} \approx 1$) (Section 4.2.4 discusses the situation for those kinematics where β_p approached 1). The distribution of β_{tof} for pions in the HMS exhibited $\sigma_\beta \approx 0.019$, which corresponded to a scintillator resolution of $\sigma_{\text{scin}} \approx 140$ ps. The efficiency of the β_{tof} calculation in the HMS was about 98% (this issue is discussed in the ‘Proton Identification’ part of this Section, following).

Coincidence Time

Coincidence time, or the difference in time of target interaction as determined by the two spectrometer triggers, was used to separate true coincidences from accidentals (see Figs. 4.4, 4.5, and 4.6). A raw time difference t_{diff} was measured by using the trigger of one spectrometer to start a TDC which was stopped by a delayed version of the other spectrometer’s trigger. The coincidence time t_{coin} was obtained by projecting back to the focal plane of each spectrometer and correcting for the actual paths of the particles in the spectrometers. Using t_{diff} from the TDC

¹⁴The potential resolution is better than this; as noted above, the timing requirements of this experiment were not critical, so minimal effort was made to optimize this resolution.

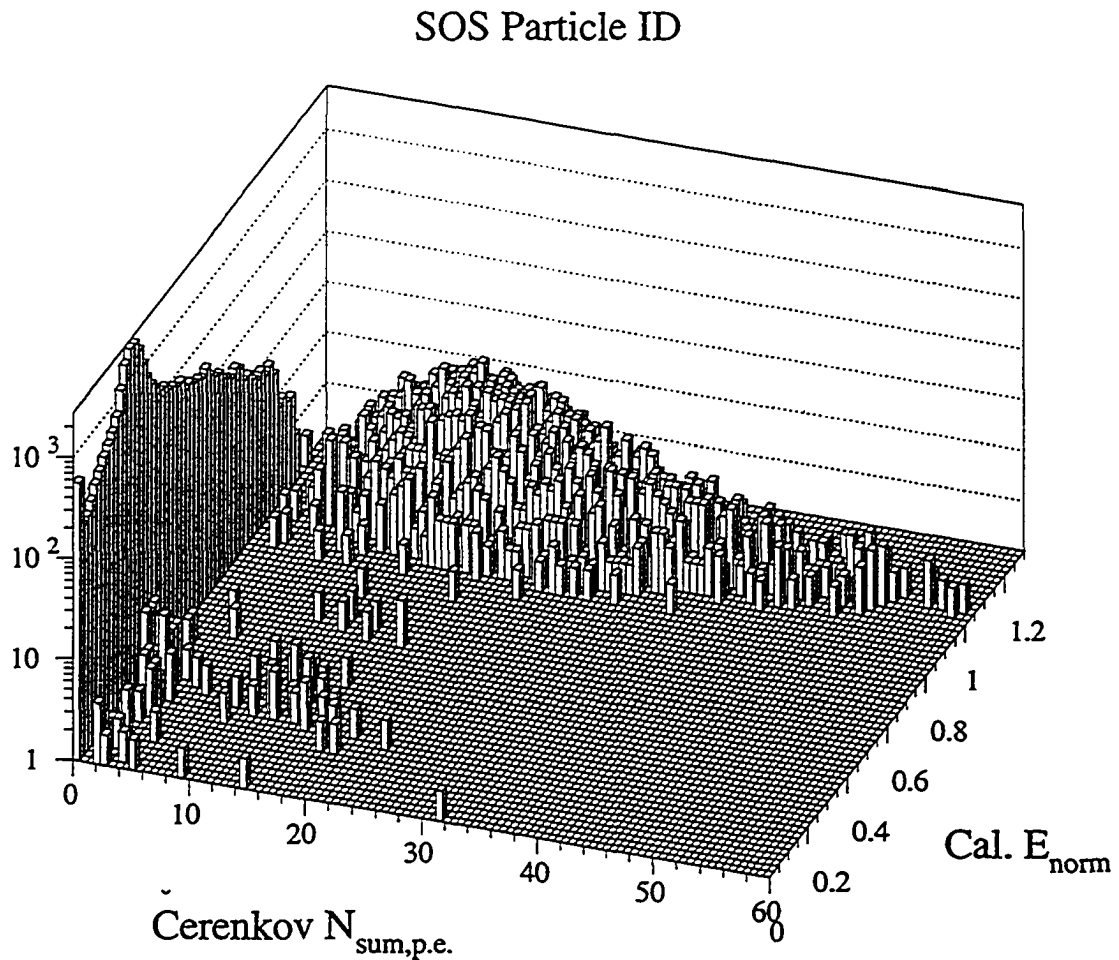


Figure 4.2: The response of the calorimeter and the Čerenkov for events of a typical run. The events at $N_{\text{sum,p.e.}} = 0$ are π^- (note the peak at $E_{\text{norm}} \approx 0.25$). The events at $N_{\text{sum,p.e.}} > 0$, $E_{\text{norm}} > 0.7$ are electrons. The events at $N_{\text{sum,p.e.}} = E_{\text{norm}} = 0$ are probably π^- that missed the calorimeter. The events at $N_{\text{sum,p.e.}} > 0$, $E_{\text{norm}} \approx 0.3$ are probably caused by π^- that produced knock-on electrons that triggered the Čerenkov. Note that the z axis is on a log scale.

SOS Particle ID

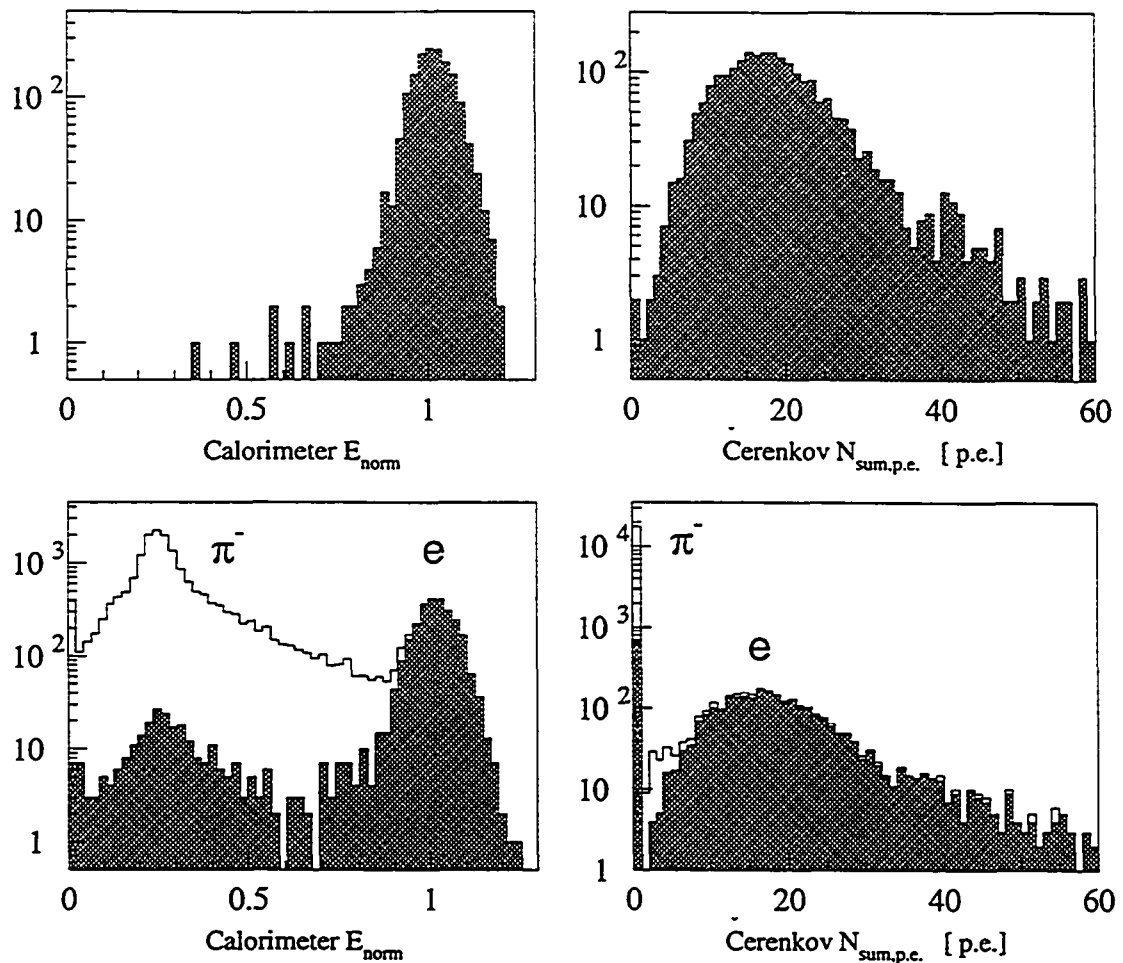


Figure 4.3: (Note log scales on all plots.) *Upper Left*) The response of the calorimeter to a clean sample of electrons (elastics, with a high-threshold Čerenkov cut). It is clear that in order to keep detection efficiency approaching 100% one requires a calorimeter cut of no higher than $E_{\text{norm}} = 0.7$. *Upper Right*) The response of the Čerenkov detector to a clean sample of electrons (elastics, with a high-threshold calorimeter cut). Here we see that, due to the fact that the signal extends closer to zero than is desirable, one requires a cut of no higher than $N_{\text{sum,p.e.}} > 1$ in order to keep detection efficiency near 100%. *Lower Left*) The unshaded curve is the response of the lead-glass calorimeter to a sample of both π^- and electrons. Note the long tail of the pion peak extending under the electron peak at $E_{\text{norm}} \approx 1$. The shaded histogram is the same sample after a $N_{\text{sum,p.e.}} > 1$ Čerenkov cut; the remaining pions indicate that the rejection efficiency of the Čerenkov with such a loose cut is roughly 98%. *Lower Right*) The unshaded curve is the response of the gas Čerenkov detector to a sample of both π^- and electrons. The shaded curve is with an $E_{\text{norm}} > 0.7$ calorimeter cut; the remaining pions (the shaded spike at zero) indicate that the rejection efficiency of the calorimeter with such a loose cut is roughly 95%. In all four cases the electron sample populates roughly the same fiducial region and energy range as do the electrons corresponding to resonance production.

started by the HMS we have

$$t_{\text{coin}} = t_{\text{diff}} - (t_{\text{fp,HMS}} + \Delta t_{\text{path,HMS}}) + (t_{\text{fp,SOS}} + \Delta t_{\text{path,SOS}}), \quad (4.16)$$

where we use the t_{fp} of Section 4.2.3, and the travel time correction for the HMS is

$$\Delta t_{\text{path,HMS}}(X_{fp,i}) = \frac{\Delta d_{\text{HMS}}(X_{fp,i})}{\beta_{\text{HMS}} c} \quad (4.17)$$

(and similarly for the SOS). Here Δd , the path-length corrections for the event, were a function of the four focal plane quantities x_{fp} , y_{fp} , x'_{fp} , and y'_{fp} (denoted collectively by $X_{fp,i}$). The corrections Δt_{path} were on the order of 1 ns for each spectrometer. At the time of this experiment Δd were determined from the COSY models of the spectrometers [Nic97]. The coincidence time resolution was typically $\sigma \approx 220$ ps for $(e, e'p)$.

Proton Identification

A combination of coincidence time and β_{tof} in the proton spectrometer (HMS) was used to separate real coincidence protons from accidental protons and from accidental positively charged pions. At the lower proton arm momentum settings, the proton- π^+ velocity separation was sufficient to distinguish between the two particle types (see Fig. 4.5). At the higher momentum settings, where the proton and π^+ β_{tof} peaks began to overlap, fewer pions were kinematically allowed and contributed a small ($< 1\%$) background after the coincidence time and β_{tof} cuts (see Fig. 4.6). In both cases the coincidence time was used to separate accidental from real coincidences. The accidental contamination of the real coincidence time peak (ranging from 0% to 11% after all other cuts, and consisting primarily of protons) was removed by sampling adjacent accidental peaks and performing a background subtraction (discussed in Section 4.3.6).

The calculation of β_{tof} in the HMS had an efficiency of roughly 98%. In other words, some 2% of tracked events failed to calculate a time of flight (and returned $\beta_{\text{tof}} = 0$). A similar number of events were distributed in a low- β_{tof} tail (see Fig. 4.4). The most likely explanation for both of these classes of events is that the proton underwent an interaction somewhere in the detector stack after the drift chambers. In such cases the reaction products could create a valid 3/4 trigger but the replay software might *a)* fail to find enough hit scintillators along the track to calculate

β_{tof} , or b) return a value of β_{tof} that was biased to the low side by decay products. A sample of $\beta_{\text{tof}} = 0$ and low- β_{tof} events revealed that they otherwise looked like a random sample of physics events (which is consistent with the above explanation). Based on this study the final data cuts (discussed in Section 4.3.8) did not exclude these $\beta_{\text{tof}} = 0$ and low- β_{tof} events.

4.2.5 Calculation of Physics Quantities

Once the events of interest were selected using PID and coincidence time cuts, the momentum components of each particle in the lab frame were calculated. The physics quantities Q^2 , W , and M_x^2 (as defined in Section 1.3.1) were then found and, after performing a boost to express proton (and η) components in the c.m. frame, $\cos\theta_\eta^*$ and ϕ_η were calculated.

A typical M_x^2 spectrum is shown in Fig. 4.7. Note that for this particular kinematic setting, peaks for both the π^0 (at $.018 \text{ GeV}^2/c^4$) and the η (at $.30 \text{ GeV}^2/c^4$) are clearly visible (both peaks were not in the acceptance for all kinematic settings). The threshold for two-pion production is at $M_x^2 = (2m_\pi)^2 = .073 \text{ GeV}^2/c^4$, and there is a sizable multi-pion background beneath the η peak. At this point in the analysis a cut on M_x^2 around the η peak defined the final state of the system (with the caveat that a substantial fraction of the events within the cut were from the multi-pion background).¹⁵

4.2.6 Efficiencies

Trigger Efficiency

The trigger for both the electron and proton spectrometer required that three of the four scintillator arrays fired (as discussed in Section 2.6.2). In the most naive analysis, one can calculate the 3/4 trigger efficiency from the individual plane efficiencies P_i and the appropriate combinatorics (the probability of planes 1 through 4 firing plus the probability of only planes 1, 2, and 3 firing, and so on):

$$P_{3/4} = P_1 \cdot P_2 \cdot P_3 \cdot P_4 + P_1 \cdot P_2 \cdot P_3 \cdot (1 - P_4) + P_1 \cdot P_2 \cdot (1 - P_3) \cdot P_4 +$$

¹⁵Take care to distinguish between the various types of backgrounds: even after the removal of pions and accidental protons using coincidence time cuts, PID cuts, and an accidental background subtraction, there remained a (true coincidence) background due the processes given in Eqs. 4.20 on page 111.

HMS Particle ID and Coincidence Time

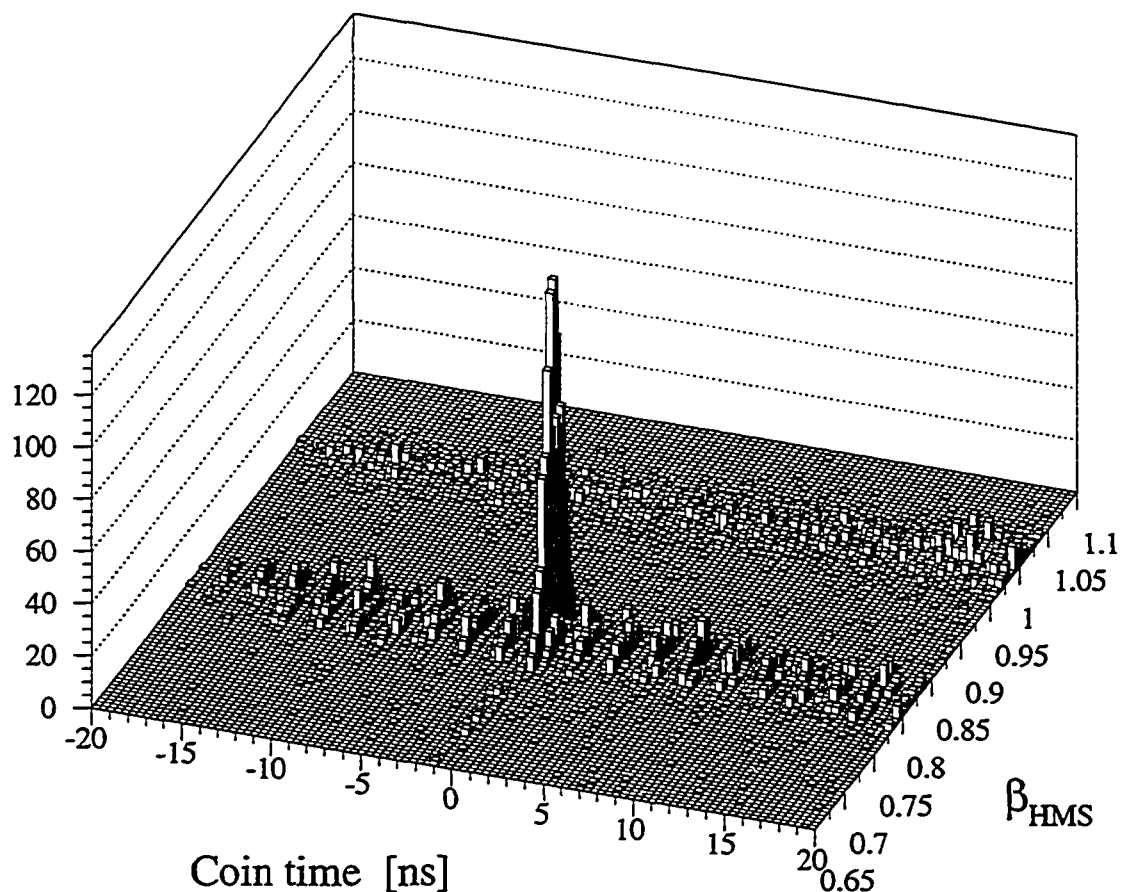


Figure 4.4: $\beta_{\text{tof,HMS}}$ and coincidence time for events of a typical run. The band of events at $\beta_{\text{tof,HMS}} \approx 1$ are π^+ , while the protons are at $\beta_{\text{tof,HMS}} \approx 0.8$. The real proton coincidences are at $t = 0$ ns, and the nominal 2 ns radio frequency (RF) structure of the beam is visible in the adjacent accidental peaks. The likely explanation for the low- β_{tof} tail emanating from the real coincidence peak is discussed in the ‘Proton Identification’ part of Section 4.2.4.

HMS Particle ID and Coincidence Time

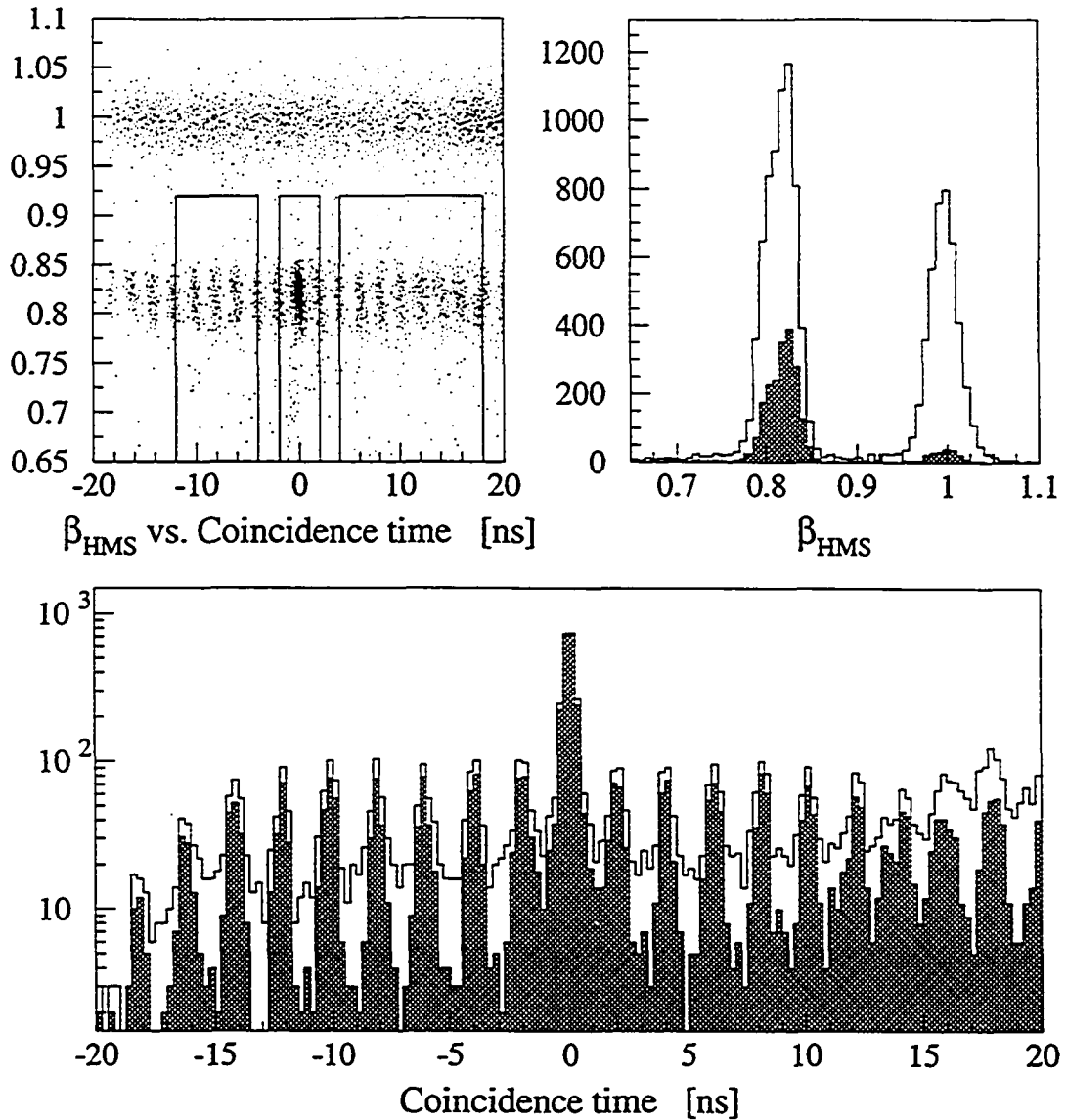


Figure 4.5: *Upper Left*) $\beta_{\text{tof,HMS}}$ and coincidence time for a kinematic setting at low proton momentum ($p_{\text{HMS}} = 1.35 \text{ GeV}/c$). Accidental coincidence pions occupy the upper ($\beta \approx 1$) band while protons occupy the lower band. Real coincidence protons are at $t = 0 \text{ ns}$, and real coincidence pions are faintly visible at $t \approx 18 \text{ ns}$. Note the (nominal) 2 ns RF structure of the beam in the proton band. The center box indicates the final cuts used to identify real coincident protons, and the two adjacent boxes indicate regions used for subtraction of accidental protons from the coincidence peak. *Upper Right*) Projection of the previous plot onto β , before (unshaded) and after (shaded) a cut around the real coincidence proton peak. Once this cut was made the protons and pions were easily separable using $\beta_{\text{tof,HMS}}$. *Bottom*) Projection of the 2-D plot onto coincidence time, before (unshaded) and after (shaded) a cut on β . This kinematic setting is representative of those with the greatest accidental:true ratios, here about 1:10. Note log scale.

HMS Particle ID and Coincidence Time

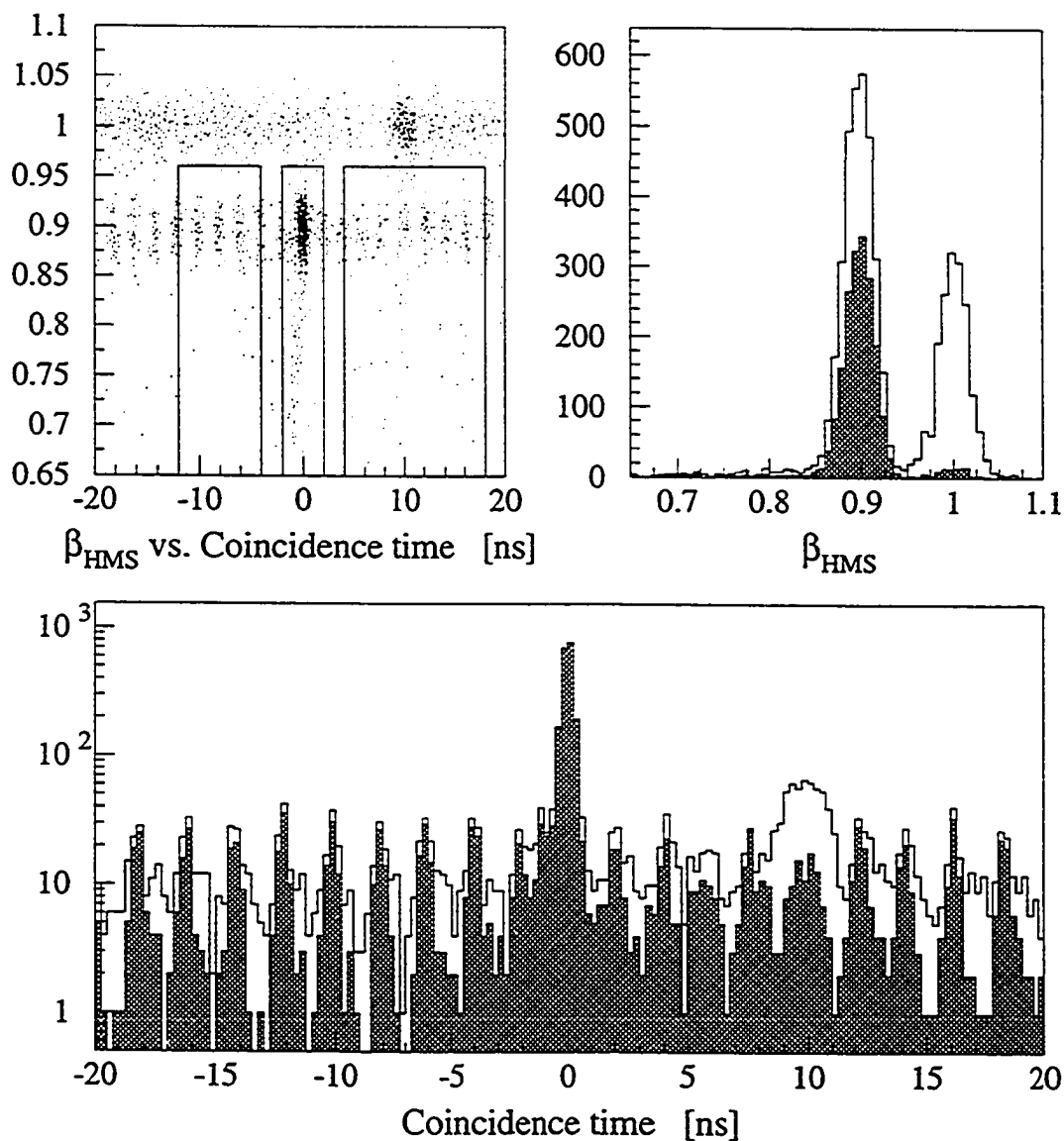


Figure 4.6: $\beta_{\text{tof,HMS}}$ and coincidence time for a kinematic setting at high proton momentum ($p_{\text{HMS}} = 1.9 \text{ GeV}/c$). The plot descriptions follow those of Fig. 4.5. At this kinematic setting the protons were closer in β to the pions, but the number of pions relative to protons was lower and the pions were still easily separable.

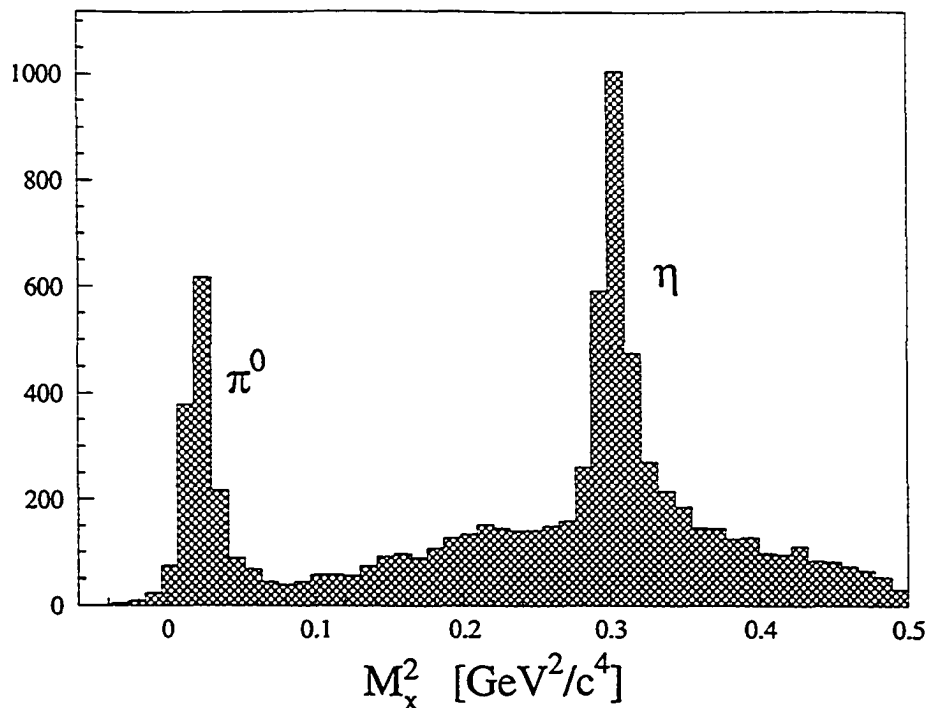


Figure 4.7: A plot of M_x^2 for one kinematic setting. Note the presence of the radiative tail extending to the right of each peak.

$$P_1 \cdot (1 - P_2) \cdot P_3 \cdot P_4 + (1 - P_1) \cdot P_2 \cdot P_3 \cdot P_4 . \quad (4.18)$$

The trigger efficiency calculated in this manner was always greater than 99.7% for each spectrometer. This is consistent with the expectation that virtually 100 % of nearly-minimum-ionizing particles (as both electrons and protons were in this experiment) passing through a 1 cm scintillator will be detected.¹⁶ The systematic uncertainty in this correction was assumed negligible.

Track Reconstruction Efficiency

The track reconstruction efficiency of each spectrometer was determined on a run-to-run basis using a subset of the data from that run. During replay, those events that fired one of the centermost scintillators in *every one* of the four scintillator planes were tagged. The tight fiducial constraints on these events ensured that they represented particles that *had* passed through the

¹⁶A minimum-ionizing particle passing through 1 cm of scintillator will lose roughly 2 MeV to ionization. If we assume a photon yield of 1 photon per 100 eV of ionization energy loss, a 10 % collection efficiency, 50 % attenuation, and a 25 % photomultiplier cathode quantum efficiency [PDG98], we can expect to collect over 200 photo-electrons for that event.

drift chambers and should have reconstructed a track. The reconstruction efficiency was simply the fraction of those tagged events for which a track was indeed reconstructed.

A study [Wes96] performed two tests of this quantity as a measure of the actual reconstruction efficiency. The first test verified that two data runs, similar except in the reported tracking efficiency (79 % versus 98 %), did indeed give the same yield to better than 1 % when corrected for the efficiency. The second test verified that this efficiency compared well (generally within 1.5 %) with the efficiency naively expected by applying the appropriate combinatorics to the individual chamber plane efficiencies (indicating that the reconstruction inefficiencies were consistent with the inefficiencies of individual planes). In the study, roughly half of the track reconstruction failures were due to only four of the six planes firing; the remainder of the time there were too many hits (> 30), or the reconstruction software failed to find space points or to link stubs (see Section 4.2.1).

In this experiment, run-to-run track reconstruction efficiency ranged from 94 % to 98 % for the electron spectrometer (SOS) and from 92 % to 97 % for the proton spectrometer (HMS). Systematic uncertainty in tracking efficiency was (conservatively) estimated to be $\sigma = 1.5$ %.

Computer and Electronic Live Time

Computer and electronic live times were calculated for each run using scaler results. The rates in this experiment were modest, and the live times correspondingly high. Computer live time ranged from 95 % to 98 %, and electronic live time was always greater than 98.8 % (99.7 %) for the HMS (SOS). The uncertainty in these corrections (based on the statistics of the scaler counts used in the calculations) was less than $\sigma = 0.1$ % in all cases, and taken to be zero.

4.3 Post-Replay Analysis

Once event ntuples were created by the replay software, the remainder of the analysis was done using these ntuples in the framework of the Physics Analysis Workstation (PAW) from CERNLIB, utilizing custom Fortran routines where necessary. The CERNLIB program MINUIT [CERNL] was used for background and all other fitting.

4.3.1 Data Checks

For each of the data runs a number of checks were performed to ensure that no obvious problems existed:

- All detectors properly functioning.
- Stable ratio of SOS raw triggers to beam charge as reported by BCM3.
- Stable target reconstruction.
- Target temperature okay (recorded every 30 seconds).
- Beam position on target okay (recorded every 30 seconds).

In addition, any run-to-run parameters that were necessary for the analysis were extracted and checked:

- Trigger and tracking efficiencies for the HMS.
- Live time of the data acquisition computer.
- Appropriate cut positions for coincidence time, proton time of flight ($\beta_{\text{tof,HMS}}$), and calorimeter energy sum (E_{norm}).

4.3.2 Normalization for Beam Charge

The normalization for beam charge was performed using the output of a resonant-cavity beam current monitor (BCM3), which was calibrated periodically using an Unser current monitor. The devices and the calibration procedure are explained in Appendix A.

For purposes of assigning a systematic uncertainty to the beam charge measurement we define the ratio $R_Q \equiv (\text{SOS pretriggers})/(Q_{\text{bcm3}})$, where the SOS pretrigger is caused by any event firing three of the four SOS scintillator planes. This ratio is histogrammed in Figs. 4.8 and 4.9 for all runs. Note that changes in R_Q are due not only to errors in the charge measurement itself but also to any conditions that could change the relative flux of particles into the spectrometer (such

as beam scraping in the beamline upstream of the target). The fact that R_Q was stable to within a few percent is indicative of the generally high quality of the beam in this experiment.¹⁷

Based on the stability of R_Q together with previous experience indicating that the error associated with calibration of the monitor was roughly $\sigma = 1\%$, a systematic uncertainty of $\sigma = 1.5\%$ was attributed to the measurement of beam charge. Further investigation may well have determined that the actual uncertainty was smaller, but the presence of other sizable systematic uncertainties (those associated with experimental acceptance, the multi-pion background subtraction, and kinematic errors) obviated the need for such studies.

4.3.3 Target Density and Length

The temperature of the liquid hydrogen was maintained at (19.00 ± 0.05) K by a calibrated heat-dependent resistor in the feedback control loop of a resistive heater. The density of the hydrogen was calculated to be (0.07230 ± 0.00036) gm/cm³. The target length was (4.36 ± 0.01) cm [Dun97].¹⁸ The purity of the target hydrogen gas was measured in March of 1997 and determined to be 99.81%.

The electron beam at TJNAF was continuous and high-current with a small beam spot, and as a result there were small density changes in the target due to deposition of heat from the beam. A study [Gus96] based on data taken prior to this experiment indicated that the effective change in target density was $(-3.8 \pm 0.4)\%$ per 100 μ A per mm of raster amplitude, assuming the same raster size in x and y and assuming that the spectrometer y_{tar} acceptance was 100%. The corresponding density change with 70% y_{tar} acceptance was $(-2.4 \pm 0.4)\%$ per 100 μ A per mm (the density change, in other words, appears to be greater near the target windows). A study of the average conditions (SOS y_{tar} acceptance and beam current) of the experiment determined that the target density correction was $\approx (3.0 \pm 0.5)\%$.

¹⁷The beam current in this experiment varied from 80 to 100 μ A. If the range had been much greater than this, the ratio R_Q might not have been so stable, because in principle the SOS pretrigger rate has a linear dependence on beam current only over some limited range.

¹⁸There was an additional target length uncertainty arising from changes of the beam position on the convex target windows. The position of the beam on the target was recorded every 30 seconds (Section 2.3) and it was determined, based on this measurement together with knowledge of the window shape, that the associated uncertainty in target length was less than $\sigma = 0.2\%$ (0.009 cm). This change in target length, however, entered the ratio R_Q (Section 4.3.2) and was taken into account in the associated uncertainty.

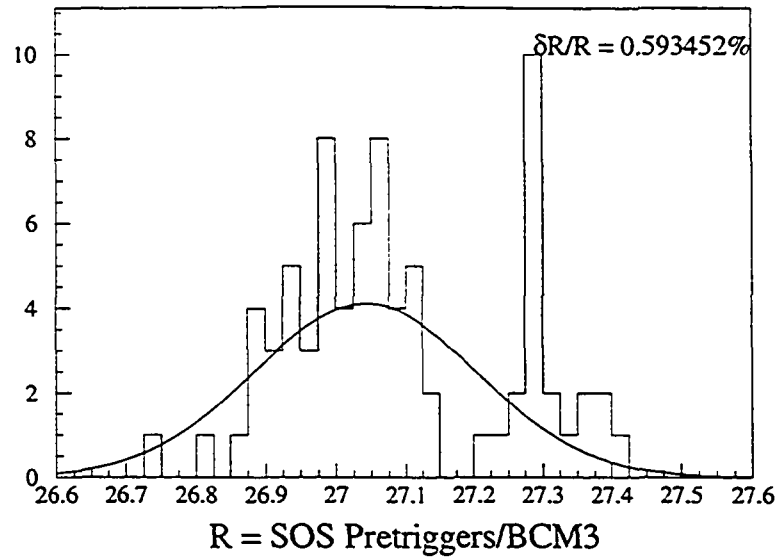


Figure 4.8: A histogram of the ratio $R_Q \equiv (\text{SOS pretriggers})/(Q_{\text{bcm3}})$ for all $Q^2 \approx 2.4 \text{ GeV}^2/c^2$ runs (arbitrary units). The distribution of R_Q appears to be non-Gaussian and, in fact, these high- R_Q runs were grouped in one period of time. Calibration of the current monitor during this period did not remove this effect, which lends weight to the possibility that the beam tune changed slightly. The estimate of systematic uncertainty was conservative, however, and assumed that this effect was due to charge measurement error.

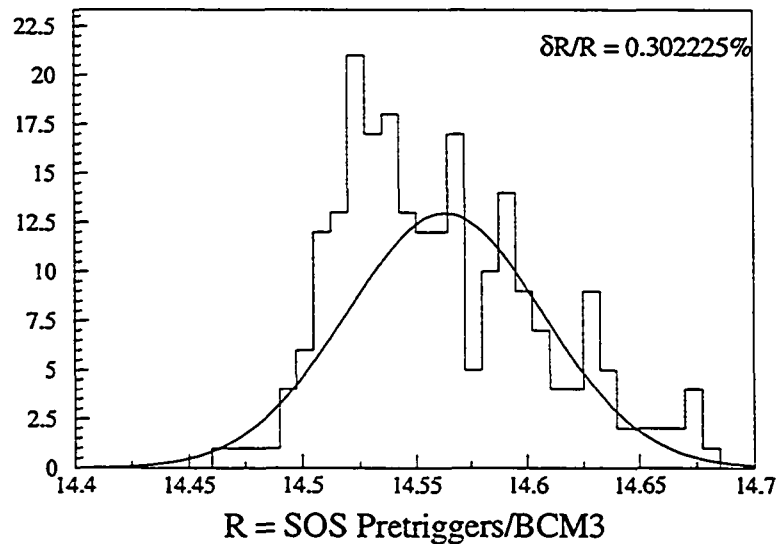


Figure 4.9: A histogram of $R_Q \equiv (\text{SOS pretriggers})/(Q_{\text{bcm3}})$ for all $Q^2 \approx 3.6 \text{ GeV}^2/c^2$ runs (arbitrary units).

4.3.4 Proton Absorption

In order for a proton to cause a trigger in the HMS it had to deposit enough energy to create above-threshold signals in at least three of the four scintillator planes in the detector stack. A small fraction ($\approx 3\%$) of protons incident upon the detectors underwent interactions in material encountered after the primary scattering and were either absorbed or deflected, and as a result created no trigger. The transmission T denotes the probability that a proton escaped such interactions and succeeded in creating a trigger in the HMS.

${}^1\text{H}(e, e')p$ and ${}^1\text{H}(e, e')p$ data were used to measure the magnitude of T as follows. Runs were selected in which elastic events were within the spectrometer acceptances, and cuts were applied to the invariant mass W and gas Čerenkov and calorimeter signals in order to select purely elastic coincidence electrons that had lost little energy to Bremsstrahlung. Cuts on the reconstructed quantities δ , y'_{tar} and x'_{tar} as determined by the SOS were then made to ensure that the elastic electrons were well inside the solid angle and momentum acceptances of the spectrometer.

Since the events were elastic, the solid angle cut on the coincidence electrons defined a corresponding cone of protons (see Fig. 4.10). It was verified that these protons were well within the solid angle and momentum acceptances of the HMS. Thus from an arbitrary initial number of events, using only cuts on SOS (electron) quantities, we selected N_c coincidence elastic events for each of the runs.

The *same* set of cuts were then applied to the SOS singles (events for which only the SOS received a trigger) for the same runs, thus defining the corresponding sets of N_s elastic electron events for which a proton was *expected* in the HMS but was *not detected*. These remaining SOS-only events were then checked to ensure that they exhibited roughly the same dependence on reconstructed quantities as that of the coincidence events.¹⁹ The measured transmission T_{meas} was $N_c/(N_c + N_s)$.

The results of the study are shown in Fig. 4.11 (both points are the sum of several low-statistics runs). The measured transmission, which shows no momentum dependence, was $T_{\text{meas}} = 0.972$ (uncertainty given below). Note also that the total proton-deuteron cross section is roughly invariant with proton momentum $|p_f|$ from about 1.5 to 3 GeV/ c (see, for example, Ref. [PDG98]);

¹⁹SOS-only events which exhibited, say, a y_{tar} dependence not seen in the coincidence data could be due to target window interactions (*i.e.*, from ${}^{27}\text{Al}(e, e'p)$), and should not be counted as absorbed-proton events. Where such dependences were observed, the cuts were tightened to remove these events from consideration.

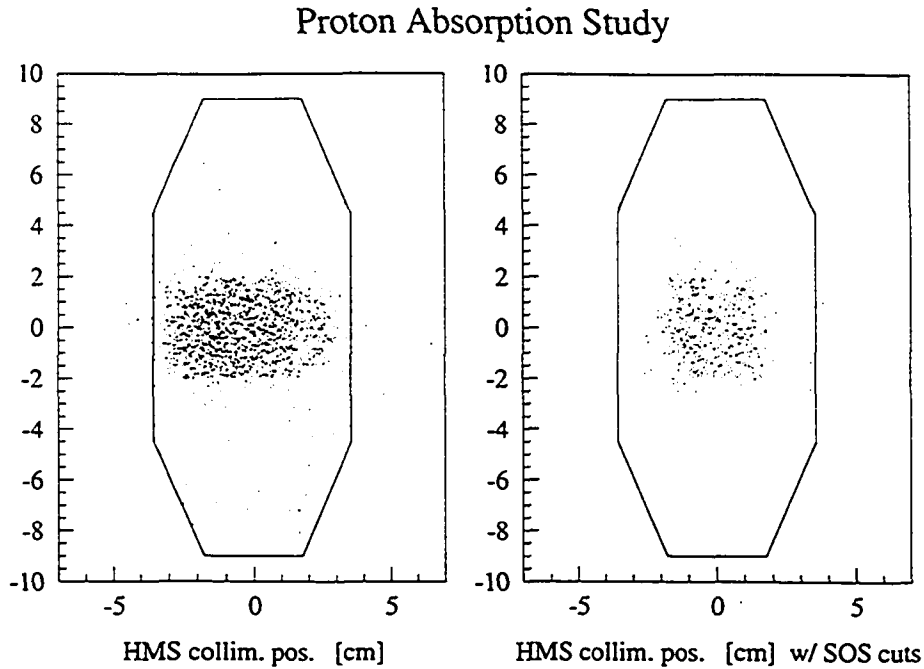


Figure 4.10: The distribution of ${}^1\text{H}(e, e'p)$ proton tracks reconstructed to the HMS collimator, before (*left*) and after (*right*) cuts made to the electron (SOS) quantities to restrict the proton cone. The ± 2 cm vertical cutoff in the left plot was caused by the limited out-of-plane acceptance of the SOS.

one might naively expect the probability for proton absorption in the detector materials to have a similar insensitivity to incident proton momentum. Based on this fact, together with the results presented above, a global 2.8% factor was applied to the resonance data to correct for proton absorption.²⁰

The statistical error associated with a straight-line fit to the two measured values of T shown in Fig. 4.11 ranged from 1.2% at $|\mathbf{p}_f| = 1.25$ GeV/ c to less than 0.4% at $|\mathbf{p}_f| = 3$ GeV/ c . We assumed an overall 1% statistical error in the measurement of T and estimated the systematic error to be less than 0.5%. A total error of $\sigma = 1.2\%$ was assigned to the value of T quoted above (*i.e.*, $T = 0.972 \pm 0.012$). Information on similar proton absorption measurements (for both the HMS and SOS) is available in Ref. [Wes97].

²⁰Independent of changes in absorption due to changing cross sections, one naively expects the proton absorption to decrease with increasing proton momentum due to the increased focussing of forward-peaked scattering. Based on the limited data presented here it appears that this effect is either small or offset by cross section changes.

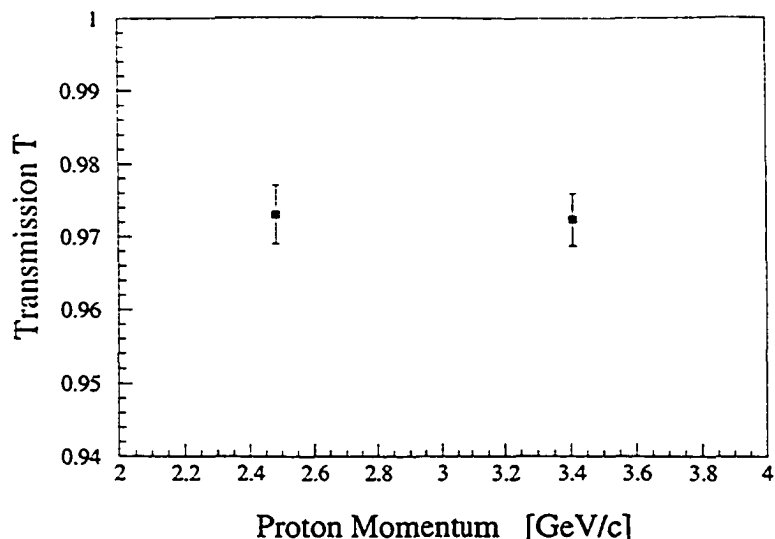


Figure 4.11: Results of the proton absorption measurements. The errors shown are statistical only.

Background Source	Contribution	Discussed in Section
Target windows [$^{27}\text{Al}(e, e'p)$]	< 2 %	4.3.5
Accidental coincidences	0 % to 11 %	4.3.6
Proton collimator/magnet rescattering (HMS y_{tar})	0 % to 7 %	4.3.6
Multi-pion events	29 % to 48 %	4.3.7

Table 4.1: Experimental backgrounds.

4.3.5 Target Window Background

The windows of the cryogenic target were made of aluminum, and contributed events to the experimental acceptance. The coincidence acceptance for such events was small, however. Data taken using ‘dummy’ empty targets indicated that after final cuts, less than 2 % of coincidence events were from the target windows. Those events were distributed smoothly in M_x^2 and so were removed in the multi-pion background subtraction. Table 4.1 gives the various sources of experimental backgrounds.

4.3.6 Accidental Coincidence and HMS y_{tar} Background Subtractions

The real coincidence proton peak contained 0 % to 11 % accidentals, depending on the kinematic setting. This background was removed by sampling regions in coincidence time adjacent to the real peak, scaling the sample for relative coincidence time ranges, and subtracting the normalized

accidental sample from the reals on a bin-by-bin basis.

Another background process arose from protons that penetrated the HMS collimator or rescattered from an aperture in the magnets. These events often resulted in a proton inside the experimental acceptance. It was discovered that these events, by virtue of multiple scattering in the collimator, suffered poor reconstruction of target position y_{tar} .^{21,22} In particular, studies with $^1\text{H}(e, e'p)$ data showed that these events, which could be identified by a missing mass inconsistent with elastic scattering, resulted in long, very flat tails in y_{tar} . For these events the expected position of the proton (based on electron kinematic information) was at the edge of the angular acceptance of the HMS (*i.e.*, at the edge of the collimator).

This collimator/magnet rescattering background was removed by sampling the y_{tar} tails outside the region of the target ($2.5 \text{ cm} < |y_{\text{tar}}| < 6 \text{ cm}$), performing the appropriate scaling for relative y_{tar} ranges, and subtracting the normalized sample from the data on a bin-by-bin basis. This subtraction ranged from 0 to 7% of the yield after all other cuts. See Ref. [Fro98] for further details.

4.3.7 Multi-Pion Background Subtraction

One of the most critical (and potentially problematic) steps in the analysis was the subtraction of background processes. In addition to the reaction

$$e + p \rightarrow e' + S_{11} \rightarrow e' + p\eta \quad (4.19)$$

we simultaneously detected processes such as

$$\begin{aligned} e + p &\rightarrow e' + \Delta^{++} \pi^- \rightarrow e' + p\pi^+ \pi^- , \\ &\rightarrow e' + p\pi^0 \pi^0 , \\ &\rightarrow e' + p\pi^+ \pi^- . \end{aligned} \quad (4.20)$$

²¹This fact was pointed out by V. Frolov.

²²Protons that passed through the entire HMS collimator lost $\approx 130 \text{ MeV}$ of kinetic energy, which (at a momentum of roughly $2 \text{ GeV}/c$) results in a change in coincidence time of $\approx 1.5 \text{ ns}$; if the proton's momentum were reasonably well-measured, however, much of this 1.5 ns offset would be removed in the coincidence time calculation. In general, one must assume that these events fall within the $\pm 2 \text{ ns}$ coincidence time cut.

After all cuts (including the M_x^2 cut) these processes taken together ranged from 29% to 48% of the resonance data. In addition to these background processes, the data contained events from interactions in the target windows ($< 2\%$ of the resonance data after final cuts), which contributed smoothly to the M_x^2 distributions in the neighborhood of the $M_x^2 = m_\eta^2$ peak. After data from all runs at a single kinematic setting were combined, therefore, the background in M_x^2 was subtracted.

Two independent background subtraction techniques were used. Here we give an overview of the techniques; details are given later in this Section. The first method (which we call ‘Technique 1’) used a functional fit to the data (peak plus polynomial background) for every $(\cos\theta_\eta^*, \phi_\eta)$ bin of a kinematic setting (integrated over W). The same procedure was carried out on both the actual data and the ‘data’ from the Monte Carlo, with the final result [for a particular $(\cos\theta_\eta^*, \phi_\eta)$ bin] obtained by renormalizing the ratio $Y_{\text{data}}/Y_{\text{MC}}$ with the Monte Carlo generating function (as described in Section 4.3.10). The advantage of this technique was that any systematic fitting problem affecting actual and Monte Carlo data in a similar way would cancel in the ratio $Y_{\text{data}}/Y_{\text{MC}}$. In principle, the disadvantage with this technique was that (for reasons discussed below) the data could not be binned in W , thus implicitly assuming a W -independent background for a particular setting. In practice, this assumption was not problematic for the kinematics of this experiment for two reasons. First, the method did allow for M_x^2 binning (hence background dependence); since the experimental acceptance imposed a tight correlation between W and M_x^2 , the need for explicit W dependence was effectively circumvented. Second, the experimental acceptance of the S_{11} was such that a typical kinematic setting spanned only $W \sim 50$ MeV (in other words, the different settings themselves were in a sense single W bins).

The second subtraction method (‘Technique 2’) applied a simple transformation to the background generated by the Monte Carlo [for each $(W, \cos\theta_\eta^*, \phi_\eta)$ bin] such that the integrated strength (for the entire setting) below and above the m_η peak matched that for the data. This transformed background was then subtracted from the data. The advantages of this technique were that the data could be binned in W (so the subtraction allowed an explicit W dependence within a setting), and that the overall strength of the peak was preserved. The relative disadvantage was that it relied more heavily on the ability of the Monte Carlo to accurately describe the experimental acceptance. In both cases, once the subtractions were made to the data for a particular bin, the yield over a small range in M_x^2 about m_η^2 was integrated.

The final results obtained with the two techniques agreed very well (total cross sections agreed to $\approx 2\%$; see Section 5.1). The final results quoted in Chapter 5 are those obtained using Technique 1, because fits to those angular distributions resulted in marginally lower χ^2 . We now discuss both strategies in detail, since they were both used to aid in understanding the systematic uncertainties associated with the multi-pion background subtraction.

Technique 1: Polynomial Fit to the Background

The data (actual or from Monte Carlo) for each setting were binned in $\cos\theta_\eta^*$ (10 bins), ϕ_η (6 bins), and M_x^2 (20 bins). To each of the 60 ($\cos\theta_\eta^*$, ϕ_η) bins for a particular kinematic setting was fit a function describing the M_x^2 distribution:

$$f(x_i) = f_{\text{peak}}(x_i) + f_{\text{bg}}(x_i) , \quad (4.21)$$

where

$$f_{\text{peak}}(x_i) = \left\{ \begin{array}{ll} p_1 \exp \left\{ -\frac{(x_i - x_0)^2}{2p_2^2} \right\} & x_i < x_0 \\ p_1 \frac{(p_3/2)^2}{(x_i - x_0)^2 + (p_3/2)^2} & x_i > x_0 \end{array} \right\} \quad (4.22)$$

and

$$f_{\text{bg}}(x_i) = b_0 + b_1(x_i - x_0) + b_2(x_i - x_0)^2 + b_3(x_i - x_0)^3 + b_4(x_i - x_0)^4 . \quad (4.23)$$

Here x_i is the value of M_x^2 at the center of the i^{th} M_x^2 bin and x_0 is the position of the peak (nominally m_η^2 but allowed to vary slightly during the fit), while p_1 - p_3 and b_1 - b_4 are parameters describing the peak and background, respectively. This form of $f_{\text{peak}}(x_i)$ was chosen because it did a good job of describing the M_x^2 distribution of the $S_{11} \rightarrow p\eta$ events (both data and Monte Carlo).

The coincidence acceptance for this experiment exhibited a tight correlation between W and M_x^2 , and most settings had a W acceptance of only about 30 to 80 MeV FWHM. Since the two variables were so highly correlated, binning in W would have also coarsely binned in M_x^2 (see Fig. 4.12), leaving M_x^2 distributions with poor (and therefore unsubtractable) 'sidebands.' For this reason the background fits were done with no binning in W . The results of the fits were subsequently used to perform subtractions on data that were binned in W . This approach was justified since any single background fit was applied to data constrained to a narrow range in W .

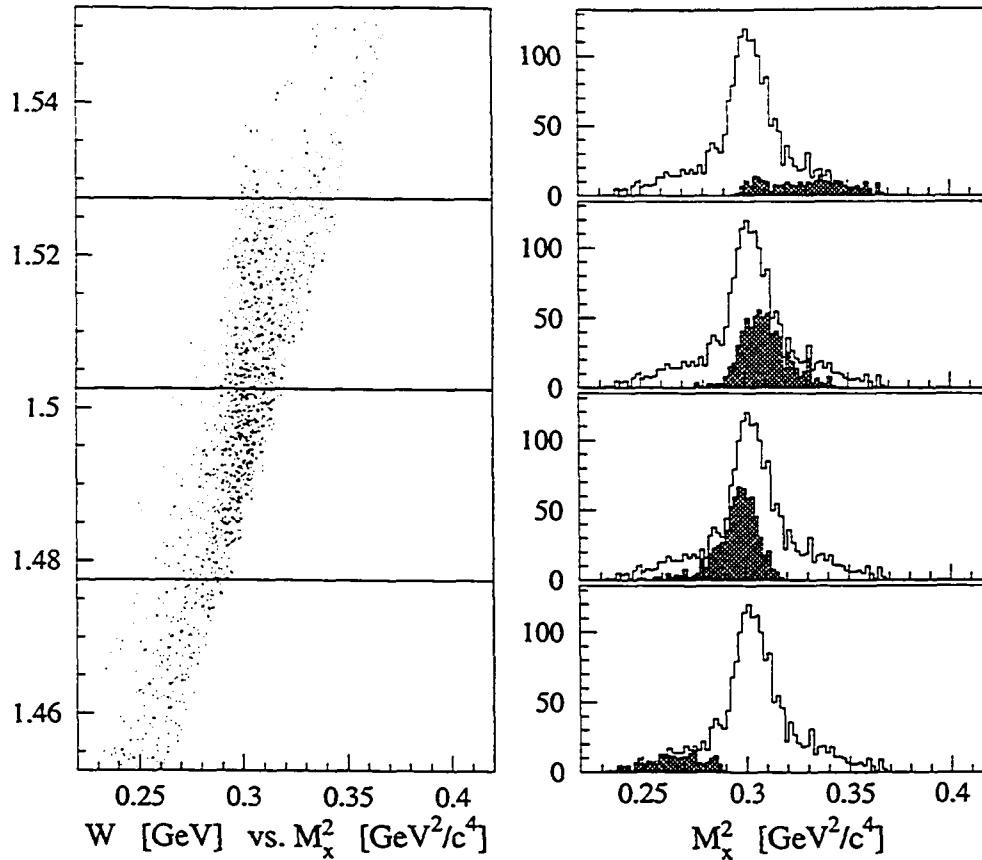


Figure 4.12: *Left*) A plot of W versus M_x^2 for one run. In this experiment the acceptance imposed a tight constraint between these two variables for any particular setting. The horizontal lines demark four 25 MeV W bins. *Right*) In each case the unshaded histogram is the M_x^2 distribution integrated over all four bins. The shaded histogram is the M_x^2 distribution for a single W bin. The high degree of correlation between W and M_x^2 means that data in a single W bin (*i.e.*, the data in a single shaded histogram) generally did not have ‘sidebands’ on both sides of the m_η^2 peak, and performing a fit to data binned in W was therefore not feasible.

Figure 4.13 shows the results for several $(\cos\theta_\eta^*, \phi_\eta)$ bins of one setting. Figure 4.14 shows the results for several settings, integrated over all $(W, \cos\theta_\eta^*, \phi_\eta)$ bins for each setting.

Technique 2: Subtraction of the Monte Carlo Background

The second background subtraction technique involved subtracting from the data a transformed version of the Monte Carlo-generated background. The transformation was a ‘tilting’ and ‘scaling’ (*i.e.*, a linear transformation) in the variable M_x^2 such that the integrated yields below and above the m_η^2 peak equaled that of the actual data. A single set of transformation parameters was derived

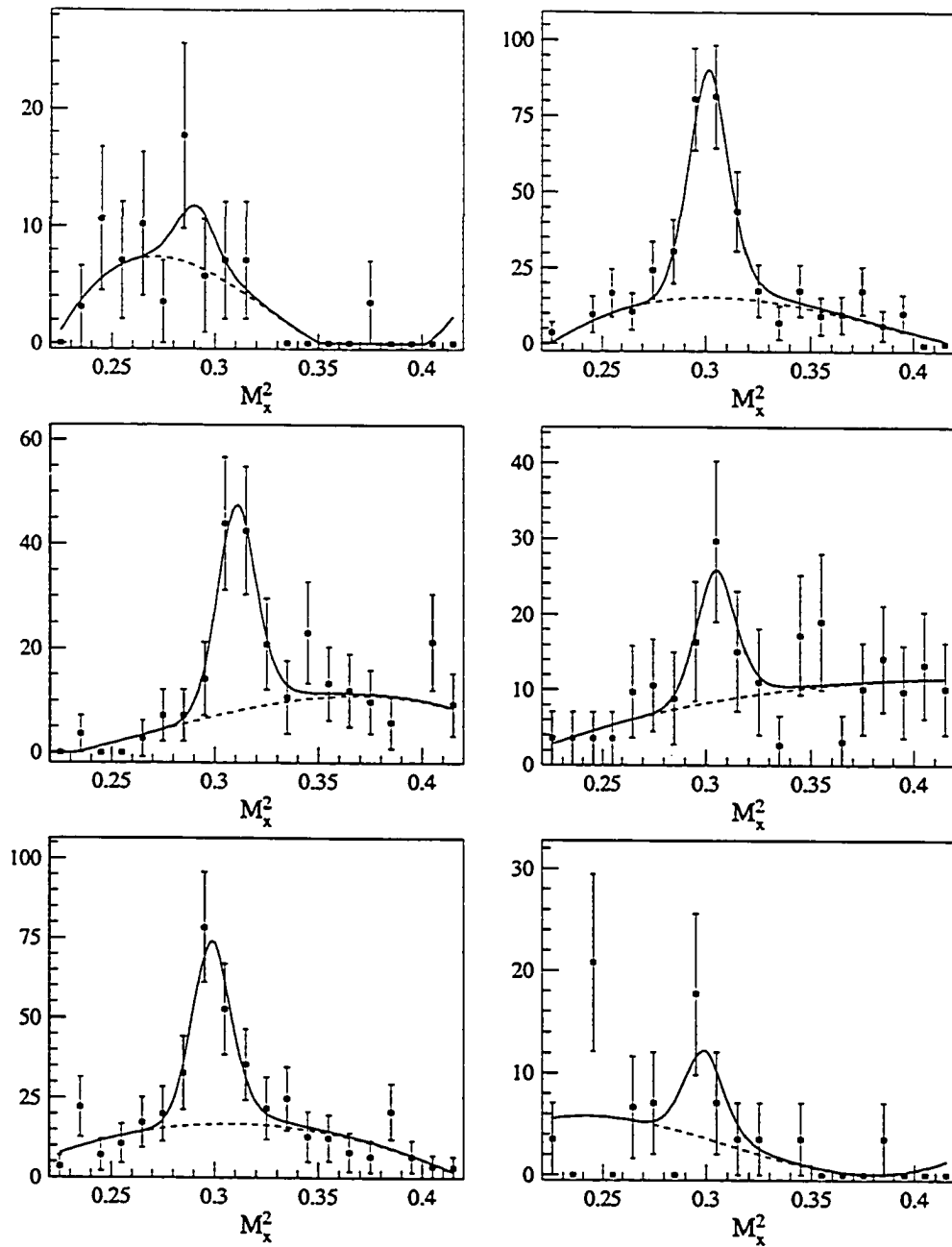


Figure 4.13: Fits to the M_x^2 distribution for several typical $(\cos \theta_\eta^*, \phi_\eta)$ bins, one kinematic setting, Technique 1 (data) (all yields have been normalized to 1 Coulomb of beam charge).

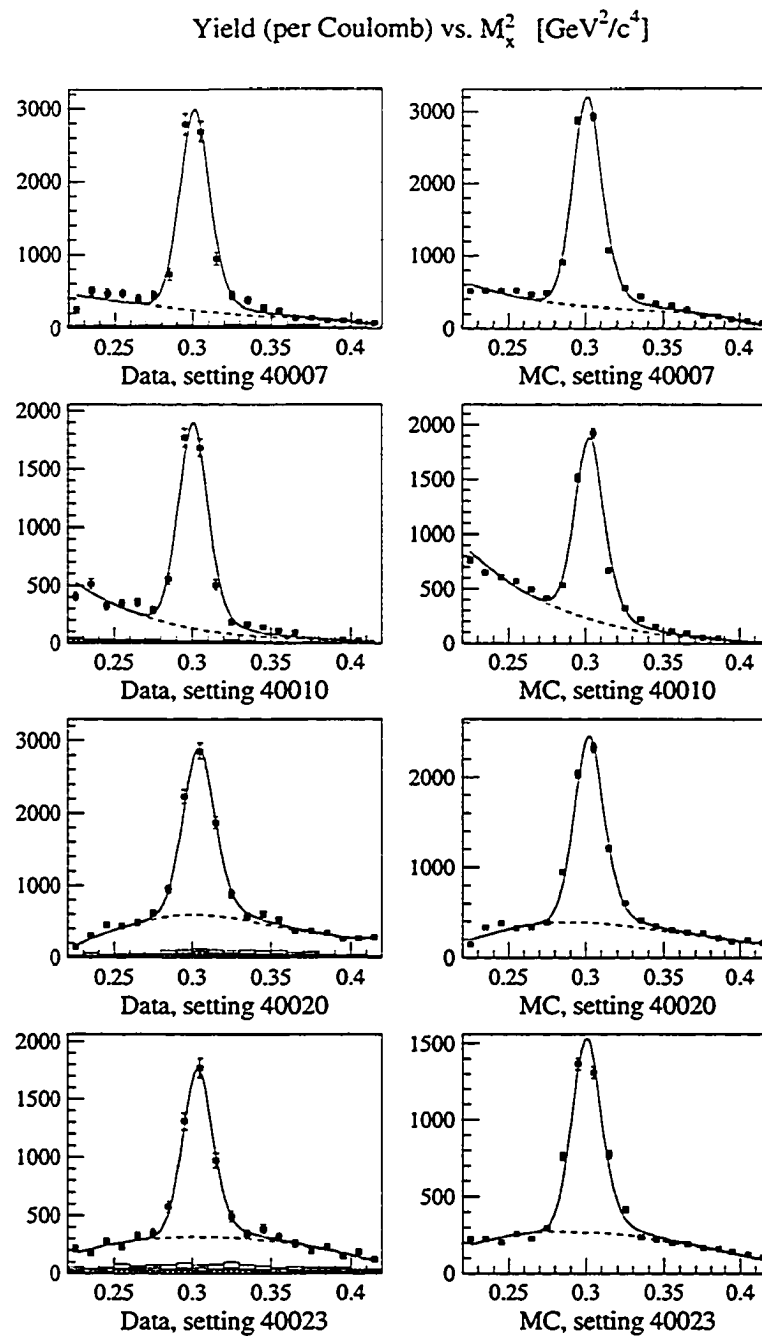


Figure 4.14: Results of background fits, using Technique 1, for several typical kinematic settings (all yields have been normalized to 1 Coulomb of beam charge). Each figure shows the integration of sixty individual $(\cos\theta_\eta^*, \phi_\eta)$ bins and their respective fits (like those shown in Fig. 4.13). Data are on the left and the corresponding Monte Carlo result is on the right. The solid line is the sum of the background and peak fits; the dashed line shows the background only. A small contribution from the accidental coincidence and HMS y_{tar} backgrounds is just visible at the bottom of the data plots (see Section 4.3.6).

for each setting, and the transformation was applied to each $(W, \cos\theta_\eta^*, \phi_\eta, M_x^2)$ bin.

Let the indices i, j, k , and l label $W, \cos\theta_\eta^*, \phi_\eta$, and M_x^2 bins, respectively, with d_{ijkl} the data yield for a particular bin. Then

$$D_{\text{below}} = \sum_{i,j,k} \sum_l^{\text{below } m_\eta^2} d_{ijkl} \quad (4.24)$$

is the yield for a particular setting integrated over all $(W, \cos\theta_\eta^*, \phi_\eta)$ bins and over some M_x^2 -region below the m_η^2 peak. Similarly,

$$D_{\text{above}} = \sum_{i,j,k} \sum_l^{\text{above } m_\eta^2} d_{ijkl} \quad (4.25)$$

is the yield for that setting integrated over all $(W, \cos\theta_\eta^*, \phi_\eta)$ bins and over some M_x^2 -region above the m_η^2 peak. The corresponding quantities for the Monte Carlo-generated background are

$$B_{\text{below}} = \sum_{i,j,k} \sum_l^{\text{below } m_\eta^2} b_{ijkl} \quad (4.26)$$

and

$$B_{\text{above}} = \sum_{i,j,k} \sum_l^{\text{above } m_\eta^2} b_{ijkl} . \quad (4.27)$$

We want to find the transformation that takes b to b' such that the integrated yield in a region below the peak equals that of the data:

$$\begin{aligned} B'_{\text{below}} &= \sum_{i,j,k} \sum_l^{\text{below } m_\eta^2} b'_{ijkl} \\ &= D_{\text{below}} , \end{aligned} \quad (4.28)$$

and similarly for a region above the peak. We let x_l be the center of the l^{th} M_x^2 bin, and x_0 the center of the nominal peak bin (or any arbitrary bin about which the transformation will rotate the Monte Carlo output). The assumption for b' of the form

$$b'_{ijkl} = b_{ijkl} [c_1 (x_l - x_0) + c_2] \quad (4.29)$$

(c_1 and c_2 constants) together with the conditions $B'_{\text{below}} = D_{\text{below}}$ and $B'_{\text{above}} = D_{\text{above}}$ leads to

equations for constants c_1 and c_2 :

$$c_1 = \frac{D_{\text{below}} - \left(\frac{B_{\text{below}}}{B_{\text{above}}}\right) D_{\text{above}}}{\langle Bx \rangle_{\text{below}} - \left(\frac{B_{\text{below}}}{B_{\text{above}}}\right) \langle Bx \rangle_{\text{above}}} \quad (4.30)$$

and

$$c_2 = \frac{D_{\text{below}} - c_1 \langle Bx \rangle_{\text{below}}}{B_{\text{below}}} , \quad (4.31)$$

where we've introduced the shorthand

$$\langle Bx \rangle_{\text{below}} = \sum_{i,j,k} \sum_l^{\text{below } m_\eta^2} b_{ijkl} (x_l - x_0) , \quad (4.32)$$

and similar for $\langle Bx \rangle_{\text{above}}$.

The Monte Carlo background yield for each $(W, \cos\theta_\eta^*, \phi_\eta, M_x^2)$ bin was transformed according to Eq. 4.29, and the result subtracted from the data yield in the corresponding bin. Figure 4.15 shows the results for several settings, integrated over all $(W, \cos\theta_\eta^*, \phi_\eta)$ bins. As in the case of Technique 1, we apply the 'fit' and subtraction to both data and Monte Carlo; in this case, however, the result of applying the technique to the Monte Carlo output is the virtually identical subtraction of the background, as expected.

The subtraction from the Monte Carlo result does not result in the *exact* removal of the Monte Carlo background because we are forcing the transformed background in the region above the peak to have the same yield as the background *plus* radiative tail. To minimize errors arising from this effect, the integration region above the peak was chosen away from the m_η^2 peak (the integration regions used were 0.23 to 0.27 and 0.38 to 0.42 GeV^2/c^4). Note that these small errors entered both the Monte Carlo and the data subtractions, and in principle cancelled in the ratio $Y_{\text{data}}/Y_{\text{MC}}$.

4.3.8 Data Cuts

The 'standard' cuts (those used in obtaining final results) are given in Table 4.2. The dependence of final results on variations in these cuts is discussed in Section 5.1. In addition to cuts on variables discussed in previous sections (spectrometer momentum, PID, etc.), a cut was made on coincidence acceptance in order to avoid errors arising from regions of low experimental acceptance.

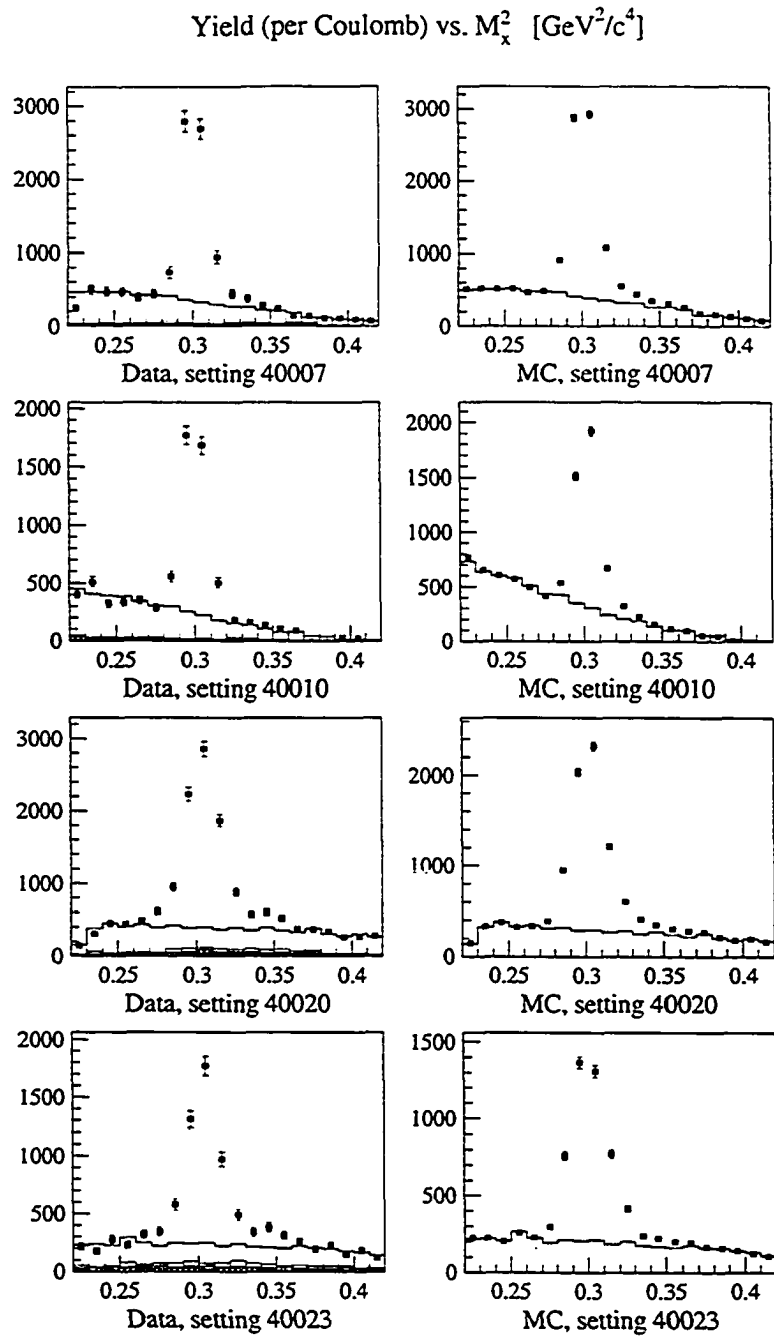


Figure 4.15: Results of background fits, using Technique 2, for several typical kinematic settings (all yields have been normalized to 1 Coulomb of beam charge). Here the solid line, which represents the background generated by the Monte Carlo simulation, is scaled to the data outside the peak region and then subtracted from the data.

In particular, when combining data for a single bin from different kinematic settings, contributions from settings in which that bin was below some acceptance threshold were neglected.

For purposes of this cut, the acceptance was calculated by Monte Carlo simulation, using resonance events only. We define the relative coincidence acceptance of a particular bin, particular setting, as

$$\mathcal{A}_{\text{rel}} = \frac{\mathcal{A}}{\mathcal{A}_{\text{max}}}, \quad (4.33)$$

where

- \mathcal{A} , the coincidence acceptance for the bin, is given by $N_{\text{det}}/N_{\text{in}}$, with
 - N_{in} equal to the number of Monte Carlo events generated in the bin (*i.e.*, the number of events passing the acceptance/rejection test of Fig. 3.1 on page 66), where the binning is done using $(W, \cos\theta_{\eta}^*, \phi_{\eta})$ calculated at the vertex of the interaction;
 - N_{det} equal to the number of Monte Carlo events detected in the bin (*i.e.*, the number of events passing both spectrometer simulations and all final cuts), where the binning is again done in vertex quantities;
- \mathcal{A}_{max} is the maximum value of \mathcal{A} for the setting in question.

The estimate of systematic uncertainty of the Monte Carlo acceptance was obtained by observing the dependence of final results on the value of this relative acceptance cut. This procedure is discussed in Section 5.1.

4.3.9 Corrections

Corrections to the data for trigger and tracking efficiencies and for target density effects and proton absorption were discussed above. In addition, the data were corrected for Q^2 dependence at each of the two kinematic points. All corrections are summarized in Table 4.3. Acceptance and radiative effects were taken into account by the procedure used to extract the differential c.m. cross section (Section 4.3.10).

Quantity	Variable	Cut
Electron momentum	δ_{SOS}	$< +5\%$
		$> -19\%$
Proton momentum	δ_{HMS}	$< +10\%$
		$> -8\%$
Relative Acceptance	A_{rel}	$> 25\%$
SOS Čerenkov	$N_{\text{sum,p.e.}}$	> 1
SOS calorimeter	E_{norm}	> 0.7
HMS TOF	β_{tof}	< 0.93 to < 1.0 (setting dependent)
Coincidence time	t_{coin}	centroid ± 2 ns
Missing mass	M_x^2	$< 0.34 \text{ GeV}^2/c^4$
		$> 0.27 \text{ GeV}^2/c^4$
HMS target position	y_{tar}	$< +2.5$ cm
		> -2.5 cm

Table 4.2: The set of standard cuts applied to the data.

Q^2 Correction

The Monte Carlo model cross section had no Q^2 dependence (aside from the gross difference between the two nominal values, $Q_{\text{nom}}^2 = 2.4$ and $3.6 \text{ GeV}^2/c^2$). The data yields were corrected ('bin-centered') in order to account for the fact that the data at each nominal Q^2 point actually covered a finite range in Q^2 [roughly ± 0.2 (0.35) GeV^2/c^2 for the low (high) Q^2 point].

The procedure used the Monte Carlo simulation to find the average Q^2 value, $\langle Q^2 \rangle$, for each $(W, \cos\theta_\eta^*, \phi_\eta)$ bin. The data yield for each bin was then adjusted according to an exponential parameterization of the Q^2 dependence:

$$Y_{\text{corr}} = Y \exp[C * (Q_{\text{nom}}^2 - \langle Q^2 \rangle)], \quad (4.34)$$

where the constant C was initially taken to be $C = -0.39 \text{ c}^2/\text{GeV}^2$ (from Ref. [Bra84]; see Fig. 4.16) and subsequently iterated to $C = -0.565 \text{ c}^2/\text{GeV}^2$ ('Exponential Fit 1' of Fig. 4.16). The maximum correction to the yield of any bin was 22 (34) % for the low (high) Q^2 point, and 90% of bins were corrected by less than 15 (22) %.

The uncertainty arising from this Q^2 correction was estimated by considering the impact on final results of two alternative forms for the correction ('Exponential Fit 2' and 'Polynomial Fit' of Fig. 4.16). The estimated systematic uncertainty in the differential cross section due to the Q^2

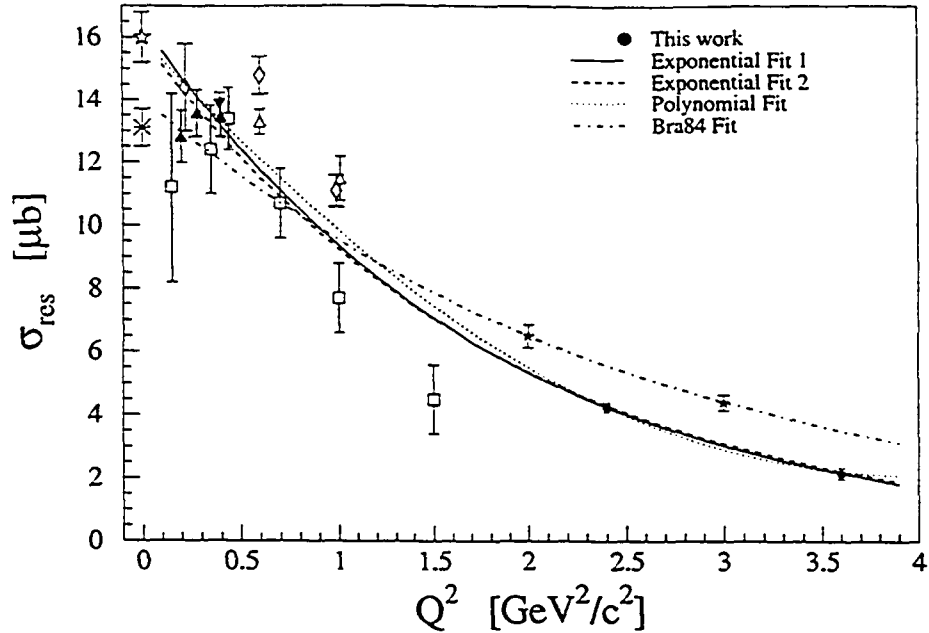


Figure 4.16: A plot of the Q^2 dependence of the cross section $\sigma_{\text{res}}(ep \rightarrow e'p\eta)$ at $W \approx 1535$ MeV, showing several reasonable parameterizations of the Q^2 dependence. The curve labeled *Exponential Fit 1* ($\sigma_{\text{res}} = 16.5 e^{-0.565 Q^2} \mu\text{b}$, where Q^2 is in $[\text{GeV}^2/c^2]$) passes through the two data points of this experiment, and was used in the final analysis to perform the Q^2 correction. *Exponential Fit 2* is constrained to go through the photoproduction data ($\sigma_{\text{res}} = 16 \mu\text{b}$ at $Q^2 = 0$). *Polynomial Fit* is a quadratic through the photoproduction data and the two data points of this experiment. *Bra84 Fit* is an exponential fit given in Ref. [Bra84] to their two data points. References to previous data are given in Fig. 5.6 on page 137.

correction was $\sigma = 1\%$ for both the low and high Q^2 points. Note that when referring to the value of Q^2 of *bin-centered* data we will use equality ($Q^2 = \dots$) instead of an approximation ($Q^2 \approx \dots$).

4.3.10 Extraction of the Differential Cross Section

The extraction of the differential c.m. cross section began with the application of run-dependent corrections (efficiencies and dead times) and the subtraction of the accidental coincidence and HMS y_{tar} backgrounds for each run. The yields for each setting (binned in W , $\cos\theta_\eta^*$, ϕ_η , and M_x^2) were then obtained by taking a weighted mean of the yields for the runs in that setting, where the weight for each run was the measured beam charge. At the setting level the multi-pion background was subtracted and the data were integrated over the appropriate M_x^2 range. The Q^2 correction was applied to each $(W, \cos\theta_\eta^*, \phi_\eta)$ bin.

The binned yields Y_{data} for each setting were then converted to c.m. cross sections. For each

Effect	Correction	Discussed in Section
PID inefficiency		4.2.4
electron (SOS)	0.4 %	
Trigger inefficiencies		4.2.6
electron (SOS)	< 0.3 %	
proton (HMS)	< 0.3 %	
Tracking inefficiencies		4.2.6
electron (SOS)	2.0 % to 6.0 %	
proton (HMS)	3.0 % to 8.0 %	
Dead times		4.2.6
computer	2.0 % to 5.0 %	
electronic (product of SOS and HMS)	0 % to 1.2 %	
Beam-induced target density change	3.0 %	4.3.3
Proton absorption	2.8 %	4.3.4
Q^2 dependence	< ± 34 %	4.3.9

Table 4.3: Corrections applied to the data.

$(W, \cos \theta_\eta^*, \phi_\eta)$ bin,

$$\sigma_{\text{data,cm}} = \frac{Y_{\text{data}}}{Y_{\text{MC}}} \sigma_{\text{MC,cm}}, \quad (4.35)$$

where the Monte Carlo yield Y_{MC} is given by Eq. 3.6 on page 68, and the Monte Carlo model cross section $\sigma_{\text{MC,cm}}$ is obtained by evaluating Eq. 3.15 on page 70 at the center of the bin. The cut on relative acceptance \mathcal{A}_{rel} was applied to each bin.

The different kinematic settings were then combined. The contribution to each global $(W, \cos \theta_\eta^*, \phi_\eta)$ bin was obtained by taking the mean result from all settings (weighted by the appropriate function of statistical uncertainties). Errors were propagated throughout the analysis, included covariance terms where appropriate (*viz.*, for the background subtractions). The angular distributions for the two Q^2 points are shown in Fig. 5.1 on page 130 and Fig. 5.2 on page 131. Tabulated cross section data are given in Appendix C.

Chapter 5

Results and Conclusions

This chapter describes the estimation of systematic uncertainties in the data, and details the procedure used to extract the W dependence and helicity amplitude $A_{1/2}^p(S_{11})$ from the differential cross sections. We compare our results to the world's data and to recent theoretical models. We then compare our measurement to a recent analysis of inclusive (e, e') scattering and use the result to constrain the $S_{11}(1535) \rightarrow p\eta$ branching fraction.

5.1 Estimation of Systematic Uncertainties

In order to perform a meaningful fit to any data set it is important that the statistical uncertainties be correct and the estimates for systematic uncertainties be reasonable. In the case of the the differential c.m. cross section, $\frac{d^2\sigma}{d\Omega_\eta^2}$, we propagated the statistical uncertainties of the data itself and the Monte Carlo simulation,¹ including the appropriate covariance terms when performing the background subtractions.

The statistical uncertainties obviously varied from point to point in the differential cross sections. Estimates of systematic uncertainties, however, were treated in one of two ways. Where the uncertainty was small or roughly uniform over the data set, or where there was no information regarding its dependence on any of the binned variables (W , $\cos\theta_\eta^*$, and ϕ_η), a global uncertainty was assumed. In some cases, however, there was clear dependence of the uncertainty on W . In

¹The Monte Carlo simulations generally had statistics ≈ 4 -8 times greater than the data.

particular, point-to-point uncertainties were assigned to the multi-pion modeling, fit and subtraction, the kinematic quantities, and the acceptance. In these cases, the uncertainty assigned to the cross section data carries the appropriate W dependence. Our cross section results are presented (Appendix C) with separate statistical and estimated systematic errors for each $(W, \cos\theta_\eta^*, \phi_\eta)$ bin.

Many of the sources of systematic error were discussed in Chapter 4. Here we cover the remaining systematic uncertainties in the differential cross sections and how we undertook their estimation. A summary of results is given in Tables 5.1 and 5.2. The statistical and systematic uncertainties that apply to the extracted values of $A_{1/2}^P$ are given in Section 5.2.4. Note that $A_{1/2}^P$ goes as the square root of the cross section (Eq. 1.32 on page 21), so the corresponding fractional uncertainties are reduced by a factor of two from those in the cross section.

The uncertainty associated with the simulation of the multi-pion background in the Monte Carlo was investigated by comparing the analysis results using different background models (Section 3.2.2). Preliminary analysis indicated that all three models yielded results that agreed within roughly 5%; at that point the use of the Δ^{++} model (Model 2) was discontinued, because it required significantly greater computation time. In final versions of the analysis, the other two models of the multi-pion background (Model 1 and Model 3) yielded cross section fits for each W bin that differed by 1% to 6% (where the largest disagreement occurred at the highest W). These W -dependent values were used for the estimated uncertainties in the corresponding cross sections. The total cross sections differed by about 2%, and the extracted values of $A_{1/2}^P$ (which are dominated by the bins nearest the resonance mass) differed by less than 1%. An uncertainty of $\sigma = 1.0\%$ was assigned to the effects of the multi-pion background model on $A_{1/2}^P$.

The uncertainty associated with the background subtraction technique was investigated in a similar manner. The results of two independent subtraction techniques (Section 4.3.7) were compared. Cross section fits for each W bin differed by 1% to 7% (where the greatest disagreement again occurred at the highest W). These W -dependent values were used for the estimated uncertainties in the corresponding cross sections. The total cross sections differed by about 2%, and the extracted values of $A_{1/2}^P$ by less than 1%. An uncertainty of $\sigma = 1.0\%$ was assigned to the effects of the multi-pion background subtraction on the helicity amplitude.

Radiative effects on the cross section were dominated by Bremsstrahlung, which lowered the

cross section by about 30 % (with all data cuts) over what would be observed in the absence of radiation. The hard corrections, in contrast, raised the cross section by about 9%. Aside from theoretical uncertainties in the method of Mo and Tsai, the uncertainty in the knowledge of radiative effects was primarily that due to the reproduction of the radiative tail. This uncertainty was estimated by studying the variation in the measured, radiatively corrected ${}^1\text{H}(e, e'p)$ cross section as a function of W cut (applied to both the data and the Monte Carlo). The upper cutoff for this region was varied from $W = 1000$ MeV to $W = 1150$ MeV in 30 MeV steps, and the ratio of data to Monte Carlo yields ranged from 0.978 to 1.01. The uncertainty due to ‘soft’ radiative effects was estimated to be $\sigma = 1.5\%$. The uncertainty due to ‘hard’ effects was neglected.

Uncertainty due to errors in measurement of kinematic quantities E , $|\mathbf{k}_f|$, θ_e , ϕ_e , $|\mathbf{p}_f|$, θ_p , and ϕ_p (the θ s and ϕ s are the in-plane and out-of-plane laboratory spectrometer angles, and the other quantities were defined in Section 1.3.1) was simulated by performing a mock analysis. The mock analysis followed the prescription of Eq. 4.35 on page 123, but used ‘data’ generated by Monte Carlo simulation. Measurement errors were simulated in the Monte Carlo ‘data’, and the analysis gave the sensitivity to these errors.

In general, the largest uncertainties encountered in this experiment were those arising from kinematic quantities associated with the incoming and outgoing electron (E , $|\mathbf{k}_f|$, and θ_e in particular). The calculation of W depends on these quantities, and measurement errors generally resulted in misbinning in W . The mock analysis indicated that the uncertainties arising from errors in these kinematic quantities were very W dependent, but in general were smallest around the resonance mass.² As a result, the final systematic errors are rather large for the measurement of the S_{11} width Γ_R , but are much smaller for the cross section at the resonance mass (and thus the amplitude $A_{1/2}^p$).

In order to minimize errors in the final physics result, ${}^1\text{H}(e, e'p)$ calibration data taken during the experiment were studied extensively. In addition to verifying the absolute cross section, the zeroth-order reconstruction matrix elements were carefully adjusted to ensure that elastic events were accurately reproduced, and that the angular agreement between the two spectrometers was good (see Appendix B).

Dependence of the cross sections on various data cuts were checked by varying those cuts

²In other words, these errors resulted in the misplacement of events from (say) low W to high W . Such a shift has little effect near the maximum of a broad peak.

Quantity	Uncertainty (σ) in		Discussed in Section
	$\frac{d^2\sigma}{d\Omega_7^2}$	$A_{1/2}^p$	
PID inefficiency			4.2.4
electron (SOS)	$\pm 0.14\%$	$\pm 0.07\%$	
Trigger inefficiencies			4.2.6
electron (SOS)	$\pm 0.3\%$	$\pm 0.15\%$	
proton (HMS)	$\pm 0.3\%$	$\pm 0.15\%$	
Tracking inefficiencies			4.2.6
electron (SOS)	$\pm 1.5\%$	$\pm 0.75\%$	
proton (HMS)	$\pm 1.5\%$	$\pm 0.75\%$	
Dead times			4.2.6
computer	$\approx 0\%$	$\approx 0\%$	
electronic (combined)	$\approx 0\%$	$\approx 0\%$	
Charge measurement	$\pm 1.5\%$	$\pm 0.75\%$	4.3.2
Target length and density	$\pm 0.6\%$	$\pm 0.3\%$	4.3.3
Beam-induced target density change	$\pm 0.5\%$	$\pm 0.25\%$	4.3.3
Proton absorption	$\pm 1.2\%$	$\pm 0.6\%$	4.3.4
Q^2 correction	$\pm 1.0\%$	$\pm 0.5\%$	4.3.9
Radiative effects	$\pm 1.5\%$	$\pm 0.75\%$	3.1.1, 3.3
Monte Carlo background generation	$\pm 1.0\%$ to 7%	$\pm 1.0\%$	3.2.2, 5.1
Multi-pion subtraction technique	$\pm 1.0\%$ to 6%	$\pm 1.0\%$	4.3.7, 5.1
Kinematic quantities			5.1
E	$\pm 1.0\%$ to 10%	$\pm 0.8\%$	
$ k_f $	$\pm 0.1\%$ to 8%	$\pm 0.5\%$	
θ_e	$\pm 0.2\%$ to 11%	$\pm 1.0\%$	
$\phi_e, p_f , \theta_p, \phi_p$	$\approx 0\%$	$\approx 0\%$	
Quadrature Sum	$\pm 4.4\%$ to 17%	$\pm 2.6\%$	

Table 5.1: Estimates of systematic uncertainties in $\frac{d^2\sigma}{d\Omega_7^2}$ and $A_{1/2}^p$, not including those arising from explicit cuts on the data. The uncertainty in $\frac{d^2\sigma}{d\Omega_7^2}$ gives a single number in the case of a global uncertainty and a range of values (for single W bins) in the case of a W -dependent uncertainty. The third column gives the resulting uncertainty in the helicity amplitude $A_{1/2}^p$ (in the case of different estimates between the two Q^2 points, the larger of the uncertainties is given).

Quantity	Variable	Cut Variation	Uncertainty (σ) in	
			$\frac{d^2\sigma}{d\Omega_n^2}$	$A_{1/2}^P$
Relative Acceptance	A_{rel}	Standard $\begin{smallmatrix} +35\% \\ -25\% \end{smallmatrix}$	$\pm 1.0\%$ to 6%	$\pm 1.0\%$
SOS Čerenkov	$N_{sum,p.e.}$	Standard $+5$ p.e.	$\pm 0.6\%$	$\pm 0.3\%$
SOS calorimeter	E_{norm}	Standard ± 0.1	$\pm 0.3\%$	$\pm 0.15\%$
HMS time of flight	β_{tof}	Standard ± 0.02	$\pm 0.1\%$	$\pm 0.05\%$
Coincidence time	t_{coin}	Standard $+2$ ns	$\pm 0.5\%$	$\pm 0.25\%$
Missing mass	M_x^2	Standard ± 0.01 GeV ² /c ⁴	$\pm 1.0\%$	$\pm 0.5\%$
HMS target position	y_{tar}	Standard ± 0.5 cm	$\pm 0.5\%$	$\pm 0.25\%$
Quadrature Sum			$\pm 1.7\%$ to 6.2%	$\pm 1.2\%$

Table 5.2: The dependence of the final results on changes to explicit cuts used in the analysis. ‘Standard’ cuts refer to those given in Table 4.2.

over reasonable (albeit arbitrary) limits. The relative acceptance as determined by Monte Carlo simulation (Section 4.3.8) was used to estimate the uncertainty in the Monte Carlo acceptance. The acceptance cut was varied from 0% (*i.e.*, no acceptance cut) to 60% (which removed roughly 50% of the data from consideration). The range of variation in the measured resonance cross section (from the ‘standard’ cut at 25%) ranged from under 1% up to 6% (at the highest W) for the low Q^2 point, and these W dependent variations were used for the estimated uncertainty σ . The high Q^2 point exhibited an estimated uncertainty of $\sigma = 1.5\%$, with no clear W dependence. The dependence on other cuts was checked in similar fashion. Note that there is no cut dependence explicitly listed for the δ (spectrometer momentum) cuts, because these dependences enter when varying the relative acceptance cut.

The estimation of uncertainties specific to the calculation of the amplitude $A_{1/2}^P$ are discussed in Section 5.2.4.

5.2 Extraction of $A_{1/2}^p$

Differential resonance cross sections are most appropriately analyzed in a partial-wave framework, especially when the angular distributions themselves exhibit clear energy dependence (indicating the presence of two or more partial waves). In the case of the present data, however, the overwhelming dominance of S -wave multipoles³ allows much of the physics to be extracted using a more primitive analysis. The angular distributions for the two Q^2 points are shown in Figs. 5.1 and 5.2.

The extraction of the helicity amplitude $A_{1/2}^p$ presented here is deliberately simplistic (details are given in Sections 5.2.1 through 5.2.4, following). In overview, the calculation involved performing a *separate* fit of Eq. 1.16 on page 16 to $\frac{d^2\sigma}{d\Omega_T^2}$ at *each* W bin (the parameterization was subsequently simplified) (Section 5.2.1). From these fits we obtained the magnitude of the E_{0+} multipole as a function of W (via Eq. 1.23 on page 17, together with an assumed value for $R = \sigma_L/\sigma_T$) (Section 5.2.2). $|E_{0+}(W)|^2$ was then fit with a Breit-Wigner plus background curve, which requires the assumption of S_{11} branching fractions (Section 5.2.3). The helicity amplitude was calculated from the value of $|E_{0+}|$ at the resonance mass using Eq. 1.27 on page 19 and fit values of the resonance mass W_R and the full width Γ_R (Section 5.2.4).

We had two goals for this extraction of results. First, we wanted a benchmark quantity for use when studying systematic errors. Second, we wanted a reasonably accurate extraction of $A_{1/2}^p$ (of less interest to this investigation were possible contributions from other multipoles, which are expected to be very small at this value of Q^2). The extent of the S -wave dominance of the differential cross sections presented here leads us to believe that the results obtained from our analysis, while not optimum, are quite accurate.

At the time of this writing the cross section data are being given to other groups that will perform more sophisticated extractions of the helicity amplitude. Note that the uncertainty of the $A_{1/2}^p$ helicity amplitude is presently dominated by uncertainties in other parameters needed for the

³This dominance is expected from previous data; see Refs. [Bec74, Ald75, Bra78, Bra84]. With the exception of the $D_{13}(1520)$, there is no experimental evidence to suggest that any resonance other than the $S_{11}(1535)$ contributes substantially to the $p\eta$ channel in the second resonance region at high momentum transfer. Figure 8 of Ref. [Bra84] shows the stiffness of the S_{11} relative to the D_{13} as a function of Q^2 ; according to that figure, at $Q^2 = 3$ (4) GeV^2/c^2 the cross section (through *all* channels) of the S_{11} is over 7 (20) times the cross section of the D_{13} . Given the small $D_{13} \rightarrow p\eta$ branching fraction ($< 1\%$; no listing in [PDG98]), we expect a D_{13} contribution to the $p\eta$ channel of order 0.1% or less at our values of Q^2 . See also Ref. [Kru95], keeping in mind that the small D -wave interference seen in that photoproduction measurement ($p\eta$ channel only) is expected to diminish by roughly a factor of thirty at our high Q^2 , due to the rapid drop of the D_{13} relative to the S_{11} as a function of Q^2 .

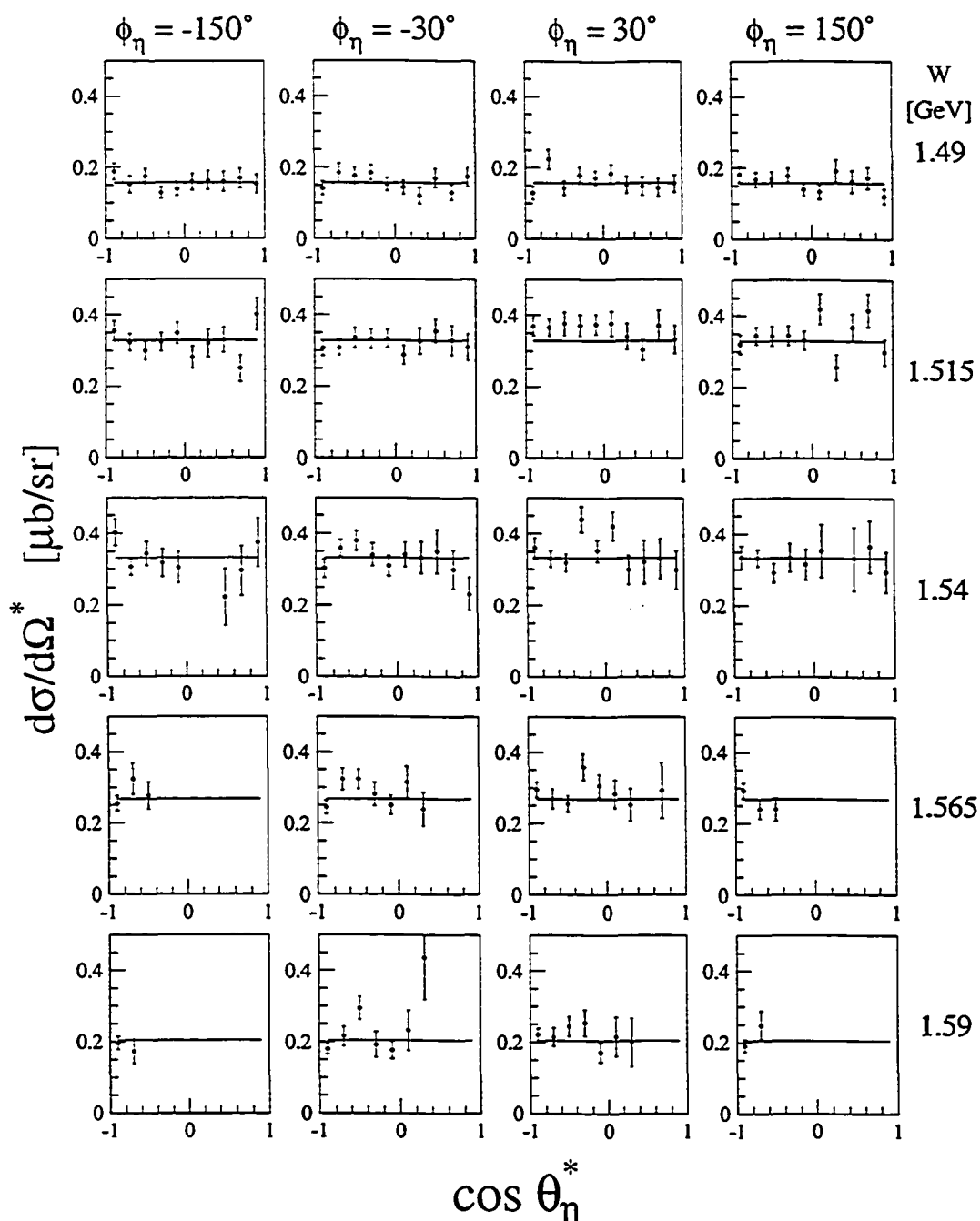


Figure 5.1: Angular distributions for the $Q^2 = 2.4 \text{ GeV}^2/c^2$ data. Each plot shows the $\cos\theta_\eta^*$ distribution for a single (W, ϕ_η) bin. The rows correspond to different bins in W , the columns to different bins in ϕ_η . The threshold for $p\eta$ production is at $W = 1.486 \text{ GeV}$ (in the lowest W bin). Note that data corresponding to $\phi_\eta = \pm 90$ degrees are not shown. The out-of-plane experimental coverage was complete only for the lowest W bin (where the data looked similar to that in the ϕ_η bins shown here), and was almost nonexistent at higher W . The lines are fits to the data, described in Section 5.2.1.

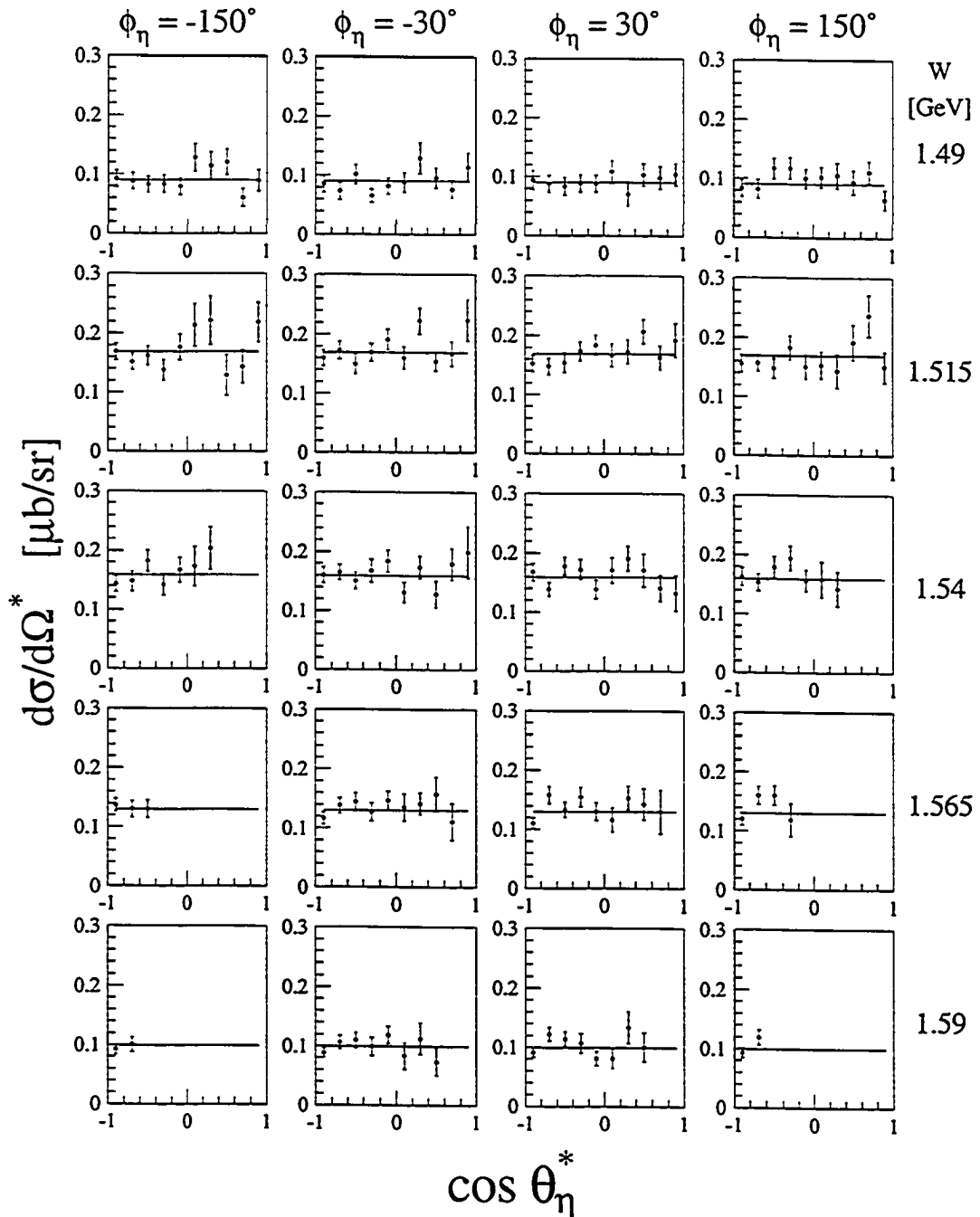


Figure 5.2: Angular distributions for the $Q^2 = 3.6 \text{ GeV}^2/c^2$ data. The general description follows that of Fig. 5.1.

calculation. In particular, the S_{11} full width Γ_R , the S_{11} branching fractions $b_\eta (\equiv \Gamma_\eta/\Gamma_R)$, b_π , $b_{\pi\pi}$, and the ratio R all have substantial uncertainties. We anticipate that this data set will be re-fit as knowledge of these quantities and of neighboring resonances improves, which justifies the simple analysis presented here.

5.2.1 Fits to the Angular Distributions

In preliminary stages of analysis we allowed the full parameterization of Eq. 1.16 on page 16 in the least-squares fits to the data.⁴ At the lowest W bin, where experimental coverage was complete, the fit parameters D , E , and F of Eq. 1.16 (those containing ϕ_η dependence) were less than 5% and consistent with zero within statistical uncertainty. The out-of-plane coverage diminished rapidly with increasing W , however, and at the higher W bins the data did not properly constrain these parameters, resulting in clearly nonphysical fits (very small improvements to the regions with coverage together with pathological behavior in the unpopulated regions).⁵ The results that we quote in this work were obtained with $D = E = F = 0$.

Setting the D , E , and F parameters to zero resulted in a change in the magnitude of the A term of less than 1% at $W = 1.49$ GeV, and the uncertainties quoted for $A_{1/2}^p$ take this into account. The χ^2/N_{df} of the fits (which ranged from 0.8 to 1.7 for all W bins at both Q^2 points) were almost unchanged [$\Delta(\chi^2/N_{df})$ ranged from 0% to 8%] by setting these three parameters to zero.

With the reduced parameterization $\frac{d^2\sigma}{d\Omega_\eta^*} = A + B \cos \theta_\eta^* + C \cos^2 \theta_\eta^*$, the fit parameters B and C were less than 7% for the low- W bins, but were poorly constrained at high W . The values were generally consistent with zero within statistical uncertainty. Since our interest lay in extracting the magnitude of the cross section at the resonance mass (as opposed to looking for small contributions from other multipoles), these two fit parameters were also set to zero for the results quoted in this work. As in the case above, setting these parameters to zero resulted in only small changes to the extracted value of the fit coefficient A (which are reflected in the systematic uncertainties), and resulted in almost no change to the χ^2/N_{df} of the fits. The results that we

⁴The method of least squares applied to Poisson-distributed data underestimates the integrated area of the data by a quantity related to the χ^2 of the fit [Bev69]. These fits were corrected for this effect (which was about 1% to 3%).

⁵Note that in a more appropriate (energy dependent) analysis these terms would be constrained by the data at low W .

quote in this work were obtained with $B = C = 0$.

5.2.2 Assumed Form of R

For the purposes of helicity amplitude calculations, the value of $R = \sigma_L/\sigma_T$ for the S_{11} was taken to be

$$R = 0.5 \sqrt{Q^2} e^{-1.3 Q^2}, \quad (5.1)$$

which is shown in Fig. 1.4 on page 9. This is a simple parameterization of the result of Ref. [Rav71] as given in Ref. [Bra84]. Note that the expected impact of the longitudinal-to-transverse ratio on the final physics result is small; our parameterization gives $R < 4\%$ at $Q^2 = 2.4 \text{ GeV}^2/c^2$, with a corresponding effect on the cross section (given $\epsilon \approx 0.5$) of about 1.5% (and less than 1% on $A_{1/2}^p$). A 100% error in this assumption, which is possible given the poor knowledge of this quantity, corresponds to an uncertainty of less than 1% in the quoted value of $A_{1/2}^p$.

5.2.3 Fits to $|E_{0+}(W)|^2$

The E_{0+} multipole was calculated for each W bin from the angular distribution fit coefficients A and the assumed form of R using Eq. 1.23 on page 17. At each Q^2 point, a relativistic Breit-Wigner plus background curve was fit to $|E_{0+}(W)|^2$:

$$\begin{aligned} \sigma_{\text{tot}}(W) &= \sigma_{\text{res}}(W) + \sigma_{\text{nr}}(W) \\ &= 4\pi \frac{|\mathbf{p}_\eta^*| W}{m_p K} |E_{0+}(W)|^2 \\ &= 4\pi \frac{|\mathbf{p}_\eta^*| W}{m_p K} \frac{W_R^2 \Gamma_R^2 |E_{0+}(W_R)|^2}{(W^2 - W_R^2)^2 + W_R^2 \Gamma^2(W)} + B_{\text{nr}} \sqrt{W - W_{\text{thr}}}. \end{aligned} \quad (5.2)$$

The parameterization of the energy-dependent width $\Gamma(W)$ in terms of S_{11} branching fractions was given in Section 3.2.1, and the other terms were defined in Section 1.3.2.

An interesting feature of the $S_{11} \rightarrow p\eta$ process arises from the threshold dependence of the cross section. As a result of the $p\eta$ threshold, *a cross section measurement of the process is largely insensitive to the effects of branching fractions and W_R individually*. Consider a relativistic

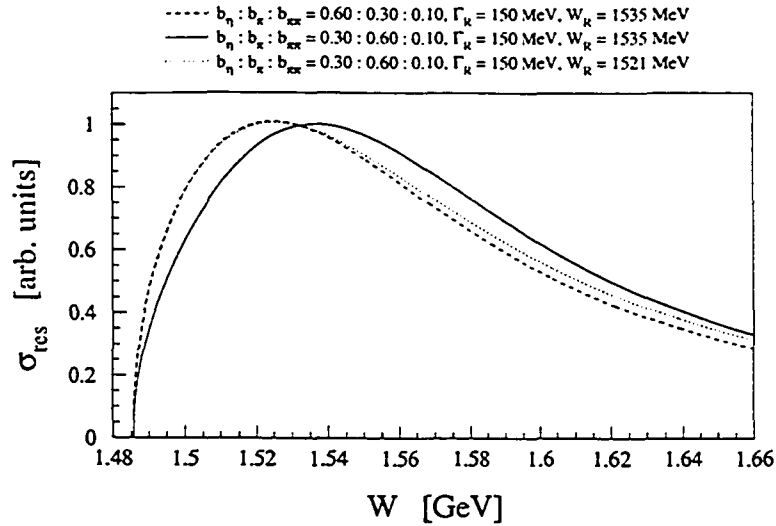


Figure 5.3: The energy dependence of a relativistic threshold Breit-Wigner curve (Eq. 5.3) for several choices of resonance mass W_R and branching fractions. The overall normalization is arbitrary.

Breit-Wigner form for the process,

$$\sigma(W) = A_{BW}^2 \frac{|p_\eta^*|}{m_p} \frac{W}{K} \frac{W_R^2 \Gamma_R^2}{(W^2 - W_R^2)^2 + W_R^2 \Gamma^2(W)}, \quad (5.3)$$

where A_{BW} is an arbitrary amplitude. Figure 5.3 shows this curve for several values of branching fractions and W_R . The effect of changing the branching fractions alone is rather obvious (the dashed and solid curves are distinguishable). Note, however, that a simultaneous change in W_R (together with a change in the amplitude A_{BW}) can largely compensate for the change in branching fractions (the dashed and dotted curves are similar, especially near threshold). Measurement of the $S_{11} \rightarrow p\eta$ process alone is insufficient to clearly distinguish between the effects of these two parameters.

As a result of this effect, we performed fits to the W distributions assuming three sets of values for the branching fractions ($b_\eta : b_\pi : b_{\pi\pi}$), as defined in Table 5.3 (we use the same values as used in Ref. [Kru95]). As expected based on the discussion above, the fits arrived at different values for the resonance mass W_R , with little difference in χ^2 to distinguish between them (the curves are nearly indistinguishable). The extracted value of Γ_R is nearly independent of the branching fraction assumption, and we find that $\Gamma_R = (154 \pm 20)$ MeV (see Fig. 5.4). The impact of the branching fraction assumption on the extracted value of $A_{1/2}^p$, however, was substantial (as can be

Fit 1	Fit 2	Fit 3
(0.55 : 0.35 : 0.10)	(0.45 : 0.45 : 0.10)	(0.35 : 0.55 : 0.10)

Table 5.3: Branching fractions ($b_\eta : b_\pi : b_{\pi\pi}$) defining Fits 1–3.

seen from Eq. 1.27 on page 19). We quote full results for the three branching fraction assumptions later, in Section 5.2.4, after a discussion of the helicity calculation. At both values of Q^2 the fitted nonresonant background term ($B_{nr} \sqrt{W - W_{thr}}$) was consistent with zero, with an uncertainty of 1% of the resonant term.

Note that there is considerable disagreement between the value of Γ_R as determined by different experiments (see Fig. 5.5). In particular, note that the data of Ref. [Bra84] indicate a full width of less than 70 MeV for the S_{11} . The recent photoproduction measurement at Mainz [Kru95] tagged the 2γ decay of the outgoing η meson, which cleanly identified the final state (they did not suffer from a multi-pion background). This fact, together with the high statistics of that experiment, lends considerable weight to that collaboration's claim of $\Gamma_R = (203 \pm 35)$ MeV for the $S_{11}(1535)$ full width. That measurement, however, only extended up to the resonance mass. It is worth pointing out that the form of the Breit-Wigner parameterization can impact the extracted resonance parameters. The parameterization used by the two other groups mentioned here is essentially the same as that used in this work, however, and so cannot account for the differences in Γ_R .

The world's data for $\sigma_{res}(ep \rightarrow e'p\eta)$ (at the resonance mass) are shown in Fig. 5.6. The data of the present work are about 30% below that of Ref. [Bra84] (found by interpolating the results of this work to $Q^2 = 3 \text{ GeV}^2/c^2$). The trend of the two new data points is also somewhat different than that found in the older data. Both of these issues will be discussed more fully in the context of the helicity amplitude calculation (Section 5.2.4).

We point out that, although the present data were taken at a different value of ε than those of Ref. [Bra84], a longitudinal cross section is almost certainly not responsible for the entire difference between the two measurements; a value of $R \approx 2.3$ (which is ruled out at low Q^2 [Bre78, Bra78]) would be necessary to account for the discrepancy.

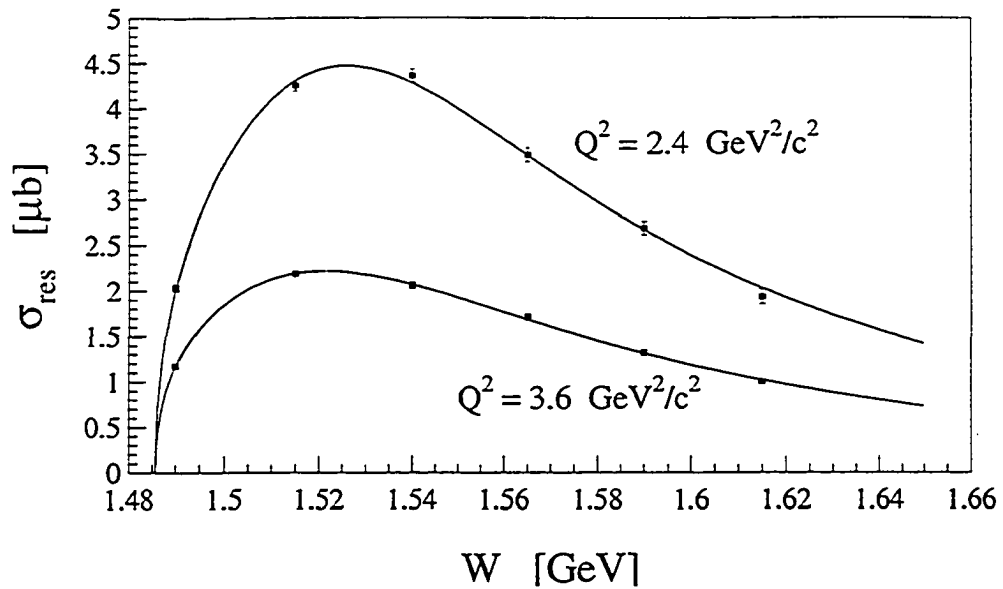


Figure 5.4: The W dependence of $\sigma_{\text{res}}(ep \rightarrow e'p\eta)$ for the two Q^2 points. The error bars are statistical only.

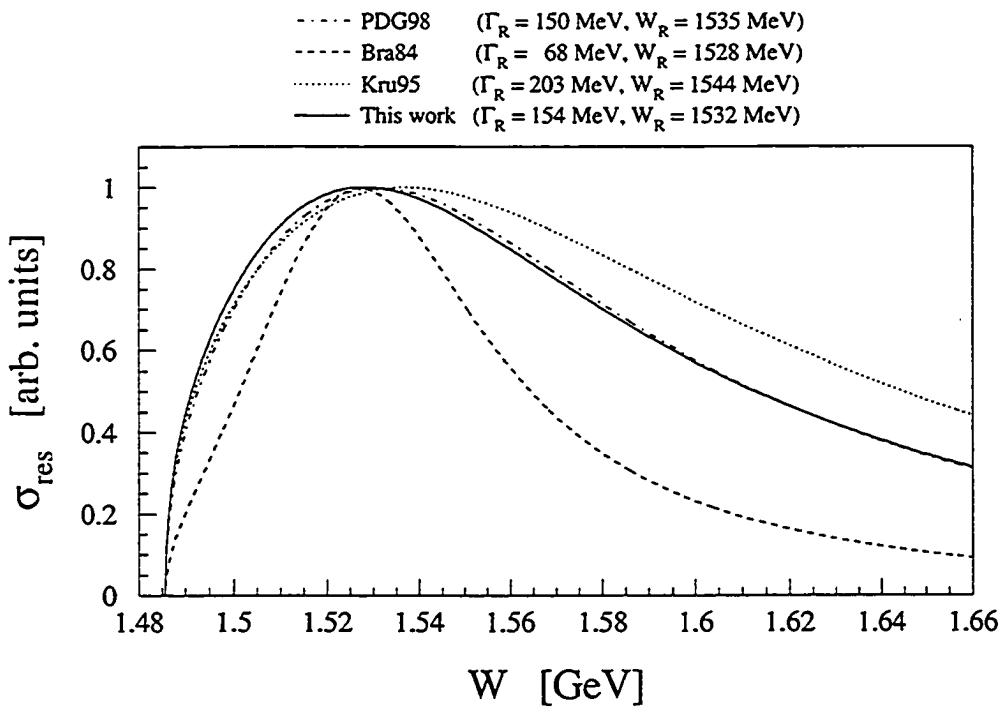


Figure 5.5: There is significant disparity in the W dependence of $\sigma_{\text{res}}(ep \rightarrow e'p\eta)$ as reported by different groups. Here we plot the energy-dependent Breit-Wigner curve using W_R and Γ_R as measured by Refs. [Bra84], [Kru95], and the present work. The curve resulting from the estimated values given by [PDG98] is also shown. The curves have been normalized to the same peak magnitude.

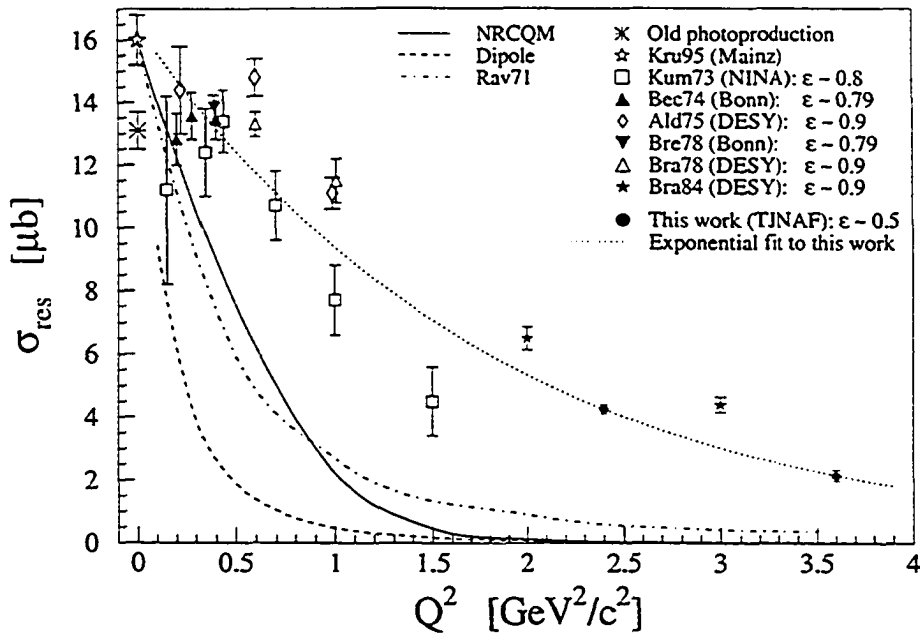


Figure 5.6: The world's data for the cross section $\sigma_{\text{res}}(ep \rightarrow e'p\eta)$ at $W \approx 1535$ MeV. The exponential fit to the two points of this work is $\sigma_{\text{res}} = 16.5 e^{-0.565 Q^2} \mu\text{b}$, where Q^2 is in $[\text{GeV}^2/c^2]$.

5.2.4 Calculation of $A_{1/2}^p$

The helicity amplitude is defined in terms of $|E_{0+}|$ at the resonance mass (Eq. 1.27 on page 19). The calculation also requires the S_{11} resonance mass W_R and full width Γ_R , as well as b_η , the branching fraction of the S_{11} to the $p\eta$ channel [the other S_{11} branching fractions enter via the energy dependent width $\Gamma(W)$ in Eq. 5.2]. The dominant uncertainty in the calculation is due to the poor knowledge of the full width Γ_R and the $p\eta$ branching fraction. The estimated values and ranges for these quantities (according to the Particle Data Group) are shown in Table 5.4. We estimated the uncertainty in $A_{1/2}^p$ due to uncertainties in Γ_R and b_η by allowing these two parameters to vary over reasonable ranges (150–200 MeV and 0.45–0.6, respectively) and looking at the resulting distribution of helicity amplitudes. This study yielded an uncertainty of $\sigma \approx 7(5) \times 10^{-3} \text{ GeV}^{-1/2}$ at the low (high) Q^2 point.

Final results of the fits to $|E_{0+}(W)|^2$ and the amplitude calculation are given in Table 5.6, where we have used our *fitted values* (which are very close to the PDG estimates) to calculate $A_{1/2}^p$. Based on the branching fraction constraint discussed in Section 5.3, we quote in Table 5.7 final results from Fit 1 ($b_\eta = 0.55$). The quoted uncertainties in $A_{1/2}^p$ are systematic and statistical

Quantity	Estimated Value	Range
W_R	≈ 1535 MeV	1520 to 1555 MeV
Γ_R	≈ 150 MeV	100 to 250 MeV
b_η	-	0.30 to 0.55
b_π	-	0.35 to 0.55
$b_{\pi\pi}$	-	0.01 to 0.10

Table 5.4: Current values for the $S_{11}(1535)$ mass, full width, and major branching fractions (according to Ref. [PDG98]).

Quantity	Uncertainty (σ) in $A_{1/2}^P$	Discussed in Section
Assumption of $D = E = F = 0$	$\pm 0.4\%$	5.2.1
Assumption of $B = C = 0$	$\pm 1.0\%$	5.2.1
Assumed value of $R = \sigma_L/\sigma_T$	$\pm 0.75\%$	5.2.3
Assumed values of Γ_R, b_η	$\pm 11\%$ to 14%	5.2.4
Quadrature Sum (except Γ_R, b_η)	$\pm 1.3\%$	
Quadrature Sum	$\pm 11\%$ to 14%	

Table 5.5: Uncertainties specific to the calculation of $A_{1/2}^P$.

in quadrature; in Table 5.7 we have included estimates (discussed above) for the uncertainties due to Γ_R and b_η .

Figure 5.7 shows the helicity amplitude results, along with points calculated from the rest of the world's $ep \rightarrow e'p\eta$ data.⁶ We differ with Ref. [Bra84] about both the amplitude of the S_{11} and the slope of its form factor. Here the 30% cross section difference between the two measurements is reduced by the square root relating $A_{1/2}^P$ to the cross section (see Eq. 1.32 on page 21).

⁶When comparing the results of this work to other measurements, as in Fig. 5.7, we calculate $A_{1/2}^P$ using the same values of W_R, Γ_R , and b_η for all data points.

Quantity	$Q^2 = 2.4 \text{ GeV}^2/c^2$				$Q^2 = 3.6 \text{ GeV}^2/c^2$				PDG98
	Fit 1	Fit 2	Fit 3	Abs. Uncert.	Fit 1	Fit 2	Fit 3	Abs. Uncert.	
W_R [MeV]	1534	1530	1524	± 3 (1)	1530	1524	1518	± 8 (4)	≈ 1535
Γ_R [MeV]	151	148	145	± 16 (5)	157	152	148	± 24 (8)	≈ 150
$A_{1/2}^P$ [$10^{-3} \text{ GeV}^{-1/2}$]	49.8	55.3	62.7	± 2 (0.5)	35.2	39.1	44.3	± 1 (0.5)	-

Table 5.6: Results of the three fits to $|E_{0+}(W)|^2$ (see Section 5.2.3) and extracted values for the helicity amplitude $A_{1/2}^P$. The (absolute) uncertainties are statistical and systematic combined in quadrature, with statistical uncertainties in parentheses. Here the uncertainties arising from the S_{11} full width and branching fractions are *not* included in the systematic uncertainty in $A_{1/2}^P$. Based on results presented in Section 5.3, we prefer Fit 1.

Quantity	Preferred Value
W_R	1532 ± 5 MeV
Γ_R	154 ± 20 MeV
$A_{1/2}^p (Q^2 = 2.4 \text{ GeV}^2/c^2)$	$(50 \pm 7) \times 10^{-3} \text{ GeV}^{-1/2}$
$A_{1/2}^p (Q^2 = 3.6 \text{ GeV}^2/c^2)$	$(35 \pm 5) \times 10^{-3} \text{ GeV}^{-1/2}$
$b_\eta = \Gamma_\eta/\Gamma_R$	> 0.45 ; best value ≈ 0.55

Table 5.7: Preferred results (Fit 1), based on the b_η constraint discussed in Section 5.3. The uncertainties are systematic (*including* estimated uncertainties in Γ_R and b_η for $A_{1/2}^p$) and statistical in quadrature. The ‘best value’ for b_η assumes complete S_{11} dominance at $Q^2 = 4 \text{ GeV}^2/c^2$.

Of the various CQM curves shown in Fig. 5.7, none—with the possible exception of the Ref. [War90] curve—exhibit a stiffness approaching that of the data. The calculation of Ref. [War90], which has (at least at low Q^2) the stiffest form factor of all the CQM variants shown, also gives an amplitude that appears too low. It should be pointed out that the proton and neutron electric and magnetic form factors predicted by this model are not well behaved above $\sim 2 \text{ GeV}^2/c^2$. Capstick and Keister [Cap95], working in a light-front framework, specifically set out to investigate the effects of relativization on baryon photo- and electroproduction observables. One of the notable results of their work is that, while the transition amplitudes of many resonances show appreciable relativistic effects, the transverse amplitude $A_{1/2}^p(S_{11}(1535))$ does not. We point out, however, that their effort is ongoing at the time of this writing [Cap98]. It appears, then, that the CQM so far fails to account for the experimentally observed Q^2 behavior of the $S_{11}(1535)$.

Figure 5.8 shows the quantity $Q^3 A_{1/2}^p$ for the $S_{11}(1535)$. This quantity is predicted by pQCD to asymptotically approach a constant at high Q^2 [Car88]; as has been pointed out previously [Isg84, Rad91], such scaling may also arise from nonperturbative contributions. While there is no strong scaling evident in the figure, there is (as noted above) a definite disagreement with the older high- Q^2 measurement about the slope of the Q^2 dependence. We point out that an extension [Sto97] of the present experiment to $Q^2 \approx 7 \text{ GeV}^2/c^2$ has been approved to run at TJNAF in the near future, and should shed more light on the Q^2 evolution of this quantity.

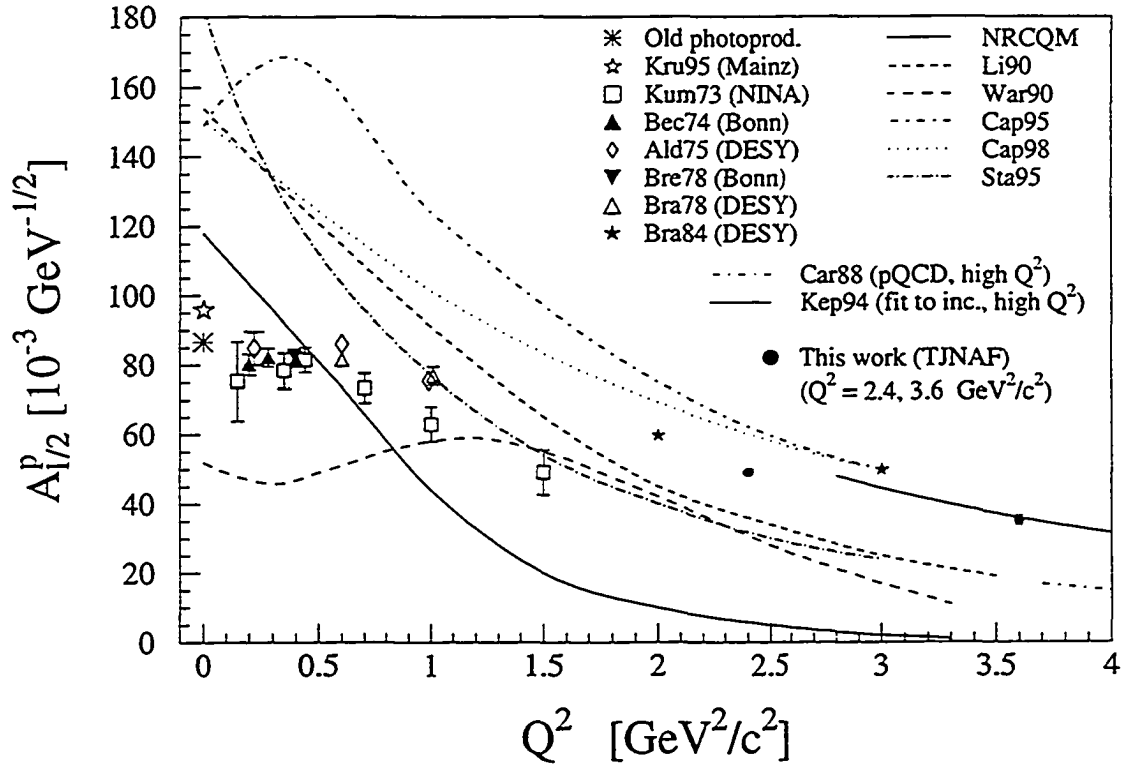


Figure 5.7: The world's data for $A_{1/2}^p(S_{11}(1535))$, measured via the $p\eta$ channel, together with some theoretical predictions. The data points are calculated from $ep \rightarrow e'p\eta$, $W \approx 1535$ MeV cross section data using Eq. 1.31 on page 21 and assuming an S_{11} full width $\Gamma_R = 150$ MeV, $b_\eta = 0.55$, and R as given by Eq. 5.1. The errors shown on previous data are statistical only. The errors shown for the present work include both statistical *and* systematic uncertainties, except for those associated with Γ_R and b_η . If either of these quantities differ from the values assumed here, *all* data points will scale together. The theoretical curves labeled [Li90] through [Sta95] are variants of the CQM. Note that the calculation of $A_{1/2}^p$ based on the fit to inclusive data, [Kep94], assumes that the second resonance region is entirely due to the $S_{11}(1535)$, which is only expected to be true at high Q^2 [Bra84]. The curve labeled [Car88] is a pQCD calculation (only the central result of that work is shown).

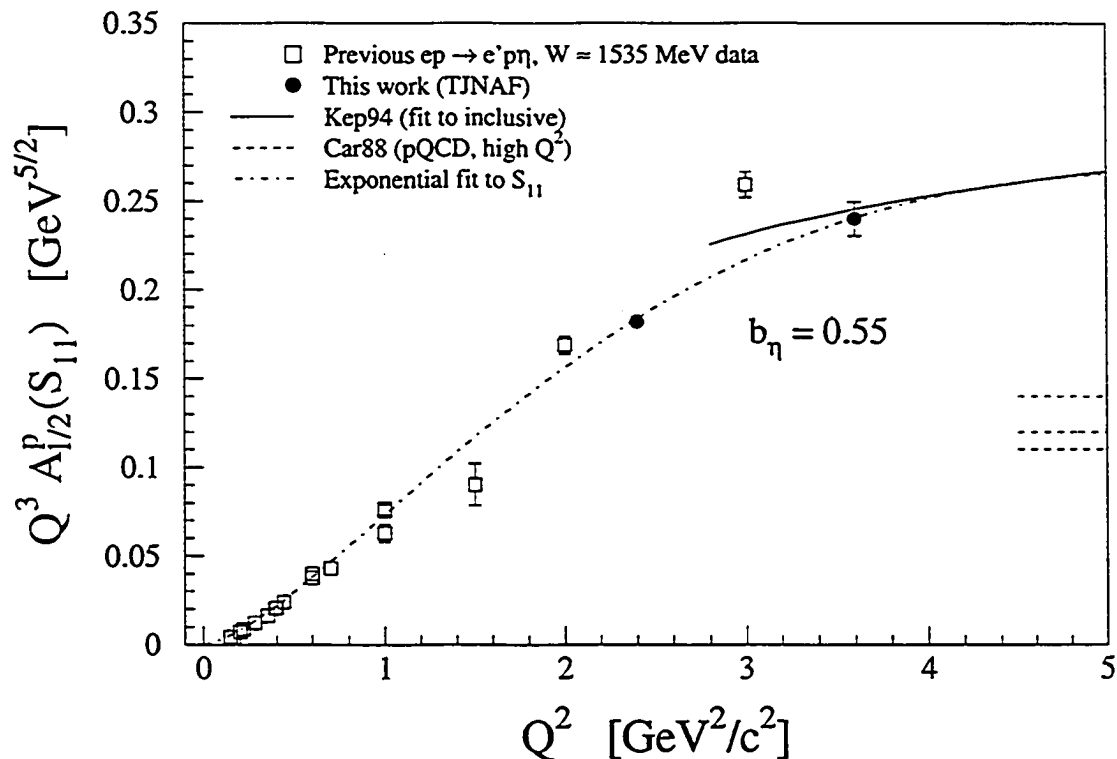


Figure 5.8: The quantity $Q^3 A_{1/2}^P(Q^2)$ for the $S_{11}(1535)$. The dashed line is an ad hoc exponential fit to the cross section given by the two points of the present work (see Fig. 5.6), and the solid line is a fit to inclusive data (as in Fig. 5.7). The errors that are shown, and the assumed values for Γ_R , b_{η} , and R , are the same as in Fig. 5.7. Ref. [Car88] gives three results, depending on the distribution amplitude used in the calculation.

5.3 A Constraint on the $S_{11} \rightarrow p\eta$ Branching Fraction

If we assume that the resonant part of the inclusive (e, e') cross section is the incoherent sum of the contributions of resonances via their various decay channels, we can use the inclusive and exclusive resonant cross sections to put a lower bound on the $S_{11}(1535) \rightarrow p\eta$ branching fraction b_η . It appears that at high momentum transfer the $S_{11}(1535)$ resonance is responsible for most of the resonant cross section in the neighborhood of $W = 1535$ MeV (see footnote 3 on page 129). At an arbitrarily high value of Q^2 , where this resonance nearly or completely dominates, we can rearrange Eq. 1.32 on page 21 to write

$$\sigma_{\text{res}}(S_{11} \rightarrow p\eta) = \frac{2m_p b_\eta}{W_R \Gamma_R} (1 + \varepsilon R) [A_{1/2}^p(S_{11})]^2, \quad (5.4)$$

where ' S_{11} ' refers to the $S_{11}(1535)$ resonance, and the cross section is at $W \approx 1535$ MeV. We can write analogous equations for other S_{11} decay channels:

$$\sigma_{\text{res}}(S_{11} \rightarrow N\pi) = \frac{2m_p b_\pi}{W_R \Gamma_R} (1 + \varepsilon R) [A_{1/2}^p(S_{11})]^2; \quad (5.5)$$

$$\sigma_{\text{res}}(S_{11} \rightarrow N\pi\pi) = \frac{2m_p b_{\pi\pi}}{W_R \Gamma_R} (1 + \varepsilon R) [A_{1/2}^p(S_{11})]^2. \quad (5.6)$$

With the incoherent summation ansatz given above, we can express the resonant part of the inclusive cross section in the second resonance region (LHS) in terms of the exclusive cross sections (RHS) (here too, all cross sections are at the S_{11} resonance mass):

$$\begin{aligned} \sigma_{\text{res}}(\text{inclusive}) &= \sigma_{\text{res}}(S_{11} \rightarrow p\eta) + \sigma_{\text{res}}(S_{11} \rightarrow N\pi) + \sigma_{\text{res}}(S_{11} \rightarrow N\pi\pi) \\ &+ \{\text{small contributions from } D_{13}\} \\ &+ \{\text{small contributions from other resonances}\}. \end{aligned} \quad (5.7)$$

We express the S_{11} contributions using Eqs. 5.4 through 5.6, and change the equality to an inequality to account for the (small) contributions from other resonances:

$$\sigma_{\text{res}}(\text{inclusive}) \geq \frac{2m_p (b_\eta + b_\pi + b_{\pi\pi})}{W_R \Gamma_R} (1 + \varepsilon R) [A_{1/2}^p(S_{11})]^2$$

$$\geq \frac{2m_p}{W_R \Gamma_R} (1 + \varepsilon R) [A_{1/2}^p(S_{11})]^2 . \quad (5.8)$$

Solving Eq. 5.4 for $\frac{2m_p}{W_R \Gamma_R} (1 + \varepsilon R) [A_{1/2}^p(S_{11})]^2$ and substituting into Eq. 5.8 yields

$$\sigma_{\text{res}} (\text{inclusive}) \geq \frac{\sigma_{\text{res}} (S_{11} \rightarrow p\eta)}{b_\eta} , \quad (5.9)$$

or

$$b_\eta \geq \frac{\sigma_{\text{res}} (S_{11} \rightarrow p\eta)}{\sigma_{\text{res}} (\text{inclusive})} . \quad (5.10)$$

Thus the resonant part of the *inclusive* (e, e') cross section in the second resonance region provides an upper bound on the $S_{11}(1535)$ cross section that one can measure *exclusively*.

Figure 5.9 shows a comparison between the resonant part of a fit to measured inclusive data [Kep94] (solid line) and exclusive $ep \rightarrow e'p\eta$ data (both at $W \approx 1535$ MeV). The data points have been scaled by $1/b_\eta$, with $b_\eta = 0.55$ (the dashed curve is an exponential fit to the two data points of this experiment). This value of b_η results in good agreement between the high- Q^2 datum of this work and the inclusive fit. As pointed out above (footnote 3 on page 129), the inclusive cross section is dominated by the $D_{13}(1520)$ at low Q^2 and the $S_{11}(1535)$ at high Q^2 .

The inset of Fig. 5.9 shows the inclusive fit and the two points of this work (with exponential fit), where the exclusive data (and fit) have been scaled by $1/b_\eta$, with $b_\eta = 0.35$. This value of b_η implies an exclusive cross section 50% *greater* than the fit to the measured inclusive cross section. Even with the ad hoc $\pm 10\%$ uncertainty we have attributed to the inclusive measurement,⁷ this discrepancy is strong evidence that the branching fraction is not this low. At present the PDG gives an estimated range of $0.30 \leq b_\eta \leq 0.55$ [PDG98], but a branching fraction at the lower end of that range is unlikely. With the incoherent summation ansatz, we find a lower bound of $b_\eta = 0.45$ with a 95% confidence level. Assuming *complete* $S_{11}(1535)$ dominance at $Q^2 = 4 \text{ GeV}^2/c^2$, we find a best value of $b_\eta = 0.55$.

⁷When making such comparisons between inclusive and exclusive measurements, one must realize that there is a fairly large uncertainty associated the subtraction of the nonresonant background from inclusive data. In addition, we are neglecting unitarity and the resulting 'cusp' effect that the threshold in one channel causes in another [Alt79]. It is in order to account for these effects that we assume an uncertainty of 10% in the inclusive measurement (the statistical uncertainties of the fit are $\approx 2\%$).

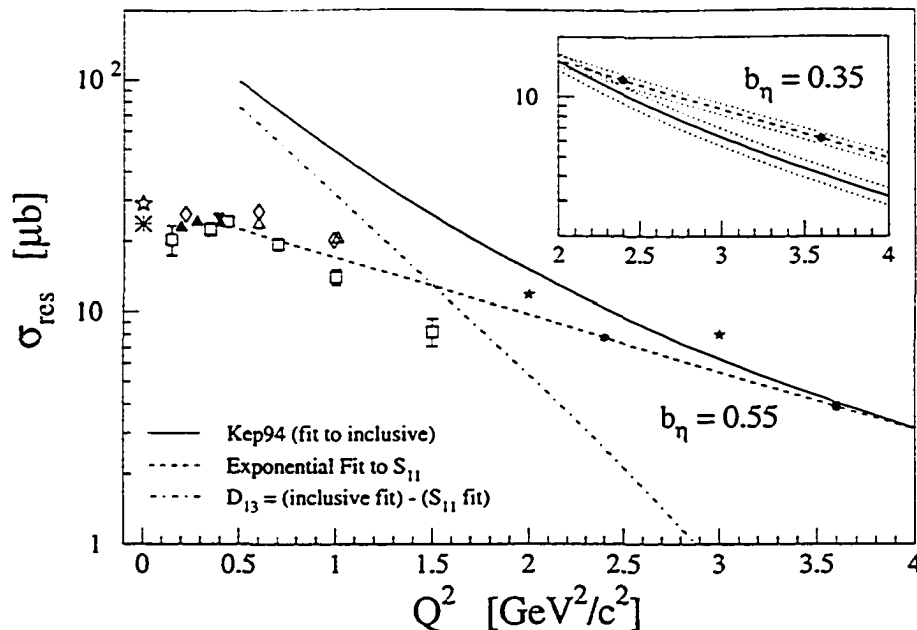


Figure 5.9: (Note log scale.) The main figure is a comparison between the resonant part of a fit to inclusive data in the second resonance region (solid line) and a fit to the two points of the present work (dashed line, see Fig. 5.6). Previous $ep \rightarrow e'p\eta$ data are shown as well, with data points and corresponding errors as in Fig. 5.7. The dashed-dotted curve (D_{13}) is the difference between the inclusive and S_{11} fits. Note the good agreement between inclusive and S_{11} (1535) fits for $b_\eta = 0.55$.

The inset is a close-up of the high- Q^2 region, showing the inclusive and S_{11} fits, but here we have assumed $b_\eta = 0.35$ (both fits are shown with error bands). This assumption puts the S_{11} several σ above the inclusive fit, which is strong evidence that the branching fraction is not this low.

5.4 Conclusions

The data presented here are of high precision and have greater statistics than any previous measurement of the $ep \rightarrow e'p\eta$ process at substantial momentum transfer; in addition, the $Q^2 = 3.6 \text{ GeV}^2/c^2$ point is the highest- Q^2 measurement of this process to date. The dominance of S -wave multipoles is confirmed and, as would be expected from previous measurements, the presence of other multipole terms is excluded down to about the 5% level.

The recent $ep \rightarrow e'p\eta$ photoproduction measurement at Mainz [Kru95] did a superb job of mapping out the energy dependence of this process up to the resonance mass, and their experimental technique precluded the need for a large background subtraction. That result, which is quite convincing, indicates a full width $\Gamma_R = (203 \pm 35) \text{ MeV}$. The energy dependence that we measure for this process bolsters the considerable evidence that the S_{11} has a full width in the range of 150

to 200 MeV (Fig. 5.4). Our data go well above the resonance mass and thus add useful information to the existing knowledge base; our analysis puts the full width at $\Gamma_R = (154 \pm 20)$ MeV. Of special note is the fact that our energy dependence is in serious disagreement with that of Ref. [Bra84] (which was, from an experimental point of view, similar to the present measurement). The results of that analysis yielded a full width for the S_{11} of less than 70 MeV—half that measured in the present work, and roughly one-third that claimed by the Mainz collaboration. The form of the Breit-Wigner parameterization used by the three groups is essentially the same, and so does not account for the differences in Γ_R .

More importantly, the new data improve our knowledge of the Q^2 evolution of the $S_{11}(1535)$ cross section and helicity amplitude $A_{1/2}^p$. While there is no doubt that the form factor of this resonance is stiff (strong at high Q^2) when compared to, say, the $D_{13}(1520)$, our data indicate a cross section about 30 % lower at $Q^2 = 3 \text{ GeV}^2/c^2$ than that of the only other high- Q^2 exclusive measurement (Ref. [Bra84]) (Fig. 5.6).

Some recent relativized versions of the CQM indicate a greater S_{11} amplitude at high Q^2 than does the NRCQM (Fig. 5.7). Even given the lower amplitude obtained from this measurement, however, the quark models consistently fail to reproduce the Q^2 dependence seen experimentally. While some of the newer variants indicate an amplitude at $Q^2 \sim 3 \text{ GeV}^2/c^2$ roughly consistent with experimental data, they also predict excess amplitude at lower Q^2 . As pointed out elsewhere [Ben96], the present situation clearly calls for continued work on nonperturbative QCD lattice calculations.

In part, the present work was intended as a search for scaling of the quantity $Q^3 A_{1/2}^p$, which could be a sign of the effects of pQCD. We see no strong evidence that this quantity is approaching a constant, but our data exhibit a markedly different trend than that of Ref. [Bra84] (Fig. 5.8), and would be consistent with an approach to scaling by $Q^2 \sim 5 \text{ GeV}^2/c^2$.

Comparison of these new data to recent inclusive data provides a constraint on the branching fraction of the S_{11} to the $p\eta$ decay channel, which is poorly known. The comparison offers strong evidence that a branching fraction near the low end of the $0.30 \leq b_\eta \leq 0.55$ range currently given by the PDG is unlikely (Fig. 5.9). We find a lower bound of $b_\eta = 0.45$.

We emphasize again that an analysis of the angular distributions presented here should ultimately be undertaken in the framework of a more complete physics model. Such a model would

take into account not only realistic background terms but would also include possible contributions from other resonances. While the results should not differ greatly from those presented here (because of the extent of the S -wave dominance), there is no doubt that our (energy independent) analysis is overly simplistic.

Several avenues of future experimental investigation promise to shed light on these and related topics. It is clear that the full value of this and other exclusive measurements of the $ep \rightarrow e'p\eta$ and $ep \rightarrow e'N\pi$ processes will only be realized once the full width and branching fractions of the $S_{11}(1535)$ are more precisely known. Only with these constraints will experimental results be able to make conclusive statements about the validity of theoretical $A_{1/2}^p$ predictions.

Polarization observables offer an exciting opportunity (especially at low Q^2) to gain insight into the structure of this resonance and to unravel the contributions of other resonances to the $p\eta$ channel. At least one such experiment now approved at TJNAF [Kel97] should obtain a fairly precise measurement of the longitudinal-to-transverse ratio R for the S_{11} . Finally, we point out that an extension [Sto97] of the present experiment to $Q^2 \approx 7 \text{ GeV}^2/c^2$ has been approved, and should run within a few years of this writing. The upcoming experiment will also (like the present work) measure the $\Delta(1232)$ via the $p\pi^0$ channel.

Appendix A

Beam Current Measurement in Hall C

There were four current measurement devices in use in Hall C around the time of this experiment. The first was a parametric current transformer (Unser monitor) and the other three were resonant-cavity Beam Current Monitors (BCM1, BCM2, and BCM3). The Unser monitor and the first two BCM cavities were on the beamline between the final arc and the Hall C target (see Fig 2.5 on page 40), while most of the associated electronics were upstairs in the Hall C electronics room. BCM3, positioned immediately upstream of the target, was a cavity used by the accelerator division's beam accounting system. While Hall C personnel did not have control of the hardware associated with this monitor, we were able to record the output of this device.

As discussed in Chapter 4, the beam charge for this experiment was measured using BCM3. At various times during the experiment BCM1 and BCM2 experienced unacceptable drifts (the causes of which were later discovered), and the output of these monitors was not used in the analysis. Therefore this Appendix has limited applicability to the present work. We offer it here partly for historical purposes, since the hardware (save minor modifications) and techniques were common to all TJNAF Hall C experiments from commissioning in 1995 through early 1997.

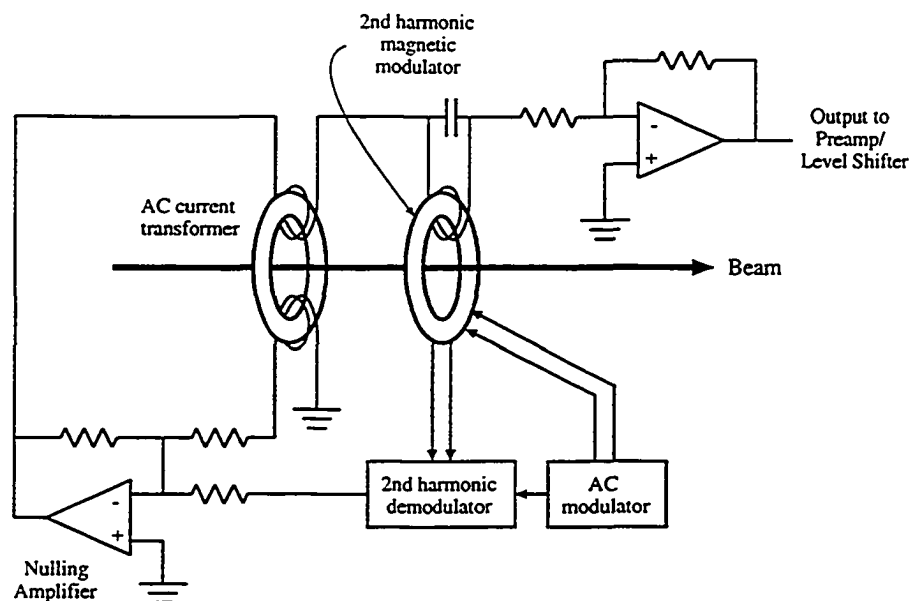


Figure A.1: A block diagram of the Unser monitor and associated electronics. The magnetic modulator in particular is oversimplified; the actual device consisted of several individual toroids.

A.1 The Unser Monitor

The Unser monitor consisted of two separate transformers in the feedback loop of a nulling amplifier, with the electron beam itself serving as the single-turn primary for both transformers (see Fig. A.1). The first transformer acted as a simple beam toroid, which could respond to transient beam conditions but not to CW beam. The second transformer (the modulation transformer) extended the frequency response of the device down to direct current (DC). An alternating current (AC) signal drove the modulation transformer into saturation at either end of its hysteresis loop. As long as the DC magnetic flux in the transformer was zero, the hysteresis loop was symmetric: there was no second-order harmonic in the voltage at the secondary. When beam with DC current i was present, the nulling circuit minimized the second harmonic of the secondary by forcing current $-i$ through the nulling winding.¹ This nulling gave the Unser monitor excellent linearity.

The Unser electronics supplied an analog signal which was input to a preamplifier/level shifter and then to a Voltage-to-Frequency (V-F) converter. The preamplifier had a gain of 10 to reduce the effects of drifts in the downstream electronics. The voltage offset provided by the level shifter ensured that the input to the V-F converter was in the linear region of that device. The output

¹The reader interested in the details of the Unser monitor design is referred to Ref. [Uns91].

of the V-F converter was fed to a scaler whose output was read by the data acquisition system every two seconds. This V-F/scaler scheme allowed convenient data acquisition, since we were ultimately interested in knowing the integrated charge (as opposed to the current on a short time scale).

The Unser monitor had a gain which was well known (about $4 \text{ mV}/\mu\text{A}$ for the Unser itself, about $4000 \text{ Hz}/\mu\text{A}$ for the entire system) and very stable. It did suffer from fairly small offset drifts which changed over the course of minutes (these drifts had been large, but prior to this experiment were improved by thermally insulating the Unser) as well as a poor signal-to-noise ratio. However, it was the only current monitor we had that could be accurately calibrated with absolute standards. Therefore the other current monitors were calibrated against the Unser (as described below).

The gain of the Unser was measured in November, 1996, midway through the present experiment. A precision DC voltage source and precision series resistors were used to supply current to a wire running through the Unser monitor, thereby simulating beam current. The scaler rates together with knowledge of the simulated beam current (measured independently) yielded for the Unser monitor and associated electronics a gain of $3.988 \pm 0.004 \text{ mV}/\mu\text{A}$.²

A.2 The Beam Current Monitors (BCM1 and BCM2)

The two other current measuring devices operated by measuring the radio-frequency (RF) power coupled out of resonant cavities in the beamline. These two BCM's had reasonable gain stability (over the course of a few days) and good noise performance. They could not measure current *absolutely*, however, because the ratio of output power to beam current through the cavity could be determined only by calculation or numerical simulation and was sensitive to details such as the quality of the surface finish on the interior of the cavity.

Every several days or so the well-known Unser gain was used to calibrate the BCM's. A calibration run consisted of alternating two-minute intervals of beam-on/beam-off (see Fig. A.2). The beam-off periods gave the zero offset of the Unser, and comparison of the Unser output to the BCM outputs during the beam-on periods yielded the BCM gains.

²A detailed account of the gain measurement procedure can be found in Ref. [Boc96].

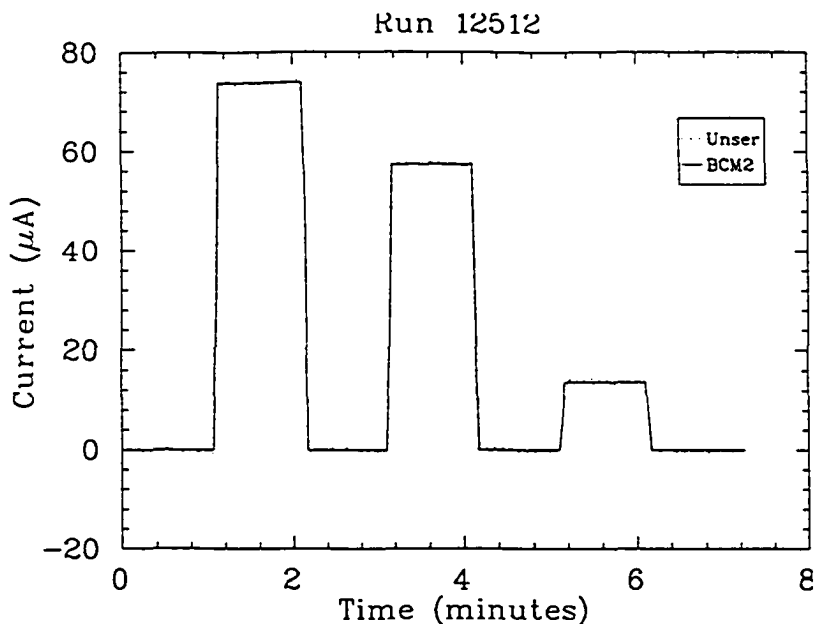


Figure A.2: Current (as reported by the Unser monitor and BCM2) versus time for a typical BCM calibration.

The RF cavities for the two BCM's were identical. They were simple (nonreentrant) cylinders constructed from #304 stainless steel positioned coaxially along the beamline. The 499 MHz time structure of the beam in the Hall C beamline excited the 1497 MHz TM_{010} mode of resonance, shown in Fig. A.3. This mode is suitable for current measurements because the electric field is radially symmetric and coupling to the beam was therefore relatively insensitive to beam position when that position was near the center of the cavity.

The quality factor of a resonant cavity is defined as $Q \equiv f_0/\Delta f$, where f_0 is the resonant frequency and Δf is the full-width at half-maximum of the resonance shape. For the TM_{010} mode in a cylindrical cavity, the resonant frequency is given by

$$f_0 = f_{010} = \frac{c}{2\pi R} \chi_{01} \quad (\text{A.1})$$

Here χ_{01} is the first root of the Bessel function J_0 and R is the radius of the cavity. At high frequencies the width Δf depends largely on the quality of the surface finish inside the cavity.

Q is, in other words, a measure of the sharpness (in frequency) of the cavity response to excitation. In addition, we must define the quality factor for two cases. The first is when the

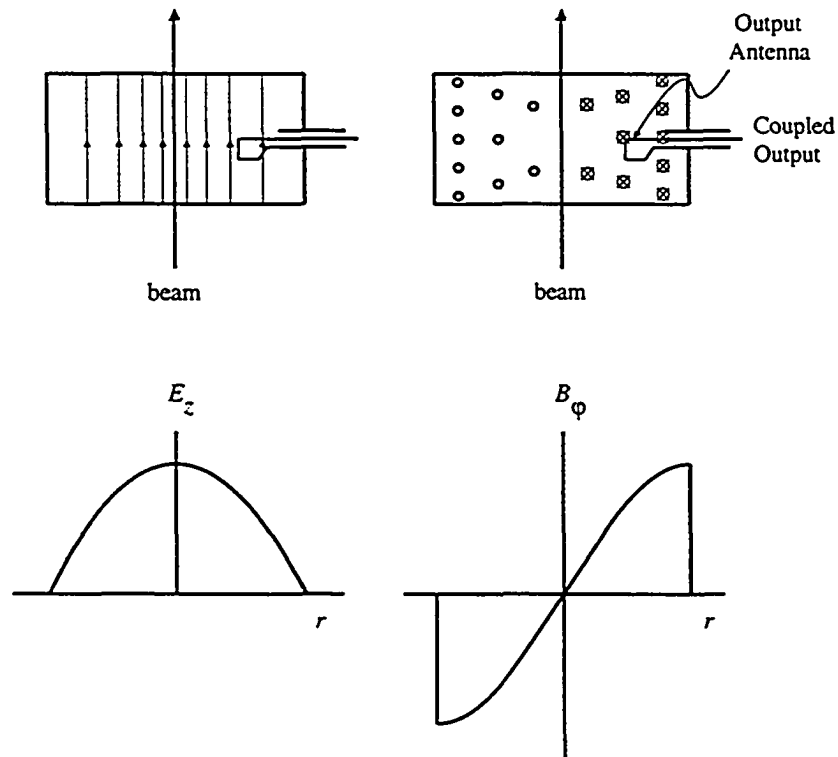


Figure A.3: Cross sections of a BCM cavity showing E_z and B_ϕ fields for the TM_{010} mode. The 'TM' stands for Transverse Magnetic, meaning that the magnetic field lines are *transverse* to the axis of the cavity (electric field lines *along* the axis). The '010' subscript means that the magnetic field variation is one-half cycle along a radial line from one side of the cylinder to the other (with no variations in the axial or circumferential directions). Note that the output antenna couples to the magnetic component of the resonance.

cavity has no output coupling, for which we have quality factor Q_0 . The second is when we have an antenna coupling power out of the cavity, for which we have *loaded* quality factor Q_l .

In a current monitor application, the power output is a maximum when $Q_l = Q_0/2$. The higher the Q_l , however, the more the output power depends on temperature if the cavity is not correctly tuned to the excitation frequency. The unloaded quality factor Q_0 of the BCM1 and BCM2 cavities was near 3000, while the loaded quality factor Q_l was nominally 500.³

A.3 The BCM Electronics

BCM1 and BCM2 employed a down-converter and an RMS-to-DC device to measure RF power coupled from the cavity (see Fig. A.4). The 1497 MHz signal from the cavity was mixed down to 100 kHz, filtered, and input to a precision RMS-to-DC chip, the Analog Devices AD637. Switchable gain preceded the AD637, which allowed us to keep the input signal level in the nominal operating range of the device for a wide range of beam currents. As with the Unser monitor, the analog output of the AD637 was input to a preamplifier/level shifter, a V-F converter, and finally to a scaler (which was read out by the data acquisition system every two seconds).

BCM3 employed electronics similar to those of BCM1 and BCM2. The major differences were a higher down-conversion frequency of 1 MHz, a lack of switchable gain, and the method used to read out the scaler.

A.4 Frequency Structure of the Hall C Beam

It is useful when dealing with the resonant cavities to look at a simple model of the frequency structure of the beam delivered to Hall C. We assume that the beam is composed of an infinite train of identical pulses (arriving at 499 MHz). First we note two properties of the Fourier Transform (FT):

1. $f(t + t_0) \iff F(\omega)e^{j\omega t_0}$ (time translation)
2. $af(t) + bg(t) \iff aF(\omega) + bG(\omega)$ (linearity)

³For complete specifications and a more thorough discussion of the operating principles of the BCM cavities, see Ref. [Nic96].

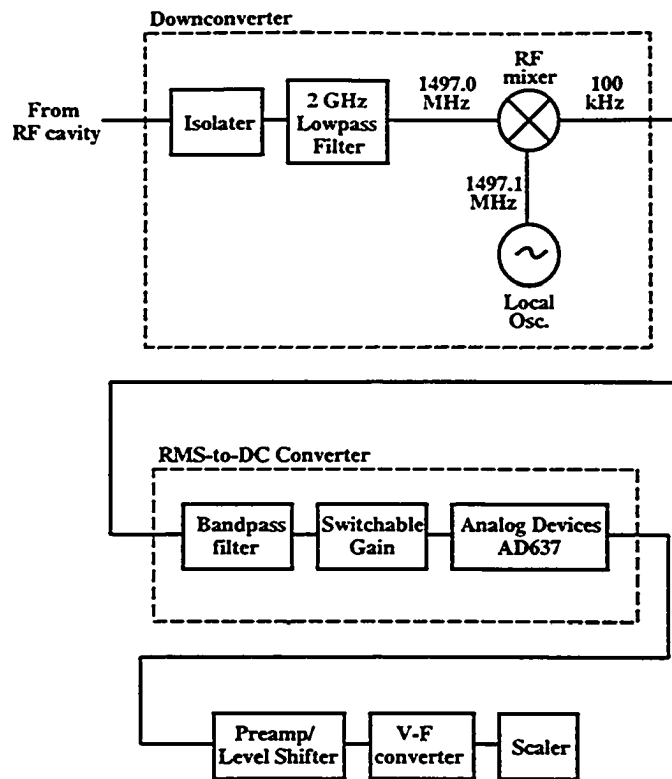


Figure A.4: A simplified schematic of the electronics used with BCM1 and BCM2.

Let each pulse in the train be described by the FT pair $f(t) \leftrightarrow F(\omega)$. Then in the time domain the pulse train is

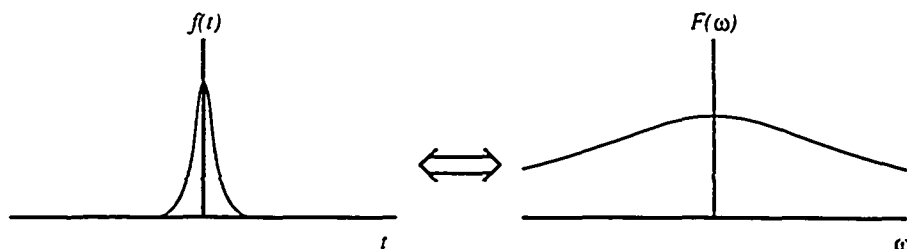
$$\begin{aligned} \text{train}(t) &= \sum_{n=-\infty}^{\infty} f(t + nt_0) \\ &= \dots + f(t - 2t_0) + f(t - t_0) + f(t) + f(t + t_0) + \dots \end{aligned}$$

whose FT (using properties 1 and 2) is

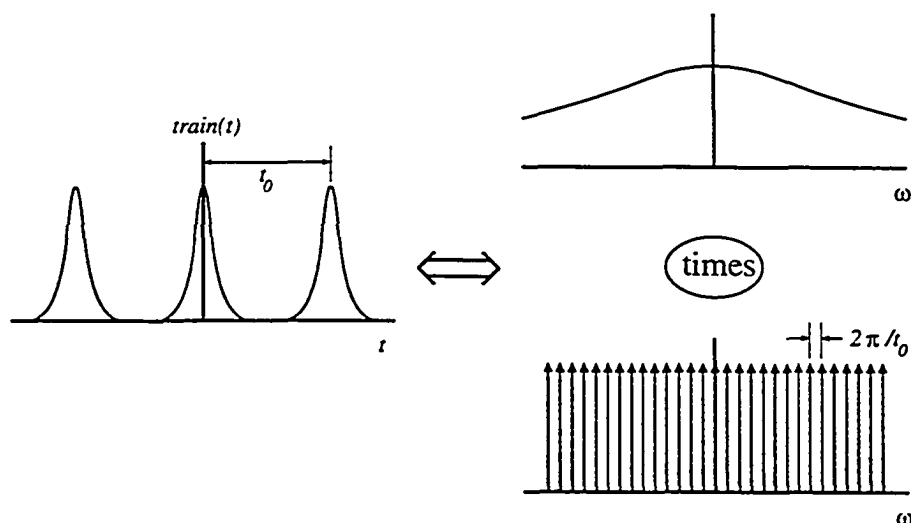
$$\begin{aligned} \text{Train}(\omega) &= \dots + F(\omega)e^{-j\omega 2t_0} + F(\omega)e^{-j\omega t_0} + F(\omega)e^{-j\omega 0} + F(\omega)e^{j\omega t_0} + \dots \\ &= F(\omega) \sum_{n=-\infty}^{\infty} e^{j\omega nt_0} \end{aligned}$$

The infinite sum is an infinite train of δ functions (in the ω domain) at $\omega = (2\pi/t_0)i$, where $i = -\infty, \dots, -1, 0, 1, \dots, \infty$. In other words, The FT of an infinite train of pulses (with

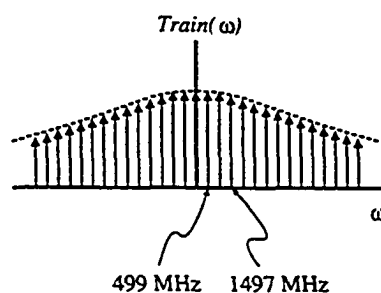
period t_0) each of form $f(t_0)$ is $F(\omega) \cdot$ [an infinite train of δ functions (with period $\omega = (2\pi)/t_0$)]. We may apply this to a simple model of the beam, modeling the individual beam pulse as a Gaussian (whose FT is also a Gaussian):



The FT of the infinite pulse train is then the FT of the individual pulse multiplied by a train of delta functions:



And the end result in the frequency domain is



Thus while the normal 'chopped' beam into Hall C was 499 MHz, the resonant cavity was excited by the third harmonic at 1497 MHz.

Note that since the Gaussian beam pulse (in the time domain) would have a duration on the order of a few picoseconds, the Gaussian envelope of the δ functions (in the frequency domain) would be *very* wide (on the order of several *hundred* GHz). For all practical purposes, the magnitude of the 1497 MHz third harmonic was the same as that of the 499 MHz fundamental. Therefore, operation of the BCM's was the same with 'chopped' 499 MHz beam as it would have been with 'unchopped' 1497 MHz structure.

Appendix B

Optimization of Reconstruction Matrix Elements

Optimization of the matrix elements M_{jklm} for each reconstructed quantity X_{tar} of each spectrometer was done using stand-alone code. Reconstruction of each quantity (δ , y_{tar} , x'_{tar} , and y'_{tar}) was optimized individually, with iteration over all four quantities as necessary.

For any of the four quantities the optimization involved several steps, utilizing data taken during previous experiments and later checked using similar data taken during the present experiment. An initial set of matrix elements was obtained from a COSY model of the spectrometer's magnetic elements. The resulting reconstructed quantities were then compared with known values, and the difference between the two minimized by varying the matrix elements.

In the case of the two slopes x'_{tar} and y'_{tar} , reconstruction was optimized using sieve slit data.¹ For a fixed z target position the data were mapped (on an event-by-event basis)

1. from the midplane of the drift chambers to the true optical focal plane via a drift and rotation;
2. from the optical focal plane back to the target using Eq. 4.3 on page 88 (which yielded reconstructed target quantities);

¹Sieve slit data was taken with a special sieve collimator (a collimator with many small holes) preceding the spectrometer and using a thin slanted carbon target whose z position along the beamline was controlled. Target position scans, or 'z scans', were obtained by changing the effective z position of the slanted carbon target. 'delta scans' were obtained by changing the central momentum of the spectrometer, allowing the quasielastic carbon peak to step across the focal plane.

3. from the target back to the sieve slit via a drift.

If the difference between the reconstructed position at the sieve and the center of an actual sieve hole was less than the radius of the hole, the event was assumed to have passed through that hole. Those events for which a successful hole assignment had been made were then used to find matrix elements that minimized the difference between the reconstructed target angles and the known angles through the center of the corresponding sieve holes.² A portion of the sieve data was reserved for checking the results of the fit.

After an initial fit was completed for the central target position $z = 0$, the sieve runs for other target positions were added to the initial data set and the procedure repeated. For every event the z position was known, and the matrix elements contributing to y_{tar} were optimized by minimizing the difference between reconstructed and actual y_{tar} . After reasonable fits to x'_{tar} , y'_{tar} , and y_{tar} were obtained, the optimization process was applied in similar fashion to the data sets at different δ . Here again the matrix elements were optimized by minimizing the difference between reconstructed and actual δ . The entire procedure was iterated until the matrix elements converged (see Figs. B.1 and B.2). At that point, focal plane quantities for ${}^1\text{H}(e, e')p$ data were checked to ensure that they exhibited no dependence on W^2 .

Once the fits of the matrix elements M_{jklm} for the individual spectrometers were satisfactory, the constraints imposed by the known solid target and sieve slit positions, together with ${}^1\text{H}(e, e')p$ and ${}^1\text{H}(e, e'p)$ data taken during this experiment, were used to determine zeroth-order matrix elements (*i.e.*, the offsets x_0 and similar of Eq. 4.3 on page 88).³ The general procedure was to

1. Fix y'_{tar} and x'_{tar} offsets of the SOS to about the 1 mrad level using the known sieve position.
2. Adjust SOS and HMS y_{tar} offsets so that the reconstructed positions reflected known position of the cryogenic target.
3. Adjust the SOS momentum and y'_{tar} offsets together with the beam energy in order to find the best match to the Monte Carlo δ and y'_{tar} distributions and the most robust reproduction

²The technique used to optimize the matrix elements was that of singular value decomposition. The treatment given here is somewhat simplified; a more thorough discussion of the technique and the software used to perform it are available in Ref. [Ass97].

³The offsets in focal plane quantities were in general a function of not only the spectrometers themselves but also the position of the beam on the target. For this reason, these offsets were determined using data taken during this experiment.

of $W = m_p$ and $|k_f| - |k_{f,\text{calc}}| = 0$ over all available ${}^1\text{H}(e, e')p$ data. Here $|k_{f,\text{calc}}| = E [1 + (2E/m_p) \sin^2(\theta_e/2)]^{-1}$, the momentum of the elastically scattered electron as calculated from its scattering angle.

4. Adjust the x'_{tar} offset of the HMS to center the out-of-plane component of missing momentum for ${}^1\text{H}(e, e')p$.
5. Adjust the y'_{tar} offset of the HMS to correctly reconstruct the scattering angle of the proton in ${}^1\text{H}(e, e')p$ as calculated from the scattering angle of the elastic electron.
6. Adjust the momentum offset of the HMS to correctly reconstruct the momentum of the proton in ${}^1\text{H}(e, e')p$ as calculated from the scattering angle of the elastic electron.

In all cases, the adjustments to zeroth-order matrix elements were within the expected uncertainties of the quantity in question.

For ${}^1\text{H}(e, e')p$ scattering, the three-momentum transfer \mathbf{q} (calculated from electron spectrometer and beam quantities) and the three-momentum \mathbf{p}_f of the outgoing proton (measured by the proton spectrometer) should lie in the same direction.⁴ Fig. B.3 shows the distribution of θ_{pq} , the angle between \mathbf{q} and \mathbf{p}_f , summed over three elastic settings covering much of the spectrometer phase space populated by the resonance data in this experiment. The narrow distribution (zero is excluded by vanishing phase space) is indicative of the quality of the reconstruction and the good angular agreement between the spectrometers.

⁴This is strictly true only in the absence of Bremsstrahlung, which we approximate by considering only those events for which $W \approx m_p$.

SOS Sieve Reconstruction

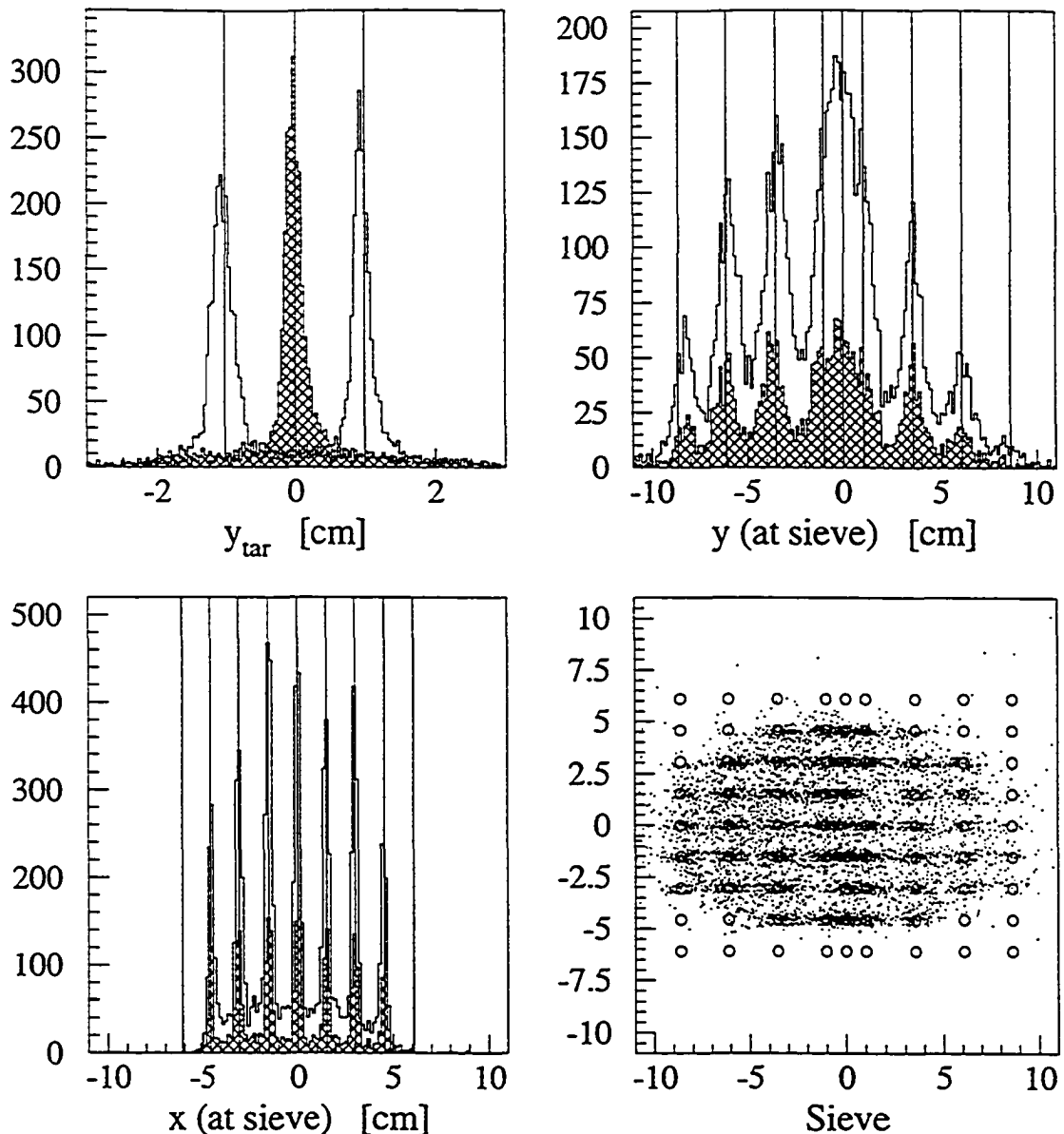


Figure B.1: SOS y_{tar} and sieve slit reconstruction. *Upper Left*) Reconstructed y_{tar} . Three runs are shown, each using a different solid target position along the beamline ($z_{tar} = -2, 0,$ and 2 cm, corresponding to $y_{tar} = -1, 0,$ and 1 cm, indicated by lines). *Upper Right*) Reconstructed y'_{tar} (in-plane slope) projected to the sieve slit. The lines indicate the hole positions. The filled histogram is that of the $y_{tar} = 0$ run, while the unfilled is the sum of all three runs. *Lower Left*) Reconstructed x'_{tar} (out-of-plane slope) projected to the sieve slit. The lines indicate the hole positions. Filled and unfilled histograms are the same as in the previous plot. *Lower Right*) Reconstructed x'_{tar} versus y'_{tar} , projected to the sieve, showing the sieve hole pattern. For orientation purposes, two of the off-center hole positions actually have no holes, and the central hole is half the diameter of the other holes.

HMS Sieve Reconstruction

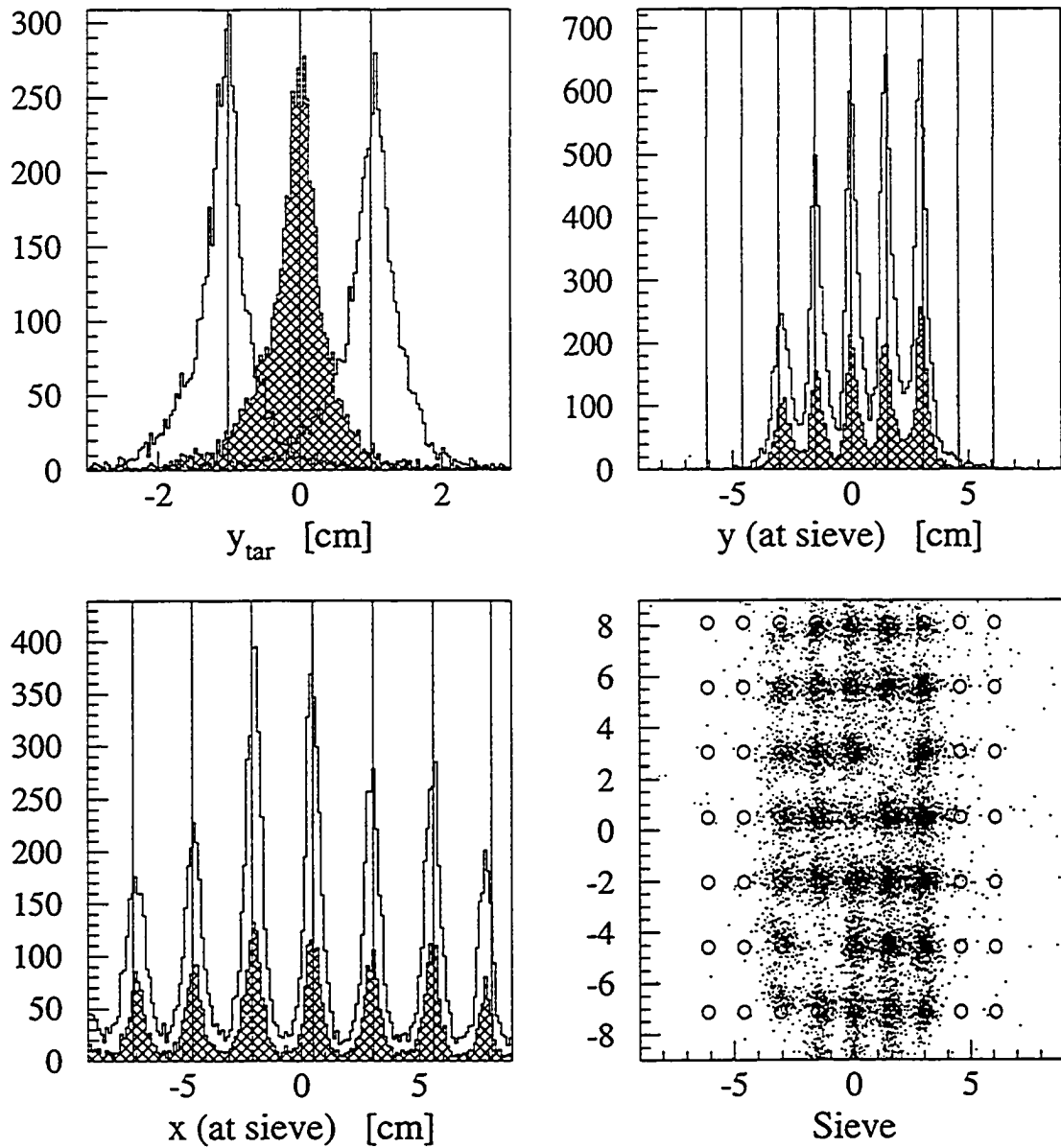


Figure B.2: HMS y_{tar} and sieve slit reconstruction. The four histograms are the same as those in Fig. B.1.

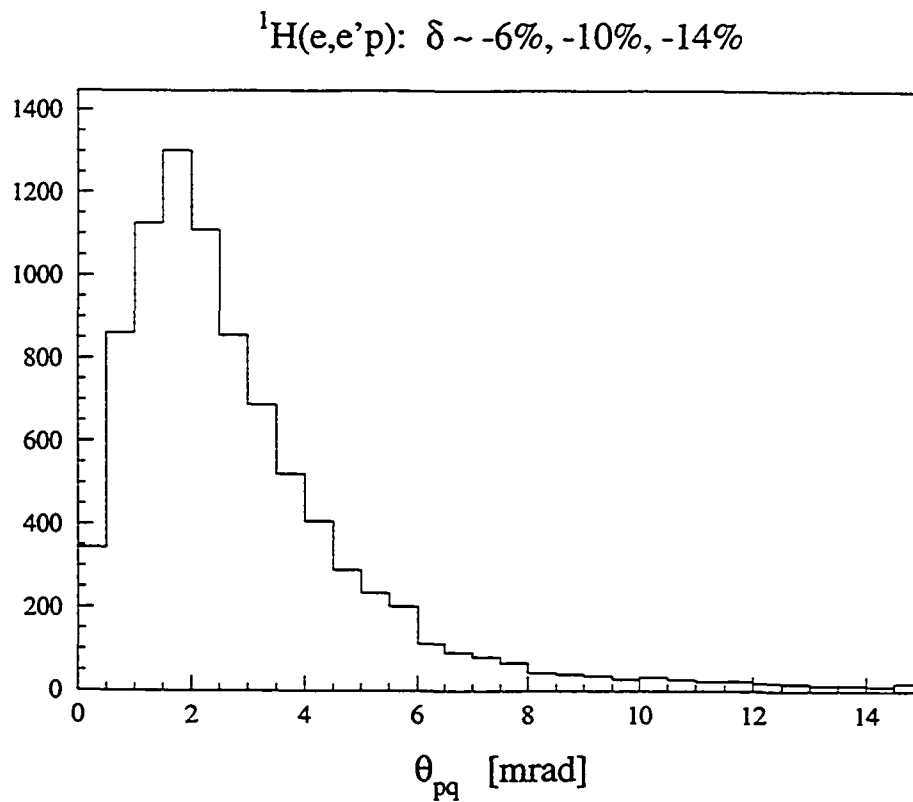


Figure B.3: The distribution of θ_{pq} summed over three ${}^1\text{H}(e, e'p)$ settings.

Appendix C

Tabulated Cross Section Data

The differential cross section data are given below. The data are also available in electronic form upon request from Jefferson Lab (contact Chris Armstrong, csa@jlab.org, or the Jefferson Lab User Liaison office). The data include the correction to the nominal Q^2 value (see Section 4.3.9). Entries containing zeros for the cross section and for the corresponding errors are those without experimental coverage, and must be handled appropriately when performing fits to the data. Both the statistical and systematic uncertainties are absolute (not fractional).

$$Q^2 = 2.4 \text{ GeV}^2/c^2$$

W [GeV]	$\cos \theta_\eta^*$	ϕ_η [deg.]	ϵ	$\frac{d^2\sigma}{d\Omega_\eta}$ [$\frac{\mu\text{b}}{\text{sr}}$]	stat err [σ]	syst err [σ]
1.490	-.90	-150.0	.515	.186	.023	.026
1.490	-.90	-90.0	.517	.188	.022	.027
1.490	-.90	-30.0	.515	.148	.021	.021
1.490	-.90	30.0	.511	.136	.019	.019
1.490	-.90	90.0	.516	.125	.016	.018
1.490	-.90	150.0	.515	.184	.023	.026
1.490	-.70	-150.0	.520	.156	.024	.022
1.490	-.70	-90.0	.512	.140	.021	.020
1.490	-.70	-30.0	.509	.181	.027	.026
1.490	-.70	30.0	.514	.214	.028	.030
1.490	-.70	90.0	.514	.140	.022	.020
1.490	-.70	150.0	.514	.184	.023	.026
1.490	-.50	-150.0	.512	.181	.023	.025
1.490	-.50	-90.0	.513	.162	.023	.023
1.490	-.50	-30.0	.509	.179	.025	.025

1.490	-.50	30.0	.510	.163	.025	.023
1.490	-.50	90.0	.516	.196	.025	.028
1.490	-.50	150.0	.514	.170	.022	.024
1.490	-.30	-150.0	.513	.123	.016	.017
1.490	-.30	-90.0	.510	.145	.022	.020
1.490	-.30	-30.0	.514	.179	.021	.025
1.490	-.30	30.0	.517	.190	.025	.027
1.490	-.30	90.0	.516	.149	.021	.021
1.490	-.30	150.0	.514	.172	.021	.024
1.490	-.10	-150.0	.515	.133	.019	.019
1.490	-.10	-90.0	.515	.193	.028	.027
1.490	-.10	-30.0	.513	.151	.019	.021
1.490	-.10	30.0	.511	.179	.021	.025
1.490	-.10	90.0	.512	.190	.029	.027
1.490	-.10	150.0	.511	.139	.018	.020
1.490	.10	-150.0	.515	.145	.023	.020
1.490	.10	-90.0	.514	.198	.036	.028
1.490	.10	-30.0	.514	.155	.022	.022
1.490	.10	30.0	.516	.175	.027	.025
1.490	.10	90.0	.510	.189	.032	.027
1.490	.10	150.0	.514	.131	.021	.018
1.490	.30	-150.0	.514	.153	.027	.022
1.490	.30	-90.0	.512	.162	.041	.023
1.490	.30	-30.0	.516	.120	.024	.017
1.490	.30	30.0	.512	.152	.025	.021
1.490	.30	90.0	.515	.109	.030	.015
1.490	.30	150.0	.516	.189	.034	.027
1.490	.50	-150.0	.516	.170	.030	.024
1.490	.50	-90.0	.515	.165	.037	.023
1.490	.50	-30.0	.515	.175	.028	.025
1.490	.50	30.0	.512	.149	.026	.021
1.490	.50	90.0	.512	.179	.038	.025
1.490	.50	150.0	.517	.175	.034	.025
1.490	.70	-150.0	.507	.172	.029	.024
1.490	.70	-90.0	.519	.149	.029	.021
1.490	.70	-30.0	.516	.143	.023	.020
1.490	.70	30.0	.515	.153	.029	.022
1.490	.70	90.0	.511	.153	.033	.022
1.490	.70	150.0	.517	.178	.031	.025
1.490	.90	-150.0	.518	.164	.028	.023
1.490	.90	-90.0	.514	.168	.029	.024
1.490	.90	-30.0	.512	.170	.027	.024
1.490	.90	30.0	.520	.160	.026	.023
1.490	.90	90.0	.510	.130	.025	.018
1.490	.90	150.0	.511	.119	.022	.017
1.515	-.90	-150.0	.512	.356	.029	.017
1.515	-.90	-90.0	.513	.350	.025	.017
1.515	-.90	-30.0	.513	.312	.022	.015
1.515	-.90	30.0	.512	.371	.026	.018
1.515	-.90	90.0	.513	.292	.023	.014
1.515	-.90	150.0	.512	.330	.028	.016
1.515	-.70	-150.0	.513	.332	.025	.016
1.515	-.70	-90.0	.514	.259	.027	.013
1.515	-.70	-30.0	.512	.311	.023	.015
1.515	-.70	30.0	.512	.362	.026	.018

1.515	-.70	90.0	.512	.287	.027	.014
1.515	-.70	150.0	.511	.349	.025	.017
1.515	-.50	-150.0	.512	.311	.028	.015
1.515	-.50	-90.0	.000	.000	.000	.000
1.515	-.50	-30.0	.513	.339	.030	.017
1.515	-.50	30.0	.515	.378	.034	.018
1.515	-.50	90.0	.515	.392	.051	.019
1.515	-.50	150.0	.515	.355	.029	.017
1.515	-.30	-150.0	.513	.327	.028	.016
1.515	-.30	-90.0	.000	.000	.000	.000
1.515	-.30	-30.0	.514	.348	.030	.017
1.515	-.30	30.0	.515	.376	.033	.018
1.515	-.30	90.0	.000	.000	.000	.000
1.515	-.30	150.0	.510	.341	.028	.017
1.515	-.10	-150.0	.511	.350	.031	.017
1.515	-.10	-90.0	.000	.000	.000	.000
1.515	-.10	-30.0	.515	.343	.028	.017
1.515	-.10	30.0	.514	.375	.030	.018
1.515	-.10	90.0	.000	.000	.000	.000
1.515	-.10	150.0	.513	.323	.028	.016
1.515	.10	-150.0	.514	.298	.034	.015
1.515	.10	-90.0	.000	.000	.000	.000
1.515	.10	-30.0	.512	.285	.029	.014
1.515	.10	30.0	.513	.385	.037	.019
1.515	.10	90.0	.000	.000	.000	.000
1.515	.10	150.0	.515	.401	.045	.020
1.515	.30	-150.0	.512	.317	.042	.015
1.515	.30	-90.0	.000	.000	.000	.000
1.515	.30	-30.0	.508	.332	.040	.016
1.515	.30	30.0	.511	.339	.040	.016
1.515	.30	90.0	.000	.000	.000	.000
1.515	.30	150.0	.511	.264	.041	.013
1.515	.50	-150.0	.513	.309	.037	.015
1.515	.50	-90.0	.000	.000	.000	.000
1.515	.50	-30.0	.512	.373	.036	.018
1.515	.50	30.0	.511	.319	.032	.016
1.515	.50	90.0	.000	.000	.000	.000
1.515	.50	150.0	.512	.369	.042	.018
1.515	.70	-150.0	.515	.271	.042	.013
1.515	.70	-90.0	.507	.430	.105	.021
1.515	.70	-30.0	.517	.348	.046	.017
1.515	.70	30.0	.515	.367	.048	.018
1.515	.70	90.0	.512	.435	.082	.021
1.515	.70	150.0	.515	.429	.051	.021
1.515	.90	-150.0	.512	.389	.047	.019
1.515	.90	-90.0	.513	.398	.053	.019
1.515	.90	-30.0	.513	.296	.040	.014
1.515	.90	30.0	.512	.348	.043	.017
1.515	.90	90.0	.514	.244	.038	.012
1.515	.90	150.0	.512	.287	.039	.014
1.540	-.90	-150.0	.513	.408	.038	.028
1.540	-.90	-90.0	.511	.317	.031	.021
1.540	-.90	-30.0	.511	.312	.026	.021
1.540	-.90	30.0	.509	.356	.029	.024
1.540	-.90	90.0	.508	.315	.031	.021

1.540	-.90	150.0	.512	.336	.033	.023
1.540	-.70	-150.0	.511	.311	.024	.021
1.540	-.70	-90.0	.000	.000	.000	.000
1.540	-.70	-30.0	.507	.373	.025	.025
1.540	-.70	30.0	.512	.342	.024	.023
1.540	-.70	90.0	.000	.000	.000	.000
1.540	-.70	150.0	.510	.339	.025	.023
1.540	-.50	-150.0	.509	.353	.036	.024
1.540	-.50	-90.0	.000	.000	.000	.000
1.540	-.50	-30.0	.509	.394	.029	.027
1.540	-.50	30.0	.510	.326	.026	.022
1.540	-.50	90.0	.000	.000	.000	.000
1.540	-.50	150.0	.507	.306	.028	.021
1.540	-.30	-150.0	.509	.330	.042	.022
1.540	-.30	-90.0	.000	.000	.000	.000
1.540	-.30	-30.0	.510	.367	.035	.025
1.540	-.30	30.0	.509	.450	.038	.030
1.540	-.30	90.0	.000	.000	.000	.000
1.540	-.30	150.0	.508	.362	.044	.024
1.540	-.10	-150.0	.515	.303	.046	.020
1.540	-.10	-90.0	.000	.000	.000	.000
1.540	-.10	-30.0	.508	.314	.030	.021
1.540	-.10	30.0	.513	.360	.033	.024
1.540	-.10	90.0	.000	.000	.000	.000
1.540	-.10	150.0	.515	.313	.045	.021
1.540	.10	-150.0	.000	.000	.000	.000
1.540	.10	-90.0	.000	.000	.000	.000
1.540	.10	-30.0	.509	.351	.038	.024
1.540	.10	30.0	.511	.404	.042	.027
1.540	.10	90.0	.000	.000	.000	.000
1.540	.10	150.0	.510	.354	.080	.024
1.540	.30	-150.0	.000	.000	.000	.000
1.540	.30	-90.0	.000	.000	.000	.000
1.540	.30	-30.0	.511	.334	.048	.023
1.540	.30	30.0	.510	.307	.043	.021
1.540	.30	90.0	.000	.000	.000	.000
1.540	.30	150.0	.000	.000	.000	.000
1.540	.50	-150.0	.514	.194	.084	.013
1.540	.50	-90.0	.000	.000	.000	.000
1.540	.50	-30.0	.508	.361	.066	.024
1.540	.50	30.0	.512	.330	.064	.022
1.540	.50	90.0	.000	.000	.000	.000
1.540	.50	150.0	.516	.377	.099	.025
1.540	.70	-150.0	.509	.325	.082	.022
1.540	.70	-90.0	.000	.000	.000	.000
1.540	.70	-30.0	.512	.299	.056	.020
1.540	.70	30.0	.510	.340	.063	.023
1.540	.70	90.0	.000	.000	.000	.000
1.540	.70	150.0	.512	.343	.078	.023
1.540	.90	-150.0	.504	.355	.072	.024
1.540	.90	-90.0	.000	.000	.000	.000
1.540	.90	-30.0	.504	.266	.061	.018
1.540	.90	30.0	.504	.324	.060	.022
1.540	.90	90.0	.000	.000	.000	.000
1.540	.90	150.0	.506	.286	.060	.019

1.565	-.90	-150.0	.507	.260	.022	.018
1.565	-.90	-90.0	.505	.198	.021	.014
1.565	-.90	-30.0	.508	.239	.019	.017
1.565	-.90	30.0	.505	.291	.021	.020
1.565	-.90	90.0	.507	.239	.024	.017
1.565	-.90	150.0	.506	.286	.021	.020
1.565	-.70	-150.0	.506	.310	.042	.021
1.565	-.70	-90.0	.000	.000	.000	.000
1.565	-.70	-30.0	.506	.314	.030	.022
1.565	-.70	30.0	.505	.273	.027	.019
1.565	-.70	90.0	.000	.000	.000	.000
1.565	-.70	150.0	.508	.232	.027	.016
1.565	-.50	-150.0	.511	.280	.040	.019
1.565	-.50	-90.0	.000	.000	.000	.000
1.565	-.50	-30.0	.506	.337	.029	.023
1.565	-.50	30.0	.509	.267	.024	.018
1.565	-.50	90.0	.000	.000	.000	.000
1.565	-.50	150.0	.509	.254	.035	.018
1.565	-.30	-150.0	.000	.000	.000	.000
1.565	-.30	-90.0	.000	.000	.000	.000
1.565	-.30	-30.0	.507	.313	.036	.022
1.565	-.30	30.0	.506	.379	.040	.026
1.565	-.30	90.0	.000	.000	.000	.000
1.565	-.30	150.0	.000	.000	.000	.000
1.565	-.10	-150.0	.000	.000	.000	.000
1.565	-.10	-90.0	.000	.000	.000	.000
1.565	-.10	-30.0	.507	.249	.029	.017
1.565	-.10	30.0	.506	.311	.034	.021
1.565	-.10	90.0	.000	.000	.000	.000
1.565	-.10	150.0	.000	.000	.000	.000
1.565	.10	-150.0	.000	.000	.000	.000
1.565	.10	-90.0	.000	.000	.000	.000
1.565	.10	-30.0	.503	.310	.047	.021
1.565	.10	30.0	.507	.285	.042	.020
1.565	.10	90.0	.000	.000	.000	.000
1.565	.10	150.0	.000	.000	.000	.000
1.565	.30	-150.0	.000	.000	.000	.000
1.565	.30	-90.0	.000	.000	.000	.000
1.565	.30	-30.0	.502	.240	.050	.017
1.565	.30	30.0	.506	.275	.051	.019
1.565	.30	90.0	.000	.000	.000	.000
1.565	.30	150.0	.000	.000	.000	.000
1.565	.50	-150.0	.000	.000	.000	.000
1.565	.50	-90.0	.000	.000	.000	.000
1.565	.50	-30.0	.000	.000	.000	.000
1.565	.50	30.0	.000	.000	.000	.000
1.565	.50	90.0	.000	.000	.000	.000
1.565	.50	150.0	.000	.000	.000	.000
1.565	.70	-150.0	.000	.000	.000	.000
1.565	.70	-90.0	.000	.000	.000	.000
1.565	.70	-30.0	.000	.000	.000	.000
1.565	.70	30.0	.503	.309	.087	.021
1.565	.70	90.0	.000	.000	.000	.000
1.565	.70	150.0	.000	.000	.000	.000
1.565	.90	-150.0	.000	.000	.000	.000

1.565	.90	-90.0	.000	.000	.000	.000
1.565	.90	-30.0	.000	.000	.000	.000
1.565	.90	30.0	.000	.000	.000	.000
1.565	.90	90.0	.000	.000	.000	.000
1.565	.90	150.0	.000	.000	.000	.000
1.590	-.90	-150.0	.504	.200	.019	.016
1.590	-.90	-90.0	.507	.182	.023	.015
1.590	-.90	-30.0	.505	.177	.015	.014
1.590	-.90	30.0	.507	.226	.017	.018
1.590	-.90	90.0	.503	.203	.024	.016
1.590	-.90	150.0	.504	.198	.018	.016
1.590	-.70	-150.0	.507	.195	.037	.016
1.590	-.70	-90.0	.000	.000	.000	.000
1.590	-.70	-30.0	.510	.210	.026	.017
1.590	-.70	30.0	.504	.214	.025	.017
1.590	-.70	90.0	.000	.000	.000	.000
1.590	-.70	150.0	.506	.236	.039	.019
1.590	-.50	-150.0	.000	.000	.000	.000
1.590	-.50	-90.0	.000	.000	.000	.000
1.590	-.50	-30.0	.501	.298	.033	.024
1.590	-.50	30.0	.504	.236	.027	.019
1.590	-.50	90.0	.000	.000	.000	.000
1.590	-.50	150.0	.000	.000	.000	.000
1.590	-.30	-150.0	.000	.000	.000	.000
1.590	-.30	-90.0	.000	.000	.000	.000
1.590	-.30	-30.0	.502	.192	.036	.015
1.590	-.30	30.0	.505	.254	.038	.020
1.590	-.30	90.0	.000	.000	.000	.000
1.590	-.30	150.0	.000	.000	.000	.000
1.590	-.10	-150.0	.000	.000	.000	.000
1.590	-.10	-90.0	.000	.000	.000	.000
1.590	-.10	-30.0	.504	.185	.025	.015
1.590	-.10	30.0	.506	.170	.029	.014
1.590	-.10	90.0	.000	.000	.000	.000
1.590	-.10	150.0	.000	.000	.000	.000
1.590	.10	-150.0	.000	.000	.000	.000
1.590	.10	-90.0	.000	.000	.000	.000
1.590	.10	-30.0	.499	.220	.057	.018
1.590	.10	30.0	.503	.201	.053	.016
1.590	.10	90.0	.000	.000	.000	.000
1.590	.10	150.0	.000	.000	.000	.000
1.590	.30	-150.0	.000	.000	.000	.000
1.590	.30	-90.0	.000	.000	.000	.000
1.590	.30	-30.0	.498	.471	.131	.038
1.590	.30	30.0	.497	.215	.074	.017
1.590	.30	90.0	.000	.000	.000	.000
1.590	.30	150.0	.000	.000	.000	.000
1.590	.50	-150.0	.000	.000	.000	.000
1.590	.50	-90.0	.000	.000	.000	.000
1.590	.50	-30.0	.000	.000	.000	.000
1.590	.50	30.0	.000	.000	.000	.000
1.590	.50	90.0	.000	.000	.000	.000
1.590	.50	150.0	.000	.000	.000	.000
1.590	.70	-150.0	.000	.000	.000	.000
1.590	.70	-90.0	.000	.000	.000	.000

1.590	.70	-30.0	.000	.000	.000	.000
1.590	.70	30.0	.000	.000	.000	.000
1.590	.70	90.0	.000	.000	.000	.000
1.590	.70	150.0	.000	.000	.000	.000
1.590	.90	-150.0	.000	.000	.000	.000
1.590	.90	-90.0	.000	.000	.000	.000
1.590	.90	-30.0	.000	.000	.000	.000
1.590	.90	30.0	.000	.000	.000	.000
1.590	.90	90.0	.000	.000	.000	.000
1.590	.90	150.0	.000	.000	.000	.000
1.615	-.90	-150.0	.503	.149	.024	.017
1.615	-.90	-90.0	.499	.158	.033	.018
1.615	-.90	-30.0	.502	.154	.018	.017
1.615	-.90	30.0	.504	.187	.020	.021
1.615	-.90	90.0	.505	.106	.025	.012
1.615	-.90	150.0	.503	.114	.018	.013
1.615	-.70	-150.0	.000	.000	.000	.000
1.615	-.70	-90.0	.000	.000	.000	.000
1.615	-.70	-30.0	.502	.145	.024	.016
1.615	-.70	30.0	.505	.149	.027	.017
1.615	-.70	90.0	.000	.000	.000	.000
1.615	-.70	150.0	.000	.000	.000	.000
1.615	-.50	-150.0	.000	.000	.000	.000
1.615	-.50	-90.0	.000	.000	.000	.000
1.615	-.50	-30.0	.501	.158	.029	.018
1.615	-.50	30.0	.501	.148	.029	.017
1.615	-.50	90.0	.000	.000	.000	.000
1.615	-.50	150.0	.000	.000	.000	.000
1.615	-.30	-150.0	.000	.000	.000	.000
1.615	-.30	-90.0	.000	.000	.000	.000
1.615	-.30	-30.0	.502	.190	.040	.021
1.615	-.30	30.0	.505	.198	.037	.022
1.615	-.30	90.0	.000	.000	.000	.000
1.615	-.30	150.0	.000	.000	.000	.000
1.615	-.10	-150.0	.000	.000	.000	.000
1.615	-.10	-90.0	.000	.000	.000	.000
1.615	-.10	-30.0	.500	.138	.033	.016
1.615	-.10	30.0	.499	.118	.030	.013
1.615	-.10	90.0	.000	.000	.000	.000
1.615	-.10	150.0	.000	.000	.000	.000
1.615	.10	-150.0	.000	.000	.000	.000
1.615	.10	-90.0	.000	.000	.000	.000
1.615	.10	-30.0	.492	.129	.058	.014
1.615	.10	30.0	.503	.120	.056	.014
1.615	.10	90.0	.000	.000	.000	.000
1.615	.10	150.0	.000	.000	.000	.000
1.615	.30	-150.0	.000	.000	.000	.000
1.615	.30	-90.0	.000	.000	.000	.000
1.615	.30	-30.0	.000	.000	.000	.000
1.615	.30	30.0	.000	.000	.000	.000
1.615	.30	90.0	.000	.000	.000	.000
1.615	.30	150.0	.000	.000	.000	.000
1.615	.50	-150.0	.000	.000	.000	.000
1.615	.50	-90.0	.000	.000	.000	.000
1.615	.50	-30.0	.000	.000	.000	.000

1.615	.50	30.0	.000	.000	.000	.000
1.615	.50	90.0	.000	.000	.000	.000
1.615	.50	150.0	.000	.000	.000	.000
1.615	.70	-150.0	.000	.000	.000	.000
1.615	.70	-90.0	.000	.000	.000	.000
1.615	.70	-30.0	.000	.000	.000	.000
1.615	.70	30.0	.000	.000	.000	.000
1.615	.70	90.0	.000	.000	.000	.000
1.615	.70	150.0	.000	.000	.000	.000
1.615	.90	-150.0	.000	.000	.000	.000
1.615	.90	-90.0	.000	.000	.000	.000
1.615	.90	-30.0	.000	.000	.000	.000
1.615	.90	30.0	.000	.000	.000	.000
1.615	.90	90.0	.000	.000	.000	.000
1.615	.90	150.0	.000	.000	.000	.000

$$Q^2 = 3.6 \text{ GeV}^2/c^2$$

W [GeV]	$\cos \theta_\eta^-$	ϕ_η [deg.]	ε	$\frac{d^2\sigma}{d\Omega_\eta^2}$ [$\frac{\mu\text{b}}{\text{sr}}$]	stat err [σ]	syst err [σ]
1.490	-.90	-150.0	.464	.091	.014	.015
1.490	-.90	-90.0	.468	.081	.013	.014
1.490	-.90	-30.0	.462	.091	.016	.015
1.490	-.90	30.0	.468	.107	.020	.018
1.490	-.90	90.0	.466	.095	.015	.016
1.490	-.90	150.0	.461	.070	.013	.012
1.490	-.70	-150.0	.468	.086	.015	.015
1.490	-.70	-90.0	.463	.094	.017	.016
1.490	-.70	-30.0	.466	.080	.016	.014
1.490	-.70	30.0	.465	.094	.016	.016
1.490	-.70	90.0	.464	.110	.018	.019
1.490	-.70	150.0	.461	.084	.016	.014
1.490	-.50	-150.0	.463	.088	.015	.015
1.490	-.50	-90.0	.461	.072	.013	.012
1.490	-.50	-30.0	.462	.099	.017	.017
1.490	-.50	30.0	.464	.085	.016	.014
1.490	-.50	90.0	.462	.109	.016	.019
1.490	-.50	150.0	.463	.110	.018	.019
1.490	-.30	-150.0	.464	.077	.015	.013
1.490	-.30	-90.0	.461	.079	.013	.013
1.490	-.30	-30.0	.465	.071	.013	.012
1.490	-.30	30.0	.469	.088	.015	.015
1.490	-.30	90.0	.462	.108	.017	.018
1.490	-.30	150.0	.464	.112	.019	.019
1.490	-.10	-150.0	.464	.091	.015	.016
1.490	-.10	-90.0	.460	.093	.016	.016
1.490	-.10	-30.0	.463	.076	.014	.013
1.490	-.10	30.0	.466	.091	.016	.015
1.490	-.10	90.0	.461	.095	.015	.016
1.490	-.10	150.0	.463	.096	.016	.016
1.490	.10	-150.0	.461	.130	.023	.022
1.490	.10	-90.0	.465	.071	.017	.012
1.490	.10	-30.0	.464	.089	.017	.015
1.490	.10	30.0	.463	.109	.020	.019
1.490	.10	90.0	.465	.111	.019	.019
1.490	.10	150.0	.465	.103	.018	.017
1.490	.30	-150.0	.462	.119	.024	.020
1.490	.30	-90.0	.465	.085	.018	.014
1.490	.30	-30.0	.466	.119	.029	.020
1.490	.30	30.0	.465	.073	.022	.012
1.490	.30	90.0	.466	.103	.026	.018
1.490	.30	150.0	.461	.105	.022	.018
1.490	.50	-150.0	.462	.114	.022	.019
1.490	.50	-90.0	.460	.118	.021	.020
1.490	.50	-30.0	.469	.089	.017	.015
1.490	.50	30.0	.464	.108	.021	.018
1.490	.50	90.0	.468	.100	.021	.017
1.490	.50	150.0	.464	.090	.021	.015

1.490	.70	-150.0	.463	.066	.016	.011
1.490	.70	-90.0	.464	.091	.017	.016
1.490	.70	-30.0	.460	.081	.016	.014
1.490	.70	30.0	.463	.089	.018	.015
1.490	.70	90.0	.464	.098	.019	.017
1.490	.70	150.0	.461	.101	.018	.017
1.490	.90	-150.0	.467	.087	.018	.015
1.490	.90	-90.0	.463	.105	.020	.018
1.490	.90	-30.0	.466	.107	.024	.018
1.490	.90	30.0	.464	.103	.019	.018
1.490	.90	90.0	.465	.111	.024	.019
1.490	.90	150.0	.466	.063	.021	.011
1.515	-.90	-150.0	.463	.168	.015	.009
1.515	-.90	-90.0	.465	.181	.015	.010
1.515	-.90	-30.0	.465	.167	.015	.009
1.515	-.90	30.0	.465	.152	.014	.008
1.515	-.90	90.0	.467	.165	.015	.009
1.515	-.90	150.0	.462	.154	.015	.008
1.515	-.70	-150.0	.462	.152	.014	.008
1.515	-.70	-90.0	.462	.145	.016	.008
1.515	-.70	-30.0	.467	.171	.016	.009
1.515	-.70	30.0	.463	.150	.015	.008
1.515	-.70	90.0	.461	.209	.020	.011
1.515	-.70	150.0	.463	.167	.015	.009
1.515	-.50	-150.0	.462	.168	.017	.009
1.515	-.50	-90.0	.464	.300	.044	.016
1.515	-.50	-30.0	.464	.151	.018	.008
1.515	-.50	30.0	.462	.158	.018	.008
1.515	-.50	90.0	.464	.213	.025	.011
1.515	-.50	150.0	.462	.151	.018	.008
1.515	-.30	-150.0	.463	.132	.019	.007
1.515	-.30	-90.0	.459	.171	.028	.009
1.515	-.30	-30.0	.461	.171	.016	.009
1.515	-.30	30.0	.465	.172	.018	.009
1.515	-.30	90.0	.466	.142	.031	.008
1.515	-.30	150.0	.463	.181	.022	.010
1.515	-.10	-150.0	.466	.182	.023	.010
1.515	-.10	-90.0	.465	.142	.041	.008
1.515	-.10	-30.0	.464	.189	.019	.010
1.515	-.10	30.0	.460	.178	.018	.010
1.515	-.10	90.0	.463	.178	.029	.010
1.515	-.10	150.0	.462	.145	.021	.008
1.515	.10	-150.0	.464	.205	.038	.011
1.515	.10	-90.0	.000	.000	.000	.000
1.515	.10	-30.0	.464	.166	.021	.009
1.515	.10	30.0	.465	.163	.021	.009
1.515	.10	90.0	.463	.252	.054	.013
1.515	.10	150.0	.462	.142	.023	.008
1.515	.30	-150.0	.461	.218	.043	.012
1.515	.30	-90.0	.000	.000	.000	.000
1.515	.30	-30.0	.465	.216	.024	.012
1.515	.30	30.0	.464	.171	.022	.009
1.515	.30	90.0	.458	.207	.056	.011
1.515	.30	150.0	.463	.143	.031	.008
1.515	.50	-150.0	.462	.132	.037	.007

1.515	.50	-90.0	.461	.175	.036	.009
1.515	.50	-30.0	.464	.143	.017	.008
1.515	.50	30.0	.464	.212	.023	.011
1.515	.50	90.0	.459	.256	.044	.014
1.515	.50	150.0	.462	.182	.031	.010
1.515	.70	-150.0	.463	.146	.031	.008
1.515	.70	-90.0	.465	.299	.061	.016
1.515	.70	-30.0	.463	.169	.023	.009
1.515	.70	30.0	.463	.165	.022	.009
1.515	.70	90.0	.466	.218	.030	.012
1.515	.70	150.0	.463	.227	.038	.012
1.515	.90	-150.0	.461	.200	.036	.011
1.515	.90	-90.0	.463	.163	.027	.009
1.515	.90	-30.0	.466	.240	.039	.013
1.515	.90	30.0	.460	.196	.031	.010
1.515	.90	90.0	.461	.181	.032	.010
1.515	.90	150.0	.462	.142	.027	.008
1.540	-.90	-150.0	.460	.146	.014	.009
1.540	-.90	-90.0	.459	.138	.015	.008
1.540	-.90	-30.0	.460	.171	.014	.010
1.540	-.90	30.0	.457	.169	.015	.010
1.540	-.90	90.0	.459	.149	.015	.009
1.540	-.90	150.0	.460	.164	.015	.010
1.540	-.70	-150.0	.460	.149	.018	.009
1.540	-.70	-90.0	.460	.180	.021	.011
1.540	-.70	-30.0	.461	.167	.014	.010
1.540	-.70	30.0	.463	.142	.013	.008
1.540	-.70	90.0	.459	.183	.019	.011
1.540	-.70	150.0	.458	.155	.015	.009
1.540	-.50	-150.0	.462	.180	.018	.011
1.540	-.50	-90.0	.000	.000	.000	.000
1.540	-.50	-30.0	.459	.156	.015	.009
1.540	-.50	30.0	.458	.183	.016	.011
1.540	-.50	90.0	.000	.000	.000	.000
1.540	-.50	150.0	.463	.177	.019	.010
1.540	-.30	-150.0	.462	.134	.019	.008
1.540	-.30	-90.0	.000	.000	.000	.000
1.540	-.30	-30.0	.460	.161	.020	.009
1.540	-.30	30.0	.458	.170	.018	.010
1.540	-.30	90.0	.000	.000	.000	.000
1.540	-.30	150.0	.459	.190	.022	.011
1.540	-.10	-150.0	.463	.167	.022	.010
1.540	-.10	-90.0	.000	.000	.000	.000
1.540	-.10	-30.0	.461	.183	.020	.011
1.540	-.10	30.0	.458	.152	.018	.009
1.540	-.10	90.0	.000	.000	.000	.000
1.540	-.10	150.0	.462	.146	.018	.009
1.540	.10	-150.0	.462	.187	.037	.011
1.540	.10	-90.0	.000	.000	.000	.000
1.540	.10	-30.0	.459	.166	.023	.010
1.540	.10	30.0	.459	.158	.023	.009
1.540	.10	90.0	.000	.000	.000	.000
1.540	.10	150.0	.463	.163	.032	.010
1.540	.30	-150.0	.463	.204	.039	.012
1.540	.30	-90.0	.000	.000	.000	.000

1.540	.30	-30.0	.462	.164	.021	.010
1.540	.30	30.0	.460	.188	.022	.011
1.540	.30	90.0	.000	.000	.000	.000
1.540	.30	150.0	.463	.133	.031	.008
1.540	.50	-150.0	.000	.000	.000	.000
1.540	.50	-90.0	.000	.000	.000	.000
1.540	.50	-30.0	.458	.162	.031	.010
1.540	.50	30.0	.461	.178	.031	.010
1.540	.50	90.0	.000	.000	.000	.000
1.540	.50	150.0	.000	.000	.000	.000
1.540	.70	-150.0	.000	.000	.000	.000
1.540	.70	-90.0	.000	.000	.000	.000
1.540	.70	-30.0	.459	.173	.028	.010
1.540	.70	30.0	.460	.143	.024	.008
1.540	.70	90.0	.000	.000	.000	.000
1.540	.70	150.0	.000	.000	.000	.000
1.540	.90	-150.0	.000	.000	.000	.000
1.540	.90	-90.0	.000	.000	.000	.000
1.540	.90	-30.0	.449	.212	.049	.012
1.540	.90	30.0	.452	.151	.034	.009
1.540	.90	90.0	.000	.000	.000	.000
1.540	.90	150.0	.000	.000	.000	.000
1.565	-.90	-150.0	.455	.135	.011	.010
1.565	-.90	-90.0	.459	.111	.011	.008
1.565	-.90	-30.0	.457	.119	.011	.009
1.565	-.90	30.0	.454	.112	.009	.008
1.565	-.90	90.0	.457	.118	.011	.009
1.565	-.90	150.0	.454	.126	.011	.009
1.565	-.70	-150.0	.456	.137	.014	.010
1.565	-.70	-90.0	.457	.153	.030	.011
1.565	-.70	-30.0	.453	.142	.014	.010
1.565	-.70	30.0	.455	.160	.015	.012
1.565	-.70	90.0	.456	.106	.019	.008
1.565	-.70	150.0	.457	.159	.015	.012
1.565	-.50	-150.0	.458	.136	.016	.010
1.565	-.50	-90.0	.000	.000	.000	.000
1.565	-.50	-30.0	.455	.151	.016	.011
1.565	-.50	30.0	.456	.135	.014	.010
1.565	-.50	90.0	.000	.000	.000	.000
1.565	-.50	150.0	.457	.159	.017	.012
1.565	-.30	-150.0	.000	.000	.000	.000
1.565	-.30	-90.0	.000	.000	.000	.000
1.565	-.30	-30.0	.454	.132	.017	.010
1.565	-.30	30.0	.455	.156	.017	.011
1.565	-.30	90.0	.000	.000	.000	.000
1.565	-.30	150.0	.461	.121	.029	.009
1.565	-.10	-150.0	.000	.000	.000	.000
1.565	-.10	-90.0	.000	.000	.000	.000
1.565	-.10	-30.0	.457	.154	.017	.011
1.565	-.10	30.0	.458	.126	.016	.009
1.565	-.10	90.0	.000	.000	.000	.000
1.565	-.10	150.0	.000	.000	.000	.000
1.565	.10	-150.0	.000	.000	.000	.000
1.565	.10	-90.0	.000	.000	.000	.000
1.565	.10	-30.0	.455	.135	.025	.010

1.565	.10	30.0	.453	.131	.025	.010
1.565	.10	90.0	.000	.000	.000	.000
1.565	.10	150.0	.000	.000	.000	.000
1.565	.30	-150.0	.000	.000	.000	.000
1.565	.30	-90.0	.000	.000	.000	.000
1.565	.30	-30.0	.456	.148	.020	.011
1.565	.30	30.0	.454	.153	.020	.011
1.565	.30	90.0	.000	.000	.000	.000
1.565	.30	150.0	.000	.000	.000	.000
1.565	.50	-150.0	.000	.000	.000	.000
1.565	.50	-90.0	.000	.000	.000	.000
1.565	.50	-30.0	.456	.157	.032	.012
1.565	.50	30.0	.454	.147	.029	.011
1.565	.50	90.0	.000	.000	.000	.000
1.565	.50	150.0	.000	.000	.000	.000
1.565	.70	-150.0	.000	.000	.000	.000
1.565	.70	-90.0	.000	.000	.000	.000
1.565	.70	-30.0	.450	.111	.035	.008
1.565	.70	30.0	.452	.155	.041	.011
1.565	.70	90.0	.000	.000	.000	.000
1.565	.70	150.0	.000	.000	.000	.000
1.565	.90	-150.0	.000	.000	.000	.000
1.565	.90	-90.0	.000	.000	.000	.000
1.565	.90	-30.0	.000	.000	.000	.000
1.565	.90	30.0	.000	.000	.000	.000
1.565	.90	90.0	.000	.000	.000	.000
1.565	.90	150.0	.000	.000	.000	.000
1.590	-.90	-150.0	.455	.096	.008	.007
1.590	-.90	-90.0	.453	.095	.009	.007
1.590	-.90	-30.0	.454	.091	.008	.006
1.590	-.90	30.0	.452	.093	.008	.007
1.590	-.90	90.0	.452	.123	.011	.009
1.590	-.90	150.0	.452	.097	.008	.007
1.590	-.70	-150.0	.457	.098	.012	.007
1.590	-.70	-90.0	.000	.000	.000	.000
1.590	-.70	-30.0	.453	.104	.011	.007
1.590	-.70	30.0	.454	.127	.012	.009
1.590	-.70	90.0	.000	.000	.000	.000
1.590	-.70	150.0	.453	.125	.013	.009
1.590	-.50	-150.0	.000	.000	.000	.000
1.590	-.50	-90.0	.000	.000	.000	.000
1.590	-.50	-30.0	.453	.110	.013	.008
1.590	-.50	30.0	.453	.114	.013	.008
1.590	-.50	90.0	.000	.000	.000	.000
1.590	-.50	150.0	.000	.000	.000	.000
1.590	-.30	-150.0	.000	.000	.000	.000
1.590	-.30	-90.0	.000	.000	.000	.000
1.590	-.30	-30.0	.454	.118	.020	.008
1.590	-.30	30.0	.451	.113	.018	.008
1.590	-.30	90.0	.000	.000	.000	.000
1.590	-.30	150.0	.000	.000	.000	.000
1.590	-.10	-150.0	.000	.000	.000	.000
1.590	-.10	-90.0	.000	.000	.000	.000
1.590	-.10	-30.0	.453	.117	.015	.008
1.590	-.10	30.0	.451	.098	.014	.007

1.590	-.10	90.0	.000	.000	.000	.000
1.590	-.10	150.0	.000	.000	.000	.000
1.590	.10	-150.0	.000	.000	.000	.000
1.590	.10	-90.0	.000	.000	.000	.000
1.590	.10	-30.0	.453	.088	.023	.006
1.590	.10	30.0	.449	.071	.016	.005
1.590	.10	90.0	.000	.000	.000	.000
1.590	.10	150.0	.000	.000	.000	.000
1.590	.30	-150.0	.000	.000	.000	.000
1.590	.30	-90.0	.000	.000	.000	.000
1.590	.30	-30.0	.452	.112	.029	.008
1.590	.30	30.0	.453	.127	.029	.009
1.590	.30	90.0	.000	.000	.000	.000
1.590	.30	150.0	.000	.000	.000	.000
1.590	.50	-150.0	.000	.000	.000	.000
1.590	.50	-90.0	.000	.000	.000	.000
1.590	.50	-30.0	.456	.073	.029	.005
1.590	.50	30.0	.450	.097	.026	.007
1.590	.50	90.0	.000	.000	.000	.000
1.590	.50	150.0	.000	.000	.000	.000
1.590	.70	-150.0	.000	.000	.000	.000
1.590	.70	-90.0	.000	.000	.000	.000
1.590	.70	-30.0	.000	.000	.000	.000
1.590	.70	30.0	.000	.000	.000	.000
1.590	.70	90.0	.000	.000	.000	.000
1.590	.70	150.0	.000	.000	.000	.000
1.590	.90	-150.0	.000	.000	.000	.000
1.590	.90	-90.0	.000	.000	.000	.000
1.590	.90	-30.0	.000	.000	.000	.000
1.590	.90	30.0	.000	.000	.000	.000
1.590	.90	90.0	.000	.000	.000	.000
1.590	.90	150.0	.000	.000	.000	.000
1.615	-.90	-150.0	.451	.065	.007	.007
1.615	-.90	-90.0	.449	.074	.008	.008
1.615	-.90	-30.0	.449	.075	.007	.008
1.615	-.90	30.0	.453	.077	.007	.008
1.615	-.90	90.0	.448	.080	.009	.008
1.615	-.90	150.0	.448	.076	.008	.008
1.615	-.70	-150.0	.451	.078	.011	.008
1.615	-.70	-90.0	.000	.000	.000	.000
1.615	-.70	-30.0	.450	.077	.009	.008
1.615	-.70	30.0	.451	.086	.009	.009
1.615	-.70	90.0	.000	.000	.000	.000
1.615	-.70	150.0	.455	.084	.011	.009
1.615	-.50	-150.0	.000	.000	.000	.000
1.615	-.50	-90.0	.000	.000	.000	.000
1.615	-.50	-30.0	.448	.086	.011	.009
1.615	-.50	30.0	.446	.095	.012	.010
1.615	-.50	90.0	.000	.000	.000	.000
1.615	-.50	150.0	.000	.000	.000	.000
1.615	-.30	-150.0	.000	.000	.000	.000
1.615	-.30	-90.0	.000	.000	.000	.000
1.615	-.30	-30.0	.454	.100	.017	.010
1.615	-.30	30.0	.451	.070	.013	.007
1.615	-.30	90.0	.000	.000	.000	.000

1.615	-.30	150.0	.000	.000	.000	.000
1.615	-.10	-150.0	.000	.000	.000	.000
1.615	-.10	-90.0	.000	.000	.000	.000
1.615	-.10	-30.0	.450	.089	.019	.009
1.615	-.10	30.0	.452	.089	.018	.009
1.615	-.10	90.0	.000	.000	.000	.000
1.615	-.10	150.0	.000	.000	.000	.000
1.615	.10	-150.0	.000	.000	.000	.000
1.615	.10	-90.0	.000	.000	.000	.000
1.615	.10	-30.0	.448	.068	.017	.007
1.615	.10	30.0	.454	.042	.013	.004
1.615	.10	90.0	.000	.000	.000	.000
1.615	.10	150.0	.000	.000	.000	.000
1.615	.30	-150.0	.000	.000	.000	.000
1.615	.30	-90.0	.000	.000	.000	.000
1.615	.30	-30.0	.451	.081	.024	.008
1.615	.30	30.0	.446	.075	.018	.008
1.615	.30	90.0	.000	.000	.000	.000
1.615	.30	150.0	.000	.000	.000	.000
1.615	.50	-150.0	.000	.000	.000	.000
1.615	.50	-90.0	.000	.000	.000	.000
1.615	.50	-30.0	.450	.061	.030	.006
1.615	.50	30.0	.450	.059	.029	.006
1.615	.50	90.0	.000	.000	.000	.000
1.615	.50	150.0	.000	.000	.000	.000
1.615	.70	-150.0	.000	.000	.000	.000
1.615	.70	-90.0	.000	.000	.000	.000
1.615	.70	-30.0	.000	.000	.000	.000
1.615	.70	30.0	.000	.000	.000	.000
1.615	.70	90.0	.000	.000	.000	.000
1.615	.70	150.0	.000	.000	.000	.000
1.615	.90	-150.0	.000	.000	.000	.000
1.615	.90	-90.0	.000	.000	.000	.000
1.615	.90	-30.0	.000	.000	.000	.000
1.615	.90	30.0	.000	.000	.000	.000
1.615	.90	90.0	.000	.000	.000	.000
1.615	.90	150.0	.000	.000	.000	.000

Appendix D

List of Collaborators

C. S. Armstrong², V. V. Frolov⁷,
P. Stoler⁷ (co-spokesman), J. Napolitano⁷ (co-spokesman),
G. Adams⁷, A. Ahmidouch^{3,4}, K. Assamagan³, S. Avery³, O. K. Baker^{3,8}, P. Bosted¹,
V. Burkert⁸, R. Carlini⁸, J. Dunne⁸, T. Eden³, R. Ent⁸, D. Gaskell⁶, A. P. Grosse¹², P. Guèye³,
W. Hinton³, C. E. Keppel^{3,8}, W. Kim⁵, M. Klusman⁷, D. Koltenuk⁹, D. Mack⁸, R. Madey^{3,4},
D. Meekins², R. Minehart¹⁰, J. Mitchell⁸, H. Mkrtchyan¹¹, G. Niculescu³, I. Niculescu³,
M. Nozar⁷, J. W. Price⁷, V. Tadevosyan¹¹, L. Tang^{3,8}, M. Witkowski⁷, S. Wood⁸

¹ *Physics Department, American University, Washington D.C. 20016, USA*

² *Department of Physics, College of William & Mary, Williamsburg, VA 23187, USA*

³ *Physics Department, Hampton University, Hampton, VA 23668, USA*

⁴ *Physics Department, Kent State University, Kent, OH 44242, USA*

⁵ *Physics Department, Kyungpook National University, Taegu, South Korea*

⁶ *Physics Department, Oregon State University, Corvallis, OR 97331, USA*

⁷ *Physics Department, Rensselaer Polytechnic Institute, Troy, NY 12180, USA*

⁸ *Thomas Jefferson National Accelerator Facility, Newport News, VA 23606, USA*

⁹ *Physics Department, University of Pennsylvania, Philadelphia, PA 19104, USA*

¹⁰ *Physics Department, University of Virginia, Charlottesville, VA 22903, USA*

¹¹ *Yerevan Physics Institute, Yerevan, Armenia*

¹² *Honorary Collaborator (wink!)*

Bibliography

- [NOTE] The Jefferson Lab User Liaison office can provide assistance locating unpublished TJNAF documents.
- [Abb94] D. Abbott and D. F. Geesaman, *Wire translation in the HMS and SOS Spectrometers*, TJNAF Hall C document (unpublished) (1994).
- [Abb95] D. J. Abbott, *et al.*, *The CODA System and its Performance in the First Online Experiments at CEBAF*, Proceedings of the 1995 IEEE Conference on Real-Time Computer Applications in Nuclear, Particle and Plasma Physics (May 1995), pp. 147–151.
- [Ald75] J. Alder, *et al.*, *Nuc. Phys.* **B91** 386 (1975).
- [All94] C. R. Allton, *et al.*, *Phys. Rev.* **D49** 474 (1994).
- [Alt79] K. H. Althoff, *et al.*, *Z. Phys.* **C1** 327 (1979).
- [Arr96] J. Arrington, *Optimizing the Performance of the Hall C Detectors* (talk proceedings), (unpublished) (1996).
- [Ass97] K. A. Assamagan, D. Dutta, and P. Welch, *Hall C Matrix Element Optimization Package*, TJNAF Hall C document (unpublished) (1997).
- [Baj69] R. Bajpai and A. Donnachie, *Nuc. Phys.* **B12** 274 (1969).
- [Bec74] U. Beck, *et al.*, *Phys. Lett.* **51B** 103 (1974).
- [Ben91] M. Benmerrouche and N. Mukhopadhyay, *Phys. Rev. Lett.* **67** 1070 (1991), and references therein.

- [Ben95] M. Benmerrouche, *et al.*, Phys. Rev. **D51** 3237 (1995).
- [Ben96] M. Benmerrouche, *et al.*, Phys. Rev. Lett **77** 4716 (1996).
- [Ben97] M. Benmerrouche, George Washington/TJNAF Workshop on N^* Physics (October 1997).
- [Benn91] C. Bennhold and H. Tanabe, Nuc. Phys. **A530** 625 (1991).
- [Bev69] P. R. Bevington, *Data Reduction and Error Analysis for the Physical Sciences*, McGraw-Hill (1969).
- [Ber90] M. Berz, Nuc. Inst. and Meth., **A298** 426 (1990); Nuc. Inst. and Meth., **A298** 473 (1990).
- [Blu93] W. Blum and L. Rolandi, *Particle Detection with Drift Chambers*, Springer-Verlag (1993).
- [Boc96] C. Bochna, *Unser Monitor Absolute Calibration*, TJNAF Hall C Document (unpublished) (1996).
- [Bol94] J. Bolz, P. Kroll, and J. G. Körner, Z. Phys. **A350** 145 (1994).
- [Bra78] F. Brasse, *et al.*, Nuc. Phys. **B139** 37 (1978).
- [Bra84] F. Brasse, *et al.*, Z. Phys. **C22** 33 (1984).
- [Bre78] H. Breuker, *et al.*, Phys. Lett. **74B** 409 (1978).
- [Bur88] V. Burkert, *Excited Baryons 1988*, Proceedings of the Topical Workshop, World Scientific (1988), pp. 122-139.
- [Bur98] V. Burkert, personal communication (1998).
- [But94] F. Butler, *et al.*, Nuc. Phys. **B430** 179 (1994).
- [Cap86] S. Capstick and N. Isgur, Phys. Rev. **D34** 2809 (1986).
- [Cap88] S. Capstick, *Excited Baryons 1988*, Proceedings of the Topical Workshop, World Scientific (1988), pp. 32-53.
- [Cap92] S. Capstick, Phys. Rev. **D46** 1965 (1992); Phys. Rev. **D46** 2864 (1992).
- [Cap95] S. Capstick and B. D. Keister, Phys. Rev. **D51** 3598 (1995).

- [Cap98] This is a calculation in the light-front model of Ref. [Cap95], but (in contrast to the published work) using standard convention for the normalization of states, and incorporating several other changes to the calculation. This effort is ongoing at the time of this writing. S. Capstick, personal communication, (1998).
- [Car86] C. E. Carlson, Phys. Rev. **D34** 2704 (1986).
- [Car88] C. E. Carlson and J. L. Poor, Phys. Rev. **D38** 2758 (1988).
- [Car95] C. E. Carlson and N. Mukhopadhyay, Phys. Rev. Lett. **74** 1288 (1995).
- [CDR91] *Conceptual Design Report*, TJNAF Document (unpublished) (1991).
- [CERNL] *HBOOK—Statistical Analysis and Histogramming*, CERN Program Library Long Writeup Y250, Version 4.24 (1995); *PAW—Physics Analysis Workstation*, CERN Program Library Long Writeup Q121, (1995); *MINUIT—Function Minimization and Error Analysis*, CERN Program Library Long Writeup D506, Version 94.1 (1994).
- [Clo90] F. Close and Z. Li, Phys. Rev. **D42** 2194 (1990).
- [Cop69] L. A. Copley, G. Karl, and E. Obryk, Nuc. Phys. **B13** 303 (1969).
- [Cum96] W. Cummings, The SOS Handbook, Rev. 1.1, TJNAF Hall C Document (unpublished) (1996).
- [Den94] J. Denschlag, Diplomarbeit, Universität Mainz (1994).
- [Dre72] S. D. Drell and K. Johnson, Phys. Rev. **D6** 3249 (1972).
- [Dun97] J. Dunne, *Cryo and Dummy Target Information*, TJNAF Hall C document (unpublished) (1997).
- [Dyt95] S. Dytman, *et al.*, Phys. Rev. **C51** 2710 (1995).
- [Ear73] R. A. Early, Nucl. Inst. and Meth., **109** 93 (1973).
- [Ent97] R. Ent, personal communication (1997).
- [EPI94] W. A. Watson III, *et al.*, Nuc. Inst. and Meth., **A352** 118 (1994); M. Knott, *et al.*, Nuc. Inst. and Meth., **A352** 486 (1994).

- [Fey71] R. P. Feynman, *et al.*, Phys. Rev. D3 2706 (1971).
- [Fos82] F. Foster and G. Hughes, Z. Phys. C14 123 (1982).
- [Fro98] V. Frolov, dissertation, Rensselaer Polytechnic Institute (unpublished) (1998).
- [Gar85] M. Gari and W. Krümpelmann, Z. Phys. A322 689 (1985).
- [Gee93] D. F. Geesaman, *Tracking in the SOS Spectrometer*, TJNAF Hall C document (unpublished) (1993).
- [Gel64] M. Gell-Mann, Phys. Lett. 8 214 (1964).
- [God85] S. Godfrey and N. Isgur, Phys. Rev. D32 189 (1985).
- [Gre64] O. W. Greenberg, Phys. Rev. Lett. 13 598 (1964).
- [Gro93] F. Gross, *Relativistic Quantum Mechanics and Field Theory*, John Wiley & Sons, Inc. (1993).
- [Gue96] P. Guèye, *et al.*, *Hall C Beam Energy Measurement*, TJNAF Hall C document (unpublished) (1996).
- [Gus96] K. Gustafsson, *Cryotarget Density Dependence on Beam Current*, TJNAF Hall C document (unpublished) (1996).
- [Hai79] R. Haidan, dissertation, Hamburg University (unpublished) (1979).
- [Hal84] F. Halzen and A. D. Martin, *Quarks and Leptons: An Introductory Course in Modern Particle Physics*, John Wiley & Sons (1984).
- [Han63] L. N. Hand, Phys. Rev. 129 1834 (1963).
- [Har89] L. H. Harwood, *et al.*, CEBAF-PR-89-006 (1989).
- [Hen65] A. Hendry, *et al.*, Phys. Lett. 18 171 (1965).
- [Heu70] C. Heusch, *et al.*, Phys. Rev. Lett. 25 1381 (1970).
- [Hor73] R. Horgan and R. H. Dalitz, Nuc. Phys. B66 135 (1973).
- [Hor74] R. Horgan, Nuc. Phys. B71 514 (1974).

- [Isg77] N. Isgur and G. Karl, Phys. Lett. **72B** 109 (1977).
- [Isg78] N. Isgur and G. Karl, Phys. Lett. **74B** 353 (1978).
- [Isg83] N. Isgur and J. Paton, Phys. Lett. **124B** 247 (1983); Phys. Rev. **D31** 2910 (1985).
- [Isg84] N. Isgur and C. H. Llewellyn Smith, Phys. Rev. Lett. **52** 1080 (1984).
- [Isg91] N. Isgur, *Modern Topics in Electron Scattering*, B. Frois and I. Sick, eds., World Scientific (1991), pp. 2-27.
- [Jac59] M. Jacob and G. C. Wick, Ann. Phys. **7** 404 (1959).
- [Jon65] H. F. Jones, Nuovo Cimento **40** 1018 (1965).
- [Kai95] N. Kaiser, *et al.*, Phys. Lett. **B362** 23 (1995).
- [Kai97] N. Kaiser, *et al.*, Nuc. Phys. **A612** 297 (1997).
- [Kel97] J. J. Kelly, *et al.*, TJNAF Proposal E96-01, *Recoil Polarization in η Electroproduction* (1996).
- [Kep94] C. Keppel, *et al.*, Workshop on CEBAF at Higher Energies, p. 237 (1994). This is a global fit to SLAC resonance electroproduction data. A similar fit, but to a reduced data set, is found in L. M. Stuart, *et al.*, preprint hep-ph/9612416, referenced with the author's permission (accepted for publication in Phys. Rev. D, 1998). In the kinematic region where we employ these fits (*i.e.*, $Q^2 \approx 3.6 \text{ GeV}^2/c^2$, $W \approx 1.5 \text{ GeV}$), they are in agreement at the 2% level. Both of these fits are similar to earlier work done by Bodek [A. Bodek, Phys. Rev. **D20** 1471 (1979)] and by Stoler (Refs. [Sto91a, Sto91b]).
- [Kon80] R. Koniuk and N. Isgur, Phys. Rev. **D21** 1868 (1980).
- [Kon90] W. Konen & H. J. Weber, Phys. Rev. **D41** 2201 (1990).
- [Kno95] G. Knöchlein, *et al.*, Z. Phys. **A352** 327 (1995).
- [Kra93] G. Krafft and A. Hofler, *How the Linac Beam Position Monitors Work*, CEBAF-TN-93-004 (1993).
- [Kro92] P. Kroll, M. Schürmann, and W. Schweiger, Z. Phys. **A342** 429 (1992).

- [Kru95] B. Krusche, *et al.*, Phys. Rev. Lett. **74** 3736 (1995).
- [Kub76] T. Kubata and K. Ohta, Phys. Lett. **65B** 374 (1976).
- [Kum73] P. Kummer, *et al.*, Phys. Rev. Lett. **30** 873 (1973).
- [Lee74] M. Leenen, dissertation, Bonn University, P.I.B. 1-248 (1974).
- [Lei92] D. Leinweber, *et al.*, Phys. Rev. **D46** 3067 (1992).
- [Leo94] W. R. Leo, *Techniques for Nuclear and Particle Physics Experiments*, Springer-Verlag (1994).
- [Lep80] G. P. Lepage and S. J. Brodsky, Phys. Rev. **D22** 2157 (1980).
- [Li90] Z. Li and F. Close, Phys. Rev. **D42** 2207 (1990).
- [Li95] Z. Li Phys. Rev. **D52** 4961 (1995).
- [Li96] Z. Li and R. Workman, preprint (1995).
- [Mac98] D. Mack, personal communication (1998).
- [Mak94] N. Makins, dissertation, Massachusetts Institute of Technology (unpublished) (1994).
- [Mak98] N. Makins, R. Ent, D. Wasson, *et al.*, to be published.
- [Mar97] E. Marcus, *Vegan: The New Ethics of Eating*, McBooks Press, Ithaca, NY (1997).
- [Mee98] D. Meekins, dissertation, College of William & Mary (unpublished) (1998).
- [Mo69] L. W. Mo and Y. S. Tsai, Rev. Mod. Phys. **41** 205 (1969).
- [Muk95] N. Mukhopadhyay, *et al.*, Phys. Lett. **364B** 1 (1995).
- [Muk96] N. Mukhopadhyay, *et al.*, CEBAF/INT Workshop on N^* Physics (September, 1996).
- [Neu92] D. Neuffer, *et al.*, *A Brief Summary of Hall C Beam Energy Measurement*, TJNAF Hall C document (unpublished) (1992).
- [Nic96] G. Niculescu, *Resonant Cavities Used as Beam Current Monitors*, TJNAF Hall C document (unpublished) (1996).

- [Nic97] G. Niculescu, *On Pathlengths and Corrected Coincidence Time*, TJNAF Hall C document (unpublished) (1997).
- [Nic98] I. Niculescu, dissertation, Hampton University (unpublished) (1998). At the time of this writing, the dissertation of I. Niculescu (which revolves around a fit to recent TJNAF inclusive data) was in progress. The fitting strategy is similar to that of Ref. [Kep94], which we use elsewhere in this work.
- [OBr74] J. T. O'Brien, H. Crannel, *et al.*, *Phys. Rev. C* **9**, 1418 (1974).
- [ONe94] T. G. O'Neill, dissertation, California Institute of Technology (unpublished) (1994).
- [PDG76] Particle Data Group, *Rev. Mod. Phys.* **48** S157 (1976).
- [PDG98] C. Caso, *et al.*, *European Physical Journal*, **C3**, 1 (1998).
- [Per87] D. H. Perkins, *Introduction to High Energy Physics*, Third Edition, Addison-Wesley Publishing Co., Inc. (1987).
- [Pev61] A. Pevsner, *et al.*, *Phys. Rev. Lett.* **7** 421 (1961).
- [Pot98] D. Potterveld, personal communication.
- [Pre92] W. H. Press, *et al.*, *Numerical Recipes in Fortran*, Second Ed., Cambridge University Press (1992).
- [Pri95] J. W. Price, *et al.*, *Phys. Rev. C* **51** R2283 (1995).
- [Rad91] A. V. Radyushkin, *Nuc. Phys. A* **527** 153c (1991).
- [Rav71] F. Ravndal, *Phys. Rev. D* **4** 1466 (1971).
- [Rol92] B. Rollin, *Animal Rights and Human Morality*, Prometheus Books, Buffalo, NY (1992).
- [Ruj75] A. De Rújula, H. Georgi, S. L. Glashow, *Phys. Rev. D* **12** 147 (1975).
- [Sau78] R. Sauerwein, dissertation, Bonn University, Bonn-IR-78-13 (1978).
- [Spi96] M. Spiegel, *The Dreaded Comparison: Human and Animal Slavery*, Mirror Books, New York (1996).

- [Sta95] R. Stanley and H. Weber, Phys. Rev. C52 435 (1995).
- [Sto91a] P. Stoler, Phys. Rev. Lett. 66 1003 (1991).
- [Sto91b] P. Stoler, Phys. Rev. D44 73 (1991).
- [Sto93] P. Stoler, Phys. Reports 226 103 (1993).
- [Sto97] P. Stoler, *et al.*, Extension to TJNAF E94-14, *Baryon Resonance Electroproduction at High Momentum Transfer*, (1997).
- [TAS82] TASSO Note 192, (1982).
- [Ter98] B. Terburg, dissertation, University of Illinois (unpublished) (1998).
- [Tia94] L. Tiator, Nuc. Phys. A580 455 (1994).
- [Tra80] "Transport—A Computer Program for Designing Charged Particle Beam Transport Systems," K. L. Brown, *et al.*, CERN 80-04, Super Proton Synchrotron Division (1980).
- [Tsa61] Y. S. Tsai, Phys. Rev. 122 1898 (1961).
- [Tsa74] Y. S. Tsai, Rev. Mod. Phys. 46 815 (1974).
- [Uns91] K.B. Unser, "The Parametric Current Transformer, a Beam Current Monitor Developed for LEP", CERN SL/91-42 (1991); documentation on the Unser is also available from the manufacturer, Bergoz.
- [Veg98] Vegan Outreach, *Why Vegan?*, 211 Indian Dr., Pittsburgh, PA 15238 (1998).
- [Wac76] K. Wacker, DESY, Internal Report F1-76/4 (1976).
- [Wal69] R. L. Walker, Phys. Rev 182 1729 (1969).
- [War90] M. Warns, *et al.*, Z. Phys. C45 613 (1990); Z. Phys. C45 627 (1990); Phys. Rev. D42 2215 (1990).
- [Wes96] D. van Westrum, *Measurement of the Tracking Efficiency*, TJNAF Hall C document (unpublished) (1996).
- [Wes97] D. van Westrum, *Measurement and Estimation of Proton Absorption in the Hall C Spectrometers*, TJNAF Hall C document (unpublished) (1997).

- [Yan91] C. Yan, *Preliminary User's Manual of the High Momentum Spectrometer at CEBAF*, TJNAF Hall C document (unpublished) (1991).
- [Yan92] C. Yan, *et al.*, CEBAF-PR-92-003 (1992).
- [Yan93] C. Yan, *et al.*, CEBAF-PR-93-004 (1993).
- [Yan94] C. Yan, CEBAF-PR-94-002 (1994).
- [Yan95] C. Yan, *et al.*, CEBAF-PR-95-049 (1995).
- [Zwe64] G. Zweig, CERN Report No. 8182/Th.401 (unpublished) (1964); CERN Report No. 8419/Th.412 (unpublished) (1964).

Vita

Christopher Stephen Armstrong

The author was born in Pasadena, California, May 2, 1964. He graduated from Robinson High School in Fairfax, Virginia, June 1982 and received a B.S. Electrical Engineering from the University of Virginia in May 1987. He then spent several years working for Texas Instruments in Dallas and later at two companies in northern Virginia. He was married to Alejandra Patricia Grosse in May 1990, and began graduate school at the College of William & Mary in 1992. In May, 1994 he received a M.S. Physics, and in August 1998 a Ph.D., both from the College. He and his wife and his kids (raised in Williamsburg while Dad finished school) consider the future wide open.

